Université Ferhat ABBAS Sétif 1

FERHAT ABBAS UNIVERSITY - SETIF 1

FACULTY OF SCIENCES

THESIS

Presented to the Department of Chemistry

For obtaining the diploma of

DOCTORATE

Field: Material Science

Speciality: Chemistry **Option: Physical Chemistry**

By

SAADALLAH Yaakoub

THEME

Design and Study of the Physical Properties of New Magnetic and/or Luminescent Molecular Materials

Defended on 27/02/2025 before the Jury:

SELLOUM Djamel	Professor	Setif 1-Ferhat Abbas University	President
SETIFI Fatima	Professor	Setif 1-Ferhat Abbas University	Thesis Director
BELKHIRI Lotfi	Professor	constantine 1- Frères Mentouri University	Reviewer
KABOUB Lakhemici	Professor	Setif 1-Ferhat Abbas University	Reviewer
ADDALA Abderazak	M.C.A.	Setif 1-Ferhat Abbas University	Reviewer
SAHARI Ali	Ex-Professor	Setif 1-Ferhat Abbas University	Guest member

Acknowledgments

Table of Contents

Chapter III. Study of the Corrosion Inhibition of XC48 Carbon Steel by Triazole Based Compounds in 1M HCl Acid Medium

Chapter IV. Design and Synthesis of 1,2,4-Triazole-Based Schiff Base Ligands: Unveiling Novel Coordination Complexes with Transition Metals

List of abbreviation

SCO = Spin crossover

HS = High spin

LS = Low spin

T½ : Temperature corresponding to 50% spin state conversion

T½↑ : Half-transition temperature in the heating mode

T½↓ : Half-transition temperature in the cooling mode

χmT : Molar magnetic susceptibility times temperature

LD-LISC = Ligand-Driven Light Induced Spin Crossover

LIESST = Light Induced Excited Spin State Trapping

TIESST = Thermally Induced Excited Spin-State Trapping

SMM = single-molecule magnet

NCS = thiocyanate

dca = dicyanamide

Trz-A = 1-phenyl-N-(4H-1,2,4-triazol-4-yl)methanimine

Trz-B = 2-(((4H-1,2,4-triazol-4-yl)imino)methyl)phenol

Trz-C = 2-(((4H-1,2,4-triazol-4-yl)imino)methyl)-4-bromophenol

Trz-D = 1-(3-bromophenyl)-N-(4H-1,2,4-triazol-4-yl)methanimine

Trz-E = 1-p-tolyl-N-(4H-1,2,4-triazol-4-yl)methanimine

SQUID = Superconducting quantum interference device

XRD = X-ray diffraction

DFT = Density Functional Theory

General Introduction

This comprehensive research endeavor delves into the captivating realm of molecular materials, with a particular focus on two distinct areas – spin crossover (SCO) phenomena and corrosion inhibition. These fields, while seemingly disparate, share a common thread – the ability to manipulate and exploit molecular properties to achieve desired functionalities, paving the way for innovative technological advancements that transcend traditional boundaries.

SCO compounds possess a remarkable characteristic – the ability to undergo a reversible transition between low-spin and high-spin electronic configurations in response to external stimuli such as temperature, light, pressure, or the application of electromagnetic fields [1]. This switching behavior, often accompanied by dramatic changes in the compound's physical properties, including color, magnetism, conductivity, and structural parameters, has garnered significant attention for its potential applications in a wide array of fields, including data storage, display technologies, molecular electronics, spintronics, and sensors [2]. The prospect of harnessing these materials for the development of novel switchable devices, capable of adapting their properties on demand, has fueled intensive research efforts worldwide, driving the exploration of new synthetic routes, characterization techniques, and theoretical frameworks to deepen our understanding of these captivating systems.

However, despite the immense potential of SCO materials, several challenges related to solubility, long-term stability, and the preservation of the SCO behavior under ambient conditions have hindered the realization of practical devices based on these compounds [3]. Factors such as structural distortions, cooperative effects, and the influence of intermolecular interactions on the spin transition process have necessitated further exploration and innovative solutions to overcome these hurdles, paving the way for the development of robust and reliable SCO-based technologies.

On the other hand, corrosion, a ubiquitous phenomenon characterized by the degradation of materials due to chemical reactions with their environment, poses a significant economic and safety challenge across various industries, including oil and gas, construction, transportation, and infrastructure. The detrimental effects of corrosion not only result in substantial financial losses but also raise serious concerns regarding structural integrity, environmental impact, and potential hazards to human health and safety. Organic corrosion inhibitors have emerged as a powerful

strategy to combat this pervasive issue, offering a cost-effective and environmentally friendly approach to mitigate the corrosion of metallic structures [4].

By adsorbing onto metal surfaces, these organic molecules form protective barriers that impede the corrosion process, effectively extending the lifespan of metallic structures and reducing the need for frequent maintenance or replacement. Understanding the intricate relationships between the molecular structure, electronic properties, and corrosion inhibition performance of these organic compounds is crucial for designing effective and eco-friendly corrosion protection strategies tailored to specific industrial applications and environmental conditions.

The thesis is structured into four comprehensive chapters, each addressing a specific aspect of this multifaceted research endeavor:

Chapter 1 lays the groundwork by providing an in-depth discussion of the fundamental principles governing SCO phenomena and corrosion inhibition processes. This chapter establishes the theoretical framework and contextual background necessary for the subsequent investigations, ensuring a comprehensive understanding of the underlying concepts and their significance.

Chapter 2 delves into the diverse array of experimental methods employed for synthesizing and characterizing the studied materials. This chapter emphasizes the paramount importance of meticulous synthesis procedures and comprehensive characterization techniques in unraveling the structure and properties of the resulting compounds. Detailed descriptions of the analytical techniques, including spectroscopic, diffraction, and electrochemical methods, are provided, ensuring a thorough understanding of the experimental approaches and their applications in the context of this research.

Chapter 3 investigates the effectiveness of triazole-based organic molecules as corrosion inhibitors for carbon steel in acidic environments. Through a systematic exploration of the impact of inhibitor concentration and temperature on corrosion inhibition efficiency, this chapter reveals valuable insights into the adsorption behavior and protective mechanisms of these molecules.

Chapter 4 consists of research work carried out on the molecular magnetism of binuclear complexes bearing 1,2,4-triazole-based Schiff base ligands. Following a presentation of molecular magnetism and 'single-molecule magnets' based on a bibliographic review, it presents the synthesis and study of new binuclear complexes and coordination polymers of Cobalt (II), Iron (II), Nickel

(II), and Copper (II) using X-ray diffraction crystallography on single crystals and measurements by SQUID magnetometer. The studies of these complexes are followed by a presentation of their magneto-structural relationships, put into perspective with all the binuclear complexes studied.

References

[1] Gütlich, P., & Goodwin, H. A. (Eds.). (2004). Spin crossover in transition metal compounds I (Vol. 1). Springer Science & Business Media.

[2] Halcrow, M. A. (Ed.). (2013). Spin-crossover materials: properties and applications. John Wiley & Sons.

[3] Olguín, J. (2020). Unusual metal centres/coordination spheres in spin crossover compounds. Coordination Chemistry Reviews, 407, 213148.

[4] Landolt, D. (2003). Corrosion et chimie de surfaces des métaux (Vol. 12). PPUR presses polytechniques.

Chapter 1

<u>Literature Review</u>

Table of Contents

Chapter 1

Literature Review

In this chapter, we provide an introduction to the phenomena of spin crossover complexes and corrosion inhibitors. The chapter is divided into two main parts. In Part One, we present the basic concepts and a general description of the spin crossover phenomenon. First, we provide background on spin states in transition metal complexes and the thermodynamics governing spin crossover transitions. Next, we discuss examples of spin crossover systems, from early discovery in simple mononuclear complexes, to contemporary examples of single molecule and single ion magnets that display hysteresis and magnetic bistability. We also briefly describe potential applications of spin crossover materials in molecular electronics, sensing, actuators, displays, and data recording and storage. In the second Part, we cover the basics of corrosion inhibitors. Corrosion inhibitors are compounds that decrease the rate of corrosion reactions when added in small concentrations to corrodible metals and alloys. We first explain common mechanisms of corrosion inhibition through adsorption onto metal surfaces. We then discuss major classes of inhibitors including organic heterocyclic compounds, amines and condensation products. Finally, we provide examples of corrosion inhibitors for steels in acidic environments.

I.1 Spin crossover phenomenon

I.1.1 History and Foundation of Spin Crossover Complexes

The phenomenon of spin crossover in transition metal complexes was first discovered in 1931 by Cambi et al. through investigating temperature-dependent magnetic properties in a series of Fe(III) compounds based on dithiocarbamate ligand [1]. However, at the time there were only speculations about possible explanations for the strange thermal dependency they observed. It was not until 1956 that the notion of spin equilibrium was hypothesized by Griffith to potentially account for the magnetic phenomena he measured [2]. The first direct characterization of a thermal spin transition occurring in the solid state was seen in 1964 with the landmark paper from Baker and Bobonich on iron(II) complex [Fe(phen)$_2$(NCS)$_2$] [3]. That same year, Ewald et all, formally introduced the overarching "spin crossover" terminology [4]. Through application of ligand field theory, they detailed that the transitions between low-spin (LS) and high-spin (HS) electronic states can occur in complexes when the ligand field energy is comparable to the average energy of electron pairing in the 3d orbitals of the metal center. These breakthroughs spawned intensive investigations on an array of transition metal ions with

electronic configurations $3d^4$-$3d^7$, extending beyond just iron(II) including Fe(III), Co(II), Co(III), Mn(II), Mn(III), and Cr(II) [5-11]. Since then, investigation of spin-crossover has developed into a thriving field intersecting coordination chemistry, magnetism, and materials science due to the fundamental revelations and possibilities for stimuli-responsive applications. Figure 1 illustrates the potential electronic configurations within octahedral geometries (crystal field) for both HS and LS states of these metal ions.
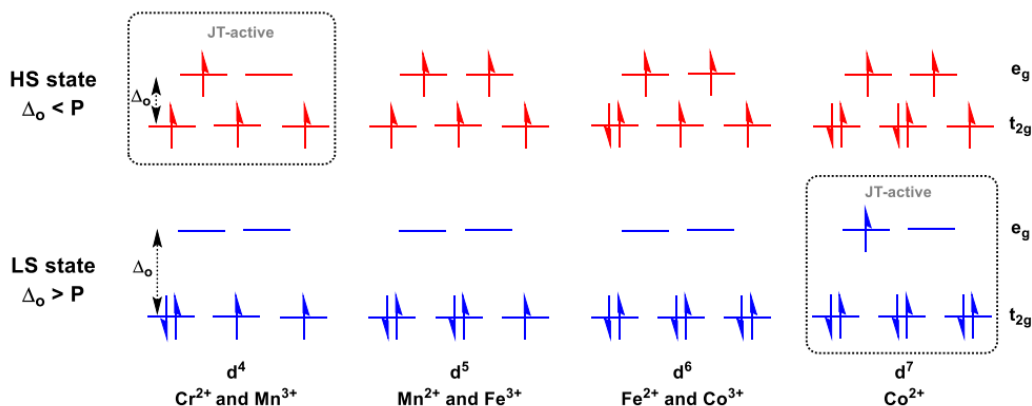
Figure I.1 depicts the crystal field splitting in octahedral environments and the electron filling diagram for HS and LS states in metal complexes with d^4 to d^7 electron configurations. The framed box highlights electronic configurations characterized by significant Jahn-Teller (JT) distortions [12].

I.1.2 Relevant Theories and Frameworks

Foundational theories including ligand field theory, crystal field theory, and molecular orbital diagrams provide the underpinning description for interpreting spin state energetics and transitions in transition metal complexes [13]. As Halcrow details, these frameworks model the electronic structure perturbations leading to spin state changes using descriptions of d-orbital splitting patterns and electron configurations [14]. Specifically, the covalent bonding between the transition metal center and donor ligands determines the relative spacing and energies of antibonding $\mathbf{e_g}$ and bonding $\mathbf{t_{2g}}$ levels, which dictates spin crossover propensity. The occupancies and multiplicity possibilities then yield different spin states. Structural changes and strains in the ligand coordination environment geometry as well as coupling to lattice vibrations (phonons) have been shown to influence spin-state interconversions and contribute to cooperative effects [14-15]. However deeper investigations into quantifying such vibrationally-coupled spin state

mechanisms remain vital. Thermodynamic models have also been critical for elucidating entropy-enthalpy compensations along with quantifying cooperativity and elastic interactions that globally impact spin transition behavior in extended networks [16].

I.1.2.1 Crystal Field Theory and Ligand Field Theory

The understanding of spin crossover complexes begins with Crystal Field Theory (CFT) and the more advanced Ligand Field Theory (LFT) which provide important conceptual frameworks for understanding spin state energetics and spin crossover behavior in transition metal complexes. CFT, first developed by the physicist Hans Bethe in 1929, uses an electrostatic approximation to model the field imparted by ligands as an array of negative point charges that splits the originally degenerate d-orbital energy levels [17-18]. The symmetry of the coordinating ligands determines specific splitting patterns, octahedral complexes exhibit a low-energy t_{2g} triplet set (d_{xy}, d_{xz}, d_{yz}) and a higher-energy e_g doublet set (d_{z^2}, $d_{x^2-y^2}$).
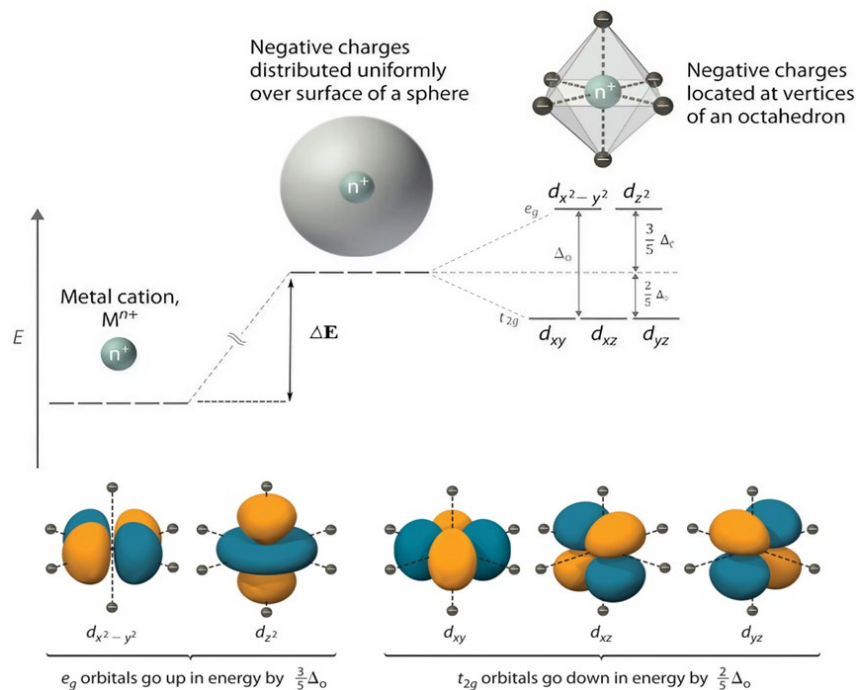
Figure I.2 illustrates how the symmetry of the crystal field affects the energy levels of the metal cation. However, in an octahedral complex with ligands or point charges located at the six vertices, the 3d orbital degeneracy is broken. The $d_{x^2-y^2}$ and d_{z^2} orbitals point their electron density directly towards the ligands, feeling greater repulsion and destabilization to higher energies. In contrast, the d_{xy}, d_{yz} and d_{xz} orbitals orient between the ligand axes, feeling less

repulsion and becoming stabilized at lower energies. This splitting between the "e_g" and "t_{2g}" sets of orbitals is denoted Δ_o.

The energy difference between them is denoted as Δ_0 or 10Dq, which depends on properties of both the metal and ligands. However, CFT has limited quantitative accuracy since it treats metal-ligand interactions as purely electrostatic. On the other hand, LFT, introduced by van Vleck in 1935, builds on CFT by also incorporating metal-ligand covalent bonding into the model, specifically between metal d and ligand p orbitals [19]. The key aspect for spin crossover behavior is that LFT accounts for how ligand identity influences the energies/splitting of t_{2g} vs e_g sets of d orbitals, which determines relative stabilization of high spin vs low spin states. For an octahedral complex with a metal ion like Fe(II), In the absence of ligands, the energy levels of a free ion are degenerate. Similarly, the presence of a spherically symmetric electrostatic potential globally shifts the energy spectrum by ΔE, However, it does not lift the degeneracy since no one of the five 3d orbitals is favored over the others, The energy levels of these orbitals can be expressed as $E_{sph} = E_{free} + \Delta E$, where E_{free} represents the energy of the free or isolated ion, (Fig.I.2). In an octahedral complex of the metal ion with six coordinated ligands, this spherical symmetry is broken. The d orbitals split into a lower energy level t_{2g} consisting of the degenerated orbitals (d_{xy}, d_{yz}, d_{xz}) and a higher energy level e_g with the degenerated orbitals (d_{z^2}, $d_{x^2-y^2}$). Where the energy levels equation is given for each of them, respectively, $E_{t_{2g}} = E_{sph} - \frac{2}{5}\Delta_0$ and $E_{e_g} = E_{sph} + \frac{3}{5}\Delta_0$, where Δ_0 is the energy difference between these two levels.
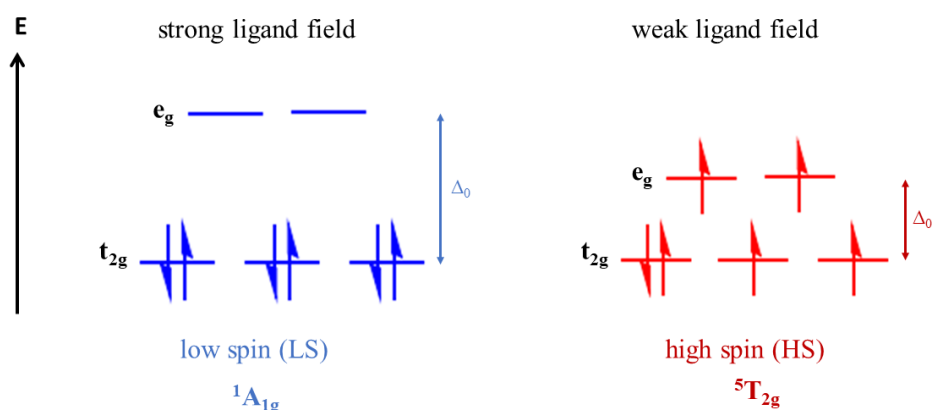
Figure I.3 depicts the electronic configurations of the LS and HS states for an Fe(II) ion within an octahedral ligand field.

When Δ_0 is small compared to the electron pairing energy (weak ligand field case), Hund's rule dictates maximum multiplicity with one electron in each d orbital first, giving an S=2 HS state denoted by the spectroscopic term $^5T_{2g}$ for Fe(II) ion. Conversely, for a strong ligand field with large Δ_0, the electrons instead fully occupy the lower t_{2g} levels first before pairing in the e_g levels. This minimizes energy but violates Hund's rule, leading to the LS state with S=0 denoted $^1A_{1g}$ in spectroscopic terms (Fig.I.3). So by tuning the ligand field splitting Δ_0 via judicious ligand choice, the spin state preference can be manipulated, resulting in spin crossover abilities under certain conditions. While qualitative, ligand field theory offers a framework for rationalizing spin crossover tendencies.
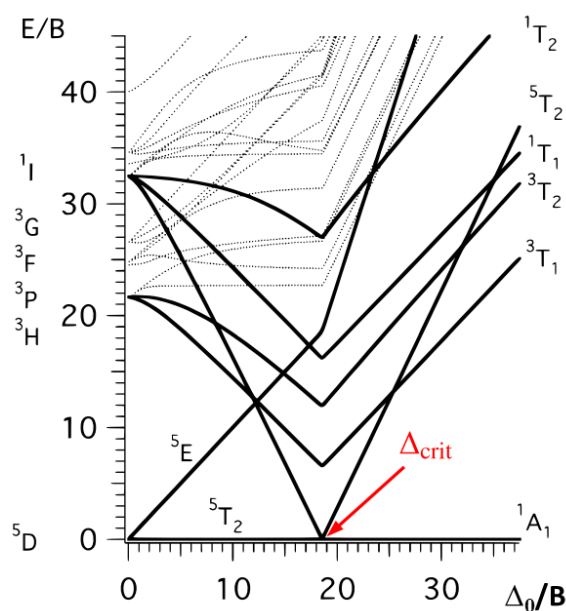
Figure I.4 Tanabe-Sugano diagram for a d^6 octahedral system showing the energy of the electronic states as a function of ligand field strength in units of the Racah parameter (electronic repulsion B).

The Tanabe-Sugano diagram is a useful tool for understanding the electronic structure and spin states of transition metal complexes. The diagram plots the energy of the spectroscopic terms for a transition metal ion as a function of the ligand field strength Δ_0 in an octahedral coordination environment. Specifically, for a d^6 metal ion, the Tanabe-Sugano diagram (Fig.I.4) shows the relative energies of the HS $^5T_{2g}$ and LS $^1A_{1g}$ states. In the free ion, the ground state as dictated by Hund's rules is the ^5D term. Under the influence of an octahedral ligand field, this ^5D

state splits into the previously mentioned $^5T_{2g}$ and $^1A_{1g}$ states. At very small ligand field strengths ($\Delta_0 \ll \Pi$, where Π is the electron pairing energy), the high-spin $^5T_{2g}$ state remains the ground state. As Δ_0 increases and approaches $\sim\Pi$, there is a crossover point Δ_{crit}, where the low-spin $^1A_{1g}$ state becomes energetically favorable and stabilizes as the ground state when ($\Delta_0 \gg \Pi$). In this way, we can conclude that the spin crossover phenomenon arises for complexes with Δ_0 values near Δ_{crit}. A small perturbation in Δ_0 (through temperature, pressure, light) can trigger interconversion between the HS ($^5T_{2g}$) and LS ($^1A_{1g}$) spin states. This switching is possible because Π lies between the two spin state ligand field energies $\Delta^{HS} < \Pi < \Delta^{LS}$.

The spin transition between the high-spin (HS) and low-spin (LS) states in spin crossover complexes involves a change in the metal-ligand bond length. In the HS state, two of the 3d electrons occupy anti-bonding e_g orbitals, causing the ligand electronic orbitals to repel each other, Which lead to an increase in the metal-ligand distance. For an FeN_6 octahedron, the Fe-ligand distance increases from $r_{LS} \approx 1.95\text{-}2.00$ Å in the BS state to $r_{HS} \approx 2.12\text{-}2.18$ Å in the HS state (a change $\Delta r_{LS \to HS} \approx 0.2$ Å or 10%) This corresponds to an increase of about 25% in the octahedral volume during this spin transition [20]. This difference can be represented using a configuration diagram with two adiabatic potential wells whose minima are shifted horizontally by $\Delta r_{LS \to HS} \approx 0.2$ Å along the metal-ligand distance and vertically in energy by $\Delta E^\circ_{HL} = E^\circ_{HS} - E^\circ_{LS}$ (Fig.I.5). This concavity difference is primarily attributed to a change in the vibration frequencies of the octahedron throughout the spin transition, with the vibration frequency $\nu(FeN)$ higher in the LS state than in the HS state ($\nu^{LS}_{FeN}/\nu^{HS}_{FeN} = 1.1\text{-}1.9$).

Given the dependence of Δ_0 on the metal-ligand bond length, and the fact that Π does not vary significantly with temperature, the ground state energy difference ΔE°_{HL} between the HS and LS states can be estimated as a function of Δ_0^{HS} and Δ_0^{LS}. Three regimes can be identified [13]:

1) $\Delta_0^{HS} < 10000$ cm^{-1}, $\Delta E^\circ_{HL} < 0$ cm^{-1}: HS ground state is lower in energy $\to$ HS state thermodynamically stable at all temperatures

2) $\Delta_0^{LS} > 23000$ cm^{-1}, $\Delta E^\circ_{HL} > 2000$ cm^{-1}: LS ground state is lower in energy $\to$ LS state stable up to very high temperatures

3) $\Delta_0^{HS} = 11000\text{-}12500$ cm^{-1}, $\Delta_0^{LS} = 19000\text{-}22000$ cm^{-1}, $\Delta E^\circ_{HL} = 0\text{-}2,000$ cm^{-1}: thermal spin crossover is possible
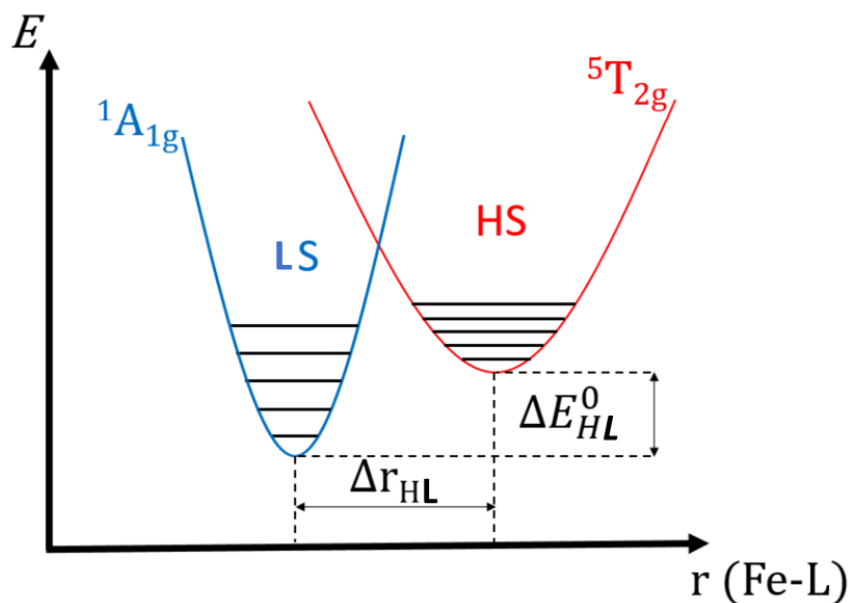
Figure I.5 configuration diagram depicting the energy variations of the two spin states for an octahedral Fe(II) complex as a function of the Fe-ligand distance [20].

I.1.2.2 Thermodynamics of Spin Crossover

Spin crossover can be described thermodynamically as an equilibrium between two phases (HS and LS state), for a system of isolated, non-interacting SCO molecules. Under typical experimental conditions where pressure and temperature can be controlled externally, the relevant thermodynamic potential is the Gibbs free energy G. The Gibbs free energy difference between the HS and LS states at constant pressure can be written as:

$$\Delta G = G_{HS} - G_{LS} = \Delta H - T\Delta S \qquad (I.1)$$

where ΔH is the enthalpy difference ($H_{HS} - H_{LS}$) and ΔS is the entropy difference ($S_{HS} - S_{LS}$). Since ΔH and ΔS are always positive for a spin crossover system, an equilibrium temperature $T_{1/2}$ can be defined where the proportions of HS and LS molecules are equal and $\Delta G = 0$. The $T_{1/2}$ is given by:

$$T_{1/2} = \frac{\Delta H}{\Delta S} \qquad (I.2)$$

The enthalpy change ΔH has contributions from both electronic (ΔH_{el}) and vibrational (ΔH_{vib}) factors. In most cases, ΔH_{el} provides the main contribution to ΔH. In contrast, the entropy change ΔS typically has a dominant vibrational contribution ΔS_{vib}, mainly from changes in

intramolecular vibrational modes due to differences in metal-ligand distances between HS and LS states. The electronic contribution ΔS_{el} comes from changes in total spin momentum S and angular orbital momentum L between states. Regarding the entropy contribution from the electronic part ΔS_{el}, this term itself can be divided into two parts: one associated with the difference in orbital degeneracy ΔS_{el}^{orb}, and the other with the difference in spin degeneracy ΔS_{el}^{spin}. The two can be written as follows:

$$\Delta S_{el}^{spin} = R \ln \left(\frac{2S_{HS}+1}{2S_{LS}+1}\right) \qquad (I.3)$$

$$\Delta S_{el}^{orb} = R \ln \left(\frac{2L_{HS}+1}{2L_{LS}+1}\right) \qquad (I.4)$$

Where $R = N_a k_B$ is the ideal gas constant, N_a is Avogadro's constant, k_B is Boltzmann's constant, and L is the orbital angular momentum. With the spin change from $^1A_1$ to $^5T_2$ in Fe(II), ΔS_{el}^{spin} is 13.38 $J \cdot K^{-1} \cdot mol^{-1}$, much smaller than typical experimental ΔS values from 40-80 $J \cdot K^{-1} \cdot mol^{-1}$[21-22]. This highlights the significance of ΔS_{vib}. From the above relations (I.1) for ΔG and $T_{1/2}$ expression (I.2), equilibrium behavior and relative stabilities can be deduced:

> ➤ $T < T_{1/2}$, so $\Delta H > T\Delta S$, Enthalpy dominates, LS state more stable ($G_{LS} < G_{HS}$)
> ➤ $T > T_{1/2}$, so $\Delta H < T\Delta S$, Entropy dominates, HS state more stable ($G_{LS} > G_{HS}$)
> ➤ $T = T_{1/2}$, so $\Delta H = T\Delta S$, Enthalpy & entropy equal, equilibrium between phases ($G_{LS} = G_{HS}$)

The thermodynamic framework therefore provides an understanding of the temperature-dependent spin state switching in these materials based on the relative magnitudes of the entropic and enthalpic differences between spin states.

I.1.3 The Different spin transition behaviors

Since the early days (1960s) of spin-crossover research, there has been an appreciation for the complex interplay between molecular structure, intermolecular interactions, and external stimuli [23]. Initially, most observed transitions were gradual spin conversions (Fig.I.6a), following statistical Boltzmann distributions [24-26]. These non-cooperative transitions involve the incremental thermal excitation of individual, non-interacting metal centers to higher spin states. A paradigm shift occurred in 1964 when Baker and Bobonich reported an abrupt, switch-

like spin transition in [Fe(phen)$_2$(NCS)$_2$] deviating from the typical gradual conversions [27]. König and Madeja later (1967) confirmed the first-order nature (Fig.I.6b) of this cooperative transition, attributing it to strong elastic intermolecular interactions as evidenced by discontinuous changes in lattice parameters [28]. Compared to the continuous lattice parameter changes seen in non-cooperative spin crossover complexes. Further investigations revealed additional complexities governing spin-state switching. Highly cooperative systems exhibit thermal hysteresis between the heating ($T_{1/2}^+$) and cooling ($T_{1/2}^-$) cycles (Fig.I.6c), indicating metastable states due to excessive instability of intermediate states [26]. The most cooperative systems can exhibit thermal hysteresis loops spanning several tens of Kelvin across the transition, with $T_{1/2}^+$ and $T_{1/2}^-$ representing the respective transition temperatures from the low spin state to the high spin state (upon heating) and from the high spin state to the low spin state (upon cooling).
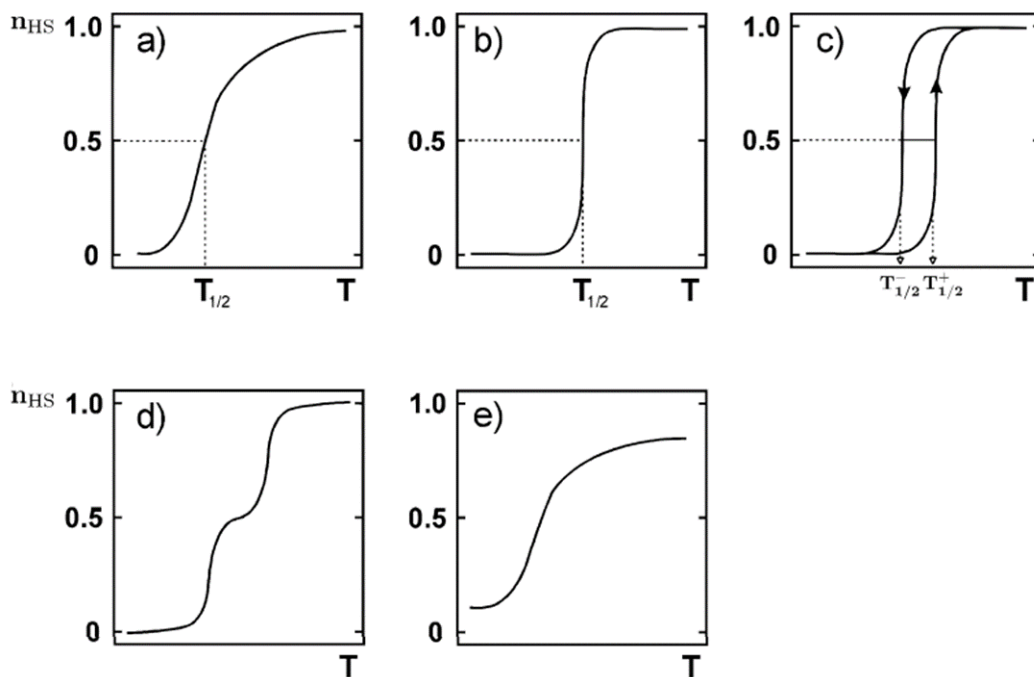
Figure I.6 depicts thermo-induced spin transition curves, plotting high spin fraction HS (n_{HS}) as a function of temperature (T). Five common transition types are represented [13]: (a) gradual spin conversion, (b) abrupt transition, (c) abrupt transition with a hysteresis loop between heating and cooling cycles, (d) multi-step transitions occurring through discrete intervals, and (e) incomplete transitions with residual high or low spin fractions persisting.

This memory effect was first reported by König and Richter in 1976 for the compound [$Fe(4,7-(CH_3)_2-phen)_2(NCS)_2$] [29]. It arises from the excessive instability associated with intermediate spin state configurations, which creates an energy barrier between the two pure low and high spin phases. This gives rise to metastable states and a difference between the heating and cooling transition temperatures evident in the hysteresis loop. The first two-step spin transition (Fig.I.6d) was observed by Zelentsov in 1981 for an Fe(III) complex with 2-bromo-salicylaldehyde-thiosemicarbazone [30]. Such multi-step transitions can also occur in polynuclear complexes, where the switching of one metal causes distortions that make the transition of a second metal less favorable [31]. In mononuclear complexes, two-step transitions can arise from competition between short-range interactions favoring HS-LS alternation and long-range interactions favoring homogeneous phases [32-34]. The presence of non-equivalent metal sites in the material, with different ligand environments, can also lead to distinct spin transition temperatures for each site [35]. In all cases, these phenomena underscore the intricacies of molecular and intermolecular factors governing spin transition behavior in these systems. Finally, Incomplete spin transitions have been observed with residual high spin fractions persisting at low temperatures or residual low spin fractions at high temperatures (Fig.I.6e) [36]. Several origins underlie this behavior. Kinetic trapping can occur at low temperatures, fixing certain molecules in metastable high spin states [26,35]. Structural defects or disorders may also locally block spin state switching for some metal centers. Additionally, decreasing particle size is known to facilitate incomplete transitions [26]. Such effects highlight the sensitivity of spin crossover phenomena to subtle structural and environmental factors. The presence of non-equivalent metal sites, with only one undergoing switching, can also lead to residual spin fractions. Overall, incomplete transitions demonstrate the intricacy of kinetic and thermodynamic factors governing spin-state bistability and interconversion in these functional materials. By linking specific switching mode observations to intermolecular interactions and structural/external considerations, we can continue expanding the applications repertoire of these fascinating functional materials.

I.1.4 Limitations or Gaps in Prior Research

Significant knowledge gaps remain in fundamentally understanding and predictively engineering spin crossover phenomena for advanced applications. While structure-property

relationships have been mapped extensively on various transition metal complexes, contemporary comprehension lacks robust quantitative models or design principles to custom-tailor spin state switching behavior a priori across diverse molecular systems and external triggers [16,37-38]. Moreover, synthetic and experimental barriers hinder systematic inquiries into emergent effects like long-range communication channels across polynuclear spin crossover networks that could enable cooperative amplification of multifunctional responses [16,39]. Bridging these gaps requires expanding rigorous theoretical descriptions of coupled spin-lattice mechanisms, developing sophisticated characterization techniques to probe spin states at the molecular level, devising rational spin-crossover material construction strategies, and interfacing with real-world device architectures. Only through comprehensive progress across modeling, experimentation, and design can the promise of spin crossover systems in areas ranging from spintronics to data storage be fully realized.

I.1.5 Effects of External Stimuli on Spin Crossover Complexes

In addition to fundamental coordination sphere factors, extensive research has focused on elucidating external stimuli that can trigger spin state interconversions by altering the relative energies of electronic configurations. A variety of external inputs have demonstrated effectiveness for inducing or modulating spin state switching in transition metal complexes exhibiting spin crossover phenomena. These can be broadly categorized into chemical stimuli that alter spin states through direct or indirect molecular interactions as well as physical stimuli that act through external energy inputs to perturb relative thermodynamics of HS and LS potential surfaces. It should be noted that temperature (T), pressure (P), light (hv), and magnetic field are the most commonly used external perturbations.

I.1.5.1 Physical Stimuli

a) Pressure-induced spin crossover

The application of external pressure can significantly impact spin transition behavior in metal complexes. Ewald first studied pressure effects on a spin-crossover Co(II) complex in 1969 [50], finding that increasing pressure leads to a decrease in volume and favors the LS state by decreasing metal-ligand distances and thus increasing ligand field strength. [45-47]. This results in a shift of the transition temperature towards higher temperatures. In the mean field

approximation, the Spiering model considers that the influence of pressure on the spin transition is determined by the magnitude of the change in the crystal lattice unit cell volume per molecule undergoing spin transition, the interactions between the molecules themselves and with the lattice [48-49]. Taking into account these terms, the variation in free enthalpy under an external pressure P is defined as:

$$\Delta G = \gamma \Delta F_{HL} + F_{int}(\gamma,T) - TS_{mix}(\gamma) + \gamma P \Delta V \qquad (I.5)$$

Where:

γ is the HS molar fraction, ΔF_{HL} is the free energy variation due to the spin transition $S_{mix}(\gamma) = -k_B[(1-\gamma)\ln(1-\gamma) + \gamma \ln(\gamma)]$ is the mixing entropy, $F_{int}(\gamma,T) = \Delta_s \gamma - \Gamma \gamma^2$ is the interaction term, with Δ_s being the difference in free energy from interactions of complexes with the host matrix, and Γ the intermolecular interaction parameter.

By introducing the elastic energy of the complexes, the terms can be grouped into electronic and elastic components:

$$\Delta F_{HL} + \Delta_s = \Delta F_{el} + \Delta F_{elast} \qquad (I.6)$$

Where: ΔF_{el} and ΔF_{elast} represent the variations in electronic and elastic free energy of the system, respectively. The formalism developed by Spiering has been useful for understanding how the transition temperature $T_{1/2}$ changes under applied pressure, as measured by various techniques like magnetic susceptibility, Mössbauer spectroscopy, and optical absorption/reflectivity spectroscopy [13,51-53].

The effects of pressure on spin transition systems can be diverse:

➢ The transition temperature increases, however the transition becomes more gradual at higher pressures [54].

➢ The transition temperature increases and a more cooperative compound with hysteresis can be obtained from one which did not initially show hysteresis [52].

➢ An incomplete spin transition can become complete with increase in transition temperature [55].

➢ In compounds that are HS over the whole temperature range, stabilization of the LS state has been achieved [57-58]

➢ Some atypical behaviors have also been observed like: increase in hysteresis width with pressure which later disappears and then reappears [Fe(hyptrz)$_3$]A$_2$.H$_2$O]; complete stabilization of HS state [[Fe(btr)$_2$(NCS)$_2$].H$_2$O] which has been attributed to a pressure-induced structural transition [56].
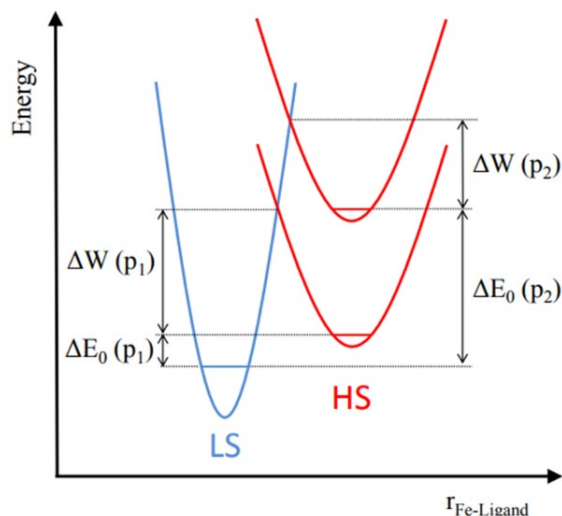
Figure I.7 depicts the impact of pressure (p$_2$ > p$_1$) on the relative positioning of the high-spin (HS) and low-spin (LS) potential wells in a Fe(II) compound [59].

Most studies show an increase in T$_{1/2}$ and a decrease in hysteresis width T$_{1/2}$ upon application of pressure. In majority of cases, upon releasing the pressure, the initial spin transition properties are recovered indicating the reversible nature of the pressure effects. However, irreversible effects have also been documented in some cases. To explain the diverse effects of pressure, modifications like incorporating pressure-dependent elastic modulus variations have been introduced into models like the one developed by Spiering. A complete understanding necessitates detailed structural and microstructural studies under pressure, which still remain scarce owing to the complex experimental environment they require.

b) Spin transition induced by magnetic field

The influence of a magnetic field on spin crossover systems is related to the stabilization of the most magnetic state, which for Fe(II) complexes is the HS state. Initial theoretical work in 1982 by Sasaki and Kambara [60] proposed a cooperative Jahn-Teller effect model to explain the perturbation caused by very strong static magnetic fields (100 T) but this was not validated experimentally later on. Experimental work in 1983 by Gütlich et al. [61] on the model

compound [Fe(phen)$_2$(NCS)$_2$] using a 5.5 T static magnetic field showed a small shift of 0.11 K in the spin transition towards lower temperatures upon cooling. Further work by Bousseksou et al [57]. using 32 T pulsed magnetic fields on the same complex revealed that when placed at the transition point, application of a magnetic field pulse increases the HS state proportion. This phenomenon was observed along the whole ascending BS → HS transition and a mean-field model was later proposed to explain it [57]. The magnetic field stabilization effect arises from the Zeeman effect, which favors the state with highest magnetic moment, i.e. HS for Fe(II). Thus, the application of a magnetic field shifts the spin transition towards lower temperatures. However, the extent of this shift is much smaller compared to effects of pressure or ligands on the spin transition. With static fields up to 20 T, the shifts are limited to around 1 K. Only with very strong pulsed fields have higher shifts of a few Kelvin been attained [57]. Nonetheless, magnetic fields present a perturbation approach that stabilizes HS states in SCO materials.

c) Light-Induced Spin State Switching

The most dramatic way to switch between LS and HS spin states is through light irradiation. Using light to produce spin changes is appealing for applications since it allows fast and simple control. Currently, there are two primary light-driven approaches:

- ligand-based switching through the ligand-driven light-induced spin change (LD-LISC) effect [62-63].

- metal-based switching via the light-induced excited spin state trapping (LIESST) effect at very low temperatures [62,64].

1. Ligand-Driven Light-Induced Spin Change (LD-LISC)

The LD-LISC effect involves photoisomerization or photocyclization (ring-closing/ring-opening reactions) of ligands in order to modulate the ligand field strength [65-67]. If the ligand field changes enough upon light irradiation, this can trigger a spin transition at the metal center. Example ligand families that have been used successfully for LD-LISC include styrylpyridines, stilbene, azobenzene, diarylethene and Schiff bases with photoactive groups [67-69]. In complexes with these ligands, trans-cis photoisomerization leads to different ligand field strengths for the two isomers, inducing spin crossover. For instance, the complex [Fe(stpy)$_4$(NCBPh$_3$)$_2$] (stpy = 4-styrylpyridine) exhibits LD-LISC behavior [68]. The trans isomer shows gradual spin crossover near 190 K while the cis isomer remains HS from 10-300

Chapter 1

Literature Review

K. Partial trans→cis photoisomerization can thus trigger HS→LS conversion upon light irradiation near room temperature.

The main limitations are fatigue over many switching cycles due to significant ligand rearrangements [70], and restriction so far to solution state systems. However, progress has been made using Langmuir-Blodgett films [71-72]. Overall, LD-LISC shows promise for spin state photoswitching near ambient conditions.

2. Light-Induced Excited Spin State Trapping (LIESST)

The LIESST effect involves direct light irradiation of the metal complex in order to induce LS to HS conversion. This photomagnetic effect was first discovered in iron(II) spin crossover compounds in 1982 by McGarvey and Lawthers [73]. In 1984, Decurtins et al [74]. demonstrated the LIESST effect in the solid state on the complex [Fe(ptz)$_6$](BF$_4$)$_2$ (ptz = 1-propyltetrazole), showing light-induced population of a metastable HS state with a lifetime longer than 11 days below 20 K. The generally accepted mechanism of LIESST, illustrated in the Jablonski diagram (Fig.I.8), involves two successive intersystem crossings [75]. Initially, light irradiation (typically 514 nm or 532 nm laser) excites the LS $^1A_1$ ground state to the Franck-Condon ^{1}MLCT (metal to ligand charge transfer) state. This quickly relaxes (within ~100 fs) to lower energy ^{3}MLCT states, followed by intersystem crossing to intermediate triplet $^3T_1$ metal-centered states. Further relaxation then reaches the metastable quintet HS $^5T_2$ state.
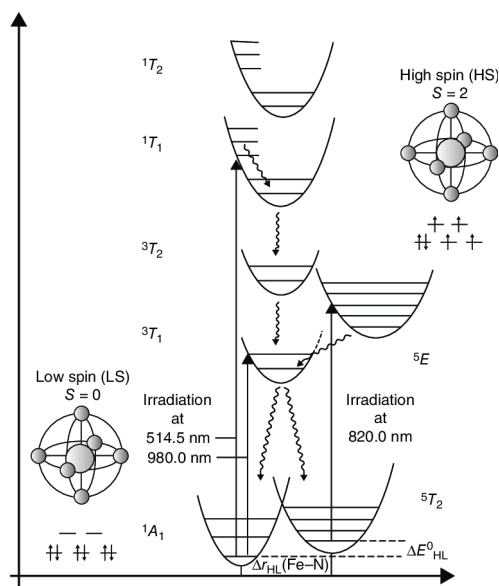
Figure I.8 Jablonski diagram showing LIESST mechanism [75].

Provided sufficiently low temperatures, relaxation barriers confine the complex in this HS $^5T_2$ state, with the $^1A_1$ ground state only repopulated through thermally activated pathways above a critical T(LIESST) limit or slower quantum tunneling [76]. However, infrared irradiation can also induce the reverse HS→LS photoswitching through the reverse-LIESST mechanism's approximate path [77]:

$$HS\ ^5T_2 \rightarrow 5E\ (NIR) \rightarrow {}^3T_1 \rightarrow {}^1A_1$$

The effective "trapping" of metastable light-induced spin state at cryogenic temperatures, and the possibilities for optical readout or erasure, underpin interest in exploiting LIESST toward applications [78-79]. However current challenges include increasing accessible temperature limits and fatigue over repeated photoswitching cycles [80].

An important focus of recent research has been on increasing the T(LIESST) limit, which is the critical temperature where relaxation from the metastable HS state accelerates and the LIESST-induced HS fraction starts to significantly decrease over time [81]. Several strategies are being pursued to improve T(LIESST) values [82]:

➢ Varying the ligand field strength through rational ligand design or substitutions
➢ Introducing disorder into the lattice to increase metastable state lifetimes
➢ Incorporating LIESST-active complexes into porous metal-organic frameworks
➢ Optimizing intersystem crossing rates through computational modeling

In addition, quantitative structure-function relationships have been identified between T(LIESST) values and thermal spin transition temperatures [83-84], with the empirical relation:

$$T(LIESST) = T_0 - 0.3T_{1/2} \qquad\qquad (I.7)$$

Where: T_0 is a constant based on the complex's structure. Such insights are guiding efforts to tune LIESST properties towards ambient temperature photoswitching.

Complementing steady-state LIESST investigations, time-resolved spectroscopies have elucidated relaxation dynamics and clarified mechanisms [85-86]. Ultrafast optical studies have tracked evolution between transient Franck-Condon, MLCT, and triplet states, providing

timescale measurements for each step ranging from femtoseconds to nanoseconds. Meanwhile, long-timescale kinetic magnetic studies probe metastable state lifetimes from microseconds to days depending on temperature. These timeresolved perspectives offer a detailed glimpse into the complex Photoswitching pathways while highlighting the key bottlenecks limiting more room temperature LIESST performance.

I.1.5.2 Insights into the Influence of Chemical Modifications

Beyond the physical stimuli that modulate its spin state, a spin crossover complex is also highly sensitive to various chemical factors. These include ligand substitution and nature, the presence of peripheral ions or solvent molecules, dilution of the metal center, as well as polymorphism and crystal packing. The latter provide important optimization handles for tuning the desired switching properties for potential applications.

a) Ligand Effects

The effect of ligands on spin crossover behavior is multifaceted, with various factors such as steric aspects, molecular symmetry, electronic properties, and electron density affecting the ligand field strength and spin state energetics. As Halcrow comprehensively reviews [40], bulky substituents near the metal center or expanded chelate rings favor the high-spin state by hindering metal-ligand bond contraction, while peripheral steric bulk can promote either spin state depending on distortion effects. Additionally, Halcrow notes that electron-withdrawing substituents may stabilize either spin state based on conjugation ability and substituent position. Elaborating on the impact of molecular symmetry, Run-Guo Wang et al [41].

find that chirality and ligand orientation in $[Fe(pybox)_2]^{2+}$ complexes significantly affect spin crossover properties, with higher symmetry favoring the low-spin state due to enhanced ligand field. Through systematic analyses, Chun-Feng Wang and colleagues [42]. propose that substituent positions predominantly influence spin transition via steric distortion rather than electronic effects. Demonstrating subtle electronic effects, Park et al [43].

show that remote ligand substitution can substantially alter crossover temperature; both temperature and enthalpy decrease across their series as substituents become more electron-withdrawing, attributed to modulated ligand field. Confirming the influence of electron density, Dey et al [44]. establish that enhanced electron donation from substituents increases crossover

temperature, ascribed to augmented d-orbital splitting favoring the high-spin state. Collectively, these works illustrate that factors modulating ligand field strength, such as steric, symmetry, conjugation pathways, and electron donation capability of substituents, can profoundly impact metal center energetics and interconversion between spin states.

b) counter-ion Effects

In the case of ionic complexes, the system requires a counter-ion. The nature and size of it greatly influences the organization of the crystalline assembly (intermolecular interactions), because the anions present in the network play a significant role on cooperativity and thus on the transition characteristics. Matsumoto's group systematically studied three iron(II) spin crossover complexes with a hexadentate Tris[2-(((2-methylimidazol-4-yl)-methylidene)-amino)-ethyl]amine (H3LMe) ligand, but different counteranions: perchlorate (ClO_4^-), tetrafluoroborate (BF_4^-), and hexafluoroarsenate (AsF_6^-) [87]. While all three complexes underwent gradual spin transitions centered around 175 K, distinct differences were observed between them. The compound with the largest AsF_6^- counterion showed the most abrupt, first-order like transition with a very narrow 1 K hysteresis loop. In contrast, the complexes with smaller BF_4^- and ClO_4^- anions displayed more gradual, second-order transitions with wider 10-15 K hysteresis regions. This demonstrates the significant impact counterion size can have on intermolecular spacing and interactions, fundamentally changing the cooperativity and transition characteristics. Detailed magnetic data highlights the systematically longer plateau region for the complex with larger AsF_6^- ions compared to the smaller BF_4^- and ClO_4^- versions. This provides direct evidence that counterion size tunes the two-step nature of the transitions by modifying the strength of intra- and intermolecular couplings.

c) Protonation Effects

The influence of protonation on SCO equilibria and dynamics has been extensively studied, with intriguing protonation-induced switching behaviors demonstrated across various complexes. As Rabelo and co-workers demonstrated, reversible protonation allows switching between faster-relaxing and slower-relaxing magnetic states in cobalt(II) complexes [88]. By tuning spin-phonon couplings through protonation, they achieved excellent control over relaxation behaviors. Intriguingly, protonation also changed relative stabilization of HS states, attributed to distortions causing loss of ligand conjugation [88]. So protonation effects depend sensitively on geometric

factors. In iron systems, Kelly and colleagues utilized protonation to generate persistent yet reversible LS state preferences, opening up pathways to analyte-responsive magneto-modulation for sensing [89]. However, Zhang et al. found that excessive protonation dramatically twisted ligand planes in some iron complexes, decomposing the complexes [90]. So protonation reactions provide a remarkably versatile, but potentially destructive tool. Reversible protonation unlocks spin-state switching capacities through delicate molecular distortions and coupling effects. When judiciously controlled, fascinating magnetic phenomena emerge with diverse functional possibilities. But things can go haywire if protonation disrupts molecular integrity. Moving forward, precise understanding and careful calibration of protonation effects—both constructive and destructive—will be key to harnessing the promise of these reactions for spin-crossover applications. There is still much to understand, but the possibilities make further elucidation incredibly exciting.

d) Solvent Effects

The nature of solvents in spin transition complexes can play a major role in influencing the transitions. Phonsri et al [91]. demonstrate the profound impact of solvent on spin crossover (SCO) properties in a series of iron(III) complexes with only the lattice solvent varying. They showed thermal spin transition temperatures can be tuned over nearly 200K just by altering the solvent molecule. Most notably, the ethanol solvate exhibited exceptional sensitivity to sample conditions, with hysteresis loops up to 80K - among the largest known SCO systems. Meanwhile, Fumanal and co-workers [92], showed replacing acetone with propylene carbonate in an iron(II) complex caused its abrupt, hysteretic SCO to disappear, instead yielding a diamagnetic derivative, due to minimal lattice distortion induced by the latter solvent. Together, these studies exhibit the solvent's surprising ability to dramatically influence SCO characteristics through subtle changes in supramolecular connectivity, lattice distortions, and interactions - findings which will greatly aid development of responsive SCO-based devices.

e) redox modulation

Recent work has demonstrated the ability to modulate spin crossover behavior in iron(II) complexes and coordination polymers through incorporation of redox-active components. Schönfeld et al [93]. synthesized an iron(II) complex with a tetrathiafulvalene equatorial ligand that enables coupled spin crossover and redox properties, though studies found limited electronic

communication between the metal and ligand. Lyu et al [94]. achieved reversible switching between high and low spin states in an iron(II) metal-organic framework by oxidizing and reducing the Au(I/III) sites of the $Au(CN)_2$ linker. Palacios-Corella et al [95]. reported a 1D polymer with alternating Fe(II) spin crossover units and polyoxometalate spacers, where injection/removal of electrons and bulky counterions via redox changes in the polyoxometalate modulated the abrupt cooperative spin transitions. Overall, these recent advances demonstrate that incorporation of redox-active ligands or components in the framework enables external tuning of spin crossover behavior through reversible redox switching.

f) polymorphism effect

The effect of polymorphism on SCO behavior is an emerging area of research, polymorphs of the same SCO complex can exhibit dramatically different magnetic properties, such as transitions between HS and LS states at different temperatures or abrupt versus gradual spin conversions. These differences originate from subtle variations in factors like crystal packing, intermolecular interactions, and distortions in the metal coordination geometries between polymorphs [96]. as demonstrated by Tailleur et al [97]. in their 2019 study on two polymorphs of [Fe(PM-PeA)$_2$(NCSe)$_2$]. They found one polymorph undergoes an abrupt spin transition with thermal hysteresis centered at room temperature, while the other exhibits a gradual spin conversion at lower temperatures. Tailleur et al. attributed these distinct behaviors to subtle differences in the crystal packing and intermolecular interactions between the two polymorphs, particularly variations in H-H contacts. This reveals the extreme sensitivity of spin crossover properties to small structural changes arising from polymorphism. Overall, their work highlights how polymorphism provides an opportunity to understand and potentially control spin crossover mechanisms starting from the same molecule. For example, Matouzenko showed heavy distortions stabilize the high spin state while moderate distortions enable spin transitions [98]. Overall, the extreme sensitivity of SCO properties to small structural changes arising from polymorphism reveals an opportunity to fundamentally understand and potentially control SCO mechanisms starting from the same molecule. Further theoretical and experimental work is essential to uncover feasibility, structural factors influencing properties, and perhaps even discover new SCO transition phenomena linked to polymorphism.

Chapter 1

Literature Review

I.1.6 Single Molecule Magnets and Slow Relaxation

Single-molecule magnets (SMMs) are a class of compounds that exhibit slow relaxation of magnetization at the molecular level below a blocking temperature, leading to magnetic bistability similar to bulk magnets. This property was first reported in 1993 by Sessoli et al [99]. in a manganese(III) cluster complex $[Mn_{12}O_{12}(CH_3COO)_{16}(H_2O)_4]$ with a large S = 10 ground spin state and significant magnetoanisotropy barrier (U_{eff}) on the order of 60-70 K that enabled magnetic hysteresis of molecular origin. In 1996, David Hendrickson and coworkers were the first to employ the term "single-molecule magnet" to refer to this phenomenon [100]. The energy barrier U_{eff} originates from zero-field splitting (ZFS) of the ground spin state caused by spin-orbit coupling and ligand field effects. This ZFS can be described by the Spin Hamiltonian:

$$\hat{H}_{ZFS} = D[\hat{S}_Z^2 - S(S+1)/3] + E(\hat{S}_X^2 - \hat{S}_Y^2) \qquad (I.8)$$

Where: D and E are the axial and rhombic ZFS parameters respectively. A large positive D-value yields an anisotropy barrier $U_{eff} = |D|S^2$ for the reversal of magnetization between the $M_S = \pm S$ spin projections along the easy axis.
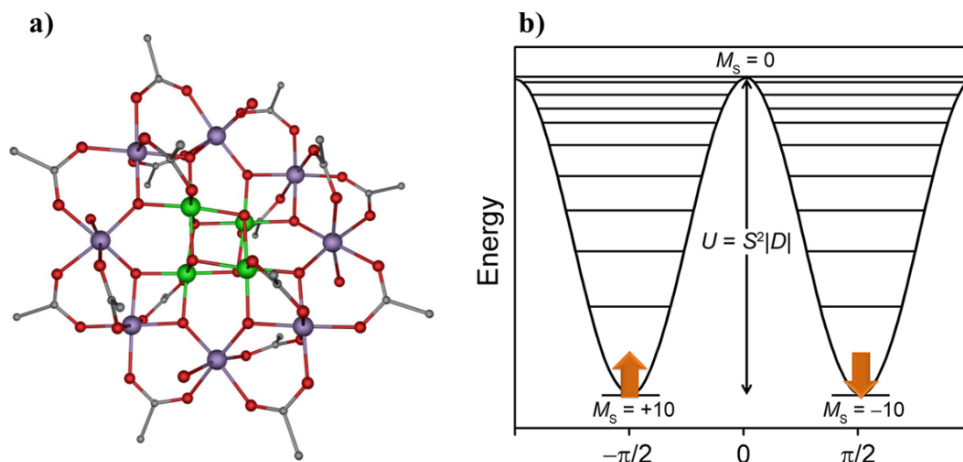
Figure I.9 (a) depicts the structure of a molecule called Mn$_{12}$-ac. The illustration uses purple for manganese(III) atoms, green for manganese(IV), gray for carbon, and red for oxygen. Hydrogen atoms are not shown for better clarity [104]. (b) Schematic representation of the splitting of the Mn$_{12}$ ground state S = 10 into 21 sublevels by ZFS and of the relaxation of the magnetization from the "spin-up" state (M_S= 10) to the "spin down" state (M_S=−10) at H = 0 and low temperature.

Two key requirements underlie such slow relaxation of magnetization:

1- a large ground state spin, derived from the metal ion coordination

2- substantial easy-axis type magnetoanisotropy imposed by spin-orbit coupling and often related to near axial symmetry of the complex's geometry, which prevents spin inversion.

Magnetic relaxation occurs through direct, Raman, and Orbach processes. Thermally activated relaxation over the barrier occurs via the Orbach process (follow Arrhenius behavior):

$$\tau = \tau_o \exp(\frac{U_{eff}}{k_B T}) \qquad\qquad (I.9)$$

where: τ_o is the pre-exponential factor, U_{eff} denotes the effective anisotropy barrier and k_B is the Boltzmann constant. Quantum tunneling of magnetization (QTM) leads to T-independent relaxation. Strategies to optimize SMM properties focus on maximizing ground spin state, incorporating easy-axis anisotropy, and limiting QTM.
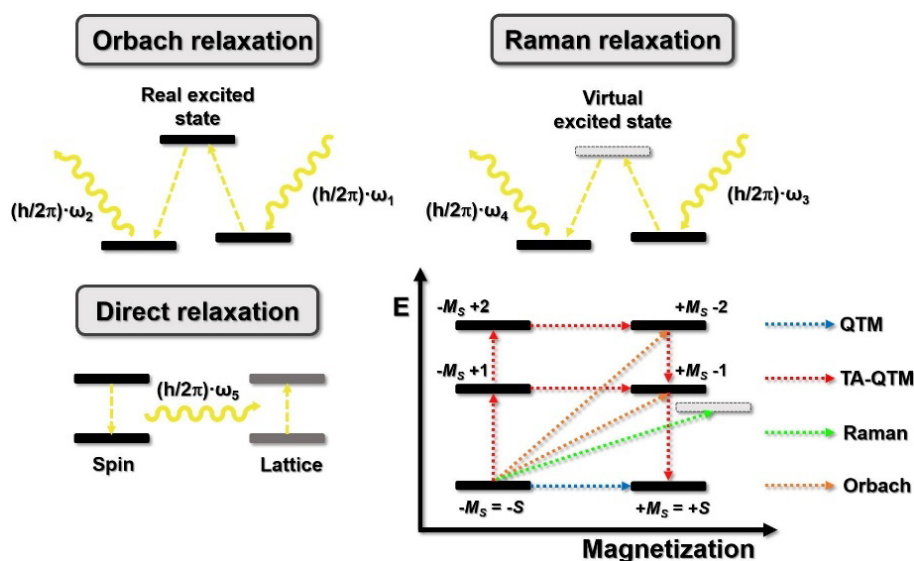
Figure I.10 depicts the main magnetization relaxation mechanisms: Orbach process (top left), where spins thermally "jump" over an energy barrier; the Raman process (top right), where local vibrations assist spin transitions, impacting the temperature-dependent relaxation rate; and the Direct process (bottom left), where phonons directly excite transitions, particularly at high temperatures. In reality, combinations (bottom right) like quantum tunneling of magnetization (QTM) and thermally assisted tunneling (TA-QTM) often play a role, making relaxation behavior a complex interplay of these various mechanisms [105].

Research has also targeted combining SMM properties with SCO behavior, where transition metal complexes exhibit reversible switching between HS and LS electron configurations in response to external stimuli like temperature, light irradiation, pressure or applied magnetic fields, yet SCO favors diamagnetic LS states whereas SMMs inherently require metastable, paramagnetic HS configurations with maximum possible spin angular momentum as the ground state. Approaches to reconciling SMM and SCO functionality within a singular molecular or ionic complex include light-induced excited spin-state trapping (LIESST) to photo-populate HS states in SCO compounds at low temperatures where they normally rest in LS form, designing multi-component systems where distinct molecular constituents or ions within a Solid State structure exhibit either SCO or SMM characteristics separately without detrimental interactions, and synthesizing bicomponent ion-pair systems with segregated SCO and SMM functionality such as the bicomponent ion-pair compound $[Co(Brphterpy)_2][Co(NCS)_4]\cdot2MeCN$ which displays gradual, incomplete thermal SCO in the $[Co(Brphterpy)_2]^{2+}$ cation and field-induced slow magnetic relaxation consistent with single-ion magnet (SIM) behavior in the pseudotetrahedral $[Co(NCS)_4]^{2-}$ anion [101].
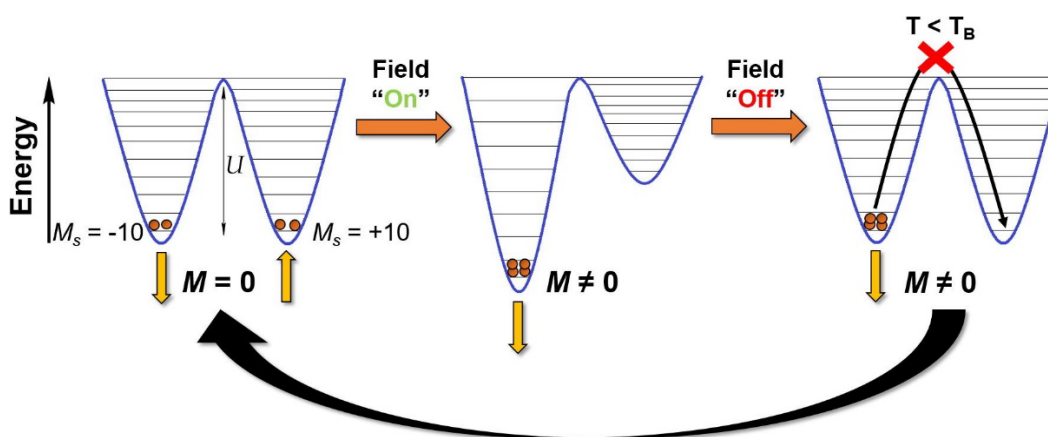
Figure I.11 depicts: (left) the equilibrium magnetization directions (yellow arrows) in the absence of an external magnetic field; (center) the material's magnetization caused by an external field and the stabilization of sublevels with $M_S < 0$; and (right) the blocked magnetization with no field when the temperature is lower than the blocking temperature (T_B) [104].

Subtle alteration of the coordination environment in Co(II) complexes coordinated by tetrathiafulvalene (TTF)-decorated terpyridine ligands can switch the magnetic response between thermal spin crossover transitions centered on the TTF moieties and field-induced slow magnetic

relaxation dynamics arising from the Co(II) sites [102]. This illustrates the intrinsic relationships between SCO and SMM phenomena in certain transition metal complexes where minor structural modifications interconvert between the two types of bistable magnetic behavior. Chen and coworkers [103].

reported examples of cobalt(II) complexes [Co(12-TMC)(CH$_3$CN)$_2$](X)$_2$ (12-TMC =1,4,7,10-tetramethyl-1,4,7,10-tetraazacyclododecane, X = BF$_4^-$, PF$_6^-$) that display both spin crossover properties and field-induced slow relaxation of magnetization. The five-coordinate cobalt(II) complexes undergo a gradual spin state change from low spin (S = 1/2) to high spin (S = 3/2) at higher temperatures. Under an applied DC field, they also exhibit the characteristic slow magnetic relaxation dynamics indicative of single-ion magnet (SIM) behavior originating from the S = 1/2 spin state. The magnetic studies suggest significant spin-orbit coupling enables both direct and Raman-like relaxation processes in these complexes. This work presents a novel approach to identify new single molecule magnets among spin crossover cobalt(II) systems.

I.1.7 Schiff Base Ligands in Spin Crossover Research

Schiff bases have a long history coordinating transition metal ions, but have only recently unlocked potential for SCO systems [106]. Fine-tuning through modifying substituents on aldehyde/amine precursors enables optimizing properties like solubility, intermolecular interactions, and structural landscapes around the metal center. Schiff base ligands with {N$_3$O$_2$} donor sets have proven to be useful for synthesizing mononuclear Fe(III) complexes that exhibit spin crossover phenomena [107]. By using cyanido ligands, low-spin Fe(III) Schiff base complexes can be reliably obtained, while other pseudohalido ligands like NCS$^-$, NCO$^-$, and N$_3^-$ result in high-spin complexes instead [108]. An important finding is that Schiff bases derived from 2-hydroxy-1-naphthaldehyde (with a napet backbone) display varying spin crossover behaviors depending on the choice of terminal ligand. Gradual, abrupt, and even hysteretic transitions were observed for different napet complexes [107,108-110]. Furthermore, Schiff base ligands containing tetradentate N$_2$O$_2$ donor sets have proven very effective at stabilizing spin crossover in iron(III) complexes [111]. Variation of both the equatorial Schiff base and axial bridging ligands in 1D polymeric systems allows tuning of the spin transition temperature and properties [111]. Both [FeN$_4$O$_2$] and [FeN$_6$] coordination environments have also been successfully constructed using Schiff bases of varying denticities and donor atoms, leading to

SCO activity [112]. Notable examples covered include complexes with tetradentate, tridentate, bidentate, and tripodal tris-bidentate Schiff base ligands, which have shown abrupt, hysteretic, stepwise and multiple SCO behavior [113-117]. Careful structural modification of the ligands by substituent variation allows tuning of SCO transition temperature, abruptness/cooperativity, width of thermal hysteresis, and incorporation of added functionalities like luminescence. Chiral Schiff base ligands have also enabled selective crystallization of homochiral SCO complexes with potential for magneto-optical applications [112].

I.1.8 Applications of Spin Crossover Complexes and Materials

The unique multifunctional attributes of spin crossover complexes that combine electronic, magnetic, optical, and structural modulations have driven extensive research into potential applications. By leveraging spin state switching through external triggers, SCO systems could power molecular electronic devices, sensors, or data storage and logic operations [118]. Spin crossover systems have been incorporated into prototypes of various devices including sensors, actuators, displays and data storage or memory elements [118-120]. Most progress has involved thin films that can be fabricated through techniques like layer-by-layer assembly, Langmuir-Blodgett deposition, electropolymerization and inkjet printing of SCO coordination compounds. Integration into electronic circuits to function as transistors, memory units, or logic devices offers possibilities for spintronics [121]. Crystal engineering approaches have incorporated SCO complexes into solid state materials motifs and mechanically-active actuators. Multifunctional SCO polymer composites also present opportunities where spin switching modulates bulk properties like shape, color, conductivity and permeability. Medical usages have also been proposed for SCO species such as high contrast bioimaging, drug delivery systems with targeted release, [119,122]. Despite promising potential, substantial barriers around operational stability, reversible switching cycling, and interfacing challenges have inhibited practical adoption of spin crossover complexes in real-world devices or commercial technologies thus far [123].

I.2 corrosion inhibitors

I.2.1 introduction on corrosion and protection

Corrosion is the degradation of a material, most commonly metals, through chemical or electrochemical reactions that occur when it contacts an aggressive environment. It affects structures, infrastructure, and construction, particularly steel which sees widespread usage but has high corrosion susceptibility from exposure to moisture, immersion, soil and aggressive solutions. The intricate corrosion processes arise from numerous interdependent factors related to the metal, environment composition, temperature and more. Consequently, despite being commonplace, corrosion remains complex and widely studied.

Fundamentally, corrosion reverts metals/alloys to more stable oxide, sulfide, carbonate or salt states naturally found in their environments [124]. Three main corrosion protection strategies target: the material itself, the surface, or the interacting medium. Selecting specific metals/alloys, geometries and processing for an application exemplifies adapting the base material. Surface treatments like coatings and paintings physically separate the metal from corrosion triggers. Finally, adding inhibitors to the environment reduces its aggression and oxidative tendency.

Inhibitors attract industry interest as an easily implemented, cost-effective anti-corrosion technique directly employed in pickling, oil extraction and closed systems. Their uniqueness lies in mitigating corrosion by modifying the interaction at the environment rather than metal.

I.2.2 history of corrosion inhibition

As with many fields, pinpointing the precise temporal origin of corrosion inhibition is difficult. Corrosion itself was already recognized by the Romans, with the 1st century AD scholar Pliny the Elder outlining coating methods to protect iron and bronze [125]. While corrosion studies arose in the 17th century, scientific examination of mitigation methods began in the 19th century [126]. Decades ago, an observation was made – mineral deposits forming in pipes transporting some natural waters had a protective effect. Rather than continually enhance pipe corrosion resistance, adjusting transported solution mineral levels causing these "preservative" limescale deposits was more practical [127]. Before 1945, fewer than 30 references on corrosion inhibition existed. A 1948 paper by Waldrip cited a 1943 report on

safeguarding oil well corrosion. [128] Numerous inhibition publications spanning aviation, boilers, cooling loops, diesel motors and more released between 1945-1954 signify substantial technological advancement. [129] Over the last 40 years, an exponential rise occurred in summaries, papers and other works – by 1970, 647 inhibition-focused articles were published [130]. In 2022, around 35,362 articles covered this topic, highlighting major field expansion [131].

I.2.3 Definition of Corrosion Inhibitors

The National Association of Corrosion Engineers (NACE) has put forth a definition of a corrosion inhibitor as a chemical substance that, when added in small concentrations to a corrosive environment, effectively stops, decreases, or prevents the corrosion interaction between a metal and its surrounding environment [132]. However, this definition is restrictive in some ways and too broad in others when it comes to properly classifying substances as corrosion inhibitors. Specifically, the NACE definition excludes substances that reduce corrosion rates but do not meet the first condition of "checking, decreasing, or preventing" the metal-environment interaction. For example, adding acids or bases to adjust pH can reduce corrosion rates significantly, but does not constitute inhibition under this definition [129]. On the flip side, some compounds that should be excluded based on the definition, like oxygen scavengers that consume oxygen, can also be reasonably considered inhibitors in some cases [133].

Additionally, the meaning ascribed to "inhibitor" in this definition is too narrow to cover the general concept of slowing down the corrosion process of a metal by any means. As an example, adding the element chromium to iron to produce stainless steel reduces corrosion, but characterizing chromium as a corrosion inhibitor goes against the semantic interpretation in the NACE definition [129].

In summary, while providing a starting point, the NACE definition has limitations when it comes to unambiguously classifying substances as corrosion inhibitors across all contexts and use cases. Some judgment and discretion is still required to determine what constitutes inhibition based on the specifics of the metal-environment system and mechanisms involved.

I.2.4 Conditions of Use

Inhibitors can be utilized as the only means of corrosion protection in two ways: as permanent protection, which allows the use of non-alloyed ferrous metals with satisfactory corrosion resistance, though monitoring of the installation is required [134]; or as temporary protection during periods when the part or system is especially vulnerable to corrosion like during storage, pickling, or cleaning. In the latter case, controlling the inhibitor system is simpler since predicting the inhibitor's performance over time is easier.

Inhibitors can also be combined with other protection methods like: providing additional safeguarding for high corrosion resistant alloys; or adding inhibitors to surface coatings including paint, grease, oil, etc. [129].

I.2.5 Key Factors for Inhibitor Utilization and Performance

there are several essential functions that an effective corrosion inhibitor must fulfill, including lowering the corrosion rate without impacting mechanical properties, remaining stable in the environment, being effective at low concentrations, non-toxic, and being cost effective for industrial use [135-136]. Building on this, Jevremović et al, further elaborate on the most important criteria to consider when selecting appropriate corrosion inhibitors. These key factors include:

➢ Interaction with surface to adsorb and form protective film (self-healing ability)
➢ Solubility to allow inhibitor transport to surface
➢ Reactivity to form protective films in situ
➢ Sacrificial behavior to protect surface
➢ Balancing molecular properties like solubility, reactivity, size
➢ Considering environmental factors like toxicity

In summary, optimizing corrosion inhibition requires balancing various molecular characteristics and surface interactions to achieve performance under the intended conditions and environment.

Both the inhibitor itself and the formulation system are important design factors.

I.2.6 Common Industrial Uses

Corrosion inhibitors have many potential applications for preventing corrosion, although their use can be limited by the large volume of the corrosive medium or the inaccessibility of some corrosive mediums. Traditional major uses of inhibitors include water treatment of drinking water, industrial process water, and boiler water; protecting oil industry infrastructure like drills, pipelines, refineries, storage tanks, and transport vessels at all stages from drilling to end use; temporarily protecting metals during acid cleaning processes, storage, or in cutting fluids; and as additives in metal paints to provide corrosion protection [129].

I.2.7 Classification of corrosion inhibitors

There are several classification systems for corrosion inhibitors that categorize them differently [129,136-138]:

➢ By composition - inhibitors can be organized into organic or inorganic (mineral) categories based on the compounds they contain.

➢ By electrochemical mechanism - inhibitors can be cathodic (slow cathodic reactions), anodic (slow anodic reactions), or mixed (slow both reactions) depending on which half-reaction of corrosion they primarily influence.

➢ By interface mechanism - classification focused on how inhibitors interact with metal surfaces, either through adsorption directly onto the metal or by forming a protective barrier film.

➢ By application - inhibitors can be categorized by the industrial processes or scenarios where they are utilized (e.g. water treatment, temporary protection, oils).
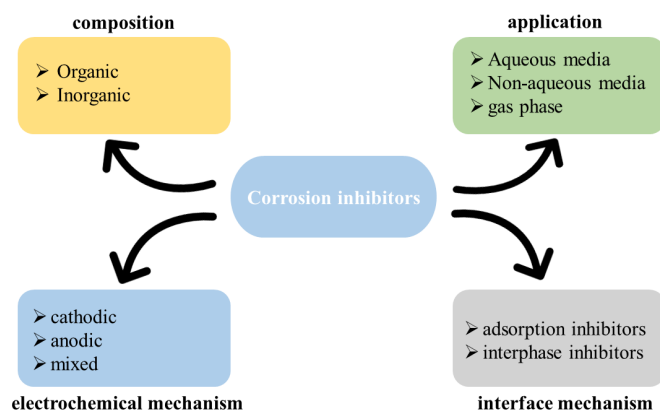
Figure I.12 provides a comprehensive overview of various categorizations of corrosion inhibitors.

The different classification approaches provide insights into the composition, functionality, underlying protective mechanisms, and appropriate usage cases for various corrosion inhibiting products. Understanding these categories aids in inhibitor development, selection, and application.

I.2.7.1 Classification by Nature of Products (composition)

Inhibitors can be broadly categorized based on their chemical composition. The two main classifications are:

i.   **Organic Inhibitors**

Organic compounds have significant potential for further development as corrosion inhibitors. Despite certain advantages of inorganic inhibitors, organic inhibitors tend to be preferred largely due to lower ecotoxicity and more environmentally friendly profiles. These substances function by adsorbing onto the metal surface and forming a more or less continuous protective barrier or film, albeit of finite thickness. This barrier prevents contact between the corrosive solution and the underlying metal [131,138]. Many diverse organic compounds can potentially serve as effective corrosion inhibitors. Starting from an initial "parent" molecule with some efficiency, increasingly complex organic compounds can be synthesized through structural modifications. The goals of such modifications may be to improve inhibition efficiency, enhance solubility in aqueous or non-aqueous solutions, increase surface wettability characteristics, optimize thermal stability at elevated temperatures, and reduce production costs [139-141]. Many common organic inhibitors leverage heteroatoms such as nitrogen, oxygen, sulfur, or phosphorus to bond with active sites on metal surfaces. Some common organic inhibitor families used in industry include: amines, amides, acetylenic alcohols, carboxylates, oxadiazoles, mercaptans, sulfoxides, phosphonates, imidazolines, triazoles, and thiazoles [142-144]. There has been substantial focus on utilizing petroleum industry byproducts and waste streams as a low-cost feedstock for producing effective oil-soluble organic corrosion inhibitors [145].

While organic inhibitors can perform extremely well under many conditions, temperature is an important consideration in inhibitor selection and application. Some organic compounds have thermal stability limitations or lose effectiveness in protecting metals at elevated temperatures, placing constraints on their useful temperature range for corrosion prevention in high temperature systems. Understanding these temperature limitations and compensating for them

with inhibitor blends or alternatives is important for ensuring robust long-term corrosion protection.

ii.   Inorganic inhibitors

Mineral inhibitors are chemical compounds commonly utilized to prevent corrosion in industrial systems. They are often employed in neutral, alkaline, or less frequently, acidic aqueous environments. When dissolved, the mineral molecules dissociate into cations and anions that interfere with corrosion reactions through various mechanisms. The most widely used inhibitory cations are calcium (Ca^{2+}) and zinc (Zn^{2+}). These divalent cations can interact with anions like hydroxide (OH^-) to form insoluble compounds that deposit on metal surfaces, shielding them from corrosion. Common inhibitory anions include oxo-anions with the general formula XO_4^{n-} such as chromates, molybdates, phosphates, silicates and more [147-148]. The oxo-anions react with metal ions to form thin passive films on metal surfaces that slow corrosion rates.

The number of mineral inhibitors in use is decreasing because many have harmful environmental side effects. However, new non-toxic organic complexes composed of chromium(III) or other cations like Zn^{2+}, Ca^{2+}, Mg^{2+}, Mn^{2+}, Sr^{2+}, Al^{2+}, Zr^{2+}, and Fe^{2+} have been developed and remain effective corrosion inhibitors [129].

Additional factors that influence the performance of mineral inhibitors include solution pH, temperature, velocity, and more. Inorganic inhibitors tend to work best at pH levels between 6-10. Higher velocities and temperatures typically accelerate corrosion reactions thus decreasing efficiency. The optimal dosage of inhibitors also depends on the specific system conditions and treatment goals. Understanding these variables allows corrosion engineers to model and predict inhibition behavior.

I.2.7.2 Classification by Electrochemical Mechanism of Action

Corrosion inhibitors can be classified based on their mechanism of action within electrochemical corrosion processes occurring in liquid phases. This process that occurs when metals are exposed to liquid environments involves two key reactions :

- an anodic reaction where the metal itself is oxidized and dissolved

$$M \longrightarrow M^{n+} + ne^-$$

Example :
$$Fe \longrightarrow Fe^{2+} + 2e^-$$
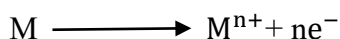
- a cathodic reaction where an oxidant species in solution is reduced.

$$2H^+ + 2e^- \longrightarrow H_2 \quad \text{(acidic deoxygenated environment)}$$

$$O_2 + 4H^+ + 4e^- \longrightarrow 2H_2O \quad \text{(acidic aerated environment)}$$
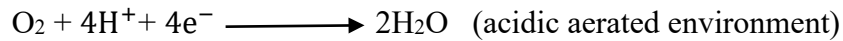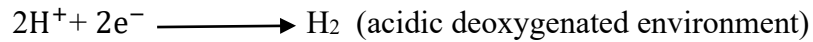
Corrosion inhibitors act to slow down either or both of these reactions, effectively decreasing the overall corrosion rate.

More specifically, if an inhibitor acts by selectively blocking surface sites where the anodic metal dissolution reaction takes place, hindering the metal's oxidation, it is termed an anodic inhibitor. Anodic inhibitors are a type of corrosion inhibitor that function by affecting the anodic portion of the metal's polarization curve. Specifically, they cause a positive shift in the corrosion potential E_{corr} to higher values, making the metal less prone to corroding. There are several ways anodic inhibitors cause this beneficial shift:

i-   decreasing the exchange current density i_0 for metal dissolution,

ii-   modifying the slope of the anodic Tafel line while maintaining Tafel-like kinetic behavior,

iii-   polarizing the metal into the passive region of the polarization curve and inducing passivation,

iv-   decreasing the passive current density i_{pass} once passivity is achieved.

Mechanisms (i) and (ii) involve manipulating the kinetics of the anodic half-reaction by reducing the rate of metal dissolution. Mechanisms (iii) and (iv) involve enhancing passivity by stimulating formation of a protective oxide film and making this film more impermeable to ion transfer [136].

Effective anodic inhibitors are often oxidizing agents or passivating chemicals that promote growth of the native oxide layer naturally present on most metal surfaces. By maintaining, repairing, or thickening this passive film, anodic inhibitors make the surface more resistant to corrosion. Adequate inhibitor concentrations above a critical threshold value are required to achieve stable passivation. If the concentration is too low, the inhibitor may actually exacerbate corrosion [136, 150-151]. The concentration-dependent effectiveness relates to the need to polarize the metal above its Flade potential E_F into the passive region [155].
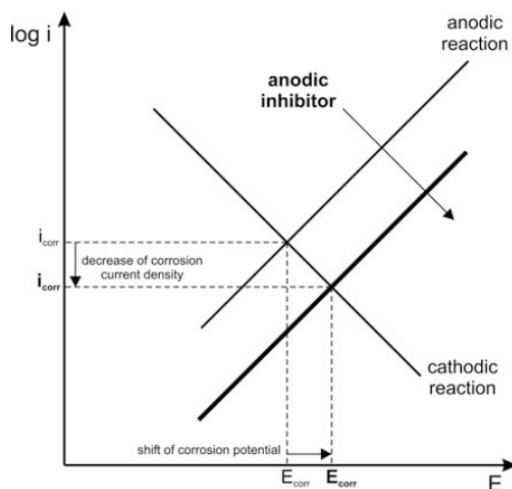
Figure I.13 Impact of an anodic inhibitor on specific electrochemical reactions within the Evans diagram [189].

Some common examples of anodic inhibitors are chromates, molybdates, silicates, nitrites, phosphates, and other oxidizing chemicals [152-153]. These compounds provide passivity and reduce the corrosion rate by forming a protective oxide layer that prevents the anodic half reaction, which involves metal ion dissolution into the surrounding environment. Anodic inhibitors are most useful and effective in acidic, oxidizing conditions where passive films require assistance to persist [154]. Overall, anodic inhibitors are an important corrosion prevention method that function by manipulating the anodic kinetics and physics to maintain a passive surface film. On the other hand, inhibitors that function by blocking surface sites where the cathodic reaction occurs, slowing the reduction of oxidants, are known as cathodic inhibitors.

Cathodic inhibitors are a type of corrosion inhibitor that acts by reducing the rate of the cathodic half-reaction in the corrosion process. The cathodic reaction represents the first step of corrosion, where the metal surface gains electrons by reducing species like oxygen or hydrogen ions. Cathodic inhibitors work through several mechanisms to slow down this electron transfer reaction. One common mechanism is precipitating out of solution as barrier films on active cathodic surface sites on the metal. Examples of precipitating inhibitors include bivalent cations like zinc, and magnesium, as well as anions like phosphates and silicates. The precipitated compounds form thin, compact oxide or hydroxide layers that block access of oxygen and hydrogen species to the surface. By preventing contact between the metal and reducing agents, the cathodic reaction kinetics decrease.

Other cathodic inhibitors function by adsorbing directly onto the metal surface. Adsorbed inhibitors increase the overpotential required for proton reduction to hydrogen gas. They also decrease the transport limited current by hindering diffusion of dissolved oxygen to the surface [156]. Both effects make it more difficult for the cathodic reaction to proceed, requiring more energy and reducing the electron transfer rate. While very effective at retarding the kinetics of the cathodic half-reaction, cathodic inhibitors are generally less efficient than anodic inhibitors at equivalent concentrations [136].
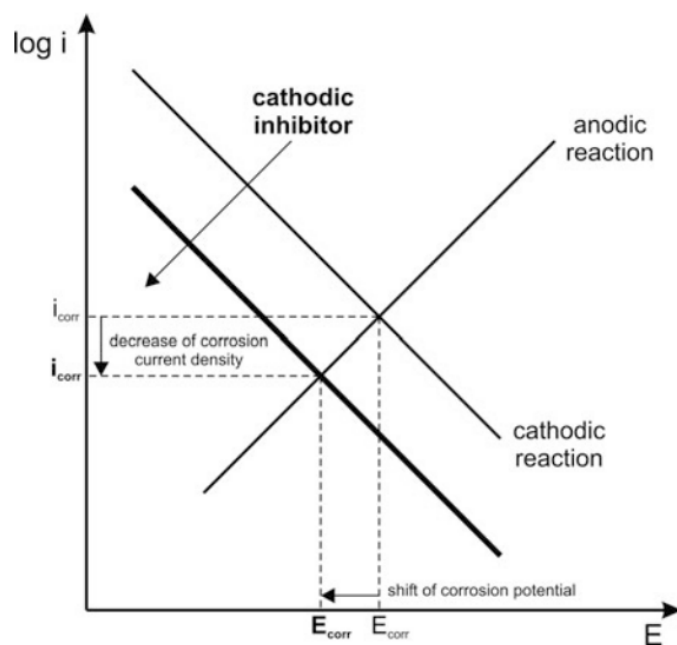
Figure I.14 Impact of an cathodic inhibitor on specific electrochemical reactions within the Evans diagram [189].

The cathodic reaction depends on the solution conditions - in aerated environments, it is the reduction of dissolved oxygen, while in acidic conditions, the reduction of protons (H^+) tends to predominate. In fact, in acidic solutions, the proton reduction reaction is so fast that the dissolved oxygen reduction reaction is often negligible in comparison [149].

One drawback of some cathodic inhibitors is they increase susceptibility to hydrogen embrittlement. As the cathodic reaction is hindered, there is more hydrogen absorbed into the metal lattice. This absorbed hydrogen can combine to form gas pockets and cracks that weaken the metal over time. However, used properly, cathodic inhibitors are useful corrosion prevention tools, especially in low-oxidant environments like alkaline solutions. By deposition of barrier

films and hindering the supply of electrons from reduction reactions, cathodic inhibitors slow the corrosion rate through surface-specific effects on the cathodic half-reaction [157-158].
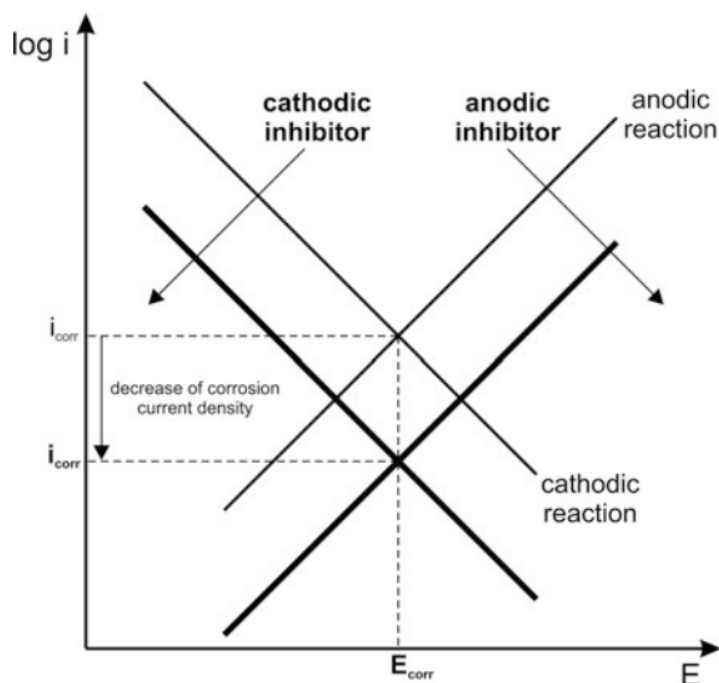
Figure I.15 Influence of a mixed inhibitor on specific electrochemical reactions within the Evans diagram [189].

While anodic and cathodic inhibitors target one reaction or the other, mixed inhibitors are capable of decreasing the rates of both the anodic metal dissolution and cathodic oxidant reduction reactions simultaneously. By concurrently hindering both half reactions, they can achieve greater reductions in the overall corrosion rate. These inhibitors are predominantly composed of organic compounds that form a protective film on the metal surface. This film is dynamic in nature, possessing the ability to self-repair or reform when damaged, a property known as self-healing.

The effectiveness of mixed inhibitors in preventing corrosion is contingent upon a multitude of factors. Firstly, the affinity of the inhibitor molecules to the metal surface plays a crucial role, as strong adsorption is essential for the formation of a stable film. Surface preparation is another critical factor, as the condition of the metal surface can influence the adhesion and uniformity of the protective layer.

The chemical composition and applied concentration of the corrosion inhibitor itself are also significant determinants of its efficacy. The presence of specific functional groups, heteroatoms, and unsaturated bonds can enhance the adsorption and film-forming capabilities of the inhibitor. Additionally, the pH of the electrolyte and the presence of dissolved salts can affect the performance of the inhibitor by altering the electrochemical processes and the solubility of the inhibitor molecules [159-160]. Temperature and pressure are also important factors that influence the adsorption process of the inhibitor molecules onto the metal surface. Furthermore, mixed inhibitors often incorporate unsaturated bonds, such as double or triple bonds, which can serve as adsorption centers through the delocalized π electrons [161-163]. The presence of these unsaturated bonds can enhance the adsorption and film-forming capabilities of the inhibitor.

Most mixed inhibitors used in the oil and gas industry feature a long-chain hydrocarbon structure, typically ranging from C14 to C18, which provides additional hydrophobic interactions with the metal surface and contributes to the stability and self-healing properties of the protective film [136]. Examples of commonly used mixed inhibitors include aldehydes, thiourea, acetylene, nitrogen quaternary salts, sulfur compounds (such as thioalcohols or mercaptans and organic sulfides), sodium salts of aromatic carboxylic acids, and salts of higher fatty acids [164].

The mechanism of corrosion inhibition therefore depends on whether the inhibitor selectively blocks anodic sites, cathodic sites, or both anodic and cathodic sites on the metal surface exposed to the corrosive environment. In summary, the mechanism of action by which each type of inhibitor is distinct and relies on the characteristics of the metal and the surroundings where it is utilized.

Two noteworthy points deserve consideration regarding the classification and nature of corrosion inhibitors. Firstly, it is rare for an inhibitor to act exclusively on only either the cathodic or anodic partial reaction. In most cases, both reactions are affected to a certain extent by the inhibitor. Therefore, the classification of inhibitors as anodic, cathodic, or mixed should be viewed as a useful distinction only when the inhibitor predominantly affects one of the partial reactions while having a minimal impact on the other (Figure 16). Secondly, the examples presented clearly illustrate that a wide range of substances can act as corrosion inhibitors. Indeed, any foreign species present in the solution will interact with the metal surface, and in most cases, this interaction, such as adsorption, will decrease the rate of metal dissolution.
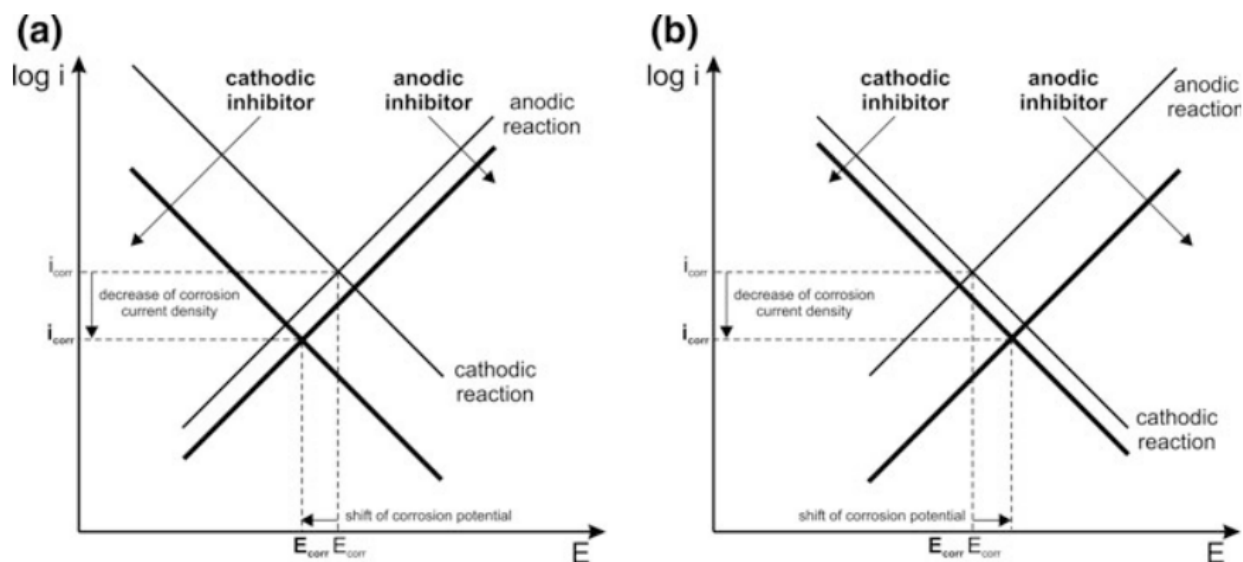
Figure I.16 The impact of a mixed inhibitor, with a predominant effect on one of the partial electrochemical reactions, within the Evans diagram [189].

Consequently, it becomes a relatively straightforward task to introduce an organic substance with some affinity for the metal surface into the solution, as such a substance will inherently act as a corrosion inhibitor [136].

Within the oil and gas industry, corrosion inhibition is typically achieved through the use of inhibitor formulations, which are mixtures comprising various compounds. These formulations are designed to provide comprehensive protection against corrosion by leveraging the synergistic effects of different inhibitor components. However, the exact compositions of these inhibitor formulations are often treated as proprietary information and are not publicly disclosed by the companies that develop and manufacture them [136].

I.2.7.3 Classification by Interface Mechanisms and Principles of Action

An alternative approach to classifying corrosion inhibitors is based on their mode of attachment and interaction with the metal surface. This classification system distinguishes inhibitors into two main categories: adsorption inhibitors, also known as "interface" inhibitors, and interphase inhibitors. Adsorption inhibitors are more commonly observed and employed in acidic environments. These inhibitors function by forming mono- or bi-dimensional films of inhibitor molecules that adsorb onto the metal surface. The adsorption process involves the inhibitor molecules forming a protective layer, typically composed of a single or double layer of

molecules, on the metal surface. In contrast, interphase inhibitors are specifically designed for use in neutral or alkaline environments. These inhibitors form three-dimensional films that not only involve the adsorption of inhibitor molecules but also integrate the dissolution products of the substrate material itself. The formation of these interphase films is a more complex process, where the inhibitor molecules interact with the metal surface and incorporate the dissolved metal ions or other corrosion products, creating a multi-layered, three-dimensional protective film.

The adsorption of inhibitor molecules onto the metal surface is a universal phenomenon driven by the presence of unsatisfied chemical bonds on the surface atoms. Surfaces, by nature, have atoms that lack complete coordination and have unfilled electronic orbitals, creating a tendency to capture and adsorb atoms and molecules from the surrounding environment. This adsorption process is governed by two main types of interactions: physisorption and chemisorption.
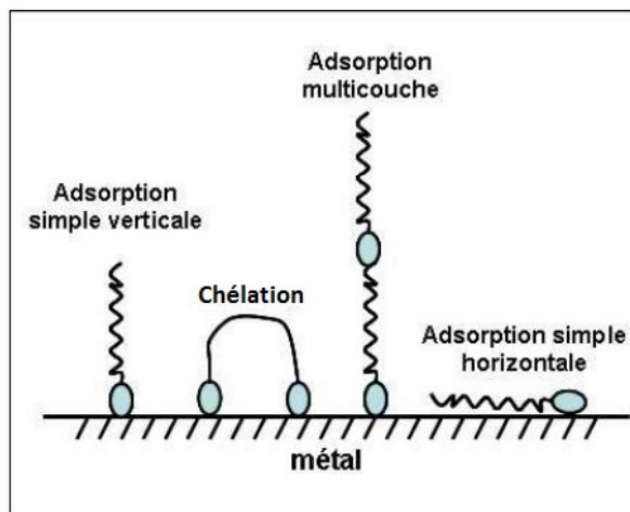
Figure I.17 Schematic representation depicting the adsorption modes of organic inhibitor molecules on a metal surface, as referenced by [136].

i.   Physisorption

Physical adsorption, also known as physisorption, is one of the primary mechanisms by which corrosion inhibitors interact with and adhere to metal surfaces. This type of adsorption is governed by relatively weak intermolecular forces, such as van der Waals forces and electrostatic interactions, between the inhibitor molecules and the metal surface. The electrostatic interactions

that drive physisorption arise from the presence of charged species or dipoles in the inhibitor molecules and the electrical charge on the metal surface. The charge on the metal surface is determined by the position of the corrosion potential of the metal relative to its zero-charge potential (E_0), which is a characteristic value for each metal-electrolyte system [165-166].

When the corrosion potential of the metal has a value lower than E_0, the metal surface carries a positive charge, favoring the adsorption of cationic inhibitor species. Conversely, when the corrosion potential is in the positive region relative to E_0, the metal surface is negatively charged, promoting the adsorption of anionic inhibitor species.

In some cases, the surface charge can be modified by pre-adsorbing an intermediate ionic layer before the inhibitor adsorbs. This occurs with quaternary ammonium inhibitors $(RNH_4)^+$ in acidic media. If the intrinsic metal surface is positively charged under those conditions, the cationic $(RNH_4)^+$ would be electrostatically repelled and not inhibit. However, introducing chloride anions first allows them to adsorb and negatively charge the surface. Then the $(RNH_4)^+$ cations can subsequentially adsorb atop the chloride layer and inhibit corrosion effectively [136,167]. So the surface charge, governed by E_{corr} vs E_0, dictates whether cations, anions, or pre-adsorbed ionic interlayers are needed for an inhibitor to adsorb and provide inhibition. This electrostatic tuning of the surface is key to optimizing inhibitor-surface interactions.

ii.   Chemisorption

Chemisorption is a more prevalent and efficient mechanism than physisorption for corrosion inhibition. It involves a transfer of electrons between the orbitals of the metal surface and the inhibitor molecule, resulting in the formation of much stronger chemical bonds with substantially higher bond energies compared to physisorption. Chemisorption is an irreversible process that is highly specific to the particular metal involved. It is a rapid phenomenon, with the rate being dependent on temperature, and characterized by a high activation energy barrier that must be overcome.

The key factor enabling chemisorption is the presence of electron-rich sites or moieties in the inhibitor molecule that can facilitate electron transfer to the metal surface. Such electron-rich centers include free electron pairs as found in anionic species, neutral molecules containing lone pairs of electrons, as well as delocalized π-electron systems associated with multiple bonds (e.g.

double or triple bonds) or aromatic rings [168-169]. The existence of unsaturated bonds is particularly advantageous for enhancing the inhibitory efficiency of organic molecules in acidic media, as they can adsorb readily onto either positively charged surfaces (via the π-electrons) or negatively charged surfaces (via partial positive charges on the unsaturated atoms). There is a clear trend observed when considering the tendency for strong chemisorptive bonding - it increases as the electrons involved become less tightly bound to the donor atom in the inhibitor molecule. In other words, the more readily the functional atoms (those providing the electron density) can donate electrons to form new bonds with the metal surface, the more effective the inhibitor will be. For a series of structurally similar organic inhibitor molecules differing only in their functional atom/group, the inhibition efficiency increases in the order $O < N < S < Se < P$, which follows the decreasing electronegativity of these atoms/groups [170-171].

Apart from the specific functional groups, several other structural factors pertaining to the inhibitor molecule can influence its adsorption behavior and consequently its inhibition performance. These include the overall molecular structure, particularly steric effects arising from the size and shape of the molecule, as well as the molecular weight. Organic inhibitors employed for acidic corrosion environments comprise a diverse array of molecules, including aromatics and macromolecules featuring linear or branched hydrocarbon chains [172]. These adsorb onto the active sites present on the metal surface without altering the fundamental mechanisms of the partial electrochemical reactions involved in corrosion. By blocking access to these reactive sites, they are able to reduce the rates of the cathodic and/or anodic corrosion processes in proportion to the fraction of active sites covered by the inhibitor layer.

Effective organic corrosion inhibitors typically possess an amphiphilic molecular structure comprising a non-polar, hydrophobic component made up primarily of carbon and hydrogen atoms (often a bulky hydrocarbon segment), coupled with a polar, hydrophilic component embodied by one or more functional groups such as -NH$_2$ (amine), -SH (mercapto), -OH (hydroxyl), or -PO$_3^{2-}$ (phosphonate) [129]. The inhibitor molecule anchors itself to the metal surface through this polar functional group, while the non-polar, bulkier segment helps sterically block further access to the surface, thereby providing corrosion protection.

Some additional structural descriptors that have been found to exert an influence on the effectiveness of organic inhibitors include: the molecular area projected onto the metal surface

(which depends on the different possible orientations and packing arrangements of the adsorbed inhibitor ions/molecules at the metal-solution interface), the molecular weight (with higher weights often correlating with improved performance up to a certain limit), precise molecular conformation adopted at the interface, and the specific nature as well as positioning of any substituents present on the core inhibitor framework [169, 173-175]. Overall, chemisorption grants organic inhibitor molecules the ability to bind tenaciously to metal surfaces in corrosive environments, thereby providing robust protection against the deleterious effects of corrosion by impeding the underlying electrochemical processes. A nuanced understanding of the structural attributes that favor chemisorptive interactions is crucial for the rational design of high-performance corrosion inhibitors tailored for specific operational conditions.
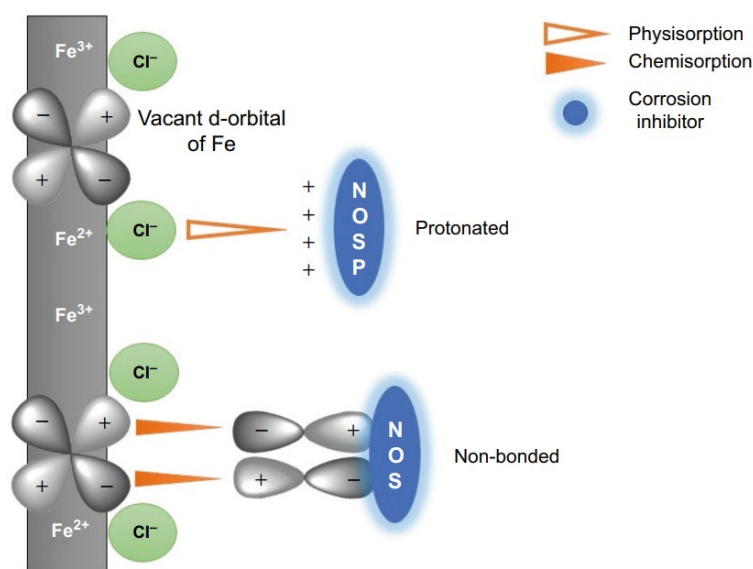
Figure I.18 illustrates the process of physical and chemical adsorption, as sourced from [190].

I.2.7.4 Classification by Field of Application

Corrosion inhibitors are widely used across many industries and application areas, with their selection being heavily influenced by the nature of the environment they need to operate in. A major categorization is based on whether the corrosive medium is aqueous or non-aqueous. For aqueous systems, inhibitors are further subdivided based on the pH (acidity/basicity) and chemical composition of the solution. In acidic aqueous media, acid corrosion inhibitors are employed. These find extensive use in processes like acid pickling of steels, where they prevent excessive metal dissolution during the controlled removal of oxide scales. The oil and gas

industry is a major user of acid inhibitors in drilling muds and well treatment fluids which are often highly acidic.

In neutral aqueous environments like cooling water systems, heat exchangers, and water-based coatings/paints, corrosion inhibitors tailored for those conditions are used. These may include phosphates, molybdates, zinc compounds and other salt formulations designed to provide corrosion resistance without disrupting process chemistry [176].

Non-aqueous media also require corrosion inhibition, with organic inhibitors being more compatible. Large volumes are used in lubricating oils and fuels like gasoline, which can pick up moisture or contain ionic contaminants that destabilize oil films and cause corrosion of metallic engine components. The inhibitors help neutralize these effects [177].

For vapor/gas phase protection, volatile corrosion inhibitors (VCIs) or vapor phase inhibitors (VPIs) with high vapor pressures are typically used. These are often amines or other organic compounds that can diffuse through an enclosed atmosphere and form protective inhibitor films on exposed metal surfaces during storage and shipping of packaged items [178].

Overall, the wide variety of corrosive conditions and industrial applications necessitates having access to a diverse array of corrosion inhibitor formulations. These inhibitor chemistries must be judiciously chosen based on factors such as the precise nature of the corrosive environment, the need for the inhibitor to be compatible with other system components, and the level of corrosion protection required for that specific situation.

I.2.8 Influence of Concentration on the Inhibitory Effect

The relationship between the amount of corrosion inhibitor adsorbed onto a metal surface and its concentration in the bulk solution can frequently be modeled using adsorption isotherm equations. While various adsorption isotherm models exist, not all are well-suited for analyzing the adsorption behavior of corrosion inhibitors. In the context of corrosion inhibition studies, three specific isotherm equations are commonly employed - the Langmuir, Temkin, or Freundlich models.

i.   **Langmuir Adsorption Isotherm:**

The Langmuir model is based on several key assumptions:

> ➢ The metal surface contains a fixed number of adsorption sites available for inhibitor species [179].
>
> ➢ Each site can accommodate no more than one adsorbed inhibitor molecule or ion [180].
>
> ➢ All surface sites are energetically equivalent with no preferential adsorption regions [181].
>
> ➢ There are no interactions between inhibitor species already adsorbed on neighboring sites [180].
>
> ➢ Adsorption is restricted to a monolayer coverage, with no multilayer formation [180].

Under these idealized conditions, the Langmuir model states that the rate of inhibitor adsorption is directly proportional to the inhibitor concentration (C_{inh}) in the solution and the fraction of surface sites that are unoccupied ($1-\theta$), where θ represents the fractional surface coverage ($0 < \theta < 1$).

$$\text{Adsorption Rate} = K_{ads}\,(1-\theta)\,C_{inh} \qquad (I.10)$$

Conversely, the rate of desorption depends solely on the fraction of occupied sites (θ):

$$\text{Desorption Rate} = K_{des}\,\theta \qquad (I.11)$$

At equilibrium, the adsorption and desorption rates are balanced:

$$K_{ads}\,(1-\theta)\,C_{inh} = K_{des}\,\theta \qquad (I.12)$$

Rearranging this equation yields the classic Langmuir adsorption isotherm:

$$\frac{\theta}{(1-\theta)} = \frac{K_{ads}}{K_{des}}\,C_{inh} = b\,C_{inh} \qquad (I.13)$$

Where: K_{ads} is the Langmuir adsorption equilibrium constant.

The surface coverage θ can then be calculated from the inhibitor concentration C as:

$$\theta = \frac{b\,C_{inh}}{1 + b\,C_{inh}} \qquad (I.14)$$

This Langmuir model has been widely applied to analyze corrosion inhibitor adsorption despite its simplifying assumptions. It often provides a reasonable approximation, especially at

lower surface coverages before lateral interactions become significant. However, when the assumptions break down, such as with inhomogeneous surfaces or strong intermolecular forces, other isotherms like Temkin or Freundlich may better represent the experimental inhibitor adsorption behavior over a wider range of concentrations and coverages.

ii.   Temkin Adsorption Isotherm:

Unlike the Langmuir model, the Temkin isotherm accounts for interactions between adsorbed inhibitor species on the metal surface. The key assumptions are:

➢ The free energy of adsorption is a linear function of surface coverage (θ) [182].

➢ The adsorption energy decreases linearly with increasing coverage due to adsorbate-adsorbate interactions [183].

➢ The chemical rate constants depend on the surface coverage [182].

➢ Adsorbed species can experience lateral attractive or repulsive forces from neighboring adsorbates [184].

The Temkin isotherm equation relates the surface coverage to the inhibitor concentration as follows:

$$\text{b } C_{inh} = \frac{\exp(a\theta)-1}{1-\exp\left(-a\left(1-\theta\right)\right)} \tag{I.15}$$

Where: a is the interaction constant related to the adsorbate-adsorbate attractive/repulsive forces, b is the adsorption coefficient and C_{inh} is the inhibitor concentration in the electrolyte solution.

The a parameter accounts for the net attractive ($a < 0$) or repulsive ($a > 0$) interactions experienced by adsorbed inhibitor species due to surrounding adsorbates.

iii.   Freundlich Adsorption Isotherm:

The Freundlich isotherm model accounts for the possibility of multilayer adsorption occurring on a heterogeneous surface composed of adsorption sites with varying binding energies [185]. It differs from the Langmuir and Temkin models which assume monolayer adsorption on energetically equivalent sites. The Freundlich isotherm equation is an empirical relationship expressed as:

$$\log \theta = \log K + \frac{1}{n}\log C_{inh} \tag{I.16}$$

Where: K and n are Freundlich constants relating to adsorption capacity and intensity

Unlike the Langmuir and Temkin equations derived from theoretical considerations, the Freundlich isotherm is a purely empirical model that does not provide explicit information about the underlying adsorption mechanism or adsorbate-adsorbent interactions [186]. However, the Freundlich isotherm can still serve as a useful tool for fitting experimental adsorption data, especially when dealing with inhibitor systems exhibiting multilayer behavior on heterogeneous metallic surfaces. Analyzing the Freundlich constants K and n allows for qualitative comparisons of the adsorption capacities and intensities between different corrosion inhibitors.

Determining which classical adsorption isotherm (Langmuir, Temkin, Freundlich, etc.) provides the best fit for a particular inhibitor system can be quite challenging. Adsorption on heterogeneous surfaces with significant lateral interactions often corresponds more closely to Temkin-type behavior.

However, caution must be exercised when interpreting calculated surface coverages from isotherm fits, as the idealized assumptions of each model may not fully capture the complex inhibitor-surface interactions occurring in real corrosion systems. Factors like surface roughness, oxide layers, co-adsorbed species, and inhibitor speciation can significantly alter adsorption. Nonetheless, adsorption isotherm analysis remains a powerful tool for quantifying inhibitor adsorption, provided the limitations of each model are acknowledged. Complementary experimental techniques probing the adsorbate-surface interface are beneficial for validating the adsorption behavior predicted by isotherm fits.

I.2.9 Influence of Temperature on Corrosion Inhibition

The influence of temperature on the performance of corrosion inhibitors, especially in aggressive acidic media, has garnered significant research attention due to its relevance in high-temperature industrial processes like acid pickling, descaling, and removal of corrosion products from metallic equipment and installations. In these harsh environments, inhibitors play a crucial role in mitigating the severe acid attack on the metal surfaces. Numerous investigations have been conducted to elucidate the effects of temperature on the inhibition efficiency for various metal-inhibitor-acid systems. Comprehensive studies on the corrosion inhibition of steel, copper, and ARMCO iron in sulfuric acid solutions over wide temperature ranges, typically 30-65°C and 20-80°C, have consistently revealed a decrease in the inhibitor's protective capability as the

temperature increases. This temperature dependence of the corrosion rate can be quantified using the Arrhenius equation, enabling the determination of the apparent activation energy (E_a) in the absence of inhibitors and the activation energy (E_{ai}) in the presence of inhibitors.

$$V_{corr} = A\exp(\frac{-E_a}{RT}) \qquad\qquad (I.17)$$

Where: Ea the activation energy, A a constant, R the gas constant, T the absolute temperature and V_{corr} the corrosion rate

Based on the relative values of Eai compared to Ea, Radovici proposed a classification scheme that distinguishes three distinct categories of inhibitor behavior:

- $E_{ai} > E_a$: In this category, the inhibitor molecules are adsorbed onto the metal substrate primarily through relatively weak electrostatic or physisorption interactions [187]. These inhibitors exhibit a significant reduction in their protective efficacy at elevated temperatures due to the temperature sensitivity of the weak physisorption bonds, which can readily desorb under thermal activation.
- $E_{ai} < E_a$: This group encompasses inhibitors that form strong chemisorption bonds with the metal surface, facilitated by the sharing or transfer of electrons between the inhibitor molecules and the substrate [187]. Remarkably, these inhibitors demonstrate an increase in their protective power with rising temperature, as the chemical adsorption process is favored under higher thermal conditions.
- $E_{ai} = E_a$: A rare scenario where the inhibition efficiency remains essentially unchanged with temperature variations, suggesting a temperature-independent adsorption mechanism [188]. However, very few inhibitor compounds exhibit this behavior.

The observed decrease in inhibitor performance at higher temperatures has been attributed to shifts in the adsorption/desorption equilibrium, favoring desorption and disrupting the protective inhibitor layer on the metal surface. Additionally, some researchers have proposed that a transition from physisorption to chemisorption mechanisms may occur as the temperature increases, which could potentially enhance the inhibition efficiency if the inhibitor molecules can form strong chemical bonds with the substrate. Significantly, several studies have indicated that despite the general trend of declining inhibitor effectiveness with temperature, a sufficiently high inhibitor concentration can still provide satisfactory corrosion protection at elevated

temperatures. By maintaining an adequate supply of inhibitor species in the solution, the adsorbed inhibitor layer on the metal surface can be replenished, counteracting the disruptive effects of thermal desorption and ensuring continued mitigation of acid attack.

This temperature-dependent behavior of corrosion inhibitors underscores the importance of carefully selecting and optimizing inhibitor formulations based on the specific operating conditions, particularly when high-temperature acid exposure is involved. A comprehensive understanding of the inhibitor-substrate interactions, adsorption mechanisms, and temperature effects is crucial for designing effective corrosion control strategies and ensuring the long-term integrity of metallic assets in harsh industrial environments.

References

[1] Cambi, L., & Gagnasso, A. (1931). Iron dithiocarbamates and nitrosodithiocarbamates. Atti. Accad. Naz. Lincei, 13, 809-813.

[2] Griffith, J. S. (1956). On the magnetic properties of some haemoglobin complexes. Proceedings of the Royal Society of London. Series A. Mathematical and Physical Sciences, 235(1200), 23-36.

[3] Baker Jr, W. A., & Bobonich, H. M. (1964). Magnetic properties of some high-spin complexes of iron (II). Inorganic Chemistry, 3(8), 1184-1188.

[4] Ewald, A. H., Martin, R. L., Ross, I. G., & White, A. H. (1964). Anomalous behaviour at the 6 A 1-2 T 2 crossover in iron (III) complexes. Proceedings of the Royal Society of London. Series A. Mathematical and Physical Sciences, 280(1381), 235-257.

[5] Reeder, K. A., Dose, E. V., & Wilson, L. J. (1978). Solution-state spin-equilibrium properties of the tris [2-(2-pyridyl) imidazole] iron (II) and tris [2-(2-pyridyl) benzimidazole] iron (II) cations. Inorganic Chemistry, 17(4), 1071-1075.

[6] Stoufer, R. C., Smith, D. W., Clevenger, E. A., & Norris, T. E. (1966). Complexes of cobalt (II). I. On the anomalous magnetic behavior of some six-coordinate cobalt (II) complexes. Inorganic Chemistry, 5(7), 1167-1171.

[7] Navon, G., & Klaeui, W. (1984). Cobalt-59 NMR of a cobalt (III) spin-crossover compound. Inorganic Chemistry, 23(17), 2722-2725.

[8] Ammeter, J. H., Bucher, R., & Oswald, N. (1974). High-spin-low-spin equilibrium of manganocene and dimethylmanganocene. Journal of the American Chemical Society, 96(25), 7833-7835.

[9] Sim, P. G., & Sinn, E. (1981). First manganese (III) spin crossover, first d4 crossover. Comment on cytochrome oxidase. Journal of the American Chemical Society, 103(1), 241-243.

[10] Halepoto, D. M., Holt, D. G., Larkworthy, L. F., Leigh, G. J., Povey, D. C., & Smith, G. W. (1989). Spin crossover in chromium (II) complexes and the crystal and molecular structure of the high spin form of bis [1, 2-bis (diethylphosphino) ethane] di-iodochromium (II). Journal of the Chemical Society, Chemical Communications, (18), 1322-1323.

[11] Kaustov, L., Tal, M. E., Shames, A. I., & Gross, Z. (1997). Spin transition in a manganese (III) porphyrin cation radical, its transformation to a dichloromanganese (IV) porphyrin, and chlorination of hydrocarbons by the latter. Inorganic chemistry, 36(16), 3503-3511.

[12] Olguín, J. (2020). Unusual metal centres/coordination spheres in spin crossover compounds. Coordination Chemistry Reviews, 407, 213148.

[13] Gütlich, P., & Goodwin, H. A. (Eds.). (2004). Spin crossover in transition metal compounds I (Vol. 1). Springer Science & Business Media.

[14] Halcrow, M. A. (Ed.). (2013). Spin-crossover materials: properties and applications. John Wiley & Sons.

[15] Dirtu, M. M., Rotaru, A., Gillard, D., Linares, J., Codjovi, E., Tinant, B., & Garcia, Y. (2009). Prediction of the spin transition temperature in FeII one-dimensional coordination polymers: An anion based database. Inorganic chemistry, 48(16), 7838-7852.

[16] Bousseksou, A., Molnár, G., Salmon, L., & Nicolazzi, W. (2011). Molecular spin crossover phenomenon: recent achievements and prospects. Chemical Society Reviews, 40(6), 3313-3335.

[17] Bethe, H. (1929). Termaufspaltung in kristallen. Annalen der Physik, 395(2), 133-208.

[18] Crichton, R. R. (2012). Biological inorganic chemistry: a new introduction to molecular structure and function. Elsevier.

[19] Van Vleck, J. H. (1935). Valence strength and the magnetism of complex salts. The Journal of Chemical Physics, 3(12), 807-813.

[20] Hauser, A. (2004). Ligand field theoretical considerations. Spin Crossover in Transition Metal Compounds I, 49-58.

[21] Sorai, M., & Seki, S. (1974). Phonon coupled cooperative low-spin 1A1high-spin 5T2 transition in [Fe (phen) 2 (NCS) 2] and [Fe (phen) 2 (NCSe) 2] crystals. Journal of Physics and Chemistry of Solids, 35(4), 555-570.

[22] Kulshreshtha, S. K., & Iyer, R. M. (1984). Nature of the high-spin (5T2) α low-spin (1A1,) transition in [Fe (bipy) 2 (NCS) 2]. Chemical physics letters, 108(5), 501-504.

[23] Nicolazzi, W., & Bousseksou, A. (2018). Thermodynamical aspects of the spin crossover phenomenon. Comptes Rendus Chimie, 21(12), 1060-1074.

[24] Stoufer, R. C., Busch, D. H., & Hadley, W. B. (1961). UNUSUAL MAGNETIC PROPERTIES OF SOME SIX-COÖRDINATE COBALT (II) COMPLEXES1—ELECTRONIC ISOMERS. Journal of the American Chemical Society, 83(17), 3732-3734.

[25] Sams, J. R., Scott, J. C., & Tsin, T. B. (1973). Tris [2-(2′-pyridyl) benzimidazole] iron (II) complexes. Some new examples of 5T2—1A1 spin equilibria. Chemical Physics Letters, 18(3), 451-453.

[26] Hernandez Gonzalez, E. M. (2015). High spatial resolution investigation of spin crossover phenomena using scanning probe microscopies (Doctoral dissertation, Toulouse 3).

[27] Baker Jr, W. A., & Bobonich, H. M. (1964). Magnetic properties of some high-spin complexes of iron (II). Inorganic Chemistry, 3(8), 1184-1188.

[28] Koenig, E., & Madeja, K. (1967). 5T2-1A1 Equilibriums in some iron (II)-bis (1, 10-phenanthroline) complexes. Inorganic Chemistry, 6(1), 48-55.

[29] König, E., & Ritter, G. (1976). Hysteresis effects at a cooperative high-spin (5T2)⇌ low-spin (1A1) transition in dithiocyanatobis (4, 7-dimethyl-1, 10-phenanthroline) iron (II). Solid State Communications, 18(3), 279-282.

[30] Zelentsov, V. V. (1987). Spin transitions in iron (III) complexes with thiosemicarbazones of O-hydroxyaldehydes. Sov. Sci. Rev. B Chem, 10, 485-512.

[31] Real, J. A., Bolvin, H., Bousseksou, A., Dworkin, A., Kahn, O., Varret, F., & Zarembowitch, J. (1992). Two-step spin crossover in the new dinuclear compound [Fe (bt)(NCS) 2] 2bpym, with bt= 2, 2'-bi-2-thiazoline and bpym= 2, 2'-bipyrimidine: experimental investigation and theoretical approach. Journal of the American Chemical Society, 114(12), 4650-4658.

[32] Köppen, H., Müller, E. W., Köhler, C. P., Spiering, H., Meissner, E., & Gütlich, P. (1982). Unusual spin-transition anomaly in the crossover system [Fe (2-pic) 3] Cl2· EtOH. Chemical Physics Letters, 91(5), 348-352.

[33] Jakobi, R., Spiering, H., & Gütlich, P. (1992). Thermodynamics of the spin transition in [FexZn1− x (2-pic) 3] Cl2· EtOH. Journal of Physics and Chemistry of Solids, 53(2), 267-275.

[34] Romstedt, H., Hauser, A., & Spiering, H. (1998). High-spin→ low-spin relaxation in the two-step spincrossover compound [Fe (pic) 3] Cl2EtOH (pic= 2-picolylamine). Journal of Physics and Chemistry of Solids, 59(2), 265-275.

[35] Fahs, A. (2022). Modélisation des effets de surfaces sur les propriétés de commutation des nanomatériaux à transition de spin: vers une analyse quantitative des énergies de surface (Doctoral dissertation, Université Paul Sabatier-Toulouse III).

[36] Ewald, A. H., Martin, R. L., Ross, I. G., & White, A. H. (1964). Anomalous behaviour at the 6 A 1-2 T 2 crossover in iron (III) complexes. Proceedings of the Royal Society of London. Series A. Mathematical and Physical Sciences, 280(1381), 235-257.

[37] Agusti, G., Cobo, S., Gaspar, A. B., Molnar, G., Moussa, N. O., Szilagyi, P. A., ... & Bousseksou, A. (2008). Thermal and light-induced spin crossover phenomena in new 3D Hofmann-like microporous metalorganic frameworks produced as bulk materials and nanopatterned thin films. Chemistry of Materials, 20(21), 6721-6732.

[38] Ekanayaka, T. K., Maity, K. P., Doudin, B., & Dowben, P. A. (2022). Dynamics of Spin Crossover Molecular Complexes. Nanomaterials, 12(10), 1742.

[39] Mallah, T., & Cavallini, M. (2018). Surfaces, thin films and patterning of spin crossover compounds. Comptes Rendus Chimie, 21(12), 1270-1286.

[40] Halcrow, M. A. (2016). The effect of ligand design on metal ion spin state—Lessons from spin crossover complexes. Crystals, 6(5), 58.

[41] Wang, R. G., Meng, Y. S., Gao, F. F., Gao, W. Q., Liu, C. H., Li, A., ... & Zhu, Y. Y. (2021). Ligand symmetry significantly affects spin crossover behaviour in isomeric [Fe (pybox) 2] 2+ complexes. Dalton Transactions, 50(9), 3369-3378.

[42] Wang, C. F., Yao, Z. S., Yang, G. Y., & Tao, J. (2019). Ligand substituent effects on the spin-crossover behaviors of dinuclear iron (II) compounds. Inorganic chemistry, 58(2), 1309-1316.

[43] Park, J. G., Jeon, I. R., & Harris, T. D. (2015). Electronic effects of ligand substitution on spin crossover in a series of diiminoquinonoid-bridged FeII2 complexes. Inorganic chemistry, 54(1), 359-369.

[44] Dey, B., Mondal, A., & Konar, S. (2020). Effect of Ligand Field Strength on the Spin Crossover Behaviour in 5-X-SalEen (X= Me, Br and OMe) Based Fe (III) Complexes. Chemistry–An Asian Journal, 15(11), 1709-1721.

[45] Slichter, C. P., & Drickamer, H. G. (1972). Pressure-induced electronic changes in compounds of iron. The Journal of Chemical Physics, 56(5), 2142-2160.

[46] Fisher, D. C., & Drickamer, H. G. (1971). Effect of pressure on the spin state of iron in ferrous phenanthroline compounds. The Journal of Chemical Physics, 54(11), 4825-4837.

[47] Grenoble, D. C., & Drickamer, H. G. (1971). Effect of Pressure on the Electronic Structure of Phthalocyanine and Iron Phthalocyanine Derivatives. The Journal of Chemical Physics, 55(4), 1624-1633.

[48] Ksenofontov, V., Spiering, H., Schreiner, A., Levchenko, G., Goodwin, H. A., & Gütlich, P. (1999). The influence of hydrostatic pressure on hysteresis phase transition in spin crossover compounds. Journal of Physics and Chemistry of Solids, 60(3), 393-399.

[49] Levchenko, G. G., Ksenofontov, V., Stupakov, A. V., Spiering, H., Garcia, Y., & Gütlich, P. (2002). Pressure effect on temperature induced high-spin–low-spin phase transitions. Chemical physics, 277(2), 125-129.

[50] Ewald, A. H., Martin, R. L., Sinn, E., & White, A. H. (1969). Electronic equilibrium between the 6A1 and 2T2 states in iron (III) dithio chelates. Inorganic Chemistry, 8(9), 1837-1846.

[51] Hauser, A., Jefti, J., Romstedt, H., & Hinek, R. (1996). Intersystem Crossing and Light-Induced Bistability in Iron (?) Spin-Crossover Compounds. Molecular Crystals and Liquid Crystals Science and Technology. Section A. Molecular Crystals and Liquid Crystals, 286(1), 217-224.

[52] Garcia, Y., Ksenofontov, V., Levchenko, G., & Gütlich, P. (2000). Pressure effect on a novel spin transitionpolymeric chain compound. Journal of Materials Chemistry, 10(10), 2274-2276.

[53] Guionneau, P., Brigouleix, C., Barrans, Y., Goeta, A. E., Létard, J. F., Howard, J. A. K., ... & Chasseau, D. (2001). CR Acad. Sci. Paris, Chimie. Chemistry, 4, 161-171.

[54] Galet, A., Gaspar, A. B., & Agusti, G. (2006). MC CHAPTER V—Towards Enhanced Photomagnetic Switching at Room Temperature Muñoz. G. Levchenko, JA Real, Eur. J. Inorg. Chem, 3571.

[55] Galet, A., Gaspar, A. B., Muñoz, M. C., Bukin, G. V., Levchenko, G., & Real, J. A. (2005). Tunable Bistability in a Three-Dimensional Spin-Crossover Sensory-and Memory-Functional Material. Advanced Materials, 17(24), 2949-2953.

[56] Garcia, Y., Ksenofontov, V., Levchenko, G., Schmitt, G., & Gütlich, P. (2000). Pressure-Induced High Spin State in [Fe (btr) 2 (NCS) 2]⊙ H2O (btr= 4, 4 '-bis-1, 2, 4-triazole). The Journal of Physical Chemistry B, 104(21), 5045-5048.

[57] Gütlich, P., Goodwin, H. A., Bousseksou, A., Varret, F., Goiran, M., Boukheddaden, K., & Tuchagues, J. P. (2004). The spin crossover phenomenon under high magnetic field. Spin Crossover in Transition Metal Compounds III, 65-84.

[58] Guionneau, P., Marchivie, M., Bravic, G., Létard, J. F., & Chasseau, D. (2002). Co (II) molecular complexes as a reference for the spin crossover in Fe (II) analogues. Journal of Materials Chemistry, 12(8), 2546-2551.

[59] Gütlich, P., Goodwin, H. A., Ksenofontov, V., Gaspar, A. B., & Gütlich, P. (2004). Pressure effect studies on spin crossover and valence tautomeric systems. Spin crossover in transition metal compounds III, 23-64.

[60] Sasaki, N., & Kambara, T. (1982). The effect of a magnetic field on the high spin to or from low-spin transitions in ferrous and ferric compounds. Journal of Physics C: Solid State Physics, 15(5), 1035.

[61] Qi, Y., Müller, E. W., Spiering, H., & Gütlich, P. (1983). The effect of a magnetic field on the high-spin α low-spin transition in [Fe (phen) 2 (NCS) 2]. Chemical physics letters, 101(4-5), 503-505.

[62] Chastanet, G., Lorenc, M., Bertoni, R., & Desplanches, C. (2018). Light-induced spin crossover—Solution and solid-state processes. Comptes Rendus Chimie, 21(12), 1075-1094.

[63] Roux, C., Zarembowitch, J., Gallois, B., Granier, T., & Claude, R. (1994). Toward ligand-driven light-induced spin changing. Influence of the configuration of 4 styrylpyridine (stpy) on the magnetic properties of FeII (stpy) 4 (NCS) 2 Complexes. crystal structures of the spin-crossover species Fe (trans-stpy) 4 (NCS) 2 and of the high-spin species Fe (cis-stpy) 4 (NCS) 2. Inorganic Chemistry, 33(10), 2273-2279.

[64] Decurtins, S., Gütlich, P., Köhler, C. P., Spiering, H., & Hauser, A. (1984). Light-induced excited spin state trapping in a transition-metal complex: The hexa-1-propyltetrazole-iron (II) tetrafluoroborate spin-crossover system. Chemical physics letters, 105(1), 1-4.

[65] Bannwarth, A., Schmidt, S. O., Peters, G., Sönnichsen, F. D., Thimm, W., Herges, R., & Tuczek, F. (2012). FeIII spin-crossover complexes with photoisomerizable ligands: experimental and theoretical studies on the ligand-driven light-induced spin change effect. European Journal of Inorganic Chemistry, 2012(16), 2776-2783.

[66] Kumar, K. S., & Ruben, M. (2021). Sublimable spin-crossover complexes: From spin-state switching to molecular devices. Angewandte Chemie International Edition, 60(14), 7502-7521.

[67] Li, F., Huang, J., Hu, Y., & Li, Q. (2019). Transport property of ligand-driven light-induced spin-change Fe-based spin crossover complexes. RSC advances, 9(22), 12339-12345.

[68] Boillot, M. L., Roux, C., Audiere, J. P., Dausse, A., & Zarembowitch, J. (1996). Ligand-driven light-induced spin change in transition-metal complexes: selection of an appropriate system and first evidence of the effect, in FeII (4-styrylpyridine) 4 (NCBPh3) 2. Inorganic chemistry, 35(13), 3975-3980.

[69] Hayami, S., Gu, Z. Z., Shiro, M., Einaga, Y., Fujishima, A., & Sato, O. (2000). First observation of light-induced excited spin state trapping for an iron (III) complex. Journal of the American Chemical Society, 122(29), 7126-7127.

[70] Gütlich, P., Gaspar, A. B., & Garcia, Y. (2013). Spin state switching in iron coordination compounds. Beilstein journal of organic chemistry, 9(1), 342-391.

[71] Boillot, M. L., & Soyer, H. (1997). Spin crossover in an amphiphilic iron (II) complex with photoisomerizable ligands: a magnetic investigation. New journal of chemistry, 21(8), 889-892.

[72] Soyer, H., Mingotaud, C., Boillot, M. L., & Delhaes, P. (1998). Spin crossover of a langmuir− blodgett film based on an amphiphilic iron (II) complex. Langmuir, 14(20), 5890-5895.

[73] McGravey, J. J., & Lawthers, I. (1982). Photochemically-induced perturbation of the 1 A⇌ 5 T equilibrium in Fe 11 complexes by pulsed laser irradiation in the metal-to-ligand charge-transfer absorption band. Journal of the Chemical Society, Chemical Communications, (16), 906-907.

[74] Decurtins, S., Gütlich, P., Köhler, C. P., Spiering, H., & Hauser, A. (1984). Light-induced excited spin state trapping in a transition-metal complex: The hexa-1-propyltetrazole-iron (II) tetrafluoroborate spin-crossover system. Chemical physics letters, 105(1), 1-4.

[75] Halcrow, M. A. (Ed.). (2013). Spin-crossover materials: properties and applications. John Wiley & Sons.

[76] Chastanet, G., Lorenc, M., Bertoni, R., & Desplanches, C. (2018). Light-induced spin crossover—Solution and solid-state processes. Comptes Rendus Chimie, 21(12), 1075-1094.

[77] Hauser, A. (1986). Reversibility of light-induced excited spin state trapping in the Fe (ptz) 6 (BF4) 2, and the Zn1− xFex (ptz) 6 (BF4) 2 spin-crossover systems. Chemical Physics Letters, 124(6), 543-548.

[78] Létard, J. F., Capes, L., Chastanet, G., Moliner, N., Létard, S., Real, J. A., & Kahn, O. (1999). Critical temperature of the LIESST effect in iron (II) spin crossover compounds. Chemical physics letters, 313(1-2), 115-120.

[79] Salmon, L., Molnár, G., Zitouni, D., Quintero, C., Bergaud, C., Micheau, J. C., & Bousseksou, A. (2010). A novel approach for fluorescent thermometry and thermal imaging purposes using spin crossover nanoparticles. Journal of Materials Chemistry, 20(26), 5499-5503.

[80] Shepherd, H. J., Molnár, G., Nicolazzi, W., Salmon, L., & Bousseksou, A. (2013). Spin crossover at the nanometre scale. European Journal of Inorganic Chemistry, 2013(5-6), 653-661.

[81] Létard, J. F., Guionneau, P., Rabardel, L., Howard, J. A., Goeta, A. E., Chasseau, D., & Kahn, O. (1998). Structural, magnetic, and photomagnetic studies of a mononuclear iron (II) derivative exhibiting an exceptionally abrupt spin transition. Light-induced thermal hysteresis phenomenon. Inorganic chemistry, 37(17), 4432-4441.

[82] Chastanet, G., Desplanches, C., Baldé, C., Rosa, P., Marchivie, M., & Guionneau, P. (2018). A critical review of the T (LIESST) temperature in spin crossover materials− What it is and what it is not. Chemistry Squared-Chem2, 2, 2.

[83] Létard, J. F., Guionneau, P., Nguyen, O., Costa, J. S., Marcén, S., Chastanet, G., ... & Goux-Capes, L. (2005). A guideline to the design of molecular-based materials with long-lived photomagnetic lifetimes. Chemistry–A European Journal, 11(16), 4582-4589.

[84] Létard, J. F. (2006). Photomagnetism of iron (II) spin crossover complexes—the T (LIESST) approach. Journal of Materials Chemistry, 16(26), 2550-2559.

[85] Sousa, C., de Graaf, C., Rudavskyi, A., Broer, R., Tatchen, J., Etinski, M., & Marian, C. M. (2013). Ultrafast Deactivation Mechanism of the Excited Singlet in the Light-Induced Spin Crossover of [Fe (2, 2′-bipyridine) 3] 2+. Chemistry–A European Journal, 19(51), 17541-17551.

[86] Cannizzo, A., Milne, C. J., Consani, C., Gawelda, W., Bressler, C., Van Mourik, F., & Chergui, M. (2010). Light-induced spin crossover in Fe (II)-based complexes: The full photocycle unraveled by ultrafast optical and X-ray spectroscopies. Coordination Chemistry Reviews, 254(21-22), 2677-2686.

[87] Yamada, M., Ooidemizu, M., Ikuta, Y., Osa, S., Matsumoto, N., Iijima, S., ... & Tuchagues, J. P. (2003). Interlayer Interaction of Two-Dimensional Layered Spin Crossover Complexes [FeIIH3LMe][FeIILMe] X (X-= ClO4-, BF4-, PF6-, AsF6-, and SbF6-; H3LMe= Tris [2-(((2-methylimidazol-4-yl) methylidene) amino) ethyl] amine). Inorganic chemistry, 42(25), 8406-8416.

[88] Rabelo, R., Toma, L., Moliner, N., Julve, M., Lloret, F., Inclán, M., ... & Cano, J. (2023). pH-Switching of the luminescent, redox, and magnetic properties in a spin crossover cobalt (ii) molecular nanomagnet. Chemical Science, 14(33), 8850-8859.

[89] Kelly, C. T., Dunne, S., Kühne, I. A., Barker, A., Esien, K., Felton, S., ... & Morgan, G. G. (2023). Proton-Induced Spin State Switching in an FeIII Complex. Angewandte Chemie, 135(18), e202217388.

[90] Zhang, R., Hong, D. L., He, X. T., Chen, F. H., Jiao, J., Zhao, X. Q., ... & Sun, B. W. (2019). Protonation-induced ligand distortion of spin-crossover complexes. Inorganic Chemistry Communications, 102, 40-44.

[91] Phonsri, W., Harding, P., Liu, L., Telfer, S. G., Murray, K. S., Moubaraki, B., ... & Harding, D. J. (2017). Solvent modified spin crossover in an iron (III) complex: Phase changes and an exceptionally wide hysteresis. Chemical Science, 8(5), 3949-3959.

[92] Fumanal Quintana, M., Jimenez-Gravalos, F., Ribas Ariño, J., & Vela Llausí, S. (2017). Lattice-solvent effects in the spin-crossover of an Fe (II)-based material. The key role of intermolecular interactions between solvent molecules. Inorganic Chemistry, 2017, vol. 56, num. 8, p. 4474-4483.

[93] Schönfeld, S., Dankhoff, K., Baabe, D., Zaretzke, M. K., Bröring, M., Schötz, K., ... & Weber, B. (2020). Iron (II) spin crossover complexes based on a redox active equatorial Schiff-base-like ligand. Inorganic Chemistry, 59(12), 8320-8333.

[94] Lyu, B. H., Ruan, Z. Y., Cui, W., Wu, S. G., Ni, Z. P., & Tong, M. L. (2023). Successive redox modulation in an iron (ii) spin-crossover framework. Inorganic Chemistry Frontiers, 10(12), 3577-3583.

[95] CarlosáWaerenborgh, J., Bruno, J. C., & Espallargas, G. (2023). Redox and guest tunable spin-crossover properties in a polymeric polyoxometalate. Chemical Science, 14(11), 3048-3055.

[96] Tao, J., Wei, R. J., Huang, R. B., & Zheng, L. S. (2012). Polymorphism in spin-crossover systems. Chemical Society Reviews, 41(2), 703-737.

[97] Tailleur, E., Marchivie, M., Negrier, P., Denux, D., Massip, S., Mondieig, D., ... & Guionneau, P. (2019). Using polymorphism to master the spin crossover mechanism in [Fe (PM-PeA) 2 (NCSe) 2]. CrystEngComm, 21(41), 6246-6251.

[98] Matouzenko, G. S., Jeanneau, E., Verat, A. Y., & Bousseksou, A. (2011). Spin crossover and polymorphism in a family of 1, 2-bis (4-pyridyl) ethene-bridged binuclear iron (II) complexes. A key role of structural distortions. Dalton Transactions, 40(37), 9608-9618.

[99] Sessoli, R., Gatteschi, D., Caneschi, A., & Novak, M. A. (1993). Magnetic bistability in a metal-ion cluster. Nature, 365(6442), 141-143.

[100] Aubin, S. M., Wemple, M. W., Adams, D. M., Tsai, H. L., Christou, G., & Hendrickson, D. N. (1996). Distorted MnIVMnIII3 cubane complexes as single-molecule magnets. Journal of the American Chemical Society, 118(33), 7746-7754.

[101] Shao, D., Deng, L. D., Shi, L., Wu, D. Q., Wei, X. Q., Yang, S. R., & Wang, X. Y. (2017). Slow Magnetic Relaxation and Spin-Crossover Behavior in a Bicomponent Ion-Pair Cobalt (II) Complex. European Journal of Inorganic Chemistry, 2017(33), 3862-3867.

[102] Tiaouinine, S., Flores Gonzalez, J., Lefeuvre, B., Guizouarn, T., Cordier, M., Dorcet, V., ... & Pointillart, F. (2021). Spin Crossover and Field-Induced Single-Molecule Magnet Behaviour in Co (II) Complexes Based on Terpyridine with Tetrathiafulvalene Analogues. European Journal of Inorganic Chemistry, 2021(24), 2374-2383.

[103] Cui, H. H., Wang, J., Chen, X. T., & Xue, Z. L. (2017). Slow magnetic relaxation in five-coordinate spin-crossover cobalt (II) complexes. Chemical Communications, 53(67), 9304-9307.

[104] Zabala-Lekuona, A. (2019). Iman Molekularrak: informazio unitate txikienaren bila. EKAIA EHUko Zientzia eta Teknologia aldizkaria, (35).

[105] Zabala-Lekuona, A., Seco, J. M., & Colacio, E. (2021). Single-Molecule Magnets: From Mn12-ac to dysprosium metallocenes, a travel in time. Coordination Chemistry Reviews, 441, 213984.

[106] Tesfaye, D., Linert, W., Gebrezgiabher, M., Bayeh, Y., Elemo, F., Sani, T., ... & Thomas, M. (2023). Iron (II) Mediated Supramolecular Architectures with Schiff Bases and Their Spin-Crossover Properties. Molecules, 28(3), 1012.

[107] Nemec, I., Herchel, R., Boča, R., Trávníček, Z., Svoboda, I., Fuess, H., & Linert, W. (2011). Tuning of spin crossover behaviour in iron (III) complexes involving pentadentate Schiff bases and pseudohalides. Dalton Transactions, 40(39), 10090-10099.

[108] Golup, A. M., Köhler, H., & Skopenko, V. V. (1986). Chemistry of Pseudohalides.

[109] Hayami, S., Gu, Z. Z., Shiro, M., Einaga, Y., Fujishima, A., & Sato, O. (2000). First observation of light-induced excited spin state trapping for an iron (III) complex. Journal of the American Chemical Society, 122(29), 7126-7127.

[110] Létard, J. F., Guionneau, P., Codjovi, E., Lavastre, O., Bravic, G., Chasseau, D., & Kahn, O. (1997). Wide Thermal Hysteresis for the Mononuclear Spin-Crossover Compound cis-Bis (thiocyanato) bis [N-(2 '-pyridylmethylene)-4-(phenylethynyl) anilino] iron (II). Journal of the American Chemical Society, 119(44), 10861-10862.

[111] Ross, T. M., Neville, S. M., Innes, D. S., Turner, D. R., Moubaraki, B., & Murray, K. S. (2010). Spin crossover in iron (III) Schiff-base 1-D chain complexes. Dalton Transactions, 39(1), 149-159.

[112] Kumar, K. S., Bayeh, Y., Gebretsadik, T., Elemo, F., Gebrezgiabher, M., Thomas, M., & Ruben, M. (2019). Spin-crossover in iron (II)-Schiff base complexes. Dalton Transactions, 48(41), 15321-15337.

[113] Weber, B., Bauer, W., Pfaffeneder, T., Dîrtu, M. M., Naik, A. D., Rotaru, A., & Garcia, Y. (2011). Influence of hydrogen bonding on the hysteresis width in iron (II) spin-crossover complexes.

[114] Weber, B., Bauer, W., & Obel, J. (2008). An iron (II) spin-crossover complex with a 70 K wide thermal hysteresis loop. Angewandte Chemie International Edition, 47(52), 10098-10101.

[115] Phonsri, W., Macedo, D. S., Vignesh, K. R., Rajaraman, G., Davies, C. G., Jameson, G. N., ... & Murray, K. S. (2017). Halogen substitution effects on N2O Schiff base ligands in unprecedented abrupt FeII spin crossover complexes. Chemistry–A European Journal, 23(29), 7052-7065.

[116] Fujinami, T., Nishi, K., Matsumoto, N., Iijima, S., Halcrow, M. A., Sunatsuki, Y., & Kojima, M. (2011). 1D and 2D assembly structures by imidazole··· chloride hydrogen bonds of iron (ii) complexes [Fe II (HL n-Pr) 3] Cl· Y (HL n-Pr= 2-methylimidazol-4-yl-methylideneamino-n-propyl; Y= AsF 6, BF 4) and their spin states. Dalton Transactions, 40(45), 12301-12309.

[117] Qin, L. F., Pang, C. Y., Han, W. K., Zhang, F. L., Tian, L., Gu, Z. G., ... & Li, Z. (2015). Optical recognition of alkyl nitrile by a homochiral iron (II) spin crossover host. CrystEngComm, 17(41), 7956-7963.

[118] Halcrow, M. A. (Ed.). (2013). Spin-crossover materials: properties and applications. John Wiley & Sons.

[119] Tsukiashi, A., Min, K. S., Kitayama, H., Terasawa, H., Yoshinaga, S., Takeda, M., ... & Hayami, S. (2018). Application of spin-crossover water soluble nanoparticles for use as MRI contrast agents. Scientific Reports, 8(1), 14911.

[120] Kitazawa, T. (2019). Synthesis and applications of new spin crossover compounds. Crystals, 9(8), 382.

[121] Hao, G. (2021). Manipulation of Spin Crossover Phenomenon in an Fe (II) Molecular Complex and Application to Molecular Spintronics (Doctoral dissertation, The University of Nebraska-Lincoln).

[122] Polyzou, C. D., Gkolfi, P., Chasapis, C. T., Bekiari, V., Zianna, A., Psomas, G., ... & Tangoulis, V. (2022). Stimuli-responsive spin crossover nanoparticles for drug delivery and DNA-binding studies. Dalton Transactions, 51(33), 12427-12431.

[123] Kumar, K. S., & Ruben, M. (2021). Sublimable spin-crossover complexes: From spin-state switching to molecular devices. Angewandte Chemie International Edition, 60(14), 7502-7521.

[124] Bénard, J., Michel, A., Philibert, J., & Talbot, J. (1969). Métallurgie Générale, Masson et Cie. Editeurs, Paris VI, 49-52.

[125] Kendig, M., & Mills, D. J. (2017). An historical perspective on the corrosion protection by paints. Progress in Organic Coatings, 102, 53-59.

[126] ŠRÁMEK, J. Í., Jakobsen, T. B., & Pelikán, J. B. (1978). Corrosion and conservation of a silver visceral vessel from the beginning of the seventeenth century. Studies in conservation, 23(3), 114-117.

[127] Li, C. G., Liu, C., Xu, W. H., Shan, M. G., & Wu, H. X. (2022). Formation mechanisms and supervisory prediction of scaling in water supply pipelines: A review. Water Research, 118922.

[128] Waldrip, H. E. (1948). Present day aspects of condensate well corrosion. Corrosion, 4(12), 611-618.

[129] Faustin, M. (2013). Étude de l'effet des alcaloïdes sur la corrosoion de l'acier C38 en milieu acide chlorhydrique 1M: application à Aspidosperma album et Geissospermum laeve (Apocynacées) (Doctoral dissertation, Antilles-Guyane).

[130] Norman, E. H. (1973). Scope and importance of inhibitor technology. Et By CC Nathan, Houston, NACE Corrosion Inhibitors. USA: Nations Association of Corrosion Engineers, 28-41.

[131] Elyoussfi, A., Outada, H., Isaad, J., Lrhoul, H., Salhi, A., & Dafali, A. (2023). Corrosion inhibitors of alloys and metals in acidic solution: A bibliometric analysis from 2010 to 2022. Int. J. Corros. Scale Inhib, 12(2), 722-740.

[132] Norman, E. H. (1965). NACE glossary of corrosion terms. Materials Protection, 4(1), 79.

[133] Fiaud, C. (2006). Inhibiteur de corrosion (Université Pierre & Marie curie, ENSC, Paris. Techniques de l'' ingénieur, Traité corrosion–Vieillissement, Vol. Cor, 1005.

[134] European Federation of Corrosion. (1975). Proceedings [of The] 4th European Symposium on Corrosion Inhibitors: 82th Manifestation of the European Federation of Corrosion, Ferrara (Italy), 15th-19th September 1975 (No. 6). Università degli studi di Ferrara.

[135] Dehghani, A., Ghahremani, P., Mostafatabar, A. H., & Ramezanzadeh, B. (2022). Plant extracts: Probable alternatives for traditional inhibitors for controlling alloys corrosion against acidic media—A review. Biomass Conversion and Biorefinery, 1-20.

[136] Jevremović, I., Chen, Y. H., Altin, A., & Erbe, A. (2020). Mechanisms of Inhibitor Action: Passivation and Self-Healing. Corrosion Inhibitors in the Oil and Gas Industry, 359-382.

[137] Landolt, D. (2003). Corrosion et chimie de surfaces des métaux (Vol. 12). PPUR presses polytechniques.

[138] Ahmed ES, J., & Ganesh, G. M. (2022). A comprehensive overview on corrosion in RCC and its prevention using various green corrosion inhibitors. Buildings, 12(10), 1682.

[139] An, K., Sui, Y., Wang, Y., Qing, Y., Long, C., Liu, X., ... & Liu, C. (2022). Synergistic control of wetting resistance and corrosion inhibition by cerium to enhance corrosion resistance

of superhydrophobic coating. Colloids and Surfaces A: Physicochemical and Engineering Aspects, 653, 129874.

[140] Singh, H., & Sharma, S. (2020, June). Designing Corrosion Inhibitors with High Aqueous Solubility and Low Tendency Towards Micellization: A Molecular Dynamics Study. In NACE CORROSION (pp. NACE-2020). NACE.

[141] Liu, Z., & Jackson, T. (2016, March). Understanding Thermal Stability and Inhibition Effectiveness of Corrosion Inhibitors at High Temperatures. In NACE CORROSION (pp. NACE-2016). NACE.

[142] Aslam, R., Serdaroglu, G., Zehra, S., Verma, D. K., Aslam, J., Guo, L., ... & Quraishi, M. A. (2022). Corrosion inhibition of steel using different families of organic compounds: Past and present progress. Journal of Molecular Liquids, 348, 118373.

[143] Verma, C., Olasunkanmi, L. O., Ebenso, E. E., & Quraishi, M. A. (2018). Substituents effect on corrosion inhibition performance of organic compounds in aggressive ionic solutions: a review. Journal of Molecular Liquids, 251, 100-118.

[144] Assad, H., & Kumar, A. (2021). Understanding functional group effect on corrosion inhibition efficiency of selected organic compounds. Journal of Molecular Liquids, 344, 117755.

[145] Al-Janabi, Y. T. (2020). An overview of corrosion in oil and gas industry: upstream, midstream, and downstream sectors. Corrosion inhibitors in the oil and gas industry, 1-39.

[146] Prasad, A. R., Kunyankandy, A., & Joseph, A. (2020). Corrosion inhibition in oil and gas industry: Economic considerations. Corrosion inhibitors in the oil and gas industry, 135-150.

[147] Nestle, A., & Nathan, C. C. (1973). Corrosion inhibitors in petroleum production primary recovery. Corrosion Inhibitors, 61-75.

[148] Pradhan, B. (2022). A study on effectiveness of inorganic and organic corrosion inhibitors on rebar corrosion in concrete: A review. Materials Today: Proceedings, 65, 1360-1366.

[149] Ma, R., Lin, G., Zhou, Y., Liu, Q., Zhang, T., Shan, G., ... & Wang, J. (2019). A review of oxygen reduction mechanisms for metal-free carbon-based electrocatalysts. npj Computational Materials, 5(1), 78.

[150] Ilevbare, G. O., & Burstein, G. T. (2003). The inhibition of pitting corrosion of stainless steels by chromate and molybdate ions. Corrosion Science, 45(7), 1545-1569.

[151] Iannuzzi, M., & Frankel, G. S. (2007). Mechanisms of corrosion inhibition of AA2024-T3 by vanadates. Corrosion Science, 49(5), 2371-2391.

[152] Sarmiento, E., González-Rodriguez, J. G., Ramirez-Arteaga, A. M., & Uruchurtu, J. (2013). Corrosion inhibition of 316L stainless steel in LiBr+ Etileneglycol+ H2O By using inorganic inhibitors. Int. J. Electrochem. Sci, 8(12), 12417-12433.

[152] Saadawy, M. (2016). Effect of inorganic anions on the pitting behaviour of austenitic stainless steel 304 in H2SO4 solution containing chloride ion. International Journal of Electrochemical Science, 11, 2345-2359.

[153] Al-Baghdadi, S., Gaaz, T. S., Al-Adili, A., Al-Amiery, A. A., & Takriff, M. S. (2021). Experimental studies on corrosion inhibition performance of acetylthiophene thiosemicarbazone for mild steel in HCl complemented with DFT investigation. International Journal of Low-Carbon Technologies, 16(1), 181-188.

[154] Abdulazeez, M. S., Abdullahe, Z. S., Dawood, M. A., Handel, Z. K., Mahmood, R. I., Osamah, S., ... & Al-Amiery, A. A. (2021). Corrosion inhibition of low carbon steel in HCl medium using a thiadiazole derivative: weight loss, DFT studies and antibacterial studies. Int. J. Corros. Scale Inhib, 10(4), 1812-1828.

[155] Uhlig, H. H., & King, P. F. (1959). The Flade potential of iron passivated by various inorganic corrosion inhibitors. Journal of the Electrochemical Society, 106(1), 1.

[156] Postlethwaite, J., & Nesic, S. (2000). Erosion-corrosion in single and multiphase flow. Uhlig's corrosion handbook, 249-272.

[157] Kulakovskaya, T. V., Vagabov, V. M., & Kulaev, I. S. (2012). Inorganic polyphosphate in industry, agriculture and medicine: Modern state and outlook. Process Biochemistry, 47(1), 1-10.

[158] Mouanga, M., Andreatta, F., Druart, M. E., Marin, E., Fedrizzi, L., & Olivier, M. G. (2015). A localized approach to study the effect of cerium salts as cathodic inhibitor on iron/aluminum galvanic coupling. Corrosion Science, 90, 491-502.

[159] Hegazy, M. A., Abdallah, M., Awad, M. K., & Rezk, M. (2014). Three novel di-quaternary ammonium salts as corrosion inhibitors for API X65 steel pipeline in acidic solution. Part I: experimental results. Corrosion Science, 81, 54-64.

[160] Ekpe, U. J., Okafor, P. C., Ebenso, E. E., Offiong, O. E., & Ita, B. I. (2001). Mutual effects of thiosemicarbazone derivatives on the acidic corrosion of aluminium. Bulletin of Electrochemistry, 17(3), 131-135.

[161] Zarrouk, A., Hammouti, B., Lakhlifi, T., Traisnel, M., Vezin, H., & Bentiss, F. (2015). New 1H-pyrrole-2, 5-dione derivatives as efficient organic inhibitors of carbon steel corrosion in hydrochloric acid medium: electrochemical, XPS and DFT studies. Corrosion Science, 90, 572-584.

[162] Ghazoui, A., Zarrouk, A., Bencaht, N., Salghi, R., Assouag, M., El Hezzat, M., ... & Hammouti, B. (2014). New possibility of mild steel corrosion inhibition by organic heterocyclic compound. J. Chem. Pharm. Res, 6(2), 704.

[163] Macdonald, D. D. (1992). The point defect model for the passive state. Journal of the Electrochemical Society, 139(12), 3434.

[164] Ghazoui, A., Zarrouk, A., Bencaht, N., Salghi, R., Assouag, M., El Hezzat, M., ... & Hammouti, B. (2014). New possibility of mild steel corrosion inhibition by organic heterocyclic compound. J. Chem. Pharm. Res, 6(2), 704.

[165] Roberge, P. R. (2006). Corrosion basics: an introduction.

[166] Fontana, M. G., & Greene, N. D. (2018). Corrosion engineering. McGraw-hill.

[167] Bentiss, F., Lebrini, M., & Lagrenée, M. (2005). Thermodynamic characterization of metal dissolution and inhibitor adsorption processes in mild steel/2, 5-bis (n-thienyl)-1, 3, 4-thiadiazoles/hydrochloric acid system. Corrosion science, 47(12), 2915-2931.

[168] Rocha-Ortiz, G., Tessensohn, M. E., Salas-Reyes, M., Flores-Moreno, R., Webster, R. D., & Astudillo-Sánchez, P. D. (2020). Homogeneous electron-transfer reaction between anionic species of anthraquinone derivatives and molecular oxygen in acetonitrile solutions: Electrochemical properties of disperse red 60. Electrochimica Acta, 354, 136601.

[169] Hackerman, N., & Makrides, A. C. (1955). Ind. Eng Chem 1954; 46, 523. J Phys Chem, 59, 707.

[170] McCafferty, E. (1979). Corrosion control by coating. Science Press, Princeton, NJ, 279.

[171] G. Trabanelli, Corrosion Mechanisms, F. Mansfeld editor, Marcel Dekker, New York, (1987) 119.

[172] Sathianandhan, B., Balakrishnan, K., & Subramanyan, N. (1970). Triazoles as inhibitors of corrosion of mild steel in acids. British corrosion journal, 5(6), 270-273.

[173] Annand, R. R., Hurd, R. M., & Hackerman, N. (1965). Adsorption of monomeric and polymeric amino corrosion inhibitors on steel. Journal of the Electrochemical Society, 112(2), 138.

[174] G. Trabanelli, F. Zucchi, G. Gullini, V. Carassiti, Werkstoffe und Korrosion, (1968) 407

[175] F. Zucchi, G. Trabanelli, G. Gullini, Eletrochimica Metallorm, 3, 407 (1968) 407.

[176] Wake, T., & Horiike, M. (2001). Corrosion inhibitors for cooling water systems. Zairyo-to-Kankyo, 50(1), 3-7.

[177] Matějovský, L., Macák, J., Pleyer, O., & Staš, M. (2018). Metal corrosion and the efficiency of corrosion inhibitors in less conductive media. JoVE (Journal of Visualized Experiments), (141), e57757.

[178] Ansari, F. A., Verma, C., Siddiqui, Y. S., Ebenso, E. E., & Quraishi, M. A. (2018). Volatile corrosion inhibitors for ferrous and non-ferrous metals and alloys: A review. International Journal of Corrosion and Scale Inhibition, 7(2), 126-150.

[179] Dieter, L. (1993). Corrosion et chimie de surface des métaux. Presses polytechniques et universitaires Romandes, Lausanne.

[180] Hammond, K. D., & Conner Jr, W. C. (2013). Analysis of catalyst surface structure by physical sorption. In Advances in Catalysis (Vol. 56, pp. 1-101). Academic Press.

[181] Liu, L., Luo, X. B., Ding, L., & Luo, S. L. (2019). Application of nanotechnology in the removal of heavy metal from water. In Nanomaterials for the removal of pollutants and resource reutilization (pp. 83-147). Elsevier.

[182] Chu, K. H. (2021). Revisiting the Temkin isotherm: Dimensional inconsistency and approximate forms. Industrial & Engineering Chemistry Research, 60(35), 13140-13147.

[183] Piccin, J. S., Dotto, G. L., & Pinto, L. A. A. (2011). Adsorption isotherms and thermochemical data of FD&C Red n 40 binding by chitosan. Brazilian Journal of Chemical Engineering, 28, 295-304.

[184] Dada, A. O., Olalekan, A. P., Olatunya, A. M., & Dada, O. J. I. J. C. (2012). Langmuir, Freundlich, Temkin and Dubinin–Radushkevich isotherms studies of equilibrium sorption of Zn2+ unto phosphoric acid modified rice husk. IOSR Journal of applied chemistry, 3(1), 38-45.

[185] Kalam, S., Abu-Khamsin, S. A., Kamal, M. S., & Patil, S. (2021). Surfactant adsorption isotherms: A review. ACS omega, 6(48), 32342-32348.

[186] Van der Bruggen, B. (2014). Freundlich isotherm. Encyclopedia of membranes. Springer Berlin Heidelberg, Berlin, Heidelberg, 1-2.

[187] Wang, L., Wang, H., Seyeux, A., Zanna, S., Pailleret, A., Nesic, S., & Marcus, P. (2023). Adsorption mechanism of quaternary ammonium corrosion inhibitor on carbon steel surface using ToF-SIMS and XPS. Corrosion Science, 213, 110952.

[188] Ding, Y., Brown, B., Young, D., Nesic, S., & Singer, M. (2017, March). Effect of temperature on adsorption behavior and corrosion inhibition performance of imidazoline-type inhibitor. In NACE CORROSION (pp. NACE-2017). NACE.

[189] Andreatta, F., & Fedrizzi, L. (2016). Corrosion inhibitors. Active Protective Coatings: New-Generation Coatings for Metals, 59-84.

[190] Ma, I. W., Ammar, S., Kumar, S. S., Ramesh, K., & Ramesh, S. (2022). A concise review on corrosion inhibitors: types, mechanisms and electrochemical evaluation studies. Journal of Coatings Technology and Research, 1-28.
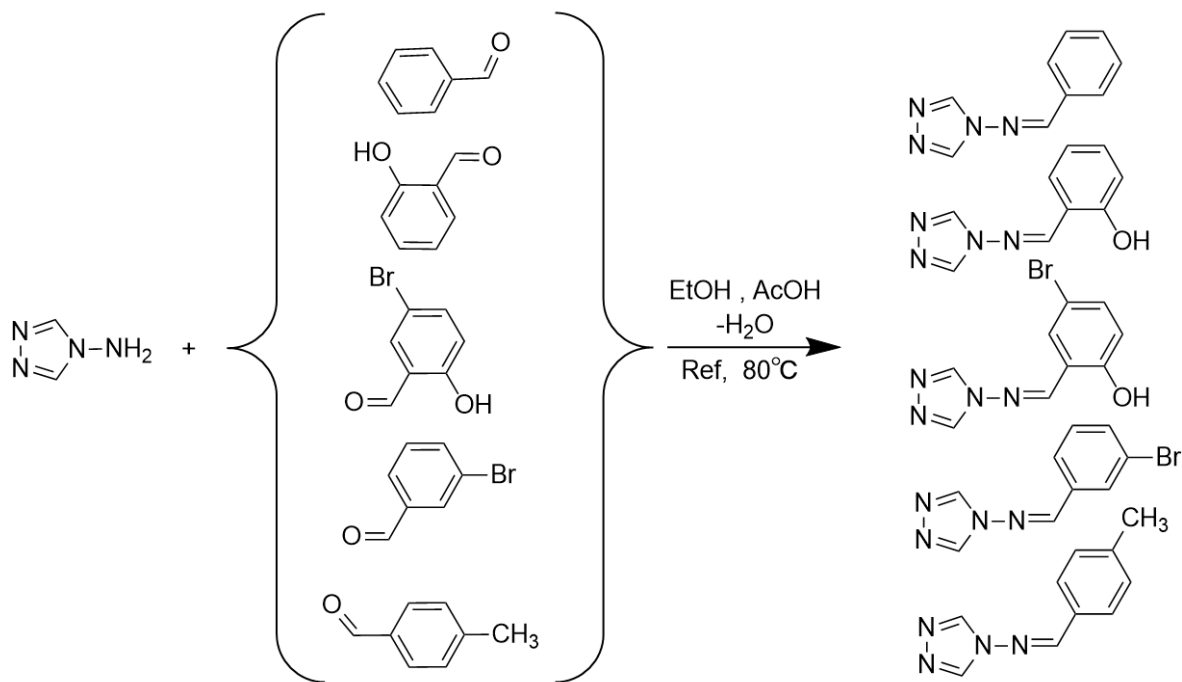
Chapter 2

experimental conditions

Table of Contents

Chapter 2

II.1 Introduction

This chapter elucidates the experimental methodologies employed and is structured into two distinct sections. The initial section delineates the diverse synthesis routes adopted for the preparation of triazole-based compounds and their corresponding metal complexes with Cu^{2+}, Co^{2+}, Fe^{2+}, and Ni^{2+} ions, which form the core of this study. The subsequent section provides a comprehensive description of the array of physicochemical, structural, and microstructural characterization techniques used to analyze and study the various materials synthesized during this research endeavor.

II.2 Structure and Synthesis of the Studied Compounds

The study investigated the corrosion inhibition efficiency of three Schiff bases, all bearing the same triazole moiety (4-Amino-4H-1,2,4-triazole) but differing in their aldehydic moieties. The names, structures, and abbreviations used for these Schiff base inhibitors are presented in Table II.1. The synthesis and characterization of these compounds were carried out, and their respective structural features were thoroughly analyzed to establish a correlation between their molecular structures and their inhibition performance towards corrosion processes.
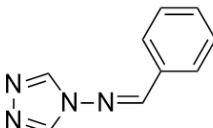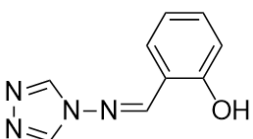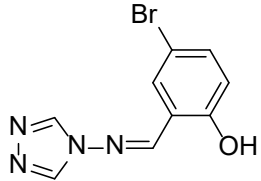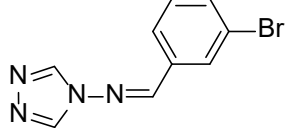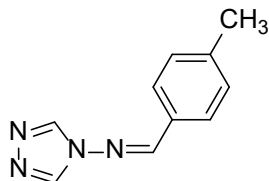

Scheme II.1 Synthesis of Trz-A, Trz-B, Trz-C, Trz-D and Trz-E

Chapter 2

experimental conditions

The triazole-based Schiff base compounds were synthesized via a condensation reaction between 4-Amino-4H-1,2,4-triazole and three different substituted benzaldehydes, as depicted in Scheme 1. An equimolar mixture consisting of 1 mmol of 4-Amino-4H-1,2,4-triazole and 1 mmol of the respective aldehyde (5-bromo-2-hydroxybenzaldehyde, 3-bromobenzaldehyde, and 4-methylbenzaldehyde) was prepared in approximately 5 ml of absolute ethanol. A catalytic amount of glacial acetic acid was added to the mixture, which was then stirred and refluxed for approximately 4 hours. After the reflux period, the reaction mixture was cooled, and the separated solid product was isolated by filtration. The obtained solid was washed with water and dried. Subsequently, the product was recrystallized from aqueous ethanol to improve its purity and crystallinity.

Table II.1 Structures, Names, and Abbreviations of Compounds Synthesized During This Study

Structure	Name	Abbreviation
	1-phenyl-N-(4H-1,2,4-triazol-4-yl)methanimine	Trz-A
	2-(((4H-1,2,4-triazol-4-yl)imino)methyl)phenol	Trz-B
	2-(((4H-1,2,4-triazol-4-yl)imino)methyl)-4-bromophenol	Trz-C
	1-(3-bromophenyl)-N-(4H-1,2,4-triazol-4-yl)methanimine	Trz-D
	1-p-tolyl-N-(4H-1,2,4-triazol-4-yl)methanimine	Trz-E

This synthetic procedure yielded the desired triazole-based Schiff base compounds, which were further characterized and evaluated for their corrosion inhibition properties.

II.3 Electrochemical characterization techniques

II.3.1 Working electrode preparation

The preparation of the working electrode involved several crucial steps. A cylindrical sample, approximately 1 cm in length, was cut from an XC48 carbon steel stock rod with a diameter of 0.62 cm. To establish an electrical connection, a suitable length of copper wire was spot-welded to one end of the sample, as shown in Figure 1. The cross-sectional surface area of the specimen was calculated to be $0.302 \ cm^2$. The surfaces of both the cut ends and the body of the sample were slightly polished to remove any traces of contaminants and to achieve a relatively flat surface at the cut edges. Subsequently, the cut sample was degreased in ethanol and coated with a rapid adhesive araldite resin and hardener. This coating was applied to improve the adhesion of the epoxy mounting resin to the metal, thereby reducing the tendency for crevice corrosion to occur at the edge of the mounting resin.
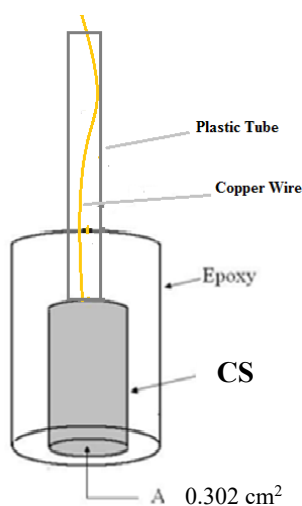

Figure II.1 schematic diagram for the working electrode

The exposed surface of the test specimen was initially prepared by polishing with a series of successively finer grades of silicon carbide abrasive papers. The initial grinding was performed using a 400-grade silicon carbide paper, followed by progressively finer abrasive grades, up to a

final polishing with a 2000-grade paper. After polishing, the specimen was degreased in ethanol, washed with distilled water, and finally dried.

The specific composition of the working electrode, as provided by the supplier, is given in Table 2 below.

Table II.2 Chemical composition of XC48 Carbon Steel in weight percentage

Elements	C	S	Mn	P	Si
wt.%	0.52-0.50	≤0.035	0.50-0.80	≤0.035	0.40 max

II.3.2 Description of Electrochemical Cells

The electrochemical tests were conducted using a cylindrical Pyrex glass cell with a double wall (to fix the working temperature), as shown in Figure 2 The cell was equipped with a lid that allowed the integration of the following components:

➢ A saturated calomel reference electrode (SCE) with a standard potential of 0.241 V with respect to the standard hydrogen electrode (SHE).

➢ A counter electrode in the form of a platinum grid, placed parallel to the working electrode to ensure a uniform distribution of field lines.

➢ A working electrode, which was the sample to be analyzed (XC48 Carbon Steel).

The tests were performed using a BioLogic SP-300 potentiostat equipped with an integrated frequency meter, enabling electrochemical impedance spectroscopy (EIS) measurements. The potentiostat was connected to a computer, allowing for control, data acquisition, and processing through the EC-Lab V11.42 software. Multiple measurements were conducted to evaluate the reproducibility of the results.

The electrochemical tests followed a specific sequence:

➢ Measurement of the corrosion potential for 25 minutes.

➢ Electrochemical impedance spectroscopy (EIS) analysis performed after 25 minutes, with a frequency range from 100 kHz to 10 mHz and a perturbation amplitude of ±10 mV with respect to the corrosion potential (E_{corr}).

➢ Potentiodynamic measurement or polarization curve ($I = f(E)$) analysis.

experimental conditions

This experimental setup and procedure ensured the accurate and reliable acquisition of electrochemical data for the investigation of the corrosion behavior of the XC48 Carbon Steel sample under various conditions.
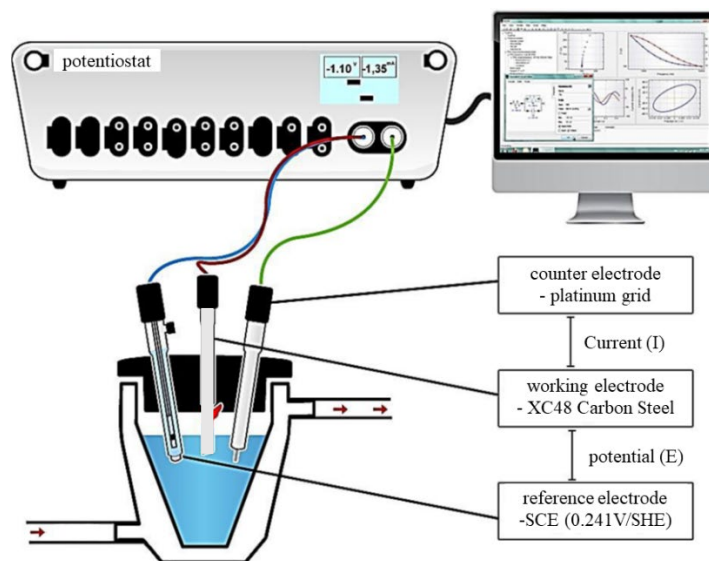
Figure II.2 Schematic representation of the experimental setup

II.4 Weight loss measurements

weight loss measurements were carried out according to the standard procedure of ASTM G31-72. These experiments were performed at 25°C with various inhibitor concentrations. Before the experiment, the previously weighed carbon steel specimens (7.76 cm^2 of surface area) were mechanically polished with various silicon carbide abrasive papers (grades 200, 400, 800, 1000 and 2000) these specimens were dipped carefully in 100 mL of 1 M HCl in the absence and presence of different concentrations of inhibitors for 24 h. After the immersion time, the CS specimens were then taken out, washed with distilled water, dried, and finally weighed again. All measurements were carried out in triplicate to ensure reproducible and reliable results. The corrosion rate (CR), inhibition efficiency ($\eta_{WL}\%$) and surface coverage (θ) can be calculated by using the following equations :

$$C_R = \frac{K \times W}{A \times t \times \rho} \qquad\qquad (\text{II.1})$$

$$\eta_{\text{WL}}\ (\%) = (1 - \frac{C_R}{C_R^0}) \times 100 \qquad \qquad \text{(II.2)}$$

$$\theta = \frac{\eta_{\text{WL}}\ (\%)}{100} \qquad \qquad \text{(II.3)}$$

Where W is the carbon steel weight loss (g), A is the exposed surface area (cm^2), t is the immersion time (h), ρ is the steel density (7.86 g/cm^3), K is a constant which depends on the corrosion rate units, in this case equals 8.76×10^4. C_R^0 and C_R are corrosion rate in absence and presence of inhibitors (mmy^{-1}).

II.5 Quantum chemical calculations

The quantum chemical calculations in the present work were performed using the Gaussian 09W software. The optimization of the neutral and cationic forms of the studied molecules was carried out using the density functional theory (DFT) method employing the B3LYP functional and the 6-311++G(d,p) basis set. The molecular geometries of both the neutral and cationic species were fully optimized at this level of theory. Subsequently, the corresponding quantum chemical parameters, such as molecular energies, frontier molecular orbitals, and other relevant descriptors, were obtained from these calculations and analyzed in detail to gain insights into the structural and electronic properties of the investigated molecules. Thus, a number of global and local molecular reactivity indices, such as: the energies of the highest occupied and lowest unoccupied molecular orbital (E$_{\text{HOMO}}$ and E$_{\text{LUMO}}$), the energy gap (ΔE), the electronegativity (χ), global hardness (η) and softness (σ) and the fraction of transferred charge (ΔN) were determined to correlate the corrosion inhibition activity with the structures of the investigated molecules. The mathematical operations related to these concepts are given as follows:

$$IP = - E_{\text{HOMO}} \qquad \qquad \text{(II.4)}$$

$$EA = - E_{\text{LUMO}} \qquad \qquad \text{(II.5)}$$

$$\chi = \frac{IP + EA}{2} \qquad \qquad \text{(II.6)}$$

$$\eta = \frac{IP - EA}{2} \qquad \qquad \text{(II.7)}$$

$$\sigma = \frac{1}{\eta} \qquad \qquad \text{(II.8)}$$

experimental conditions

The electron transfer fraction (ΔN) serves as a quantitative parameter to evaluate the electron-donating or electron-accepting capability of a molecule when interacting with a metal surface, as calculated using Equation

$$\Delta N_{(110)} = \frac{\varphi_{Fe} - \chi_{inh}}{2(\eta_{Fe} + \eta_{inh})} \tag{II.9}$$

Here, φ_{Fe} and η_{Fe} denote the work function and absolute hardness of the iron metal, respectively, with values of 4.82 eV and 0.0 eV. Similarly, χ_{inh} and η_{inh} represent the electronegativity and global hardness of the inhibitor, respectively.

Chapter 3

Study of the Corrosion Inhibition of XC48 Carbon Steel by Triazole Based Compounds in 1M HCl Acid Medium

Table of Contents

III.1 Introduction

This chapter explores the investigation of triazole-based organic compounds as potential corrosion inhibitors for XC48 carbon steel in a 1 M HCl solution. The triazoles, a class of heterocyclic compounds featuring a five-membered ring containing three nitrogen atoms, exhibit unique structural characteristics that render them promising candidates for corrosion inhibition. The presence of nitrogen atoms and an aromatic ring system within these molecules provides multiple sites for interaction with the metal surface, potentially leading to strong adsorption and the formation of a protective film.

III.2 Gravimetric analysis

The evaluation of corrosion inhibition performance is a critical aspect in numerous industries where metallic materials are exposed to aggressive environments. Among the various techniques employed, weight loss analysis, also known as gravimetric analysis, stands out as one of the simplest and most widely recognized strategies. This method provides a direct and quantitative assessment of the inhibitory efficacy of compounds by measuring the weight loss of metal samples before and after exposure to corrosive media.

In the present study, the weight loss analysis was conducted by immersing Carbon steel (CS) samples in a 1 M hydrochloric acid (HCl) solution for a duration of 24 hours at a controlled temperature of 25°C. The experiments were carried out in the absence and presence of varying concentrations of three investigated compounds, Trz-C, Trz-D, and Trz-E, to evaluate their inhibitory performance against CS corrosion in the acidic environment.

For the blank sample without any inhibitor, the weight loss was 0.224 g, corresponding to a corrosion rate of 13.40 mmy^{-1}. As the concentration of Trz-E, Trz-D, and Trz-C increased from 10^{-5} M to 10^{-3} M, a distinct trend was observed in the data, demonstrating significant improvements in corrosion resistance. The weight loss decreased progressively from 0.196, 0.170, and 0.150 g to 0.041, 0.028, and 0.021 g, respectively. Correspondingly, the corrosion rate declined from 11.73, 10.17, and 8.98 mm y^{-1} to 2.45, 1.68, and 1.26 mm y^{-1}. This reduction was accompanied by a marked increase in inhibition efficiency, which improved from 12.46%,

24.10%, and 32.99% to 81.72%, 87.46%, and 90.60%, respectively. These findings indicate a substantially enhanced protective effect against corrosion under the given conditions.

Table III.1 Weight Loss Parameters for CS Corrosion in 1 M HCl with Varying Concentrations of Trz-C, Trz-D, and Trz-E Inhibitors at 25°C

Inhibitors	Concentration (M)	Weight loss (g)	C_R (mmy^{-1})	η_{WL} (%)	Surface coverage (θ)
Blank	-	0.224	13.40	-	-
Trz-E	10^{-5}	0.196	11.73	12.46	0.1246
	5×10^{-5}	0.152	09.10	32.12	0.3212
	10^{-4}	0.121	07.24	45.97	0.4597
	5×10^{-4}	0.065	03.89	70.97	0.7097
	10^{-3}	0.041	02.45	81.72	0.8172
Trz-D	10^{-5}	0.170	10.17	24.10	0.2410
	5×10^{-5}	0.146	08.74	34.78	0.3478
	10^{-4}	0.105	06.28	53.13	0.5313
	5×10^{-4}	0.034	02.03	84.85	0.8485
	10^{-3}	0.028	01.68	87.46	0.8746
Trz-C	10^{-5}	0.150	08.98	32.99	0.3299
	5×10^{-5}	0.109	06.52	51.34	0.5134
	10^{-4}	0.052	03.11	76.79	0.7679
	5×10^{-4}	0.031	01.86	86.12	0.8612
	10^{-3}	0.021	01.26	90.60	0.9060

The obtained results, including inhibition efficiency (η_{WL}%), corrosion rate (C_R), and surface coverage (θ), are presented in Table 1.

The results unequivocally demonstrate the remarkable inhibitory capabilities of Trz-C, Trz-D, and Trz-E against the corrosion of carbon steel in 1 M HCl solution. A substantial reduction in weight loss and corrosion rate was observed with increasing concentrations of these inhibitors, accompanied by a concomitant enhancement in inhibition efficiency and surface coverage. Notably, Trz-C exhibited the most pronounced effect, exhibiting the lowest weight loss and the highest inhibition efficiency, followed by Trz-D and Trz-E. This superior corrosion protection at higher inhibitor concentrations can be ascribed to the formation of a protective film on the metal surface through the adsorption of the inhibitor molecules [1-5]. The adsorbed inhibitor film acts as a barrier, effectively shielding the steel from the aggressive acidic environment, thereby mitigating the corrosion process. The observed trend in inhibition efficiency and surface coverage is a direct consequence of the increased availability of inhibitor molecules at higher

concentrations, facilitating the formation of a more robust and extensive protective film on the metal surface.

Notably, the inhibition efficiencies obtained from the weight loss analysis almost closely align with those obtained through electrochemical methods, further validating the observed inhibition behavior. The agreement between these complementary techniques lends confidence to the analysis.

III.3 Electrochemical study

III.3.1 Concentration effect

III.3.1.1 Monitoring of Corrosion Potential Over Time

In corrosion studies, electrochemical impedance spectroscopy (EIS) measurements are typically performed at the open circuit potential (E_{ocp}). It is crucial to ensure that steady-state conditions are reached before conducting these tests, as unreliable and inaccurate data may be obtained during dynamic conditions [1]. The adsorption of inhibitor molecules on the metal surface and the initiation and progression of corrosion processes can be monitored by plotting the E_{ocp} versus immersion time. Additionally, the position of E_{ocp} can provide valuable insights into the dominance of anodic or cathodic processes.

Figure 1 displays the time-dependent open circuit potential (OCP) curves for an XC48 Carbon steel electrode immersed in 1 M HCl solution in the absence (Blank) and presence of different concentrations of three inhibitor compounds, Trz-C, Trz-D, and Trz-E, for 25 minutes of immersion at 25°C.

Figure 1 clearly shows that the initial E_{ocp} of Carbon steel (CS) is -0.522 V in the uninhibited 1 M HCl solution. As the CS electrode is immersed into the corrosive solution, the Eocp shifts sharply towards more anodic values. This observed change can be attributed to the dissolution of more active metals present in the steel composition, such as iron (Fe), aluminum (Al), and tin (Sn) [2]. A similar behavior has been reported in the literature and explained by the dissolution of the air-formed oxide layer and an initial attack on the metal surface [3-4].

It can be observed that the E_{ocp} values initially shift positively with time until reaching a relatively steady state after approximately 500 seconds, to reach near stable OCP values both in the absence and presence of the inhibitors. However, in the presence of the highest concentration

(5×10^{-4} and 10^{-3} M) of Trz-C, Trz-D, and Trz-E, the stabilization of the OCP takes longer, indicating a prolonged process of inhibitor film formation or rearrangement on the electrode surface [5].
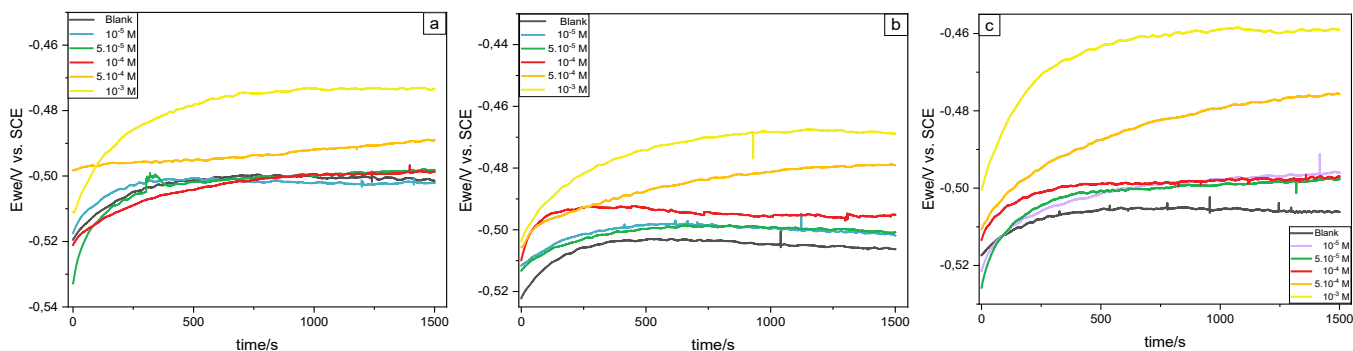
Figure III.1 OCP versus time plots for CS immersed in 1.0 M hydrochloric acid solution at 25°C. in the absence and presence of a) Trz-D, b) Trz-E and, c) Trz-C at different concentrations

Notably, as the concentration of the inhibitors increases, the OCP plots shift towards less negative values, suggesting the formation of a more stable and protective inhibitor layer on the electrode surface. This behavior is consistent with the adsorption of inhibitor molecules, creating a barrier against the corrosive environment and mitigating the corrosion process.

The shape and potential values of the OCP curves provide insights into the kinetics and mechanisms of the inhibition process, as well as the stability and effectiveness of the protective films formed by the inhibitors on the steel surface. These OCP measurements can be complemented with other electrochemical techniques and weight loss measurements to obtain a comprehensive understanding of the inhibition performance and mechanisms of the studied triazole-based inhibitors.

III.3.1.2 Potentiodynamic polarization

besides the open circuit potential study, potentiodynamic polarization curves (Tafel plots) for XC48 carbon steel were also tested to provide a good understanding of the corrosion mechanism on the metal surface. Figure 2 shows the Tafel plots of carbon steel exposed to 1 M HCl solution in the absence and presence of different concentrations of inhibitors at 25°C. The corresponding electrochemical parameters derived by extrapolating the linear segments of anodic and cathodic Tafel slopes such as corrosion current density (I_{corr}), corrosion potential (E_{corr}), anodic Tafel slope (βa), cathodic Tafel slope (βc), and inhibition efficiency ($\eta_p\%$), are listed in Table 2. The

percentage of inhibition efficiency (η%) and surface area coverage (θ) were calculated using the following equations [2]:

$$\eta_p\% = (1 - \frac{I_{corr(i)}}{I_{corr}}) \times 100 \qquad\qquad (III.1)$$

$$\theta = (1 - \frac{I_{corr(i)}}{I_{corr}}) \qquad\qquad (III.2)$$

where I_{corr} and $I_{corr(i)}$ are the uninhibited and inhibited corrosion current densities, respectively.
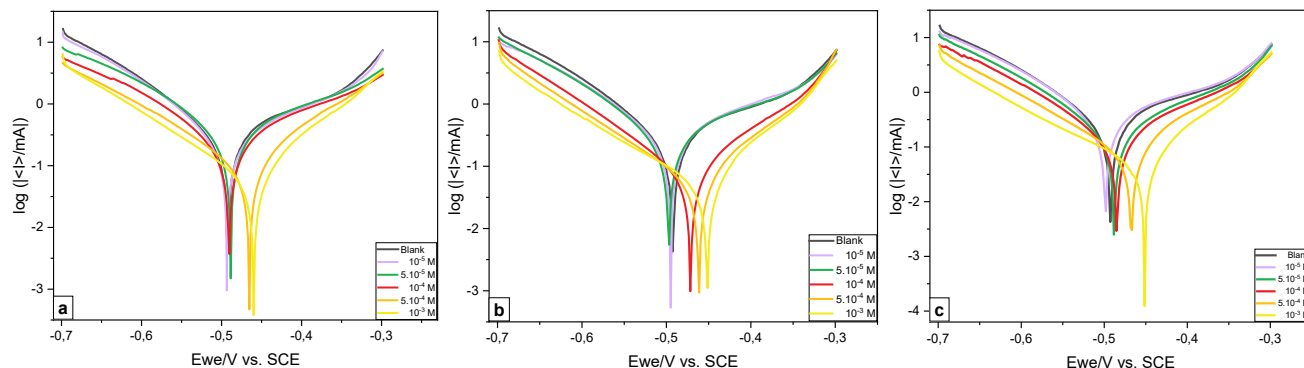
Figure III.2 Tafel curves depicting CS behavior in a 1.0 M HCl solution at 25°C, without and with the presence of, a) Trz-D, b) Trz-E, and, c) Trz-C at varying concentrations.

The Tafel plots clearly show that the addition of the triazole-based inhibitors Trz-C, Trz-D, and Trz-E to the corrosive 1 M HCl solution leads to a significant reduction in both the anodic and cathodic current densities. This reduction in current densities becomes more pronounced as the inhibitor concentration increases, suggesting that these compounds are effective in mitigating the corrosion process by hindering both the anodic metal dissolution and the cathodic hydrogen evolution reactions.

An important observation from the cathodic branches of the polarization curves is that they exhibit nearly parallel lines, as evidenced by the slight changes in the cathodic Tafel slope (βc) values, which remain close to each other across the different inhibitor concentrations. This behavior indicates that the addition of the triazole-based compounds does not significantly alter the mechanism of the hydrogen evolution reaction. It is likely that the reduction of H$^+$ ions on the XC48 steel surface follows a charge transfer mechanism, Similar behavior has also been observed in several studies involving the same alloy and environment [6-11]. In contrast to the cathodic branches, the anodic polarization curves display distinct behavior that can be divided

into two distinct sections. The first section, located between the corrosion potential (E_{corr}) and -0.335 V for all inhibitors, exhibits a sharp decrease in current density as the inhibitor concentration increases. This observation clearly confirms the formation of a protective layer or film of the inhibitor compounds on the steel surface, effectively inhibiting the anodic metal dissolution reaction. However, in the second section, at potentials higher than -0.335 V, the anodic curves converge and coincide with the behavior observed in the blank solution. This phenomenon is attributed to the desorption of inhibitor molecules from the steel surface, caused by the dissolution of the steel itself, which reduces the inhibitor efficiency [12-14]. The potential at which this desorption occurs is defined as the desorption potential (E_{des}) also called (potentiel of unpolarizability), and at potentials above E_{des}, the rate of inhibitor desorption from the steel surface exceeds the rate of adsorption, leading to a decrease in the inhibition performance.

However, even if the inhibitor is desorbed from the metal surface, it still inhibits corrosion since the anodic current densities remain slightly lower than those of the blank [18]. This clearly indicates that the adsorption and desorption of inhibitors depends on the electrode potential.

Table III.2 The Tafel parameters for CS in both uninhibited and inhibited 1 M HCl solutions at 25°C.

	C (M)	-Ecorr (mV/ECS)	i corr (µA.cm^{-2})	β a (mV)	β c (mV)	η$_p$ (%)	θ
Blank	-	492.370	328.864	208.2	120.6	-	-
Trz-E	10^{-5}	493.352	302.443	205.5	119.2	08.03	0.0803
	5×10^{-5}	488.715	275.110	161.5	120.4	16.35	0.1635
	10^{-4}	490.735	195.931	140.8	121.2	40.42	0.4042
	5×10^{-4}	465.135	076.998	082.9	120.0	76.59	0.7659
	10^{-3}	459.814	052.611	075.0	121.7	84.00	0.8400
Trz-D	10^{-5}	494.931	274.836	160.5	116.5	16.43	0.1643
	5×10^{-5}	496.818	261.101	164.2	113.7	20.61	0.2061
	10^{-4}	471.465	084.139	104.8	115.6	74.42	0.7442
	5×10^{-4}	461.312	048.783	075.8	115.3	85.17	0.8517
	10^{-3}	451.405	038.229	060.8	122.8	88.38	0.8838
Trz-C	10^{-5}	497.676	315.186	191.5	114.9	04.16	0.0416
	5×10^{-5}	487.981	217.020	169.3	120.6	34.01	0.3401
	10^{-4}	485.271	157.707	145.5	120.8	52.04	0.5204
	5×10^{-4}	467.433	074.978	085.8	123.3	77.20	0.7720
	10^{-3}	451.548	036.282	060.4	128.1	88.97	0.8897

Based on the maximum displacement in the corrosion potential (E_{corr}) compared to the blank solution, the inhibitors Trz-C, Trz-D, and Trz-E can be classified as mixed-type inhibitors with a predominant anodic effect. As shown in Table 2, the maximum variation in E_{corr} between the blank and inhibited solutions was 32.57, 40.97 and 40.82 mV for Trz-E, Trz-D, and Trz-C, respectively, towards the anodic direction. According to the established criteria [15-17], if the change in the absolute value of E_{corr} is less than 85 mV, the inhibitor can be considered a mixed-type inhibitor. Therefore, the observed shifts in E_{corr} suggest that Trz-C, Trz-D, and Trz-E exhibit mixed-type inhibition behavior, with a predominant influence on the anodic (metal dissolution) reaction.

The results in Table 2 clearly demonstrate the concentration-dependent inhibition behavior of these triazole-based compounds. As the inhibitor concentration increases, the corrosion current density decreases, leading to higher inhibition efficiency and surface coverage values. This trend is observed for all three inhibitors, indicating their effectiveness in forming protective films on the XC48 carbon steel surface and mitigating corrosion in the aggressive 1 M HCl solution. Among the three inhibitors, Trz-C demonstrates the highest inhibition efficiency, reaching an impressive value of approximately 88.97% at a concentration of 10^{-3} M. This superior performance of Trz-C suggests that it forms the most effective protective film or inhibitive layer on the steel surface. This superior inhibition performance can be attributed to its molecular structure and the associated adsorption properties on the steel surface. The presence of the bromine substituent and hydroxyl group in the phenyl ring of Trz-C may contribute to stronger interactions with the metal surface, facilitating the formation of a more compact and stable inhibitive film, effectively blocking active sites and hindering the corrosion process.

III.3.1.3 Electrochemical impedance spectroscopy (EIS)

In this section, electrochemical impedance spectroscopy (EIS) measurements were performed to gain deeper insights into the inhibition mechanisms and support the findings from potentiodynamic polarization studies. EIS allows probing the electrode/electrolyte interface without significantly perturbing the system, providing reliable data on the ongoing electrochemical processes.

The Nyquist and Bode plots of XC48 CS samples recorded at the corrosion potential (E_{corr}) and immersed in 1 M HCl without and with the addition of different concentrations of Trz-C, Trz-D, and Trz-E at 25°C are presented in Figures. 5 and 6 respectively.

As is seen, the impedance spectra shown in Figure 5 comprised of two loops, one large depressed capacitive loop at high and intermediate frequency regions, followed by one small inductive loop at low frequencies region for the blank solution and inhibitor concentrations lower than 5.10^{-5} M. it is evident that the diameter of the capacitive loop increases significantly with increasing inhibitor concentration. This observation suggests the formation of a protective adsorbed layer on the CS surface, which enhances the corrosion protection. The larger the diameter of the capacitive loop, the higher the charge transfer resistance (R_{ct}), indicating a more effective inhibition of the corrosion process. The capacitive loop is typically related to the charge transfer resistance and the electric double layer at the electrode/solution interface [19- 20].
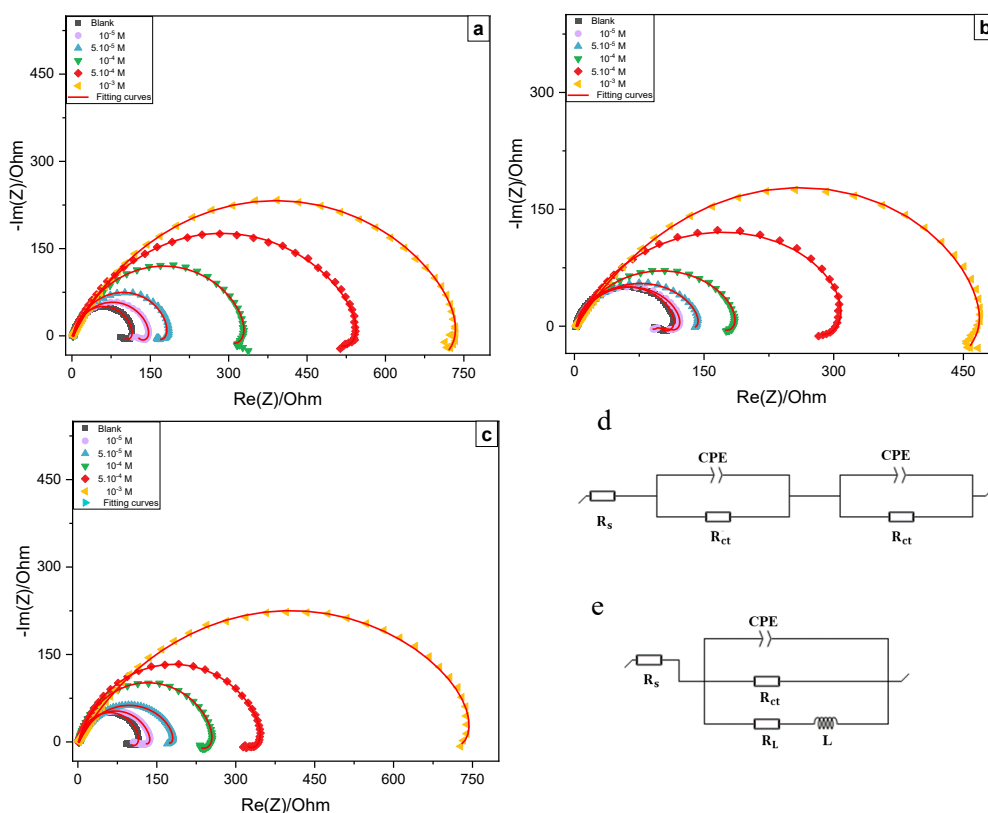

Figure III.5 Nyquist Plots and Equivalent Circuit Modeling of CS in 1.0 M HCl at 25°C in the absence and presence of, a) Trz-D, b) Trz-E, and, c) Trz-C Inhibitors at Various Concentrations

The depression of the capacitive loop can be attributed to the frequency dispersion due to the roughness and heterogeneity of the electrode surface, which is a common phenomenon in practical systems. Whereas the inductive behavior is often associated with relaxation processes of adsorbed intermediates, such as $(FeOH)_{ads}$ and $(H^+)_{ads}$, involved in the corrosion process in acidic media [21-22].

The inductive loop is typically observed in the corrosion of iron and its alloys in hydrochloric acid and sulfuric acid solutions, as per the proposed mechanism involving the following reactions:

$$Fe + H_2O \rightleftharpoons (FeOH)_{ads} + H^+ + e^-$$

$$(FeOH)_{ads} \rightleftharpoons (Fe^{2+})_{aq} + OH^- + e^-$$
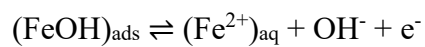
Previous studies by Keddam, Barcia, and Mattos have investigated the role of chloride and sulfate anions in iron dissolution and concluded that the inductive loop is always associated with the relaxation of $FeOH_{ads}$, independent of the anions present [23-24].

Interestingly, at higher inhibitor concentrations ($\geq 5.10^{-4}$ M), the low-frequency inductive loop observed in the uninhibited system and at lower inhibitor levels disappeared, and two-time constant was observed in the impedance spectra. This disappearance of the inductive loop suggests the formation of better-quality, adherent, and stable inhibitor films on the metal surface, further impeding the corrosion processes and associated relaxation phenomena [4]. this behavior has been reported in several previous studies [4,25-27].

It's clearly shown that the shape of all EIS plots was similar regardless of the absence and presence of Trz-C, Trz-D, and Trz-E inhibitors, which indicates that the presence of these inhibitors just reduces the steel corrosion rate by simple adsorption onto the steel surface without changing the electrochemical reaction mechanism [13-17].

To further analyze the EIS data and extract quantitative parameters, electrochemical equivalent circuit (EEC) models were employed for curve-fitting using the Ec-Lab 11.02 software. The equivalent circuit models were selected based on the observed features in the Nyquist plots, such as the presence or absence of the inductive loop. The equivalent circuit model (d) in Figure 5 was used to fit the spectra showing an inductive loop, while model (e) was

employed for spectra without the inductive loop, accounting for the degradation of the inductive behavior at higher inhibitor concentrations.

These EEC models incorporate elements such as the solution resistance (R_s), charge transfer resistance (R_{ct}), inductance (L) and its associated resistance (R_L), and constant phase elements (CPE).

Table III.3 Fitted EIS Parameters for CS in 1 M HCl Without and With Triazole Inhibitors at 25°C.

	C (M)	R_s (Ω cm^2)	R_{ct} (Ω cm^2)	C_{dl} (μF cm^{-2})	χ^2	n	η_E (%)	θ
Blank	-	2.143	118.3	117.6	0.011	0.907	-	-
Trz-E	10^{-5}	2.923	125.7	100.8	0.089	0.867	05.89	0.0589
	5×10^{-5}	2.498	149.5	128.8	0.049	0.813	20.87	0.2087
	10^{-4}	3.725	209.4	108.0	0.063	0.795	43.51	0.4351
	5×10^{-4}	3.729	398.4	112.6	0.092	0.775	70.31	0.7031
	10^{-3}	2.453	496.4	093.9	0.031	0.648	76.17	0.7617
Trz-D	10^{-5}	2.630	144.3	186.0	0.022	0.831	18.02	0.1802
	5×10^{-5}	2.548	181.9	243.0	0.078	0.786	34.96	0.3496
	10^{-4}	2.255	330.4	193.0	0.093	0.733	64.19	0.6419
	5×10^{-4}	1.905	548.6	120.0	0.037	0.693	78.44	0.7844
	10^{-3}	2.168	745.5	132.0	0.072	0.643	84.13	0.8413
Trz-C	10^{-5}	2.264	139.0	136.5	0.048	0.850	14.89	0.1489
	5×10^{-5}	2.296	193.6	209.2	0.093	0.806	38.89	0.3889
	10^{-4}	2.053	258.8	211.4	0.023	0.783	54.29	0.5429
	5×10^{-4}	2.041	355.0	179.2	0.073	0.727	66.68	0.6668
	10^{-3}	1.976	808.3	061.6	0.043	0.632	85.36	0.8536

The CPE is introduced to account for non-ideal capacitive behavior, as it provides a more accurate fitting compared to using a pure capacitance [6,19,25-27]. The impedance of the CPE is described by an expression involving a CPE constant (Y_o), the angular frequency (ω), and a dimensionless parameter (n) that accounts for the phase shift and non-ideal capacitive response [28]:

$$Z_{CPE} = Y_o^{-1}(j\omega)^{-n} \qquad\qquad (III.3)$$

The double-layer capacitance (C_{dl}) is then calculated from the CPE parameters using the Hsu and Mansfeld equation, providing insights into the electrochemical double-layer properties at the metal/solution interface [29]:

$$C_{dl} = (Y_o R_p^{1-n})^{\frac{1}{n}} \qquad\qquad (III.4)$$

The inhibition efficiency (η) and surface coverage (θ) were determined from the charge transfer resistance (R_{ct}) values using the equations below:

$$\eta_E\% = (1 - \frac{R_{ct}}{R_{ct(i)}}) \times 100 \qquad\qquad (III.5)$$

$$\theta = (1 - \frac{R_{ct}}{R_{ct(i)}}) \qquad\qquad (III.6)$$

Where R_{ct} represents the charge transfer resistance without inhibitor present, and $R_{ct(i)}$ is the charge transfer resistance measured in the inhibitor-containing solution. The impedance parameters extracted from the data fitting are summarized in Table 3. The validity of the fitted equivalent circuit model is supported by obtaining the lowest possible goodness of fit (χ^2) value.
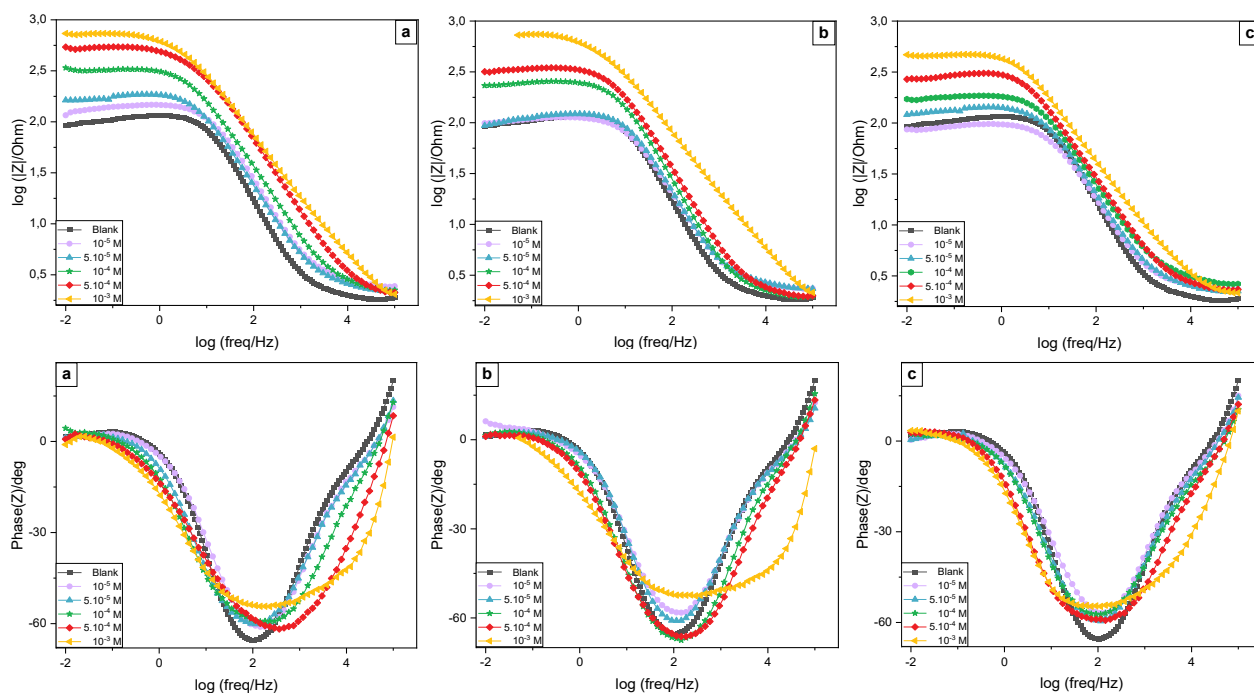
Figure III.6 Bode Impedance (log f vs log |Z|) and Phase Angle (log f vs. α) Plots for CS in 1.0 M HCl at 25°C, Without and With, a) Trz-D, b) Trz-E, and, c) Trz-C Inhibitors at Different Concentrations.

Analysis of the EIS data (Table 3) reveals that the charge transfer resistance (R_{ct}) values were significantly higher in the inhibited solutions compared to the uninhibited (blank) system, and

these R_{ct} values increased progressively with increasing inhibitor concentration. The Trz-C inhibitor exhibited the highest R_{ct} of 808.3 Ω cm^2 at 10^{-3} M concentration. Trz-D and Trz-E followed with R_{ct} values of 745.5 and 496.4 Ω cm^2, respectively, at the same 10^{-3} M concentration.

The observed increase in charge transfer resistance suggests that the triazole-based inhibitors effectively adsorb onto the carbon steel surface, forming a protective insulating layer that impedes the charge transfer processes associated with the corrosion reactions at the metal/solution interface. Consequently, this adsorbed inhibitor film results in a slower corroding system by hampering the electrochemical processes responsible for metal dissolution.

The addition of the inhibitor causes a noticeable reduction in the values of n from 0.907 (in the pure acid solution) to the range of 0.867-0648, 0.831-0.643 and 0.850-0.632 for Trz-E, Trz-D, and Trz-C respectively. This decrease in the value of n indicates an increase in surface inhomogeneity, which is attributed to the adsorption of the inhibitor molecules onto the metal surface, as suggested by El Hamdani et al [30]. In other words, the presence of the inhibitor leads to a more heterogeneous surface due to the adsorption of inhibitor molecules, resulting in a lower value of n compared to the pure acid solution without the inhibitor.

The inhibition efficiency (η_E%) followed the order Trz-C > Trz-D > Trz-E, consistent with the trend observed in the R_{ct} values, With a slight difference in efficiency between Trz-C and Trz-D. These findings showed excellent agreement with potentiodynamic polarization measurements, validating the consistency of the inhibition behavior across different electrochemical techniques.

The Bode impedance (log frequency vs log |Z|) and phase angle (log frequency vs. α) plots (figure 6), provide valuable insights into the electrochemical behavior of the system under investigation. At high frequencies, the values of log |Z| (impedance magnitude) and the phase angle (α) approach zero. This region represents the resistive behavior of the metal-solution interface, primarily governed by the solution resistance (R_s) [31]. The low impedance and near-zero phase angle at high frequencies indicate that the electrolytic solution exhibits low resistance, facilitating the initiation of the adsorption process.

As we move towards lower frequencies, the impedance magnitude ($|Z|$) increases, and the phase angle approaches $0°$. In this region, the impedance value approximately equals the charge transfer resistance (R_{ct}). The increase in absolute impedance at lower frequencies suggests improved corrosion protection, which is attributed to the adsorption of inhibitor molecules on the metal surface [32-34]. The adsorption process becomes more prominent at higher inhibitor concentrations, leading to enhanced corrosion resistance.

In the intermediate frequency range, an ideal capacitive behavior would exhibit a linear relationship between $\log |Z|$ and $\log$ frequency, with a slope of approximately -1 and a phase angle close to $-90°$ [29]. However, in practical systems, a non-ideal capacitive behavior is often observed, where the phase angle deviates from $-90°$, and the slope of the $\log |Z|$ vs. $\log$ frequency plot differs from -1. This non-ideality can be attributed to various factors, such as surface roughness, inhomogeneities, or the presence of intermediate adsorbed species. The non-ideal capacitive behavior is further manifested in the Nyquist plots, where the semicircles appear flattened or depressed, indicating a deviation from ideal capacitive behavior. This deviation is quantified by the parameter "n" where n < 1 represents a non-ideal capacitive behavior.

It is important to note that while EIS provides valuable information about the interfacial phenomena and inhibition mechanisms, complementary techniques such as potentiodynamic polarization, surface characterization, and computational studies can further enhance our understanding of the corrosion inhibition process and the structure-activity relationships of the inhibitor molecules.

III.3.2 Study of the effect of temperature measured by potentiometry and electrochemical impedance spectroscopy

The effect of solution temperature is one of the further significant factors used when assessing the inhibitory efficiency on carbon steel surface, this underscores the need to examine this specific factor to study thermodynamic parameters for evaluating corrosion behavior of carbon steel in 1M HCl solution in the absence and presence of Trz-C, Trz-D and Trz-E at a given concentration (10^{-3} M) at various temperatures ranging from 25 to 55°C by polarization and impedance tests as results are depicted in Figure 7 and figure 8, while their corresponding parameters are summarized in Tables 4 and 5 respectively.

According to the polarization results From Table 4, it can be seen that the corrosion current density increase with the increase in temperature from 25 to 55 °C for both blank and inhibited solutions, precisely more rapidly in blank solutions. Followed by decrease in inhibition efficiency and surface coverage, which indicates that the effect of the Trz-C, Trz-D and Trz-E inhibitors on XC48 carbon steel becomes less efficient as the temperature rises.
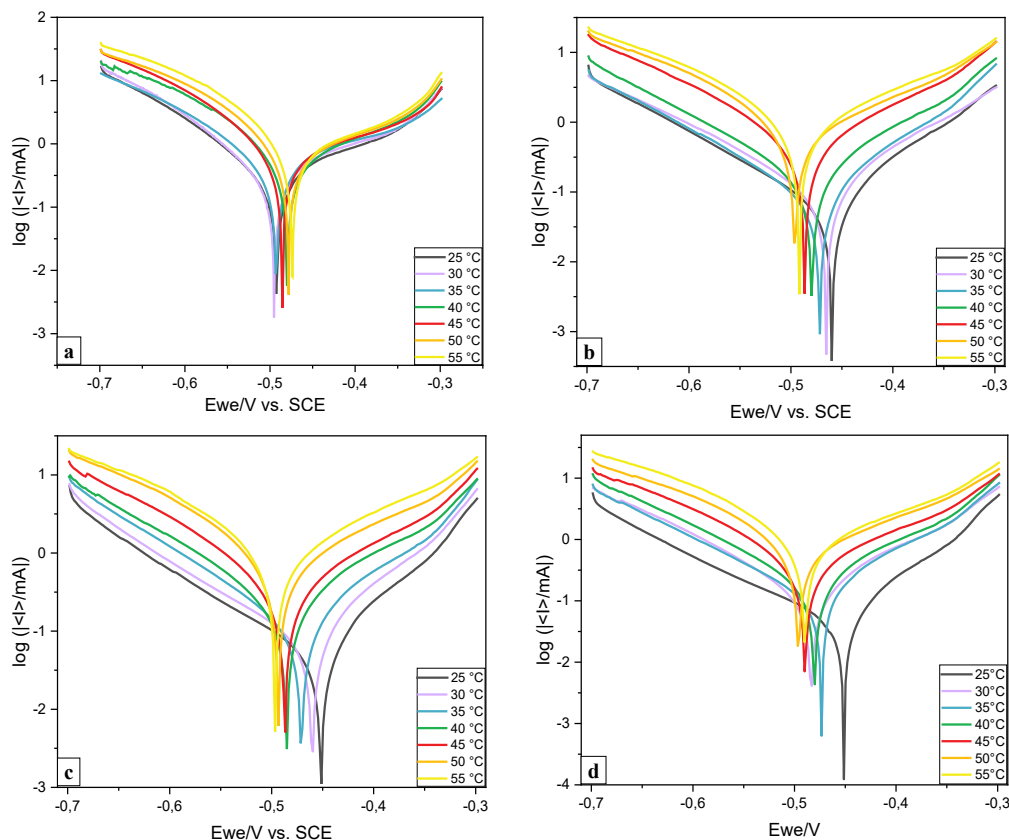
Figure III.7 Polarization curves for XC48 CS, a) in 1M HCl medium + 10^{-3} M of, b) Trz-D, c) Trz-E and, d) Trz-C at different temperatures

The increased value of corrosion current density may be due to the desorption of some adsorbed inhibitors molecules from CS surface [35]. Moreover, as shown in Figure 7, The corrosion potential moves toward the cathodic direction (inhibited solutions) as a result of rising temperatures, unlike what we've seen in the concentration effect that moves in the opposite direction. On the other hand, the impedance study shows that the diameter of the semicircle in the high and intermediate frequency region decreased significantly with increasing temperature of solutions, followed by the appearance of an inductive loop in the low-frequency region when the temperature rises exceeding 25 C, as illustrated in Figure 8, and confirmed by the inhibition

efficiency and R_{ct} values shown in Table 5, that decreased substantially with the rise in temperature. This clearly indicates that the corrosion inhibition property of the Trz-C, Trz-D and Trz-E molecules was obviously affected by the increase in temperature. The emergence of the inductive loop can be attributed to the adsorption of intermediate products formed during the anodic dissolution of the metal substrate [49-52], or the redissolution of the passive surface [53-54] suggesting a change in the inhibition mechanism at elevated temperatures. Furthermore, the decrease in charge transfer resistance (Rct) values with temperature indicates weakening of the protective film formed by the triazole derivatives on the metal surface, necessitating comprehensive thermodynamic analysis to elucidate the precise adsorption mechanism and associated energetic parameters.

Table III. 4 Electrochemical parameters obtained by potentiometry of XC48 CS in 1M HCl with and without addition of Trz-C, Trz-D and Trz-E inhibitors at different temperatures.

Inhibitors	T (°C)	-Ecorr (mV/ECS)	i corr (µA.cm-2)	β a (mV)	β c (mV)	η_P (%)	Ө
Blank	25	492.370	328.864	208.2	120.6	-	-
	30	495.200	405.439	238.4	120.9	-	-
	35	492.905	411.992	194.2	120.8	-	-
	40	479.981	486.377	201.3	100.1	-	-
	45	485.545	585.229	257.4	101.6	-	-
	50	478.088	637.111	235.2	096.8	-	-
	55	473.814	680.039	224.3	086.2	-	-
Trz-E	25	459.814	052.611	075.0	121.7	84.00	0.8400
	30	465.110	075.594	081.7	118.8	81.36	0.8136
	35	480.085	129.175	091.2	115.2	68.65	0.6865
	40	480.377	165.813	097.9	116.9	65.91	0.6591
	45	486.494	313.401	109.0	097.7	46.45	0.4645
	50	496.066	451.608	128.9	084.8	29.12	0.2912
	55	491.785	596.798	128.5	094.2	12.24	0.1224
Trz-D	25	451.405	038.229	060.8	122.8	88.38	0.8838
	30	460.352	061.411	068.5	122.4	84.85	0.8485
	35	471.216	101.464	089.2	118.5	75.37	0.7537
	40	485.097	147.032	092.5	102.2	69.77	0.6977
	45	487.116	245.714	112.6	097.5	58.01	0.5801
	50	493.588	363.355	100.0	074.1	42.97	0.4297
	55	496.355	488.374	102.7	076.3	28.18	0.2818
Trz-C	25	451.548	036.282	060.4	128.1	88.97	0.8897
	30	483.744	077.929	071.1	086.4	80.78	0.8897
	35	473.610	091.225	071.6	116.3	77.86	0.7786
	40	480.424	131.216	079.8	099.0	73.02	0.7302
	45	489.592	221.632	095.5	080.8	62.13	0.6213
	50	496.114	349.725	096.3	068.9	45.11	0.4511
	55	490.282	475.201	103.6	071.4	30.12	0.3012

In addition, Different thermodynamics parameters such like enthalpy (ΔH_a), and entropy (ΔS_a) of activation and also the activation energy (E_a) have been calculated to figure out the clear mechanism involved in the adsorption process by using the transition state and Arrhenius equations [36-37]:

$$i_{corr} = \frac{R.T}{N.h} \exp\left(\frac{\Delta S_a}{R}\right) exp\left(-\frac{\Delta H_a}{R.T}\right) \qquad (III.7)$$

$$i_{corr} = A exp\left(-\frac{E_a}{R.T}\right) \qquad (III.8)$$

Where i_{corr} is the corrosion courant density (A.cm^{-2}), h is Plank constant (6.626×10^{-34} J·s), N is Avogadro number (6.022×10^{23}), ΔH_a is Activation enthalpy and ΔS_a is Activation entropy, A is pre-exponential factor, E_a is activation energy (kJ.mol^{-1}), R is perfect gas constant (J.mol^{-1}. K^{-1}), T is absolute temperature (K).
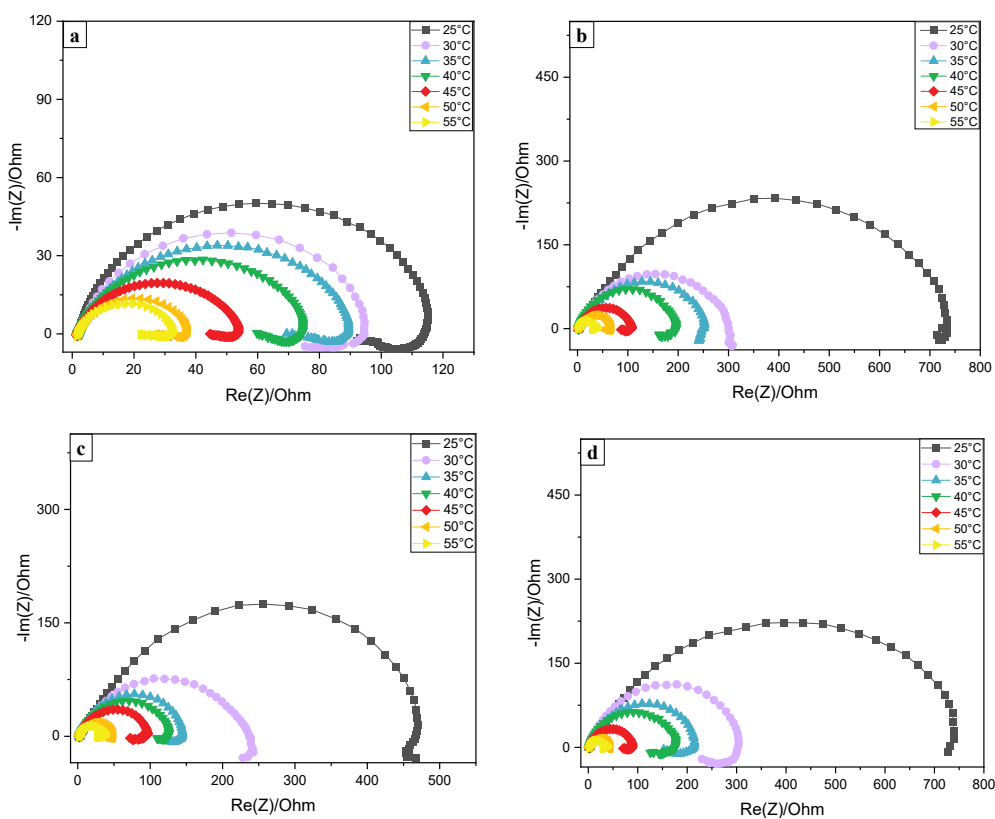
Figure III.8 Nyquist diagrams of XC48 CS a) in 1M HCl medium + 10^{-3} M of, b) Trz-D, c) Trz-E and, d) Trz-C at different temperatures

The transition state plots and Arrhenius plots for carbon steel in 1 M HCl medium without and with 10^{-3} M of Trz-C, Trz-D and Trz-C are shown in Figure 7. Where The activation energy

values (E_a) of metal dissolution were obtained from the slope of $\ln(i_{corr})$ vs $1000/T$ (Figure 9a) and the activation enthalpy (ΔH_a) and entropy (ΔS_a) values were determined from the slope and intercept of the curve $\ln(i_{corr}/T)$ vs $1000/T$ (Figure 9b). All of these different parameters are given in Table 6. As shown clearly by this table, the activation energy value increased in the presence of Trz-C, Trz-D and Trz-E compared to the blank solution, which confirms the good adsorption of these inhibitors molecules on the metal surface. According to the literature, this increase in Ea indicates the physisorption process [37-40].

Table III.5 Fitted Electrochemical parameters obtained by EIS of XC48 CS in 1M HCl with and without addition of Trz-C, Trz-D and Trz-E at different temperatures.

Inhibitors	T (°C)	R_s (Ω cm^2)	R_{ct} (Ω cm^2)	C_{dl} (μF cm^{-2})	η_E (%)	θ
Blank	25	2.143	118.3	0.117	-	-
	30	2.245	097.1	0.052	-	-
	35	2.063	091.9	0.067	-	-
	40	1.757	076.6	0.040	-	-
	45	1.610	053.5	0.150	-	-
	50	1.990	036.7	0.067	-	-
	55	1.749	032.0	0.089	-	-
Trz-E	25	2.453	496.4	0.939	76.17	0.7617
	30	3.032	236.9	0.159	59.02	0.5902
	35	3.384	144.8	0.143	36.56	0.3656
	40	2.762	126.0	0.100	39.19	0.3919
	45	2.749	096.5	0.062	44.61	0.4461
	50	1.993	048.7	0.068	24.70	0.2470
	55	2.248	035.4	0.131	09.41	0.0941
Trz-D	25	2.168	745.5	0.132	84.13	0.8413
	30	4.366	306.0	0.010	68.27	0.6827
	35	2.021	267.9	0.237	65.71	0.6571
	40	2.010	195.6	0.121	60.82	0.6082
	45	2.023	108.0	0.031	50.51	0.5051
	50	2.288	066.3	0.234	44.65	0.4465
	55	2.143	038.3	0.118	16.34	0.1634
Trz-C	25	1.976	808.3	0.062	85.36	0.8536
	30	1.355	318.1	0.183	69.48	0.6948
	35	1.269	227.0	0.216	59.53	0.5953
	40	2.062	177.3	0.125	56.77	0.5677
	45	2.155	089.4	0.215	40.23	0.4023
	50	1.965	043.9	0.042	16.56	0.1656
	55	2.061	036.7	0.138	12.58	0.1258

Generally, the positive values of ΔH_a indicate the endothermic nature of the metal dissolution process [86,87]. The value of ΔS_a without Trz-C, Trz-D and Trz-E compounds is negative, and it increases to more positive values in the presence of these inhibitors. This behavior is mostly caused by the transformation of the reagents into activated complex accompanied by an increase in disorder [41-44].
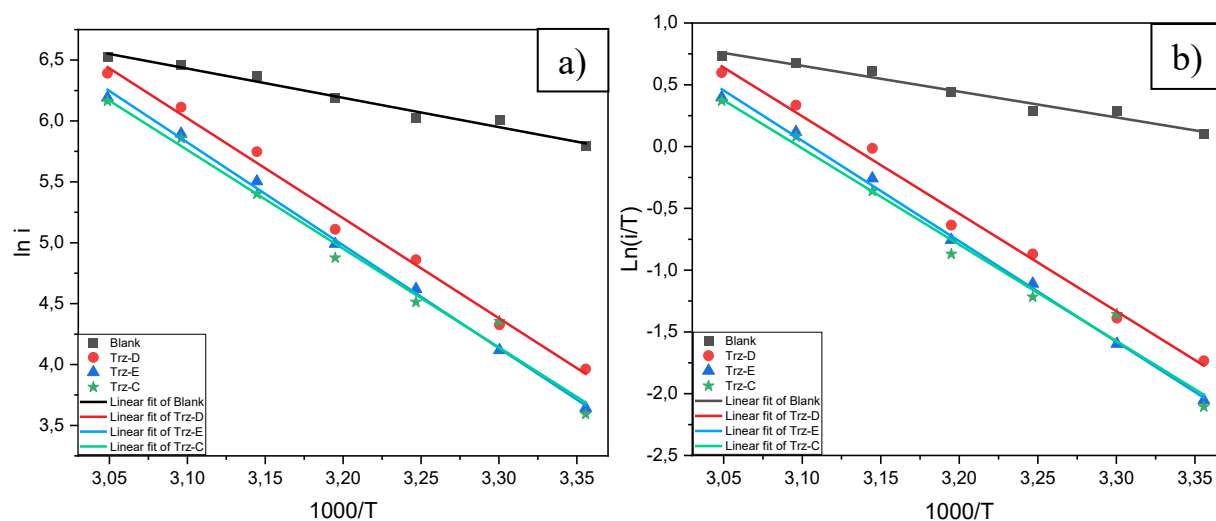
Figure III.9 Arrhenius lines were calculated from the density of the corrosion current of XC48 CS for 1M HCl in the absence and presence of Trz-C, Trz-D and Trz-E at different temperatures.

Table III.6 Thermodynamic parameters of XC48 CS in 1 M HCl in the absence and presence of Trz-C, Trz-D and Trz-E

| Medium	E_a (kJ/mol)	ΔH_a (kJ/mol)	ΔS_a (kJ/mol K)
Blank	19.96	17.36	-138.28
Trz-D	68.21	65.62	7.91
Trz-E	70.22	67.62	12.49
Trz-C	67.41	64.80	3.24

III.4 Surface analysis by scanning electron microscopy (SEM)

The surface morphology of the XC48 carbon steel samples was examined using scanning electron microscopy (SEM) after 24 hours of immersion at 25°C in 1M HCl solution, both in the absence and presence of inhibitors at an optimal concentration of 10^{-3} M for Trz-C, Trz-D, and Trz-E.

Prior to immersion, the carbon steel surface exhibited a clean and smooth appearance with minor scratches resulting from the polishing process (Figure 10a). However, after immersion in the uninhibited acidic solution, the surface morphology was significantly altered, as evidenced by the formation of numerous pits of varying depth and width (Figure 10b).
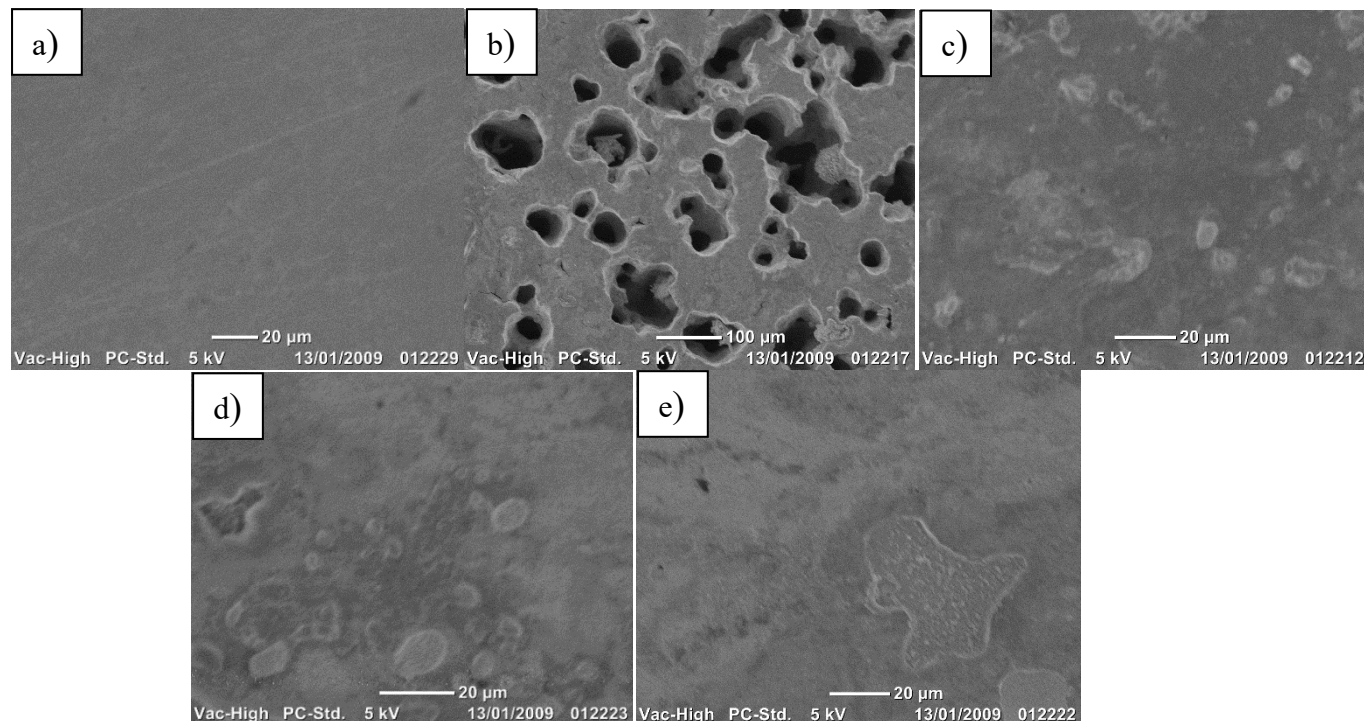
Figure III.10 Surface morphology of XC48 CS samples observed by scanning electron microscopy: (a) polished surface before exposure, (b) after 24-hour immersion in uninhibited 1.0 M HCl solution, and (c-e) after 24-hour immersion in 1.0 M HCl solution containing inhibitors Trz-C, Trz-D and Trz-E, respectively, at 25°C.

This severe damage to the surface is attributed to excessive metal dissolution, indicating that the steel undergoes widespread generalized corrosion across the entire surface in the absence of an inhibitor. In contrast, the addition of Trz-C, Trz-D and Trz-E inhibitors significantly improved the surface morphology of the carbon steel (Figure 10c-e). The pits and fractures observed in the uninhibited solution were no longer present, suggesting that the inhibitor molecules adsorb onto the metal surface in an adherent and uniform manner, resulting in effective surface coverage [45-47]. This observation implies that the high protective effect of these inhibitors can be attributed to the strong and homogeneous adsorption of the inhibitor molecules onto the metal surface,

forming a protective film that acts as a barrier, isolating the metal from the corrosive environment and thereby preventing corrosion [48].

The SEM analysis provides direct visual evidence of the protective nature of the inhibitors, demonstrating their ability to preserve the surface integrity of the carbon steel by forming a uniform and adherent film, effectively mitigating the corrosive effects of the acidic solution.

III.5 Quantum chemical calculation

To investigate the correlation between the molecular structures of Trz-C, Trz-D and Trz-E and their corrosion inhibition effect, theoretical studies were conducted using density functional theory (DFT) in gaseous phase. However, to fully evaluate the effectiveness of Trz-C, Trz-D and Trz-E as corrosion inhibitors in a 1 M HCl environment, it is essential to include the protonated forms of these molecules in addition to their neutral structures. Moreover, in order to study the reactivity of inhibitors molecules, a range of important quantum chemical descriptors including the highest occupied molecular orbital (HOMO), the lowest unoccupied molecular orbital (LUMO), the energy gap (ΔE), global hardness (η) and softness (σ), fraction of electrons transferred (ΔN_{110}), electronegativity (χ), and the electrostatic potential (ESP), for both neutral and protonated forms were calculated and presented in Table 7.

Generally, the analysis of frontier molecular orbitals (HOMO and LUMO) can provide valuable insights into the adsorption mechanism of inhibitor molecules and their interaction with the metal surface. Specifically, these orbitals can be used to elucidate the electron-donating and electron-accepting characteristics of the inhibitor molecules, respectively. Typically, inhibitors with higher E_{HOMO} value are more electron-donating, while inhibitors with lower E_{LUMO} values have a greater ability to accept electrons from the metal d-orbital, indicating higher inhibition effectiveness [5]. The geometrically optimized structures along with frontier molecular orbital (HOMO and LUMO) distributions and molecular electrostatic potential surface (ESP) for neutral and protonated (Trz-C, Trz-D and Trz-E) molecules were depicted in Figures 10 and 11. For neutral forms of these molecules, both HOMO and LUMO were almost entirely distributed over the molecular surface, taking into account that these molecules show a more planar geometry, which suggests a flat adsorption configuration of inhibitors on the iron surface, that gives a general indication for high inhibition performance [36,40].

Conversely, it should be pointed out that the protonated species exhibited some similarity in terms of LUMO distribution with the neutral molecules. Nonetheless, it is crucial to emphasize that the HOMO was predominantly located within the substituted benzene ring for Trz-D and Trz-E, unlike Trz-C, where it is distributed across the entire molecule.

As is evident from Table 7, the trend of E_{LUMO} for both neutral and protonated forms of inhibitors has followed the sequence Trz-D < Trz-C < Trz-E, which Suggesting that Trz-D has better potential to accept electrons from the metal d-orbital. Nevertheless, it is worth noting that this trend in E_{LUMO} values does not align with the order of inhibition efficiency (η%) observed from electrochemical measurements, indicating that E_{LUMO} values do not directly correlate with the inhibitive strengths of the compounds [6]. On the other hand, E_{HOMO} showed a different trend Trz-D < Trz-E < Trz-C with respect to the neutral forms, suggesting that neutral Trz-C has a tendency to be more likely to donate electrons. Whereas the protonated forms showed a similar trend as the order of inhibition efficiency observed from electrochemical measurements, giving the impression that the protonated Trz-C inhibitor has the ability to be more electro-donating than Trz-D and Trz-E.

Table III.7 The quantum chemical parameters derived from density functional theory (DFT) calculations for Trz-C, Trz-D and Trz-E corrosion inhibitors in their neutral and protonated forms.

	Trz-D		Trz-C		Trz-E	
	Neutral	**Protonated**	**Neutral**	**Protonated**	**Neutral**	**Protonated**
E_{HOMO}	-7.2355	-9.9485	-6.8687	-3.8286	-6.9008	-10.1743
E_{LUMO}	-2.7484	-6.4409	-2.6847	-1.3946	-2.3973	-6.1362
ΔE	4.4871	3.5076	4.1840	2.4340	4.5035	4.0381
IP	7.2355	9.9485	6.8687	3.8286	6.9008	10.1743
EA	2.7484	6.4409	2.6847	1.3946	2.3973	6.1362
χ	4.9919	8.1947	4.7767	2.6116	4.6490	8.1552
η	2.2435	1.7538	2.0920	1.2170	2.2517	2.0190
σ	0.4457	0.5702	0.4780	0.8217	0.4441	0.4953
$ΔN_{(110)}$	-0.0383	-0.9621	0,0104	0.9073	0.0380	-0.8260
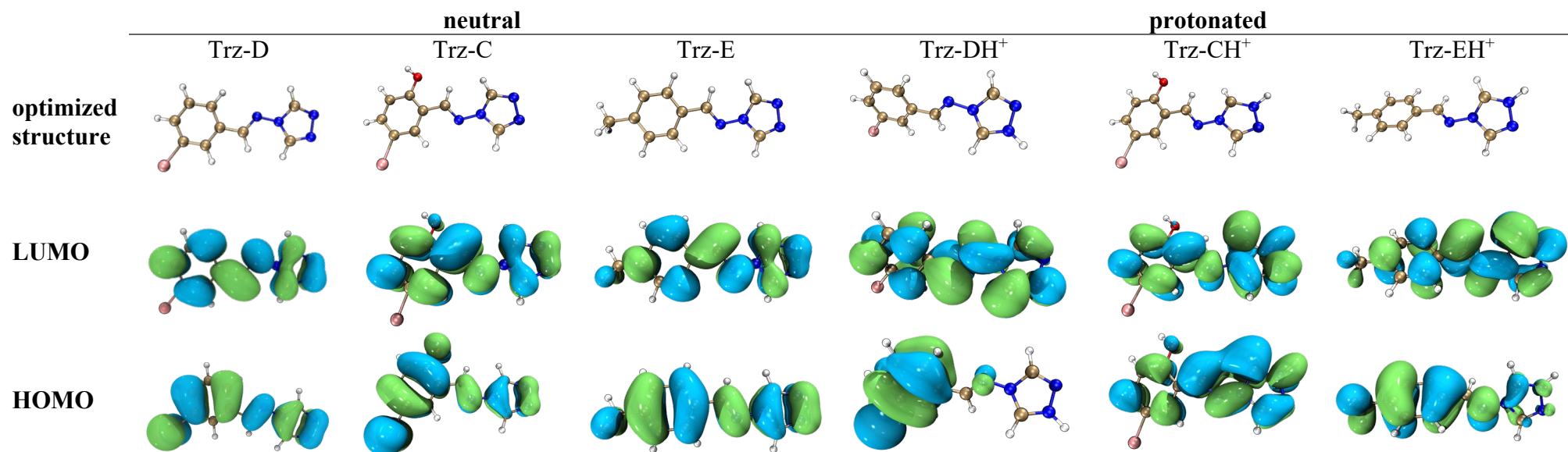
Figure III.10 Optimized molecular structures and frontier molecular orbital (LUMO and HOMO) of neutral and protonated Trz-C, Trz-D and Trz-E. color coding for different atomic elements: nitrogen (blue), oxygen (red), bromine (pink), carbon (golden), and hydrogen (white).

It's important to mention that the protonated inhibitors exhibit E_{HOMO} and E_{LUMO} values that are more negative, indicating a reduced electron-donating ability and an increased electron-accepting capacity for both Trz-D and Trz-E, unlike Trz-C, which shows more positive values, compared to the neutral forms [14]. Similarly, a low energy gap (ΔE) between the LUMO and HOMO levels directly influences the reactivity and adsorption tendencies of inhibitor molecules. This parameter, ΔE, critically characterizes molecular reactivity and adsorptive behavior. In particular, a reduced energy gap signifies heightened reactivity of the inhibitor towards the metal surface, with lower values indicating strong adsorption on metal and subsequently high inhibitive efficiency [15].

Furthermore, a smaller energy gap corresponds to greater inhibition, as it requires less energy to facilitate electron transfer from HOMO to LUMO levels [16-17]. As shown in Table 7, the difference in energy gap between Trz-C, Trz-D and Trz-E is relatively small for the protonated forms indicating similar donating and accepting electron ability [6], but it is significantly larger for the neutral forms. Notably, the ΔE of Trz-C was more than 1 eV lower than those of Trz-D and Trz-E. This remarkable difference confirms the previous findings that the Trz-C inhibitor is more effective than Trz-D and Trz-E especially in its protonated form due to its exceptional ability to donate and accept electrons to and from the CS metal surface. In addition, Electronegativity plays an important role, in understanding chemical reactivity. Which Pauling introduced as referring to the ability of a chemical species to withdraw electrons from other atoms or molecules. Essentially electronegativity serves as a measure of how well a chemical species can draw electron density towards itself [6-5]. Based on the current results, for the values of electronegativity listed in Table 7, it is evident that the order of electronegativity, for the molecules under study follows the pattern of Trz-D > Trz-C > Trz-E, in the neutral form. Given the increase, in electronegativity that occurs when species get protonated, it becomes clear that protonated Trz-D and Trz-E molecules have a stronger ability to attract electrons compared to their neutral counterparts, unlike Trz-C, which once again confirms its exceptional ability to donate electrons to the metal surface. This increase in electronegativity signifies a crucial role played by the protonated inhibitors in effectively coordinating with the metal during retro-donation [15].

Chemical hardness and softness, play a significant role in assessing the stability and reactivity of molecules. Notably, molecules with a high energy gap tend to be less effective as corrosion inhibitors. Conversely, soft molecules with a lower energy gap can serve as excellent corrosion inhibitors since they readily donate electrons to the metal. Based on this information we can conclude that the inhibition performance is inversely related to the hardness of the molecules being studied. When the molecular hardness increases it becomes more challenging for electrons to be donated [45].

In light of the information provided in Table 7 it is evident that compound Trz-C, in its protonated form exhibited the lowest η value indicative of its maximum softness attribute. This finding implies that the protonated Trz-C exhibits a strong adsorption capacity on the surface of XC48 CS, thereby achieving the highest level of inhibition efficiency.

More so, evaluating the electron transfer fraction (ΔN) is crucial as it helps determine the direction of electron flow between the inhibitor molecule and the metal surface. A positive ΔN indicates that electrons are transferred from the inhibitor molecule to the metal whereas a negative ΔN suggests the opposite emphasizing how important this parameter is, in understanding electron exchange dynamics [23]. As we can see from the data presented in Table 7, it is clear that the positive ΔN value suggests that it is very likely that electrons are transferred from the Trz-C inhibitor in both neutral and protonated forms to the metal surface. On the other hand, when we look at the other inhibitors Trz-D and Trz-E, We can reasonably conclude that electron transfer mainly occurs from the metal surface to these molecular species as indicated by the negative ΔN values, especially the protonated forms that have the most negative values. Another interesting point is that the protonated Trz-D has a more negative ΔN value compared to Trz-E, which highlights its higher tendency, for electron transfer [15].

Electrostatic potential (ESP) mapping is a powerful tool for predicting the sites of electrophilic and nucleophilic attack, as well as hydrogen bonding interactions in molecules [23]. The ESP maps of Trz-C, Trz-D and Trz-E inhibitors in their neutral and protonated forms are described in Figure 11.

| neutral			protoated		
Trz-D	Trz-C	Trz-E	Trz-DH$^+$	Trz-CH$^+$	Trz-EH$^+$
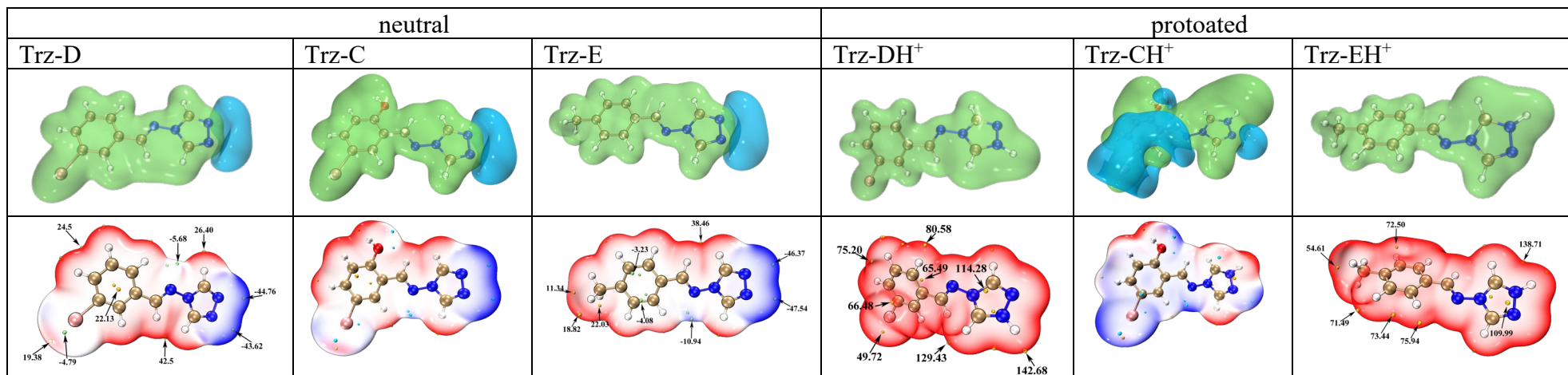
Figure III.11 Electrostatic potential maps illustrating the charge distribution over the molecular surfaces of the neutral and protonated forms of Trz-C, Trz-D and Trz-E molecules.

As illustrated in Figure 11, it can be seen that the blue color (negative) is mainly distributed on the N17 and N18 atoms for all three inhibitors in their neutral form, corresponding to nucleophilic reactivity, whereas, the positive electrostatic potentials (green color) with electrophilic reactivity distributed on the rest of the molecule. while for the protonated forms of Trz-D and Trz-E, the green (positive) region is distributed on the whole molecule, indicating that these molecules have a deficiency of electrons, making them susceptible to nucleophilic attacks and easily available to interact with Fe metal surface. Unlike Trz-C, where the blue region is observed to be concentrated on the substituted benzene ring, the central nitrogen atom and N17 atom, while the green area is distributed over the rest of the molecule. Considering the potential correlation between interaction strength and electrostatic potential (ESP) values, the distribution of ESP on the van der Waals (vdW) surface is employed to predict and identify interaction sites in different inhibitor molecules [25].

III.6 Corrosion inhibition mechanism

The corrosion inhibition mechanism of triazole-based inhibitors on carbon steel in acidic environments reveals a complex molecular interaction characterized by multifaceted protective strategies. The inhibition process fundamentally involves an intricate adsorption mechanism predicated on electronic and electrostatic interactions between molecular inhibitor structures and the metal surface. The triazole-based inhibitors (Trz-C, Trz-D, Trz-E) protect carbon steel in acidic media through physisorption, forming a protective film that blocks corrosive agents like H^+, Cl^-, and H_2O. Specifically, adsorption occurs via two primary mechanisms: (1) electron donation from heteroatoms (N, O) in the triazole molecules to vacant d-orbitals of iron atoms, and (2) electrostatic interactions between protonated triazole cations (formed in acidic media) and Cl^- ions pre-adsorbed on the positively charged steel surface (Fe^{2+}/Fe^{3+}). This process displaces water molecules from the metal surface, as described by the equation:

$$Org_{(sol)} + nH_2O_{(ads)} \rightarrow Org_{(ads)} + nH_2O_{(sol)}$$
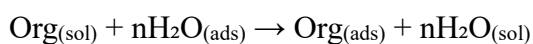
The resulting film acts as a dual anodic-cathodic inhibitor, suppressing both metal dissolution and hydrogen evolution by limiting oxygen diffusion. The adsorbed inhibitors further react with

Fe^{2+} ions to form stable $(Fe–Org)^{2+}(ads)$ complexes, enhancing the film's compactness and adherence. Inhibition efficiency depends critically on the film's thickness, coverage, and stability, which improve with higher inhibitor concentrations but degrade at elevated temperatures due to desorption. Trz-C outperforms Trz-D and Trz-E due to its superior electron-donating ability (positive ΔN), lower energy gap (ΔE), and planar molecular geometry, enabling flat adsorption for maximal surface protection. Electrochemical (EIS, polarization), morphological (SEM), and theoretical (DFT) analyses consistently validate this mechanism, showing reduced corrosion currents, increased charge transfer resistance, and visually confirmed surface integrity.

conclusion

This study unequivocally demonstrates the effectiveness of the synthesized triazole-based Schiff base compounds as corrosion inhibitors for XC48 carbon steel in 1 M HCl. The observed inhibition is attributed to the adsorption of the inhibitor molecules onto the steel surface, forming a protective film that hinders both the anodic and cathodic reactions. The superior performance of Trz-C, especially at higher concentrations and in its protonated form, due to its favorable electronic properties and its ability to form a more compact and stable protective layer. These findings highlight the potential of triazole-based Schiff bases as promising candidates for the development of novel and efficient corrosion inhibitors for industrial applications, and provide a strong foundation for further research into the optimization of their structure and performance. This work contributes significantly to the understanding of structure-activity relationships in corrosion inhibition and provides valuable insights into the design of new, high-performance corrosion inhibitors.

References

[1] Sığırcık, G., Tüken, T., & Erbil, M. (2016). Assessment of the inhibition efficiency of 3, 4-diaminobenzonitrile against the corrosion of steel. corrosion science, 102, 437-445.

[2] Salcı, A., Yüksel, H., & Solmaz, R. (2022). Experimental studies on the corrosion inhibition performance of 2-(2-aminophenyl) benzimidazole for mild steel protection in HCl solution. Journal of the Taiwan Institute of Chemical Engineers, 134, 104349.

[3] Umoren, S. A., Suleiman, R. K., Obot, I. B., Solomon, M. M., & Adesina, A. Y. (2022). Elucidation of corrosion inhibition property of compounds isolated from Butanolic Date Palm Leaves extract for low carbon steel in 15% HCl solution: Experimental and theoretical approaches. Journal of Molecular Liquids, 356, 119002.

[4] Kaya, F., Solmaz, R., & Geçibesler, İ. H. (2023). The use of methanol extract of Rheum Ribes (Işgın) flower as a natural and promising corrosion inhibitor for mild steel protection in 1 M HCl solution. Journal of Industrial and Engineering Chemistry, 122, 102-117.

[5] Wang, L., Wang, H., Seyeux, A., Zanna, S., Pailleret, A., Nesic, S., & Marcus, P. (2023). Adsorption mechanism of quaternary ammonium corrosion inhibitor on carbon steel surface using ToF-SIMS and XPS. Corrosion Science, 213, 110952.

[6] Caldona, E. B., Zhang, M., Liang, G., Hollis, T. K., Webster, C. E., Smith Jr, D. W., & Wipf, D. O. (2021). Corrosion inhibition of mild steel in acidic medium by simple azole-based aromatic compounds. Journal of Electroanalytical Chemistry, 880, 114858.

[7] Li, L., Zhang, X., Lei, J., He, J., Zhang, S., & Pan, F. (2012). Adsorption and corrosion inhibition of Osmanthus fragran leaves extract on carbon steel. Corrosion Science, 63, 82-90.

[8] Ansari, K. R., Quraishi, M. A., & Singh, A. (2014). Schiff's base of pyridyl substituted triazoles as new and effective corrosion inhibitors for mild steel in hydrochloric acid solution. Corrosion Science, 79, 5-15.

[9] Zaher, A., Aslam, R., Lee, H. S., Khafouri, A., Boufellous, M., Alrashdi, A. A., ... & Ouhssine, M. (2022). A combined computational & electrochemical exploration of the Ammi

visnaga L. extract as a green corrosion inhibitor for carbon steel in HCl solution. Arabian Journal of Chemistry, 15(2), 103573.

[10] Saraswat, V., Kumari, R., & Yadav, M. (2022). Novel carbon dots as efficient green corrosion inhibitor for mild steel in HCl solution: Electrochemical, gravimetric and XPS studies. Journal of Physics and Chemistry of Solids, 160, 110341.

[11] Lazrak, J., Ech-Chihbi, E., El Ibrahimi, B., El Hajjaji, F., Rais, Z., Tachihante, M., & Taleb, M. (2022). Detailed DFT/MD simulation, surface analysis and electrochemical computer explorations of aldehyde derivatives for mild steel in 1.0 M HCl. Colloids and Surfaces A: Physicochemical and Engineering Aspects, 632, 127822.

[12] Karthikaiselvi, R., & Subhashini, S. (2014). Study of adsorption properties and inhibition of mild steel corrosion in hydrochloric acid media by water soluble composite poly (vinyl alcohol-o-methoxy aniline). Journal of the Association of Arab Universities for Basic and Applied Sciences, 16, 74-82.

[13] Al-Amiery, A. A., Mohamad, A. B., Kadhum, A. A. H., Shaker, L. M., Isahak, W. N. R. W., & Takriff, M. S. (2022). Experimental and theoretical study on the corrosion inhibition of mild steel by nonanedioic acid derivative in hydrochloric acid solution. Scientific Reports, 12(1), 4705.

[14] Quy Huong, D., Duong, T., & Nam, P. C. (2019). Effect of the structure and temperature on corrosion inhibition of thiourea derivatives in 1.0 M HCl solution. ACS omega, 4(11), 14478-14489.

[15] Chafiq, M., Chaouiki, A., Al-Hadeethi, M. R., Salghi, R., & Chung, I. M. (2021). A joint experimental and theoretical investigation of the corrosion inhibition behavior and mechanism of hydrazone derivatives for mild steel in HCl solution. Colloids and Surfaces A: Physicochemical and Engineering Aspects, 610, 125744.

[16] Dutta, A., Saha, S. K., Adhikari, U., Banerjee, P., & Sukul, D. (2017). Effect of substitution on corrosion inhibition properties of 2-(substituted phenyl) benzimidazole derivatives on mild steel in 1 M HCl solution: a combined experimental and theoretical approach. Corrosion Science, 123, 256-266.

[17] Haque, J., Srivastava, V., Verma, C., & Quraishi, M. A. (2017). Experimental and quantum chemical analysis of 2-amino-3-((4-((S)-2-amino-2-carboxyethyl)-1H-imidazol-2-yl) thio) propionic acid as new and green corrosion inhibitor for mild steel in 1 M hydrochloric acid solution. Journal of Molecular Liquids, 225, 848-855.

[18] Faustin, M. (2013). Étude de l'effet des alcaloïdes sur la corrosoion de l'acier C38 en milieu acide chlorhydrique 1M: application à Aspidosperma album et Geissospermum laeve (Apocynacées) (Doctoral dissertation, Antilles-Guyane).

[19] Qiang, Y., Guo, L., Li, H., & Lan, X. (2021). Fabrication of environmentally friendly Losartan potassium film for corrosion inhibition of mild steel in HCl medium. Chemical Engineering Journal, 406, 126863.

[20] Kumar, R., Yadav, O. S., & Singh, G. (2017). Electrochemical and surface characterization of a new eco-friendly corrosion inhibitor for mild steel in acidic media: a cumulative study. Journal of Molecular Liquids, 237, 413-427.

[21] Gharaghooshi, A. Z., Akbarinezhad, E., Esmaeili, N., & Neshati, J. (2021). Study of Adsorption/Desorption Effect of 2-Mercaptobenzothiazole as Sweet Corrosion Inhibitor on API-5L X60 Steel. Protection of Metals and Physical Chemistry of Surfaces, 57(1), 153-167.

[22] Zhang, G., Chen, C., Lu, M., Chai, C., & Wu, Y. (2007). Evaluation of inhibition efficiency of an imidazoline derivative in CO2-containing aqueous solution. Materials Chemistry and Physics, 105(2-3), 331-340.

[23] Keddam, M., Mattos, O. R., & Takenouti, H. (1981). Reaction model for iron dissolution studied by electrode impedance: II. Determination of the reaction model. Journal of The Electrochemical Society, 128(2), 266.

[24] Barcia, O. E., & Mattos, O. R. (1990). The role of chloride and sulphate anions in the iron dissolution mechanism studied by impedance measurements. Electrochimica Acta, 35(6), 1003-1009.

[25] Haque, J., Verma, C., Srivastava, V., & Nik, W. W. (2021). Corrosion inhibition of mild steel in 1M HCl using environmentally benign Thevetia peruviana flower extracts. Sustainable Chemistry and Pharmacy, 19, 100354.

[26] Sedik, A., Lerari, D., Salci, A., Athmani, S., Bachari, K., Gecibesler, İ. H., & Solmaz, R. (2020). Dardagan Fruit extract as eco-friendly corrosion inhibitor for mild steel in 1 M HCl: Electrochemical and surface morphological studies. Journal of the Taiwan Institute of Chemical Engineers, 107, 189-200.

[27] Nandini, S., Ronald, N., Adimule, S. P., & Krishnamurthy, P. (2021). Anticorrosive effects of derivatives of 4-{[4-(dimethylamino) benzylidene] amino}-1, 2, 4-triazole on 316 stainless steel in HCl medium: Experimental and computational study. Journal of Failure Analysis and Prevention, 21(3), 1057-1076.

[28] Cao, S., Liu, D., Ding, H., Wang, J., Lu, H., & Gui, J. (2019). Task-specific ionic liquids as corrosion inhibitors on carbon steel in 0.5 M HCl solution: An experimental and theoretical study. Corrosion Science, 153, 301-313.

[29] Hsu, C. H., & Mansfeld, F. (2001). Concerning the conversion of the constant phase element parameter Y0 into a capacitance. Corrosion, 57(09).

[30] El Hamdani, N., Fdil, R., Tourabi, M., Jama, C., & Bentiss, F. (2015). Alkaloids extract of Retama monosperma (L.) Boiss. seeds used as novel eco-friendly inhibitor for carbon steel corrosion in 1 M HCl solution: Electrochemical and surface studies. Applied Surface Science, 357, 1294-1305.

[31] Macdonald, J. R., Johnson, W. B., Raistrick, I. D., Franceschetti, D. R., Wagner, N., McKubre, M. C. H., ... & Eisenberg, R. S. (2018). Impedance spectroscopy: theory, experiment, and applications (pp. 424-458). John Wiley & Sons.

[32] Shwetha, K. M., Praveen, B. M., & Devendra, B. K. (2024). A review on corrosion inhibitors: types, mechanisms, electrochemical analysis, corrosion rate and efficiency of corrosion inhibitors on mild steel in an acidic environment. Results in Surfaces and Interfaces, 100258.

[33] Al-Amiery, A. A., Kadhim, A., Al-Adili, A., & Tawfiq, Z. H. (2021). Limits and developments in ecofriendly corrosion inhibitors of mild steel: a critical review. Part 1: Coumarins. Int. J. Corros. Scale Inhib, 10(4), 1355.

[34] Wang, D., Li, Y., Chen, B., & Zhang, L. (2020). Novel surfactants as green corrosion inhibitors for mild steel in 15% HCl: Experimental and theoretical studies. Chemical Engineering Journal, 402, 126219.

[35] Fathabadi, H. E., Ghorbani, M., & Ghartavol, H. M. (2021). Corrosion inhibition of mild steel with tolyltriazole. Materials Research, 24, e20200395.

[36] He, Y., Ren, S., Wang, X., Young, D., Mohamed-Said, M., Santos, B. A. F., ... & Singer, M. (2024). Temperature dependence of adsorption and effectiveness for a pyrimidinium-type corrosion inhibitor on mild steel. Corrosion, 80(2), 177-186.

[37] Fernandes, C. M., Cordeiro, P., Menezes, V., Martins, V., dos Reis, J. S., Lee, H. S., ... & Ponzio, E. A. (2024). Selenocyanates and selenotetrazoles derivatives: A detailed experimental and theoretical evaluation as corrosion inhibitors for mild steel in aggressive environment. Electrochimica Acta, 475, 143629.

[38] Saraswat, V., Sarkar, T. K., & Yadav, M. (2024). Evaluation on corrosion mitigation capabilities of nitrogen doped carbon dots as corrosion inhibitors for mild steel in descaling solution. Materials Chemistry and Physics, 313, 128678.

[39] Ettahiri, W., Allah, A. E. M. A., Lazrak, J., Safir, E. H., Yadav, K. K., Hammouti, B., ... & Taleb, M. (2024). Synthesis, characterization, theoretical, and experimental evaluation of novel imidazolone− based compounds as eco-friendly corrosion inhibitors for mild steel. Journal of Industrial and Engineering Chemistry, 140, 631-646.

[40] Chigondo, M., & Chigondo, F. (2016). Recent natural corrosion inhibitors for mild steel: an overview. Journal of Chemistry, 2016(1), 6208937.

[41] Döner, A., Solmaz, R., Özcan, M., & Kardaş, G. (2011). Experimental and theoretical studies of thiazoles as corrosion inhibitors for mild steel in sulphuric acid solution. Corrosion science, 53(9), 2902-2913.

[42] Al-Amiery, A. A., Kadhum, A. A. H., Alobaidy, A. H. M., Mohamad, A. B., & Hoon, P. S. (2014). Novel corrosion inhibitor for mild steel in HCl. Materials, 7(2), 662-672.

[43] Somers, A. E., Hinton, B. R., de Bruin-Dickason, C., Deacon, G. B., Junk, P. C., & Forsyth, M. (2018). New, environmentally friendly, rare earth carboxylate corrosion inhibitors for mild steel. Corrosion Science, 139, 430-437.

[44] Saha, S. K., Dutta, A., Ghosh, P., Sukul, D., & Banerjee, P. (2016). Novel Schiff-base molecules as efficient corrosion inhibitors for mild steel surface in 1 M HCl medium: experimental and theoretical approach. Physical Chemistry Chemical Physics, 18(27), 17898-17911.

[45] Habeeb, H. J., Luaibi, H. M., Abdullah, T. A., Dakhil, R. M., Kadhum, A. A. H., & Al-Amiery, A. A. (2018). Case study on thermal impact of novel corrosion inhibitor on mild steel. Case studies in thermal engineering, 12, 64-68.

[46] Okafor, P. C., Ebenso, E. E., & Ekpe, U. J. (2010). Azadirachta indica extracts as corrosion inhibitor for mild steel in acid medium. International journal of electrochemical science, 5(7), 978-993.

[47] Cao, Z., Tang, Y., Cang, H., Xu, J., Lu, G., & Jing, W. (2014). Novel benzimidazole derivatives as corrosion inhibitors of mild steel in the acidic media. Part II: Theoretical studies. Corrosion Science, 83, 292-298.

[48] Saraswat, V., Yadav, M., & Obot, I. B. (2020). Investigations on eco-friendly corrosion inhibitors for mild steel in acid environment: Electrochemical, DFT and Monte Carlo Simulation approach. Colloids and Surfaces A: Physicochemical and Engineering Aspects, 599, 124881.

[49] Canto, J., Rodríguez-Díaz, R. A., Martinez-de-la-Escalera, L. M., Neri, A., & Porcayo-Calderon, J. (2023). Corrosion Inhibition in CO2-Saturated Brine by Nd3+ Ions. Molecules, 28(18), 6593.

[50] Hurtado, M. D. R. F., Sumodjo, P. T. A., & Benedetti, A. V. (2003). Electrochemical studies with a Cu–5wt.% Ni alloy in 0.5 M H2SO4. Electrochimica Acta, 48(19), 2791-2798.

[51] Prabhu, D., & Rao, P. (2013). Garcinia indica as an environmentally safe corrosion inhibitor for aluminium in 0.5 M phosphoric acid. International Journal of Corrosion, 2013(1), 945143.

[52] Porcayo-Calderon, J., Rodriguez-Diaz, R. A., Porcayo-Palafox, E., Colin, J., Molina-Ocampo, A., & Martinez-Gomez, L. (2015). Effect of Cu addition on the electrochemical

corrosion performance of Ni3Al in 1.0 M H2SO4. Advances in materials science and engineering, 2015(1), 209286.

[53] Amin, M. A., Khaled, K. F., Mohsen, Q., & Arida, H. A. (2010). A study of the inhibition of iron corrosion in HCl solutions by some amino acids. Corrosion science, 52(5), 1684-1695.

[54] Bouamra, B., Djellab, M., Bentrah, H., Chala, A., Kherief, S., & Taoui, H. (2023). Ghars date extract/iodide ions system as an eco-friendly corrosion inhibitor for API 5L X70 steel in sulfuric acid. Journal of the Chinese Chemical Society, 70(9), 1734-1745.

Chapter 4

Design and Synthesis of 1,2,4-Triazole-Based Schiff Base Ligands: Unveiling Novel Coordination Complexes with Transition Metals

Table of Contents

Chapter 4

Unveiling Novel Coordination Complexes with Transition Metals

IV.1 Introduction

Schiff bases, named after Hugo Schiff, are an important class of organic compounds characterized by the presence of an imine or azomethine group (-CH=N-) [1]. These compounds are typically synthesized through the condensation reaction between primary amines and carbonyl compounds, usually aldehydes. In this study, we focus on the synthesis of a series of novel Schiff base ligands derived from 4-amino-1,2,4-triazole and various substituted benzaldehydes. The 1,2,4-triazole moiety is of particular interest due to its wide range of applications. Beyond its known biological activities and potential for coordination with metal ions, the 1,2,4-triazole moiety also promotes applications in the field of molecular magnetism and serves as an effective corrosion inhibitor [2-5]. These diverse properties make these Schiff bases promising candidates for applications in medicinal chemistry, coordination chemistry, materials science, and industrial protection.

IV.2 Ligand Synthesis

The synthesis of the Trz-X ligand family (1,2,4-Triazole-Based Schiff Base) is carried out in a single step as shown in scheme 1. These ligands will be identifiable according to the formalism of the type Trz-X, where X refers to the identification letter of the substituted benzaldehyde used in the synthesis. This naming convention allows for easy differentiation between the various compounds in the series.

The general reaction involves the nucleophilic addition of the amino group of 4-amino-1,2,4-triazole to the carbonyl carbon of the substituted benzaldehyde, followed by the elimination of water to form the imine bond. This condensation reaction is carried out using ethanol as a solvent and catalyzed by a small amount of glacial acetic acid. The reactions are conducted at a temperature of 80°C for 4 hours, yielding the desired Schiff base products. After purification by recrystallization from a 1:1 mixture of H_2O/acetonitrile, the products are obtained with an average yield of 70%.

IV.2.1 X-Ray Diffraction Analysis

It's important to note that the determination of a structure in the crystalline state by X-ray diffraction provides access not only to the molecular conformation but also to the interactions that the molecule forms within the crystal. A detailed study of these interactions is often

valuable, as it can reveal important information about hydrogen bonding, π-π stacking, and other intermolecular forces that influence the compound's properties and behavior in the solid state. This comprehensive structural information contributes significantly to our understanding of the Trz-X compounds and their potential applications. The structural data for each compound are given in the appendix.

IV.2.1.1 The ligand 1-phenyl-N-(4H-1,2,4-triazol-4-yl)methanimine (Trz-A)

Single crystals suitable for X-ray diffraction were obtained by recrystallization from a 1:1 solvent mixture of water and acetonitrile. The X-ray diffraction analysis of these crystals provided definitive proof of the molecular structure of the Trz-X compounds. This method was particularly exemplified in the case of Trz-A, where the crystal structure unambiguously confirmed the expected Schiff base formation and the overall molecular geometry.
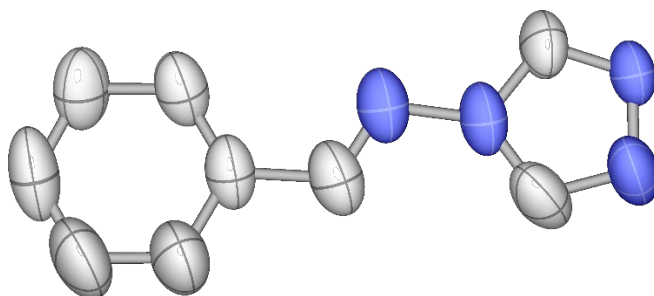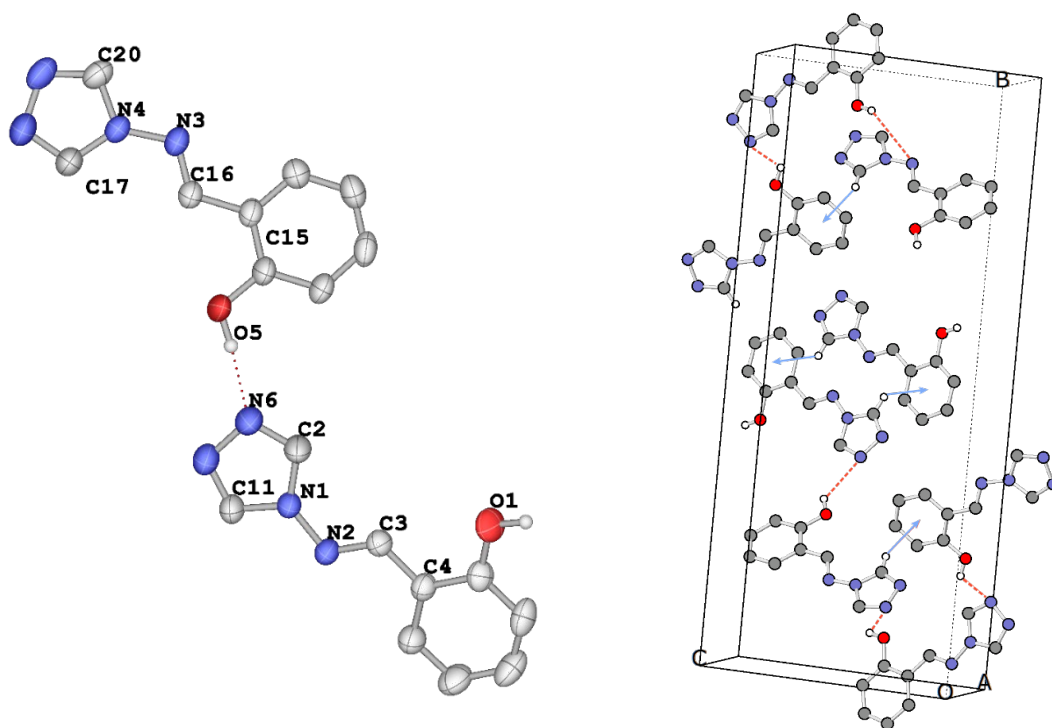

Figure IV.1 ORTEP view of the Ligand Trz-A with partial atom numbering. The ellipsoids contain 50% of the electron density

IV.2.1.2 The ligand 2-(((4H-1,2,4-triazol-4-yl)imino)methyl)phenol (Trz-B)

The Trz-B ligand is crystallized in a mixture of H_2O/acetonitrile, forming white crystals. The single-crystal X-ray diffraction study of the Trz-B ligand reveals that the space group is monoclinic (P2$_1$/n). Two distinct molecules, oriented differently, comprise the asymmetric unit of the title compound, Trz-B ($C_{18} H_{16} N_8 O_2$). Both molecules in the asymmetric unit are nearly planar, as evidenced by the dihedral angles of -176.29(15)° for C(11)-N(1)-N(2)-C(3) and -174.12(16)° for C(16)-N(3)-N(4)-C(20). The characteristic bond lengths and angles of ligand Trz-B are presented in Table 2. As clearly shown in Figure 2, The crystal packing of ligand Trz-B is characterized by a non-uniform arrangement of molecules, which contributes to the overall

complexity and irregularity of the packing structure. Despite this irregularity, the molecules seem to adopt specific orientations relative to each other, likely driven by the need to maximize favorable interactions, such as hydrogen bonds and CH-π interactions, while minimizing steric repulsions. The crystal packing of the ligand reveals two significant intermolecular interactions that contribute to its overall structure. Firstly, a weak CH-π interaction is observed between the phenol and triazole moieties of adjacent ligand molecules. This interaction involves the phenol ring of one ligand and the triazole ring of a neighboring ligand. Secondly, the structure is further stabilized by a hydrogen bond network. This hydrogen bond forms between the hydroxyl group of the phenol on one ligand and the nitrogen atom of the triazole ring on an adjacent ligand. This hydrogen bonding further strengthens the crystal lattice, linking neighboring molecules in a specific orientation. Together, these interactions play a crucial role in determining the three-dimensional arrangement of the molecules within the crystal lattice.
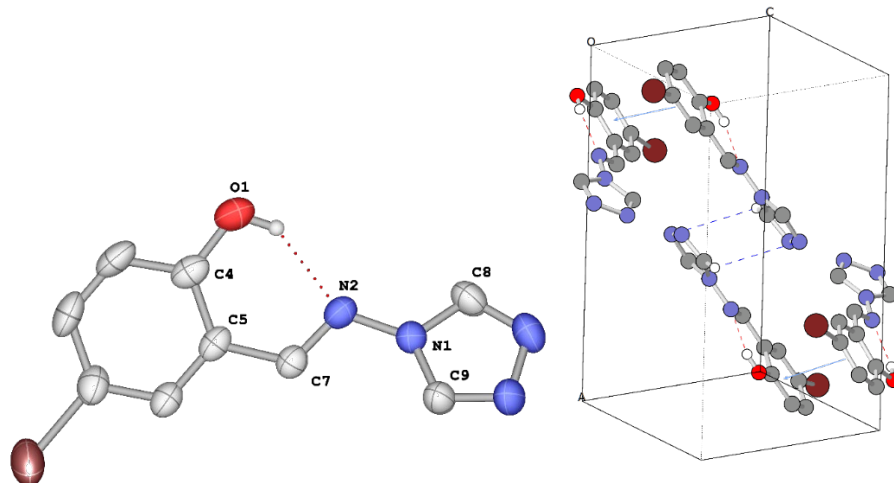

Figure IV.2 ORTEP view of the Ligand Trz-B with partial atom numbering. The ellipsoids contain 50% of the electron density (left). Main intermolecular interactions related to crystal packing, with CH-π interactions shown in blue lines and hydrogen bonding in red dotted lines (right). Hydrogen atoms are not included for clarity, except for those participating in CH-π interactions and linked to Oxygen atoms, which are represented by small spheres.

Table IV.2 Bond lengths and angles of the Trz-B ligand

Bond lengths (Å)		Bond angles (°)	
N(1)-C(11)	1.3456(18)	C(11)-N(1)-C(2)	104.59(12)
N(1)-C(2)	1.3473(19)	N(7)-C(11)-N(1)	111.67(14)
N(1)-N(2)	1.3999(16)	C(3)-N(2)-N(1)	115.82(12)
N(2)-C(3)	1.2735(17)	N(2)-C(3)-C(4)	121.11(13)
C(3)-C(4)	1.4560(19)	C(11)-N(1)-N(2)	122.43(12)
N(4)-C(17)	1.350(2)	C(20)-N(4)-C(17)	104.45(13)
N(4)-C(20)	1.3421(19)	N(8)-C(17)-N(4)	110.73(15)
N(3)-N(4)	1.4005(16)	C(16)-N(3)-N(4)	116.01(13)
N(3)-C(16)	1.2674(19)	N(3)-C(16)-C(15)	120.97(14)
C(15)-C(16)	1.4569(19)	C(17)-N(4)-N(3)	133.92(13)

IV.2.1.3 The ligand 2-(((4H-1,2,4-triazol-4-yl)imino)methyl)-4-bromophenol (Trz-C)

The Trz-C ligand crystallizes as white crystals when grown in a mixture of water and acetonitrile. X-ray diffraction analysis of a single crystal reveals that the compound adopts a monoclinic crystal system, specifically belonging to the space group P2$_1$/C.

Figure IV.3 ORTEP view of the Ligand Trz-C with partial atom numbering. The ellipsoids contain 50% of the electron density (left). Main intermolecular and intramolecular interactions related to crystal packing, with π-π Stacking interactions are represented in blue lines, CH···X interactions shown in blue dotted lines and hydrogen bonding in red dotted lines (right). Hydrogen atoms are not included for clarity, except for those participating in CH···X interactions and linked to Oxygen atoms, which are represented by small spheres.

The molecular structure of Trz-C is nearly flat, as evidenced by the dihedral angle between the atoms C8-N1-N2-C7, which measures 158.5(3)°. This angle, being close to 180°, indicates minimal twisting or deviation from planarity. Key structural parameters, including characteristic bond lengths and angles for the ligand, are compiled and presented in Table 3 for reference. An intramolecular hydrogen bond is observed between the phenol group and the central nitrogen atom of the ligand. The crystal packing of the Trz-C ligand exhibits two weak intermolecular interactions: a π-π stacking between bromophenol groups of adjacent ligands at a distance of 3.73 Å with a slight slip of 0.98 Å, and a CH···N interaction involving the terminal nitrogen of one ligand and the triazole moiety of another.

**Table IV.3** Bond lengths and angles of the Trz-C ligand

Bond lengths (Å)		Bond angles (°)	
N(1)-C(9)	1.358(4)	C(9)-N(1)-C(8)	104.8(3)
N(1)-C(8)	1.354(4)	C(9)-N(1)-N(2)	131.8(3)
N(1)-N(2)	1.401(4)	C(7)-N(2)-N(1)	115.0(3)
N(2)-C(7)	1.289(4)	N(2)-C(7)-C(5)	121.1(3)
C(7)-C(5)	1.469(4)	C(4)-C(5)-C(7)	122.3(3)
C(5)-C(4)	1.420(4)		
C(4)-O(1)	1.353(4)		

IV.2.1.4 The ligand 1-(3-bromophenyl)-N-(4H-1,2,4-triazol-4-yl)methanimine (Trz-D)

The Trz-D ligand forms white crystals when crystallized from a water/acetonitrile mixture. Single-crystal X-ray diffraction analysis reveals an orthorhombic crystal system with space group $P2_12_12_1$. The molecule is nearly planar, evidenced by the C11-N3-N2-C3 dihedral angle of -173.9(5)°, indicating minimal deviation from planarity. Detailed structural parameters are presented in Table 4. The crystal packing of Trz-D features π-π stacking interactions between bromobenzene groups of adjacent ligands, with a distance of 3.36 Å. Notably, no hydrogen bonds are observed in the crystal structure. This leads to a parallel, zigzag molecular network arrangement. The absence of hydrogen bond donors in Trz-D results in crystal packing primarily directed by weaker interactions, such as the observed π-π stacking.

Unveiling Novel Coordination Complexes with Transition Metals

Table IV.4 Bond lengths and angles of the Trz-D ligand

| Bond lengths (Å)		Bond angles (°)	
N(3)-C(11)	1.339(5)	C(11)-N(3)-C(2)	104.5(3)
N(3)-C(2)	1.347(5)	C(11)-N(3)-N(2)	122.2(3)
N(3)-N(2)	1.407(4)	N(2)-C(3)-C(4)	121.4(3)
N(2)-C(3)	1.264(5)	C(2)-N(3)-N(2)	133.1(3)
C(3)-C(4)	1.463(5)	C(3)-N(2)-N(3)	116.6(3)
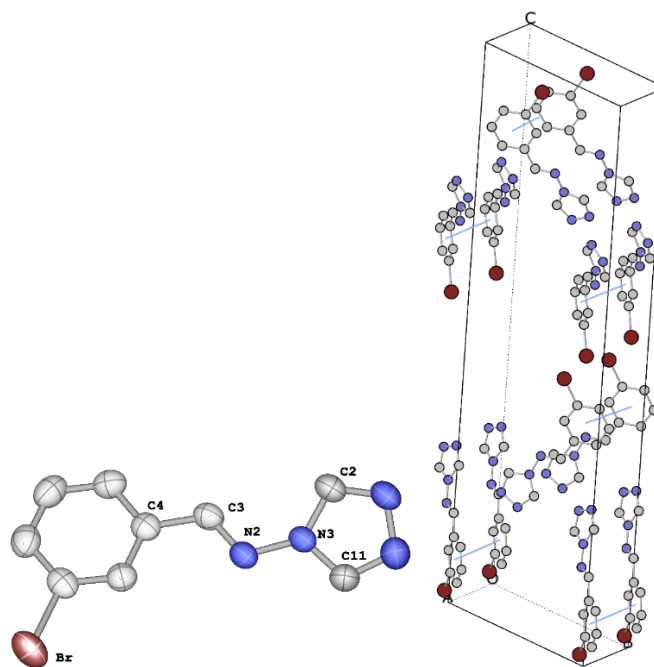
Figure IV.4 ORTEP view of the Ligand Trz-D with partial atom numbering. The ellipsoids contain 50% of the electron density (left). Main intermolecular interactions related to crystal packing, with π-π Stacking interactions are represented in blue lines (right). Hydrogen atoms are not included for clarity.

IV.2.1.5 The ligand 1-p-tolyl-N-(4H-1,2,4-triazol-4-yl)methanimine (Trz-E)

The Trz-E ligand crystallizes into white crystals from a water/acetonitrile mixture. Single-crystal X-ray diffraction analysis reveals a trigonal crystal system with space group R$\bar{3}$. The molecule exhibits near-planarity, as shown by the C12-N2-N1-C6 dihedral angle of -176.6(2)°, indicating minimal deviation from a flat structure. Crystal packing of Trz-E is characterized by

CH⋯N interactions between the terminal nitrogen of one ligand and either the triazole or toluene moieties of neighboring molecules. These interactions play a crucial role in determining the overall crystal structure. Table 5 provides a comprehensive list of key structural parameters, including characteristic bond lengths and angles for the Trz-E ligand. The lack of strong, directional hydrogen bonding interactions results in a more disordered molecular arrangement within the crystal structure. This absence of hydrogen bonds allows for greater flexibility in molecular positioning, leading to a less predictable and more complex packing pattern. The crystal structure is thus primarily governed by weaker, non-directional forces, which contribute to the observed irregular distribution of Trz-E molecules throughout the lattice.
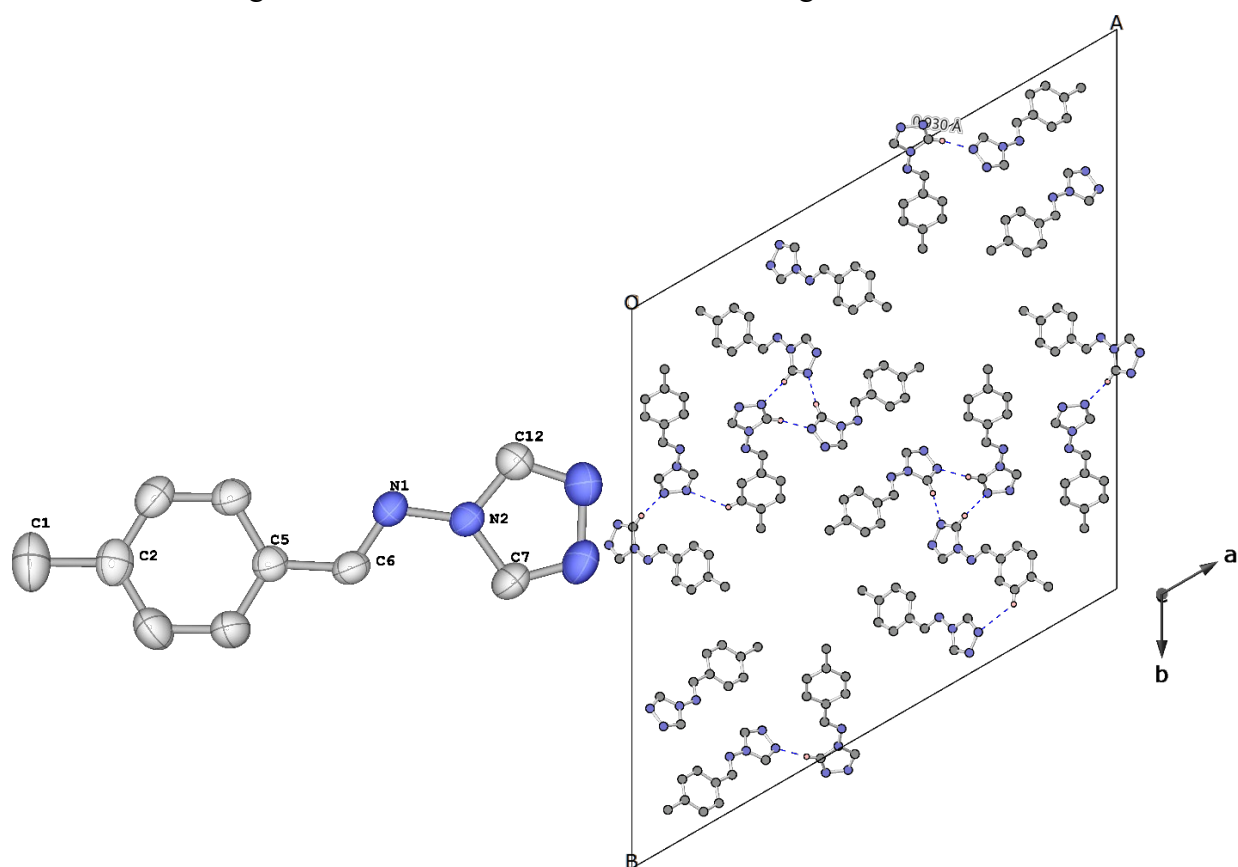
Figure IV.5 ORTEP view of the Ligand Trz-E with partial atom numbering. The ellipsoids contain 50% of the electron density (left). Main intermolecular interactions related to crystal packing view along the c-axis, with C-H⋯X interactions shown in blue dotted lines (right). Hydrogen atoms are not included for clarity, except for those participating in C-H⋯X interactions, which are represented by small spheres.

Table IV.5 Bond lengths and angles of the Trz-E ligand

Bond lengths (Å)		Bond angles (°)	
N(2)-C(7)	1.363(3)	C(12)-N(2)-C(7)	104.89(18)
N(2)-C(12)	1.352(3)	C(12)-N(2)-N(1)	122.02(18)
N(1)-N(2)	1.396(2)	C(7)-N(2)-N(1)	133.09(19)
N(1)-C(6)	1.273(3)	N(1)-C(6)-C(5)	120.90(19)
C(6)-C(5)	1.461(3)	C(6)-N(1)-N(2)	116.06(17)

IV.3 Coordination Chemistry: Preparation of Transition Metal Complexes Co (II), Ni (II), Fe (II) and Cu (II)

IV.3.1 Mononuclear Cu (II) Complexes

a. Compound [Cu(Trz-A)₂(NCS)₂]

The compound [Cu(Trz-A)$_2$(NCS)$_2$] abbreviated as **C1** was synthesized using a slow diffusion method. The complex C1 was prepared by adding Copper(II) chloride to a methanol solution containing two equivalents of the Trz-A ligand and two equivalents of potassium thiocyanate (KNCS) at room temperature. This reaction initially produced a green solution. After evaporation and recrystallization via slow diffusion of diethyl ether into an acetonitrile solution, dark green crystals of C1 were obtained with a yield of 28% (based on isolated crystals).
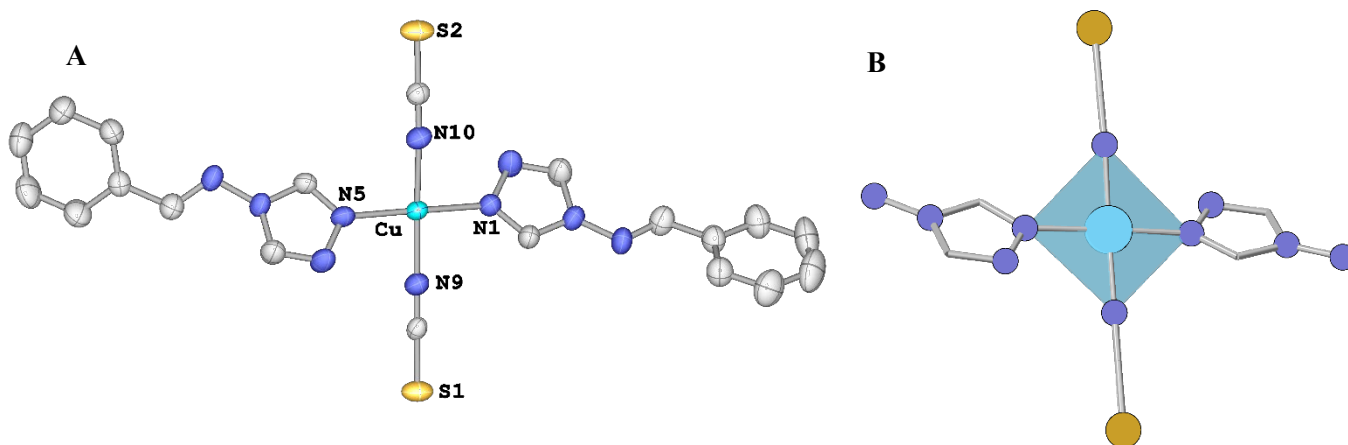
Figure IV.6 ORTEP view of complex **C1** with partial atom numbering (A) and its simplified structure (B). The ellipsoids contain 50% of the electron density (left). Hydrogen atoms are not included for clarity.

The complex C1 crystallizes in the Monoclinic P2₁ system, forming dark green crystals. The asymmetric unit of this compound is shown in figure 7. The structure reveals that the Cu(II) ion is surrounded by two monodentate ligands (Trz-A) and two thiocyanate anions [NCS]⁻, forming a square planar geometry with N(1)-Cu(1)-N(5) and N(9)-Cu(1)-N(10) angles of 178.3(2)° and 175.8(2)°, respectively. The packing exhibits weak CH···S interactions involving the sulfur of the thiocyanate and the aromatic ring and/or the central carbon of another ligand from adjacent complexes, as well as C-H···N interactions between the aromatic ring and the central nitrogen of the ligand from adjacent complexes. The bond lengths and angles around the Cu(II) ion are summarized in table 6.

Table IV.6 Bond lengths and angles of the C1 complex

Bond lengths (Å)		Bond angles (°)	
Cu(1)-N(5)	2.015(5)	N(9)-Cu(1)-N(10)	175.8(2)
Cu(1)-N(1)	2.015(5)	N(9)-Cu(1)-N(1)	89.15(19)
Cu(1)-N(10)	1.949(5)	N(10)-Cu(1)-N(1)	90.92(19)
Cu(1)-N(9)	1.939(5)	N(9)-Cu(1)-N(5)	89.90(19)
		N(10)-Cu(1)-N(5)	90.1(2)
		N(1)-Cu(1)-N(5)	178.3(2)

Starting from the assumption that the formation of a binuclear or polynuclear Cu(II) complex with the Trz-A ligand was possible, numerous reaction conditions were tested with the aim of obtaining the binuclear or polynuclear complex. Parameters such as stoichiometry, starting metal salts, temperatures (25 to 80°C), and solvents (MeOH, EtOH, Acetone, DMF, CH₂Cl₂, CH₃CN) were varied. For each sample, several recrystallization conditions and methods were tested, including liquid-liquid diffusion, gas-phase diffusion, slow evaporation, and solvothermal methods. Despite these sustained synthetic efforts, no reaction conditions allowed for the isolation of the targeted binuclear or polynuclear complex. The only species that crystallized were the mononuclear complexes described above. The inability to obtain the desired polynuclear complexes is likely attributed to their inherent instability in solution, leading to reversible dissociation during recrystallization, as supported by previous research [6-10]. This suggests that while the formation of binuclear or polynuclear species might be possible, they are not stable enough to be isolated under the tested conditions.
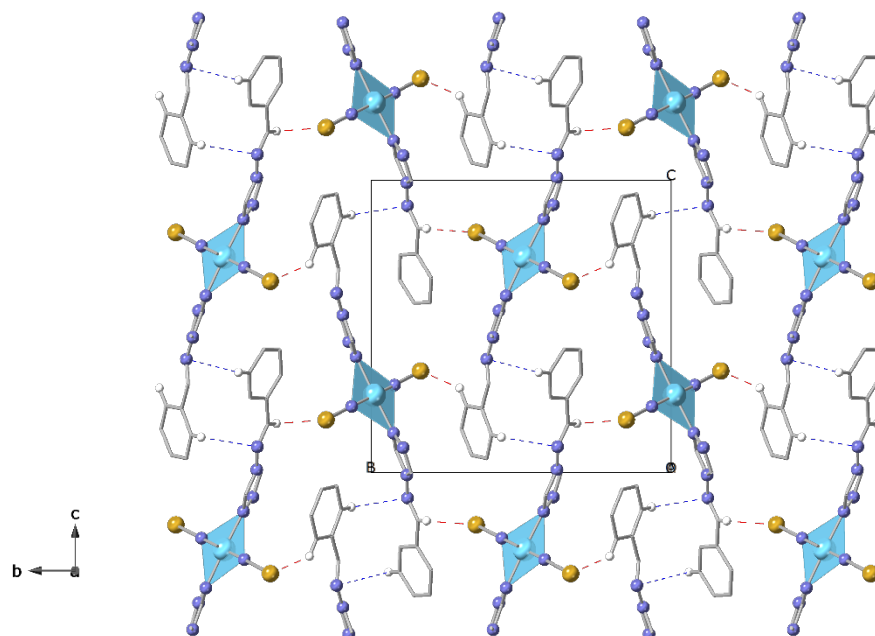
Figure IV.7 Crystal packing of C1, highlighting intermolecular interactions: C-H···S interactions (red dashed lines) and CH···N interactions (blue dashed lines), View along the a-axis.

IV.3.2 Structural Properties of Binuclear Complexes of Ni(II), Co(II), and Fe(II)

IV.3.2.1 Ligand Trz-D

Three metal-organic complexes, $[Co_2(Trz-D)_5(NCS)_4]\cdot DMF$ (C2), $[Fe_2(Trz-D)_5(NCS)_4]\cdot DMF$ (C3), and $[Ni_2(Trz-D)_5(NCS)_4]\cdot DMF$ (C4), were synthesized via a slow diffusion method. The synthesis involved reacting two equivalents of the Trz-A ligand and two equivalents of potassium thiocyanate (KNCS) with the respective metal salts ($CoCl_2$, $FeCl_2$, and $NiCl_2$) in methanol at room temperature. The initial reaction mixtures exhibited bright pink, deep red, and purple colors for C2, C3, and C4, respectively. Following evaporation and recrystallization via slow diffusion of diethyl ether into a DMF solution, red pink (C2), dark red (C3), and purple (C4) crystals were obtained. The yield for all three compounds was 23%, based on isolated crystals.

The coordination chemistry of the Trz-D ligand proved to be remarkably similar for metals such as Co(II), Fe(II), and Ni(II). Furthermore, the complexes formed with these metals exhibited only very minor structural differences from one another. The relevant bond distances and angles for complexes C2-4 are presented in Table 7. These complexes all crystallize in the centrosymmetric monoclinic space group C2/c. Their structure reveals two crystallographically

independent metal(II) ions (Co^{2+}, Fe^{2+} and Ni^{2+}), each coordinated to two thiocyanate [NCS]$^-$ anions, one terminal monodentate Trz-D ligand, and three bridging bidentate Trz-D ligands. These bridging ligands connect the metal(II) ions, forming a binuclear compound. A free DMF molecule completes the coordination sphere.
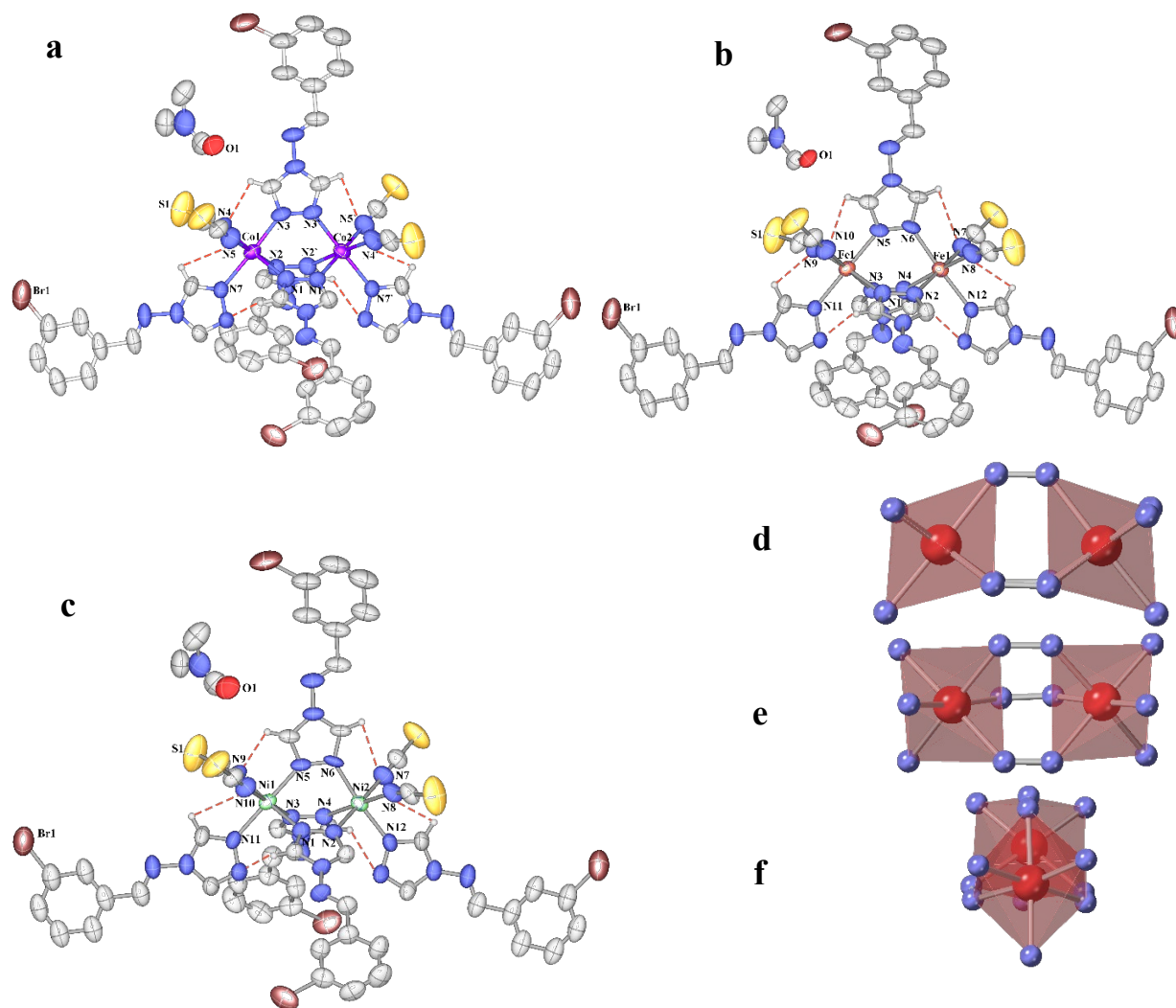
Figure IV.8 ORTEP view of C2, C3 and C4 with partial atom numbering (a,b and c). Hydrogen atoms are omitted for clarity, except for those represented by small spheres participating in the intramolecular C-H···N interactions (red dashed lines). The ellipsoids contain 50% of the electron density. Views along the μN4→μN2 axis (d), Mital1→μN10 axis (e) and Mital1→Mital2 axis (C) showing the distortion of the two octahedral geometries around the metal ions.

The ligand arrangement is symmetric, with both metal ions exhibiting identical coordination with nitrogen atoms. The coordination spheres of the metal ions are related by C_2 symmetry and adopt a slightly distorted octahedral geometry, primarily in the N4-M-N1 bonds with an angle of 173.68° (Figure 8). The ligands arrangement is stabilized by six weak intramolecular C-H···N interactions, with H···N distances between hydrogen and the nitrogen of the (NCS)- anion is 2.984 Å and 3.179 Å for the distance between hydrogen and the nitrogen of the Trz-D ligand. The coordination environment of the metal centers in compounds C2, C3, and C4 exhibits interesting structural features. The average metal-nitrogen (M-N) bond length of 2.14 Å is consistent with high-spin metal(II) ions (Co^{2+} and Fe^{2+}), as reported in previous studies [11-13].
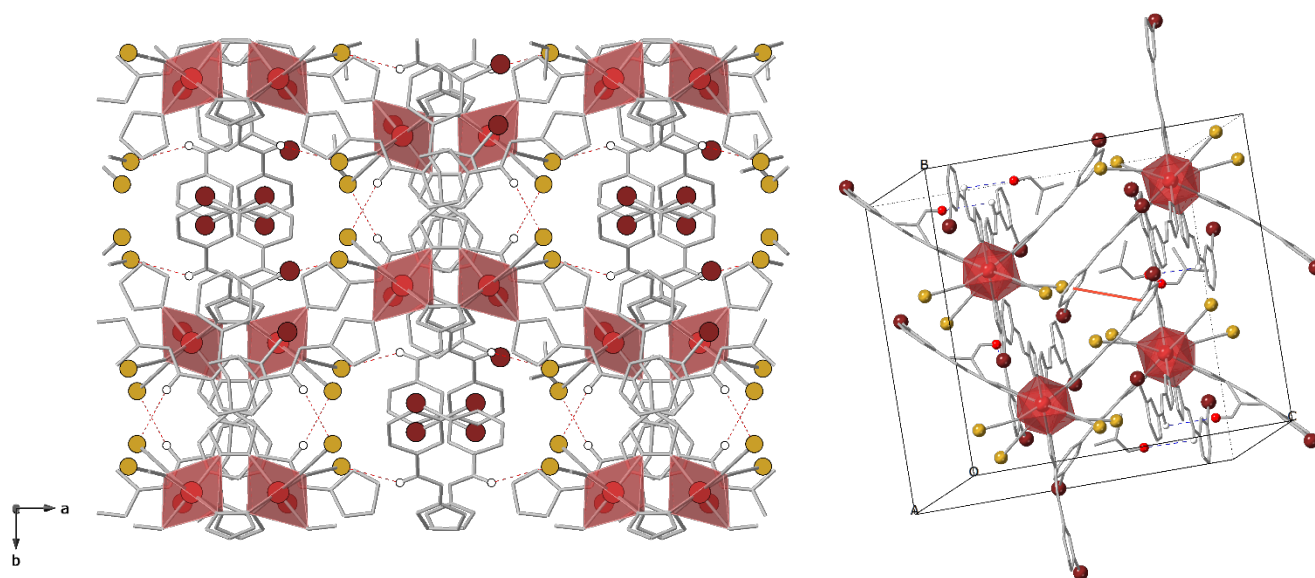
Figure IV.9 Crystal packing of C3: View along the c-axis showing intermolecular C-H···S interactions (red dashed lines) (left), π-π Stacking and C-H···O interactions are represented in red lines and blue dashed lines respectively (right).

However, the coordination sphere shows slight distortion from ideal octahedral geometry. This distortion is primarily due to the presence of two notably shorter M-N bonds involving the thiocyanate anions, measuring 2.095 and 2.080 Å for C2, 2.126 and 2.107 Å for C3 and for C4 measuring 2.065 and 2.045 Å. These shorter bonds contrast with the longer M-N bonds to the other Trz-D ligands. The overall charge neutrality of the complexes is maintained by the presence of four thiocyanate [NCS]⁻ anions per binuclear unit. This arrangement balances the

positive charges of the two metal(II) ions, resulting in electrically neutral coordination compounds. The minimal distance between the metallic centers Co···Co, Fe···Fe, and Ni···Ni in complexes C2, C3, and C4 is on the order of 3.936, 4.024, and 3.828 Å respectively.

Since C1 lacks classical hydrogen bond donors, the crystal packing is directed by weaker intermolecular interactions such as C-H···X and π-π interactions (Figure 9). The π-π network consists of phenyl groups from the ligands facing each other at a distance of 4.102 Å with a slight shift of 1.02 Å. C-H···O interactions involving the oxygen of DMF and the hydrogen of the central carbon of the Trz-D ligand are also observed, with a C-H···O distance of 3.043 Å. Additionally, C-H···S interactions exist between the sulfur of the thiocyanate and the central carbon of a Trz-D ligand from adjacent complexes, with H···S distance of 2.86 Å.

IV.3.2.2 Ligand Trz-E

a. Solid-state structure of a Co (II) complex

The compound $[Co_2(Trz-E)_5(NCS)_4]$, abbreviated as C5, was synthesized using a slow diffusion method. The synthesis involved adding Cobalt(II) chloride to a methanol solution containing two equivalents each of the Trz-E ligand and potassium thiocyanate (KNCS) at room temperature, initially producing a bright pink solution. After evaporation and recrystallization via slow diffusion of diethyl ether into an acetonitrile solution, red pink crystals of C5 were obtained with a yield of 25%, based on the isolated crystals. The complex C5 crystallizes in the Triclinic P$\bar{1}$ system. The asymmetric unit of this compound is shown in figure 10. The structure reveals two crystallographically independent Co(II) ions, each coordinated to two thiocyanate [NCS]⁻ anions, one terminal monodentate Trz-E ligand and three bridging bidentate Trz-E ligands. These bridging ligands connect the Co(II) ions, forming a binuclear compound. The relevant bond distances and angles for this complex are presented in Table 8. The ligand arrangement is symmetric, with both metal ions exhibiting identical coordination with nitrogen atoms. The ligands arrangement is stabilized by four weak intramolecular C-H···N interactions, with H···N distances between hydrogen and the nitrogen of the [NCS]⁻ anion is 2.99 Å.
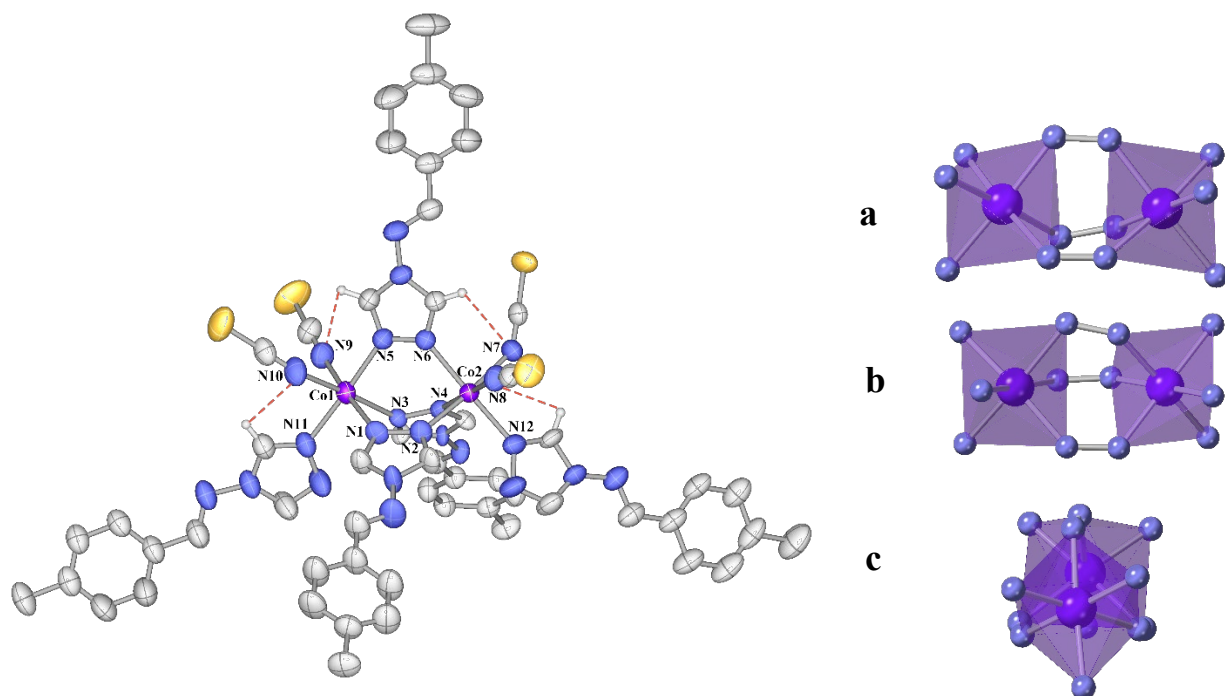
Figure IV.10 ORTEP view of C5 with partial atom numbering (left). Hydrogen atoms are omitted for clarity, except for those represented by small spheres participating in the intramolecular C-H···N interactions (red dashed lines). The ellipsoids contain 50% of the electron density. Views along the $\mu N2 \rightarrow \mu N4$ axis (a), $Co1 \rightarrow \mu N9$ axis (b) and $Co1 \rightarrow Co2$ axis (c) showing the distortion of the two octahedral geometries around the metal ions (right).

The coordination environment of the metal centers in compound C5 exhibits interesting structural features. The average Co-N bond length of 2.136 Å is consistent with a high-spin Co(II) ion. However, the coordination sphere slightly distorts from ideal octahedral geometry, primarily in the N4-Co-N1 bonds with an angle of 174.446° (Figure 10). This distortion is primarily due to the presence of two notably shorter Co-N bonds involving the thiocyanate anions, measuring 2.108 and 2.070 Å. These shorter bonds contrast with the longer Co-N bonds to the other Trz-E ligands. The overall charge neutrality of the complexes is maintained by the presence of four thiocyanate [NCS]⁻ anions per binuclear unit. This arrangement balances the positive charges of the two Co(II) ions, resulting in electrically neutral coordination compounds.
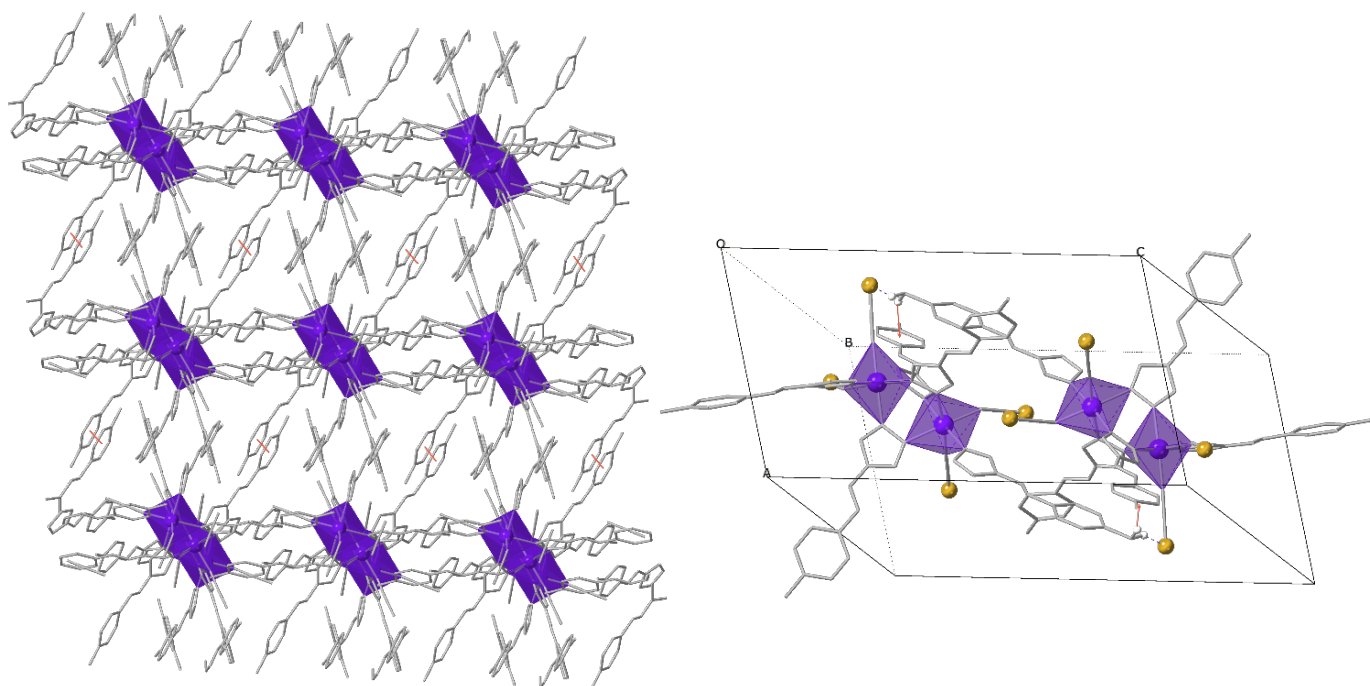
Figure IV.11 Crystal packing of C5: View along the c-axis showing intermolecular π-π interactions (red lines) (left), and C-H⋯S and C-H⋯π interactions are represented in blue dashed lines and red lines respectively (right).

The minimal distance between the metallic centers Co1⋯Co2 is on the order of 4.265 Å. The crystal packing is directed by weaker intermolecular interactions such as C-H⋯X, C-H⋯π and π-π interactions (Figure 11). The π-π network consists of aromatic ringes from the ligands facing each other at a distance of 1.412 Å with a slight shift of 0.492 Å. C-H⋯π interactions involving the hydrogen of the methyl group and the aromatic ring of the neighboring complexes are also observed, with a H⋯π distance of 1.828 Å. Additionally, C-H⋯S interactions exist between the sulfur of the thiocyanate and the hydrogen of the methyl group of Trz-E ligand from adjacent complexes, with H⋯S distance of 0.883 Å.

b. Solid-state structure of Ni (II) complex
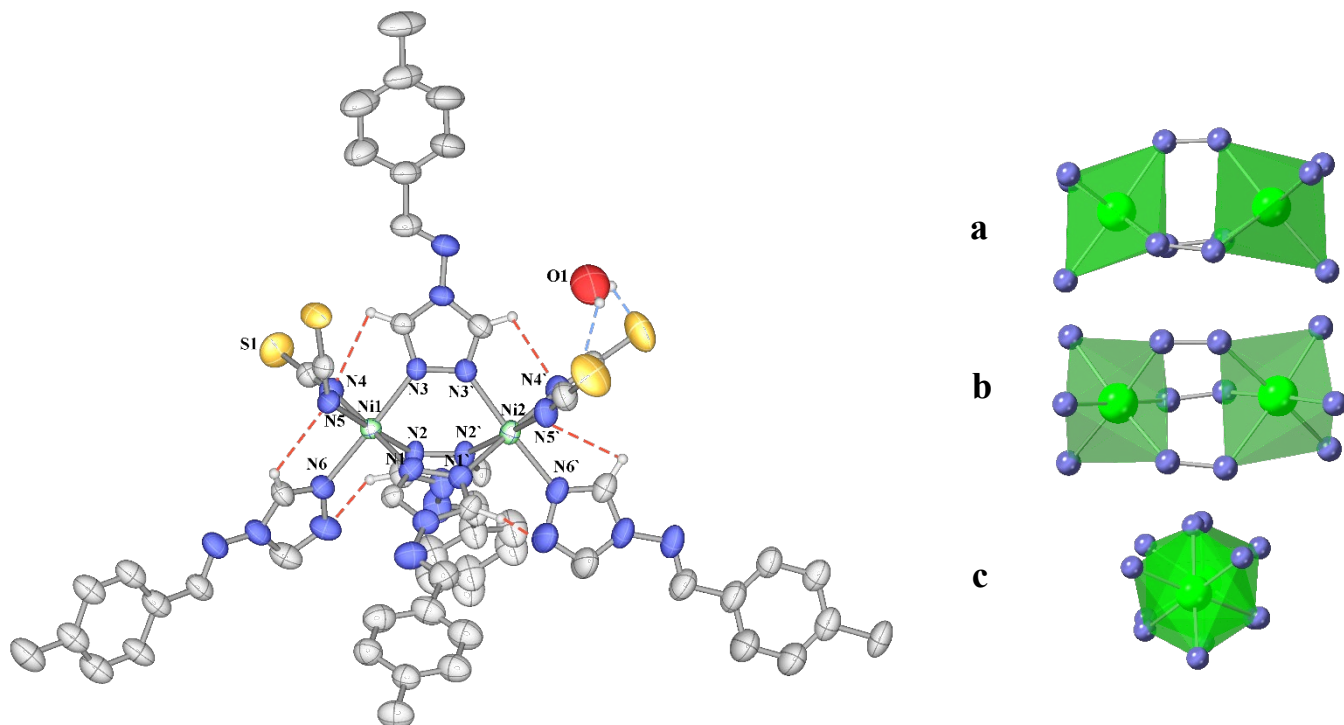
Figure IV.12 ORTEP view of C6 with partial atom numbering (left). Hydrogen atoms are omitted for clarity, except for those represented by small spheres participating in the intramolecular C-H⋯N interactions (red dashed lines) and O-H⋯S interactions (blue dashed lines). The ellipsoids contain 50% of the electron density. Views along the μN2→μN4 axis (a), Co1→μN9 axis (b) and Co1→Co2 axis (c) showing the distortion of the two octahedral geometries around the metal ions (right).

The compound $[Ni_2(Trz-E)_5(NCS)_4].H_2O$, abbreviated as C6, was synthesized using a slow diffusion method. The synthesis involved adding Nickel(II) chloride to a methanol solution containing two equivalents each of the Trz-E ligand and potassium thiocyanate (KNCS) at room temperature, initially producing a purple solution. After evaporation and recrystallization via slow diffusion of Ethanol into a Water solution, purple crystals of C6 were obtained with a yield of 24%, based on the isolated crystals. The complex C6 crystallizes in the Triclinic P$\bar{1}$ system.

The asymmetric unit of this compound is shown in figure 12. The structure reveals two crystallographically independent Ni(II) ions, each coordinated to two thiocyanate [NCS]⁻ anions, one terminal monodentate Trz-E ligand and three bridging bidentate Trz-E ligands. These bridging ligands connect the Ni(II) ions, forming a binuclear compound. A free H_2O molecule completes the coordination sphere.
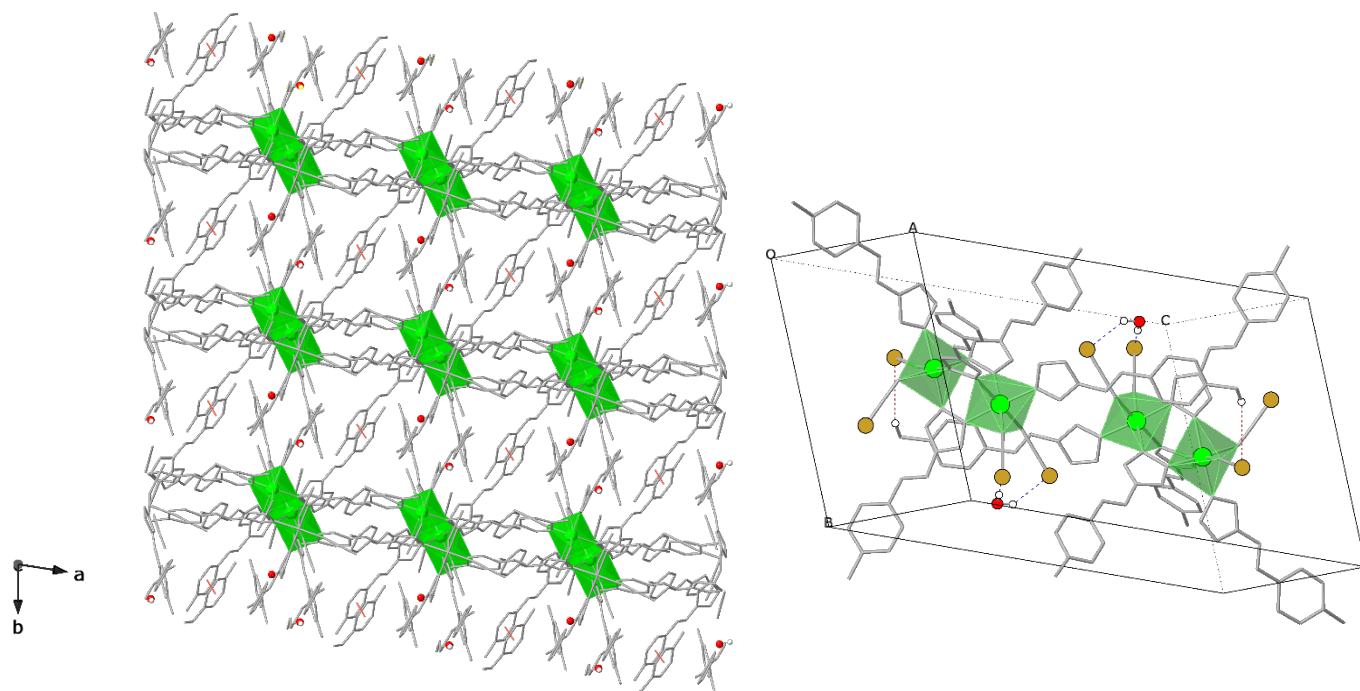
Figure IV.13 Crystal packing of C6: View along the c-axis showing intermolecular π-π interactions (red lines) (left), O-H···S and C-H···S interactions are represented in blue dashed lines and red lines respectively (right).

The relevant bond distances and angles for this complex are presented in Table 9. The ligand arrangement is symmetric, with both metal ions exhibiting identical coordination with nitrogen atoms. The arrangement of the C6 compounds is stabilized by hydrogen bonding O-H···S between a water molecule and sulfur atoms of thiocyanate anions and by six weak intramolecular C-H···N interactions, with H···N distances between hydrogen and the nitrogen of the [NCS]⁻ anion is 2.926 Å and 2.883 Å for the distance between hydrogen and the nitrogen of the Trz-E ligand.

The coordination environment of the metal centers in compound C6 exhibits interesting structural features. However, the coordination sphere slightly distorts from ideal octahedral geometry, primarily in the N2-Ni-N5 bonds with an angle of 175.554° (Figure 12). This distortion is primarily due to the presence of two notably shorter Ni-N bonds involving the thiocyanate anions, measuring 2.038 and 2.110 Å. These shorter bonds contrast with the longer Ni-N bonds to the other Trz-E ligands.

The overall charge neutrality of the complexes is maintained by the presence of four thiocyanate [NCS]$^-$ anions per binuclear unit. This arrangement balances the positive charges of the two Ni(II) ions, resulting in electrically neutral coordination compounds. The minimal distance between the metallic centers Ni1···Ni2 is on the order of 3.837 Å. The crystal packing is directed by weaker intermolecular interactions such as C-H···X and π-π interactions (Figure 13). The π-π network consists of aromatic ringes from the ligands facing each other at a distance of 1.401 Å with a slight shift of 0.510 Å. C-H···S interactions exist between the sulfur of the thiocyanate and the hydrogen of the methyl group of Trz-E ligand from adjacent complexes, with H···S distance of 3.344 Å.

IV.3.2.3 Ligand Trz-A

a. Solid-state structure of a Co (II) complex

The binuclear compound [Co$_2$(Trz-A)$_5$(NCS)$_4$]·H$_2$O·EtOH, designated as C7, was synthesized via a slow diffusion method. This process involved reacting Cobalt(II) chloride with a methanol solution containing equimolar amounts of Trz-A ligand and potassium thiocyanate (KNCS) at ambient temperature, initially yielding a bright pink solution. Subsequent evaporation and recrystallization through slow diffusion of ethanol into an aqueous solution produced red pink crystals of C7 with a 22% yield. C7 crystallizes in the triclinic P$\bar{1}$ system, with its asymmetric unit illustrated in Figure 14. The structure comprises two crystallographically distinct Co(II) ions, each coordinated to six nitrogen atoms: two from thiocyanate [NCS]$^-$ anions, one from a terminal monodentate Trz-A ligand, and three from bridging bidentate Trz-A ligands. These bridging ligands facilitate the formation of the binuclear complex, with free H$_2$O and EtOH molecules completing the coordination sphere.
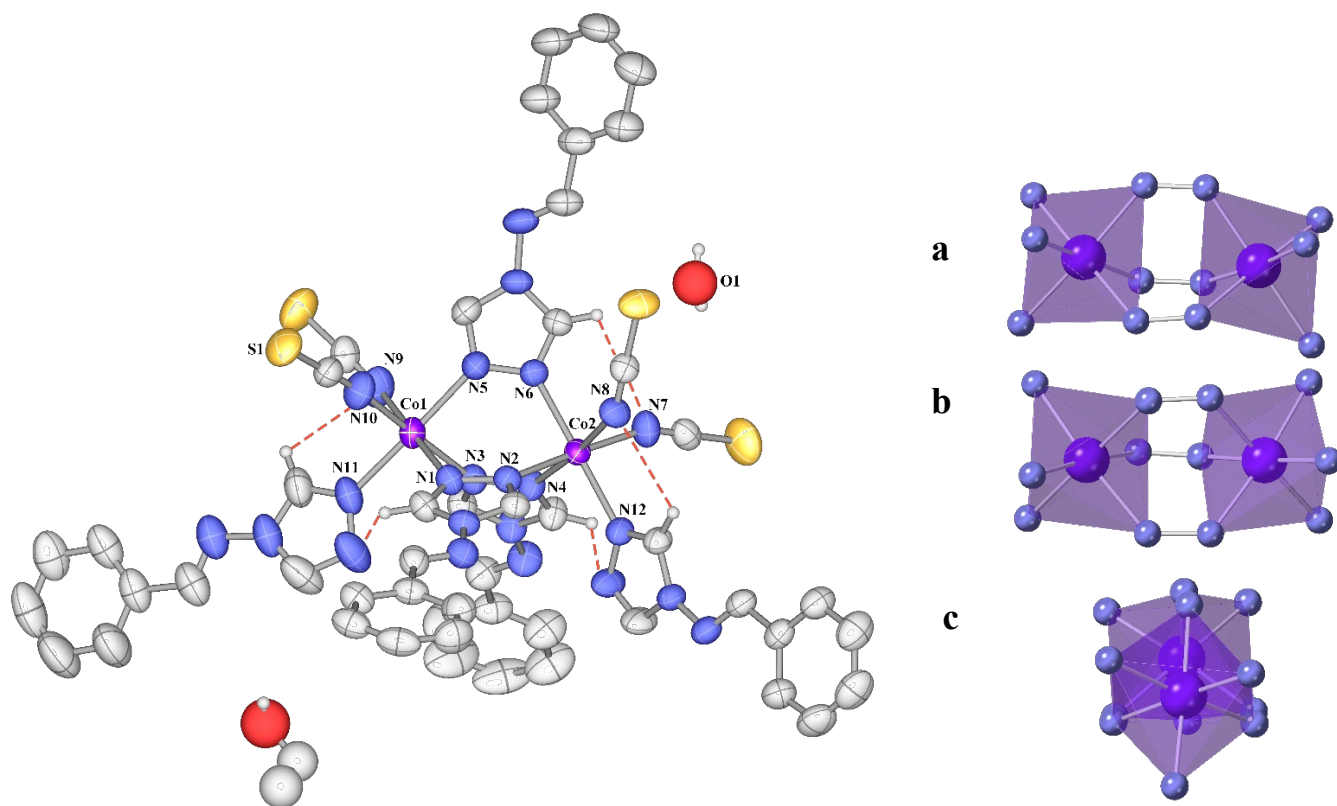
Figure IV.14 ORTEP view of C7 with partial atom numbering (left). Hydrogen atoms are omitted for clarity, except for those represented by small spheres participating in the intramolecular C-H···N interactions (red dotted lines). Views along the μN2→μN4 axis (A), Co1→μN9 axis (B) and Co1→Co2 axis (C) showing the distortion of the two octahedral geometries around the metal ions (right).

The symmetric arrangement of ligands results in identical nitrogen coordination for both metal ions. This configuration is stabilized by five weak intramolecular C-H···N interactions, with H···N distances of 3.399 Å to the [NCS]⁻ anion's nitrogen and 2.938 Å to the Trz-A ligand's nitrogen. Table 10 presents the most relevant bond distances and angles for this complex, providing detailed insight into its molecular structure. The metal centers in compound C7 display noteworthy structural characteristics in their coordination environment. The Co(II) ions exhibit an average Co-N bond length of 2.131 Å, indicative of a high-spin state. However, the octahedral

geometry around the cobalt centers shows subtle deviations from ideality. This distortion is most pronounced in the N5-Co-N2 angle, which measures 174.553°, deviating from the expected 180° in a perfect octahedron (Figure 14).
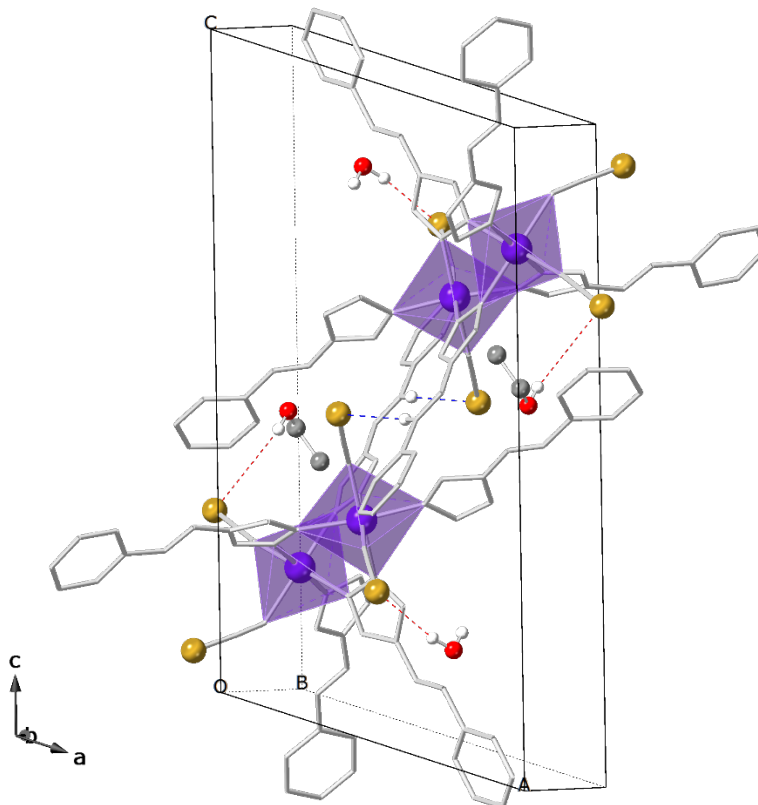
Figure IV.15 Crystal packing of C7, View along the c-axis showing intermolecular O-H···S hydrogen bonding (red dashed lines), and C-H···S interactions are represented in blue dashed lines.

The distortion is further emphasized by the presence of two distinctly shorter Co-N bonds involving the thiocyanate anions. These bonds measure 2.098 Å and 2.083 Å, respectively, and stand in contrast to the longer Co-N bonds formed with the Trz-A ligands. This variation in bond lengths contributes to the overall distortion of the octahedron, resulting in a unique electronic and geometric environment around the Co(II) centers. The binuclear complex C7 maintains electrical neutrality through a balanced arrangement of charged components. Four thiocyanate [NCS]⁻ anions counterbalance the positive charges of the two Co(II) ions in each binuclear unit, resulting in a net neutral coordination compound. The structure's binuclear nature is evidenced

by the proximity of the cobalt centers, with a Co1···Co2 distance of 3.922 Å. Intermolecular interactions, particularly hydrogen bonding, significantly influence the crystal packing of C7. As illustrated in Figure 15, O-H···S hydrogen bonds form between the oxygen atoms of water and ethanol molecules and the sulfur atoms of thiocyanate anions with H···S distances of 2.626 and 3.333 Å respectively.

b. Solid-state structure of a Ni (II) complex

The binuclear compound [Ni$_2$(Trz-E)$_5$(NCS)$_4$]·H$_2$O, designated as C8, was synthesized via a slow diffusion method. This process involved reacting Nickel(II) chloride with a methanol solution containing equimolar amounts of Trz-A ligand and potassium thiocyanate (KNCS) at ambient temperature, initially yielding a purple solution. Subsequent evaporation and recrystallization through slow diffusion of ethanol into an aqueous solution produced purple crystals of C7 with a 25% yield. C7 crystallizes in the triclinic P$\bar{1}$ system, with its asymmetric unit illustrated in Figure 16. The structure comprises two crystallographically distinct Ni(II) ions, each coordinated to six nitrogen atoms: two from thiocyanate [NCS]$^-$ anions, one from a terminal monodentate Trz-A ligand, and three from bridging bidentate Trz-A ligands. These bridging ligands facilitate the formation of the binuclear complex, with a free H$_2$O molecule completing the coordination sphere.

The symmetric arrangement of ligands results in identical nitrogen coordination for both metal ions. This configuration is stabilized by six weak intramolecular C-H···N interactions, with H···N distances of 3.072 Å to the [NCS]$^-$ anion's nitrogen and 2.934 Å to the Trz-A ligand's nitrogen. Table 11 presents the most relevant bond distances and angles for this complex, providing detailed insight into its molecular structure. The metal centers in compound C7 display noteworthy structural characteristics in their coordination environment. The octahedral geometry around the Nickel centers shows subtle deviations from ideality. This distortion is most pronounced in the N4-Co-N1 angle, which measures 174.714°, deviati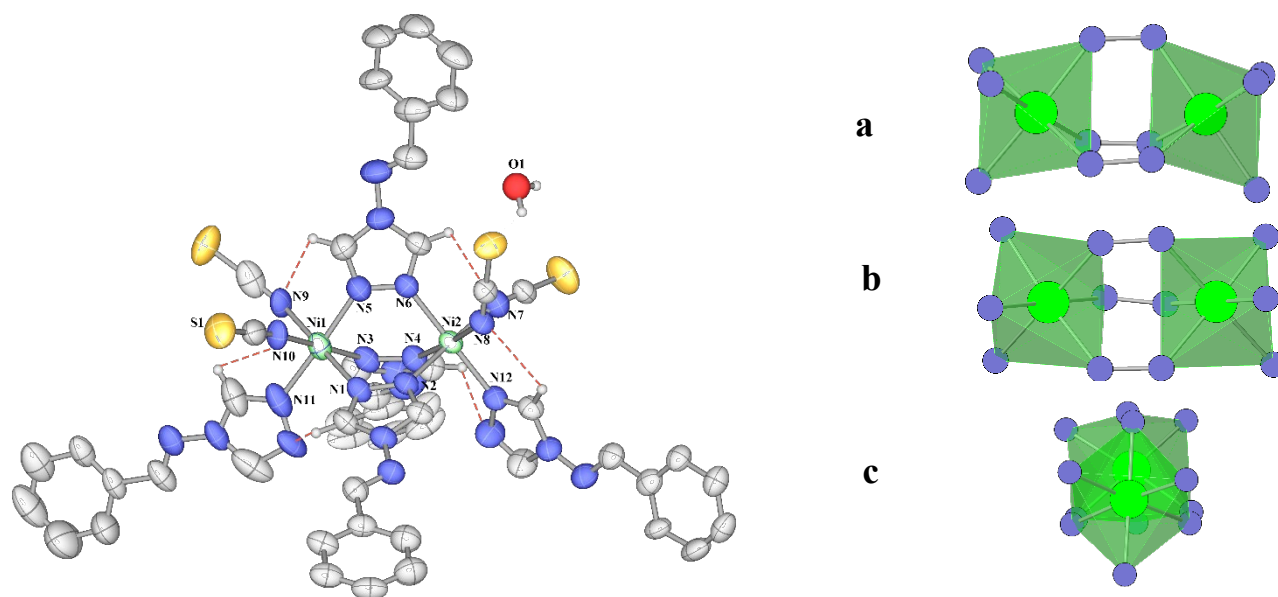ng from the expected 180° in a perfect octahedron (Figure 16). The distortion is further emphasized by the presence of two distinctly shorter Ni-N bonds involving the thiocyanate anions. These bonds measure 2.037 Å and 2.087 Å, respectively, and stand in contrast to the longer Ni-N bonds formed with the Trz-A ligands.

Figure IV.16 ORTEP view of C8 with partial atom numbering (left). Hydrogen atoms are omitted for clarity, except for those represented by small spheres participating in the intramolecular C-H···N interactions (red dotted lines). Views along the μN2→μN4 axis (A), Ni1→μN9 axis (B) and Ni1→Ni2 axis (C) showing the distortion of the two octahedral geometries around the metal ions (right).

This variation in bond lengths contributes to the overall distortion of the octahedron, resulting in a unique electronic and geometric environment around the Ni(II) centers. The binuclear complex C8 maintains electrical neutrality through a balanced arrangement of charged components. Four thiocyanate [NCS]⁻ anions counterbalance the positive charges of the two Ni(II) ions in each binuclear unit, resulting in a net neutral coordination compound. The structure's binuclear nature is evidenced by the proximity of the cobalt centers, with a Ni1···Ni2 distance of 3.821 Å.

Intermolecular interactions, particularly hydrogen bonding, significantly influence the crystal packing of C8. As illustrated in Figure VI.17, O-H···S hydrogen bonds form between the oxygen atoms of water molecule and the sulfur atoms of thiocyanate anions with H···S distances of 3.544 Å.
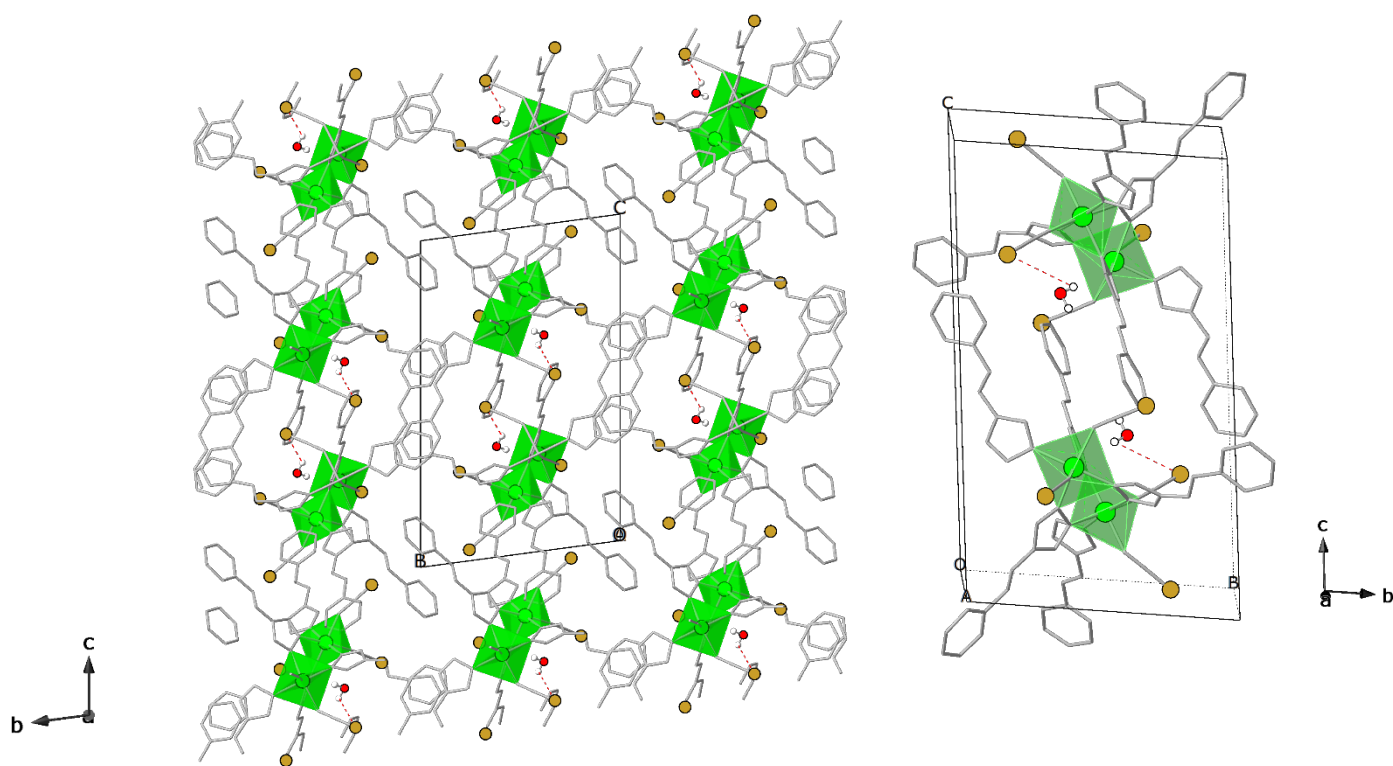
Figure IV.17 Crystal packing of C8: View along the c-axis showing intermolecular O-H···S hydrogen bonding (red dashed lines).

IV.3.3 Coordination Polymers of Cu(II) and Co(II) Complexes

IV.3.3.1 One-Dimensional Coordination Polymer of the Complex [Co(dca)$_4$(Trz-E)$_2$].MeOH

The complex [Co(dca)$_4$(Trz-E)$_2$].MeOH, abbreviated as C9, crystallizes as a one-dimensional coordination polymer in the triclinic P-1 space group. The structure's fundamental unit comprises a cobalt center (Co1) with an octahedral coordination environment. This environment is composed of two terminal monodentate Trz-E ligands, and four bridging bidentate dicyanamide (dca) anions. Notably, the methanol molecule in the formula is not coordinated to the cobalt center but exists as a solvate molecule within the crystal lattice.

The binding mode of the ligands plays a crucial role in defining the structure's extended network. The Trz-E ligands coordinate to the Co1 atom through the nitrogen of their triazole group, serving as terminal ligands. In contrast, the dicyanamide anions act as bridging ligands, connecting adjacent cobalt centers.
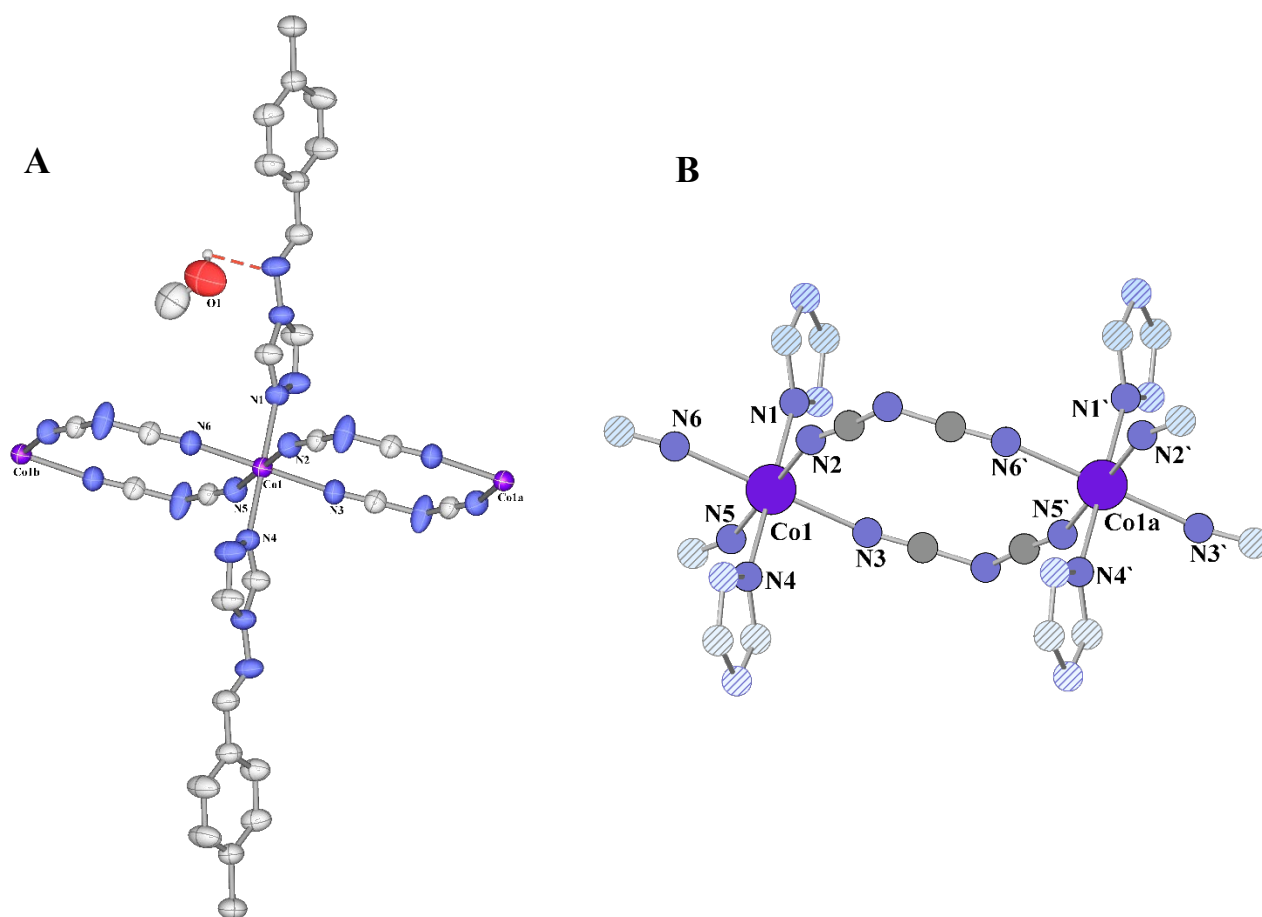
Figure IV.18 presents two views of the complex C9 structure: (A) An ORTEP diagram showing the Trz-E ligand complexation, with selected atoms labeled. (B) A simplified representation of the coordination spheres around Co1 and Co1a. In view B, only the coordinating atoms are shown in detail, while a hatched sphere represents the remainder of the ligand. Red dotted lines indicate hydrogen bonds. All thermal ellipsoids are drawn at the 50% probability level.

This arrangement of ligands results in the formation of a one-dimensional network that propagates perpendicular to the crystallographic a-axis. It's noteworthy that the cobalt centers are linked exclusively through these dicyanamide bridges, with the Trz-E ligands remaining terminal. The ligand structure shows an intramolecular hydrogen bond between the methanol and the central nitrogen atom of the Trz-E ligand. The structural details of this complex, including specific bond distances, are provided in Table 12.
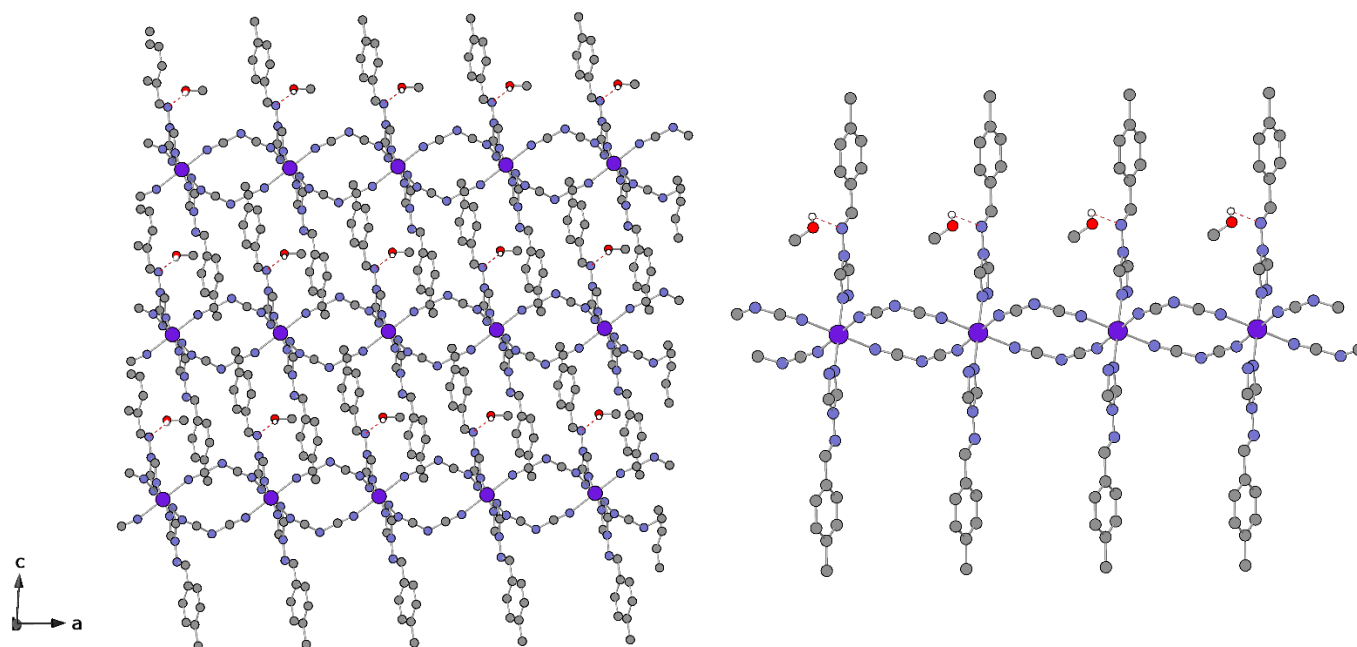
Figure IV.19 illustrates two aspects of the C9 compound: Left: The packing arrangement of C9 molecules viewed along the ac plane. Right: A representation of the 1-D coordination network formed by C9 in the ac planes, highlighting the extended structure of the compound. The atoms are color-coded as follows: Cobalt (purple), Oxygen (red), Nitrogen (blue), Carbon (gray), and Hydrogen (white).

These coordination networks are arranged in the packing via the formation of hydrogen bonds including an uncoordinated methanol molecule per unit cell as well as the dicyanamide molecules carried by the cobalt and the Trz-E ligands.

IV.3.3.2 Two-Dimensional Coordination Polymers of Cu(II) Complexes
a.   Cu(II) complex with the ligand 1,10-phenanthroline-5,6-dione

All used chemicals were reagent grade, procured from commercial sources, and used without purification. The solvents were purified by standard procedures.

$CuSO_4 \cdot 5H_2O$ (25 mg, 0.1 mmol), 1,10-phenanthroline-5,6-dione (21 mg, 0.1 mmol) and Nadca (18 mg, 0.2 mmol) were dissolved in 20 mL of H_2O/DMF (v/v, 3:1) and then the solution was

sealed in a 25 mL Teflon reactor and kept under autogenous pressure at 403 K for 2 days. After cooling to room temperature at a rate of 10 Kh^{-1}, green crystals of compound 1 were obtained (yield 44%).

In the structure of *catena*-poly[bis(dicyanamido)(1,10-phenanthroline-5,6-dione)copper(II)], [Cu(dca)$_2$(C$_{12}$H$_6$N$_2$O$_2$)], abbreviated as C10, the Cu center adopts the usual (4+2) coordination (Figure 21): the four equatorial Cu-N distances are clustered around 2.0 Å, while the axial distances are both in excess of 2.5 Å (Table 13). Two differently bridged dca ligand are present. Two of the equatorial sites are occupied by a pair of inversion-related dicyanamid ligands which are coordinated via the terminal N atoms, thus generating an eight-membered ring (Figure 21); such 8 membered rings, as schematically shown in Figure 20, are known in the literature, and a CSD search (2023) has shown over 20 structures with a variety of metal ions [14]. The other two equatorial sites are occupied by the bidentate 1,10-phenanthroline-5,6-dione, coordinated via the N atoms. By contrast, the second dicyanamido ligand which bridges two Cu centers related by translation along [001], in each case via one of the axial sites (Figure 21), but now both the central N atom and one of the terminal N atoms are involved. This binding mode is rare and in combination with the other mode even unprecedented to the best of our knowledge.
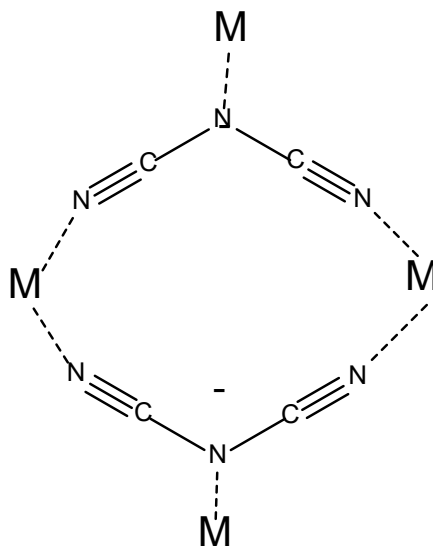
Figure IV.20 Binding sites for metal ions on the dicyanamide anion, dca
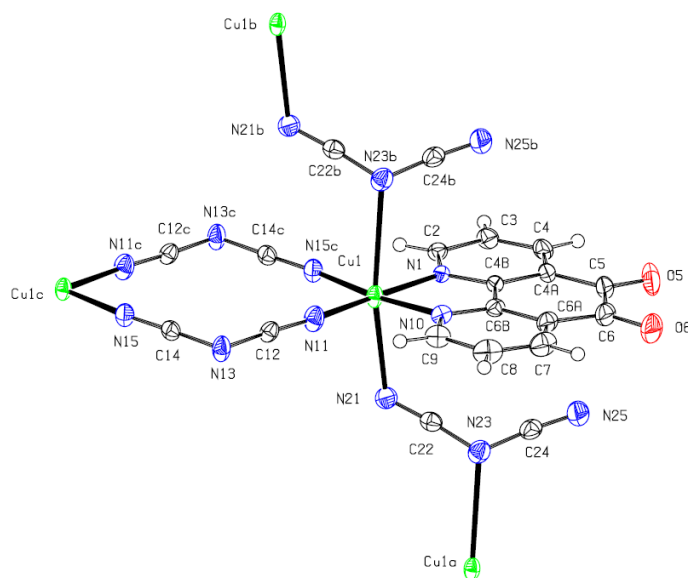
Figure IV.21 The structure of the compound C10 shows the different coordination modes of the two dicyanamido ligands. Displacement ellipsoids are drawn at the 50% probability level and the atoms marked with 'a', 'b' or 'c' are at the symmetry positions (x, y, -1 + z), (x, y, 1+ z) and (1 - x, 1 - y, 1 - z), respectively.

The resulting coordination polymer takes the form of a ribbon ladder of spiro-fused rings, in which 12-membered rings centered at (0.5, 0.5, 0.5 + n) alternated with 20-membered rings centered at (0.5, 0.5, n), where n represents an integer in each case (Figure 22). Within the ribbon, the shortest Cu$\cdots$Cu distance along the chain is 6.661(3) Å, while that across the 12-membered ring is 7.063(3) Å. Hence, there are two distinct modes of binding for the two independent biscyanamide ligands: one forms double bridges between two metal centers, with each using the two terminal N atoms, while the other employs one terminal N atom and the central amidic N atom: the involvement of the central N is unusual although not hitherto unknown [15].

Table IV.13 Cu-N distances (Å).

Cu-N1	1.9936 (12)	Cu-N10	2.0103 (13)
Cu-N11	1.9545 (15)	Cu-N15^i	1.9606 (14)
Cu-N21	2.5094 (13)	Cu-N23^{ii}	2.7359 (14)

Symmetry codes: (i) 1 - x, 1 - y, 1- z ; (ii) x, y, 1 + z

There are two short intermolecular contacts involving C-H bonds (Table 14, Figure 22), but both exhibit C-H⋯X (X = N or O) angles less than 140°, and so cannot be regarded as being structurally significant [16].

Table IV.14 Hydrogen-bond geometry (Å, °)

D-H⋯A	D-H	H⋯A	D⋯A	D-H⋯A
C3-H3⋯N21ⁱⁱⁱ	0.95	2.54	3.312 (2)	139
C8-H8⋯O5ⁱᵛ	0.95	2.36		

Symmetry codes: (iii) x-1, y, z; (iv) x+1, -y+3/2, z+1/2.
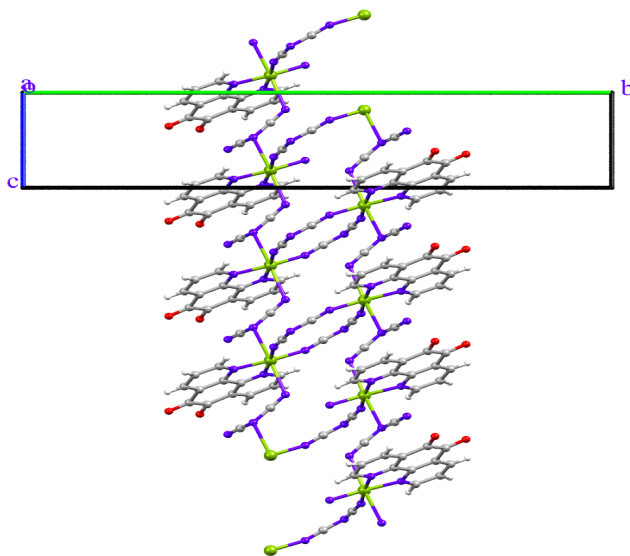
Figure IV.21 Part of the crystal structure showing the formation of a coordination polymer ribbon running parallel to [001].
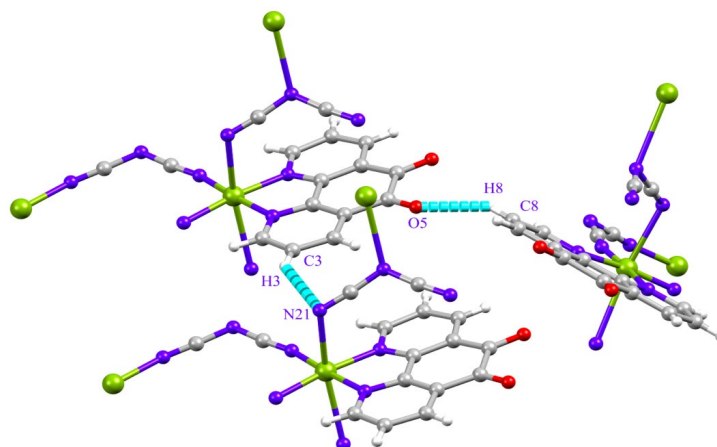
Figure IV.22 C-H⋯N and C-H⋯O hydrogen bond interactions in compound C10.

There are four short contacts between N or O atoms and adjacent five and six-membered rings (Table 15, Figure 23). The contact involving a pyridyl ring lies within the coordination polymer ribbon, and so has no influence on the overall dimensionality for the structure. The other two contacts both involve the quinonoid ring, which is far from being aromatic, as evidenced by the long bond C5-C6, 1.548(2) Å, linking the two carbonyl units. The two ribbons are linked by C-O···π stacking interactions involving the five-membered ring enclosing the Cu atom (Table 15, Figure 23). These weak non-covalent interactions help to stabilize and establish a 2-D network.

Table IV.15 Short C-N···π and C-O···π contacts (Å, º)

C-X···Cg	X···Cg	C···Cg	C-X···Cg
C24-N25···Cg1[i]	3.571 (2)	3.171 (2)	87.00 (13)
C24-N25···Cg2[i]	3.360 (2)	3.496 (2)	87.00 (13)
C24-N25···Cg4[ii]	2.928 (2)	3.131 (2)	89.03 (14)
C6-O6···Cg4[iii]	3.118 (2)	4.264 (2)	158.19 (16)

Symmetry codes: (i) x, y, -1+z; (ii) x, y, z; (iii) x, 1.5-y, -0.5+z

Cg1, Cg2 and Cg4 represent the centroids of the rings respectively [Cu(1)-N(1)-C(4B)-C(6B)-N(10), [N(1)-C(2)-C(3)-(4)-C(4A)-C(4B)], [C(4A)-C(4B)-C(6B)-C(6A)-C(6)-C(5), respectively.
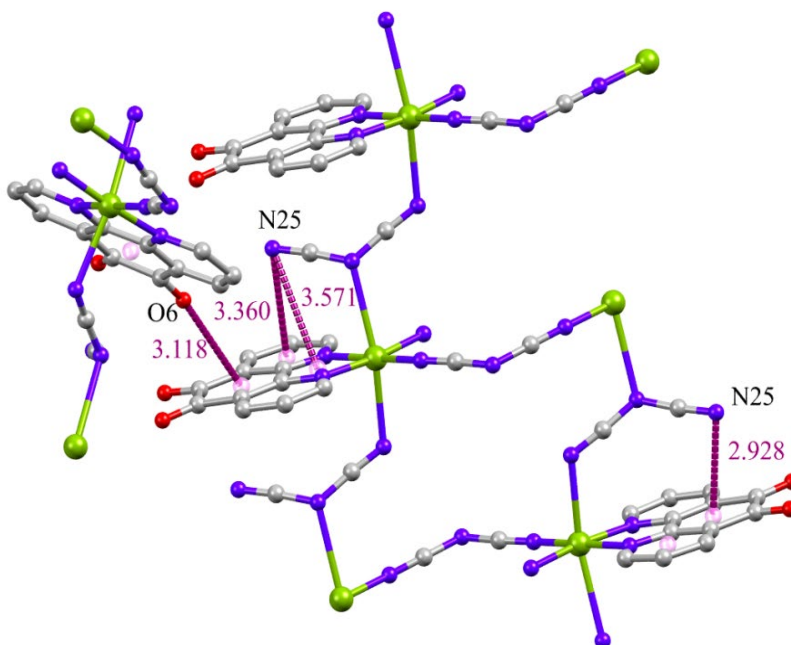
Figure IV.23 C-N···π and C-O···π interactions in the structure in compound C10.

b. Cu(II) complex with the ligand Trz-C

The complex [Cu(Trz-C)$_2$(NCS)$_2$], abbreviated as C11, forms a 2-D network structure that crystallizes in two distinct forms within the centrosymmetric monoclinic system P2$_1$/n, depending on the crystallization conditions (Figure 24). C11a appears as brown crystals when methanol diffuses into an acetone solution, while C11b forms green crystals when acetonitrile diffuses into a DMF solution. Both structures comprise two bridging bidentate Trz-C ligands, two bridging ambidentate thiocyanate anions, and a copper atom (Cu1). The Trz-C ligands coordinate to Cu1 via the triazole group's nitrogen atom and feature an intramolecular hydrogen bond between the phenol group and the central nitrogen. Similarly, the thiocyanate anions coordinate to Cu1 through both nitrogen and sulfur atoms. This coordination pattern links the metal centers, creating the 2-D network. A selection of distances is shown in Table 16.
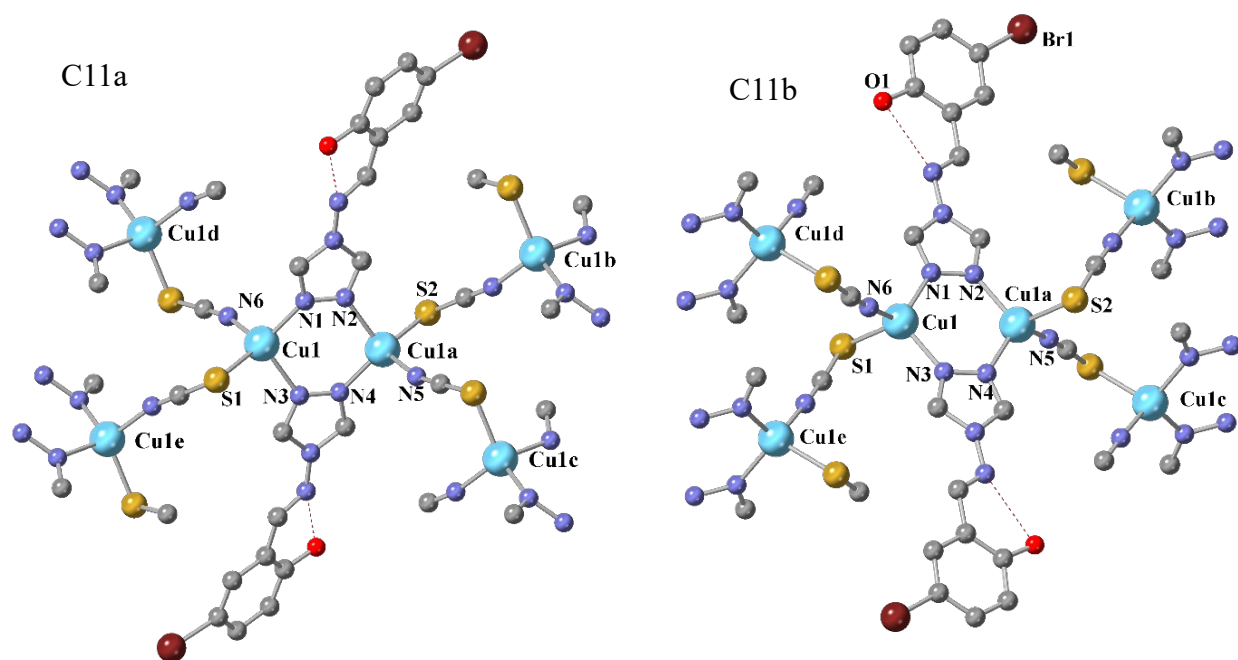
Figure IV.24 The structure of C11a and C11b with partial atom numbering. Hydrogen atoms are not included for clarity, except for the hydrogen atoms represented by small spheres participating in O-H···N interactions (red dotted lines). The ellipsoids contain 50% of the electron density.
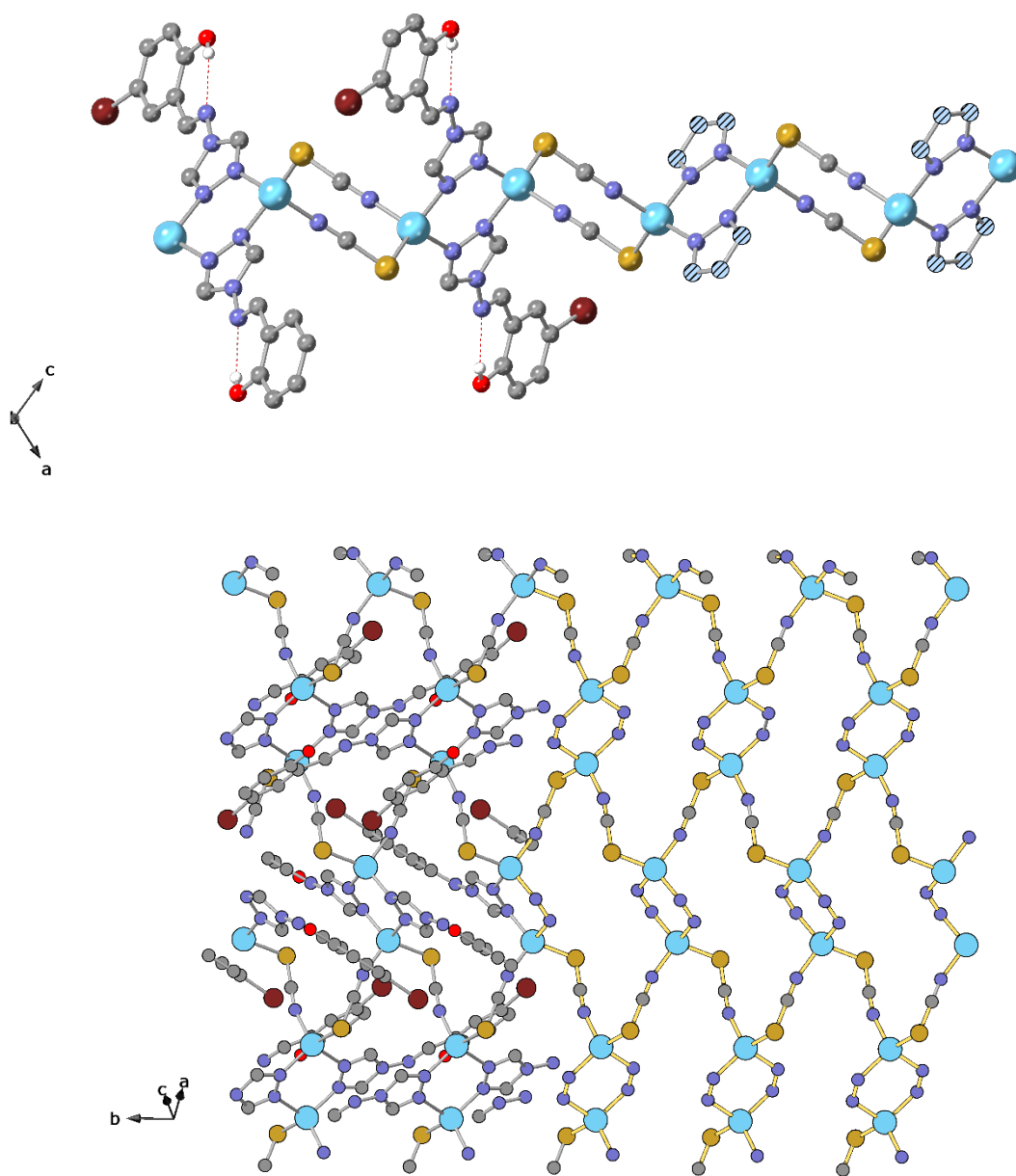
Figure IV.25 Structure of C11 and simplified network describing its topology in the ac plane. Hydrogen bonds are represented by red dotted lines (top), and Superposition of the complex structure with the simplified network describing its topology viewed in the ab plane (bottom). Atoms: Cu (light blue); S (yellow); O (red); N (blue); C (gray).

IV.4 Magnetic properties of binuclear Co(II) and Fe(II) complexes

Magnetic property studies were conducted on complexes C2, C3, C5, C7and C9 using single-crystal samples under a 10 kOe magnetic field. Complexes C2, C5, and C7 exhibit varying

degrees of antiferromagnetic behavior, while C3 demonstrates spin-crossover properties. These measurements, performed on high-quality crystals, provide insights into the relationship between the molecular structures of these compounds and their diverse magnetic behaviors. The observed antiferromagnetic interactions in three complexes and the spin-crossover phenomenon in C3 contribute to our understanding of magnetic properties in this class of materials.

IV.4.1 Cobalt (II)

IV.4.1.1 Binuclear Complexes

Complex C2, containing two Co(II) ions, exhibits clear antiferromagnetic behavior as revealed by magnetic susceptibility measurements conducted under a 10 kOe field from 300 K to 1.5 K. The room temperature $\chi_m T$ value aligns with expectations for two Co(II) ions, but as the temperature decreases, a continuous decline in magnetic susceptibility is observed. This antiferromagnetic coupling between the Co$\cdots$Co centers is evidenced by a sharp decrease in the $\chi_m T$ product, which approaches zero at low temperatures. Further supporting this interpretation, the magnetization plot displays an almost linear behavior with very low magnetization values at high magnetic fields. These combined observations strongly indicate that the magnetic moments of the cobalt ions align in opposite directions at lower temperatures, resulting in a diminished overall magnetic moment for the complex.
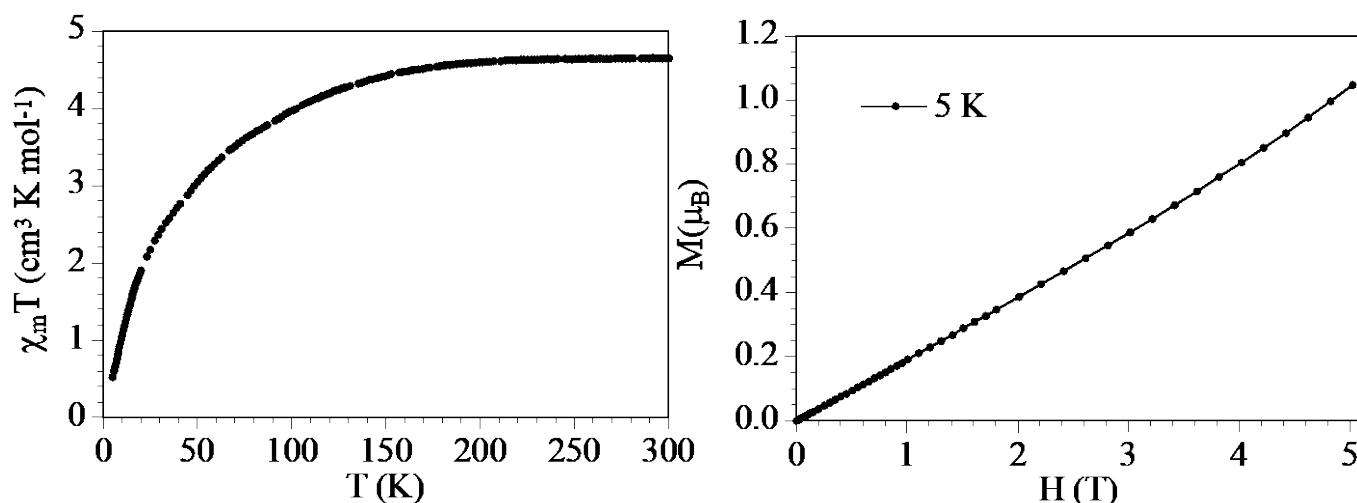
Figure IV.26 a) Plot of the χmT product as a function of temperature for compound C2; b) Magnetization data as a function of the applied magnetic field.

Complex C5 exhibits magnetic behavior similar to C2, as revealed by susceptibility measurements conducted under a 10 kOe field from 300 K to 0 K. The χmT value at room temperature aligns with expectations for two Co(II) ions. The magnetic profile shows two distinct phases: a gradual decrease in susceptibility from 300 K to 140 K, followed by a pronounced drop to 0 K. This pattern, particularly the sharp reduction in χmT approaching zero at low temperatures, strongly indicates antiferromagnetic coupling between the Co$\cdots$Co centers. Corroborating this interpretation, the magnetization data exhibits near-linear behavior with minimal values at high fields. These observations point to a system where the cobalt ions' magnetic moments increasingly oppose each other as temperature decreases, characteristic of antiferromagnetic interactions.
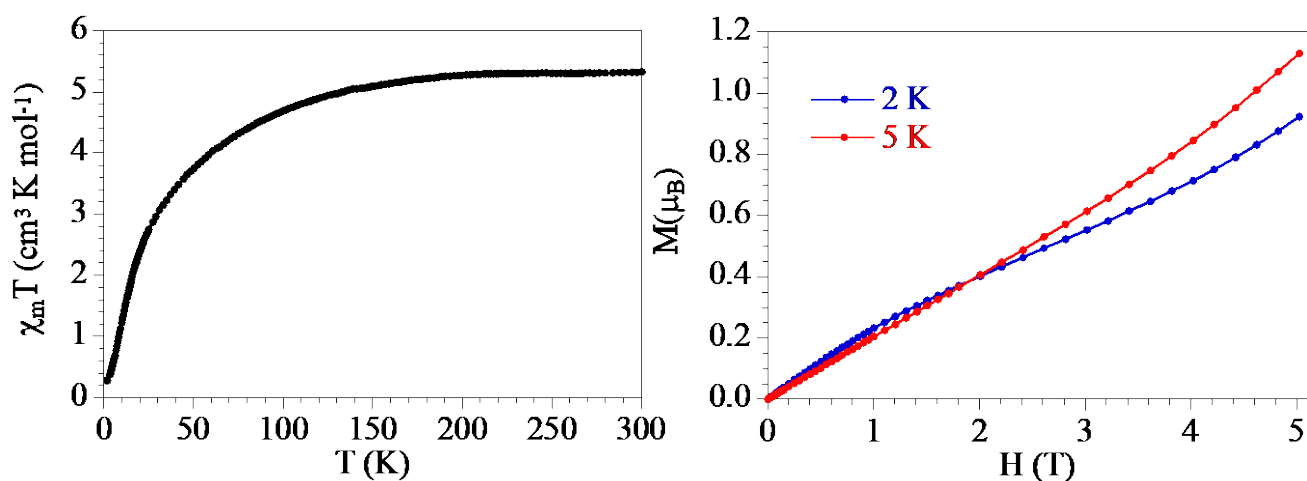
Figure IV.27 a) Plot of the χmT product as a function of temperature for compound C5; b) Magnetization data as a function of the applied magnetic field.

The complex C7 demonstrates magnetic properties closely aligned with those of C2 and C5, based on susceptibility measurements conducted under a 10 kOe field from 300 K to 0 K. The room temperature χmT value corresponds to the expected value for two Co(II) ions. The magnetic susceptibility exhibits a biphasic behavior: a subtle decrease from 300 K to 150 K, followed by a dramatic decline to 0 K. This pattern, particularly the sharp reduction in χmT approaching zero at low temperatures, strongly indicates antiferromagnetic coupling between the Co$\cdots$Co centers. The magnetization data further supports this interpretation, showing an almost linear relationship with notably low values at high magnetic fields. These observations

collectively suggest that as temperature decreases, the magnetic moments of the cobalt ions increasingly align in opposite directions, characteristic of antiferromagnetic interactions.

Figure IV.28 a) Plot of the χmT product as a function of temperature for compound C7; b) Magnetization data as a function of the applied magnetic field.

IV.4.1.2 One-Dimensional Coordination Polymer

The One-Dimensional Coordination Polymer C9 complex, ([Co(dca)$_4$(Trz-E)$_2$].MeOH), exhibits field-induced slow magnetic relaxation characteristic of a single-molecule magnet (SMM), arising from the interplay of significant magnetic anisotropy and the suppression of quantum tunneling of magnetization (QTM).

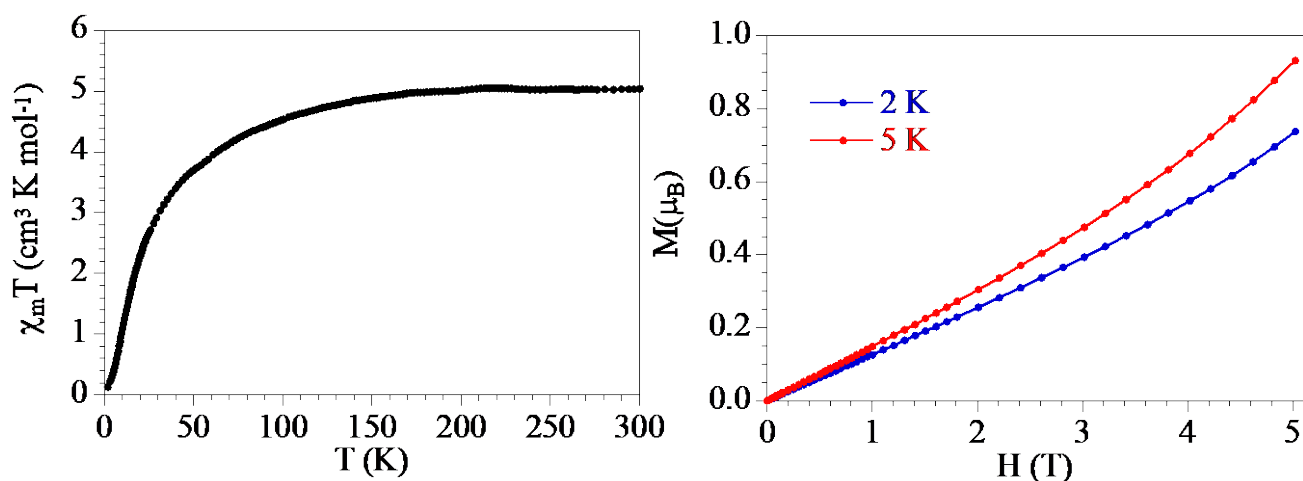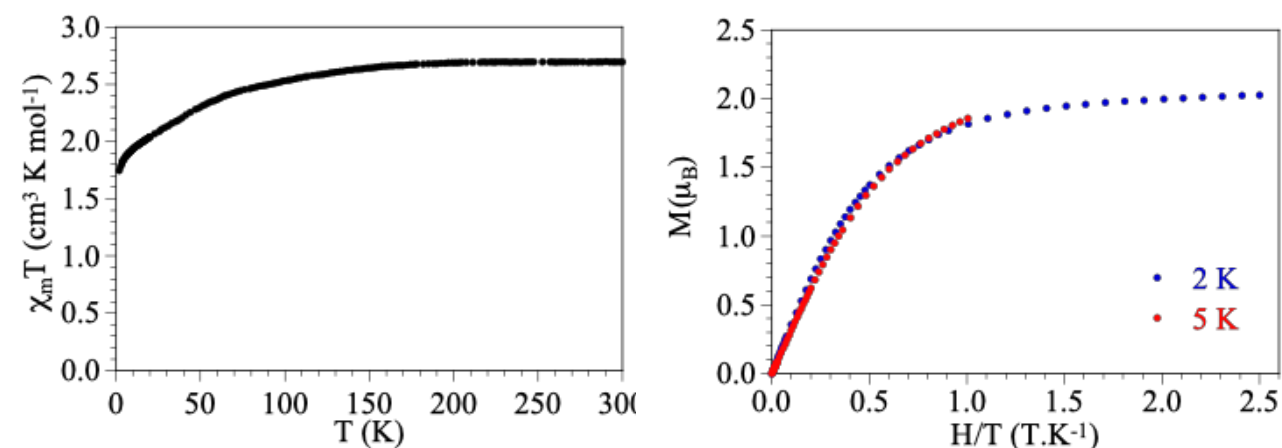
Figure IV.29 a) Plot of the χmT product as a function of temperature for compound C7; b) Magnetization data as a function of the applied magnetic field.

DC susceptibility measurements confirm an isolated high-spin Co(II) ion (S = 3/2) at room temperature, with a decreasing χmT product upon cooling indicative of spin-orbit coupling, a crucial factor in generating magnetic anisotropy in octahedral Co(II) systems, as widely documented in the literature [17-19]. This anisotropy, further corroborated by magnetization measurements, is essential for establishing an energy barrier to spin reversal, similar to observations in other mononuclear Co(II) and Fe(II) complexes exhibiting SMM-like behavior [20].
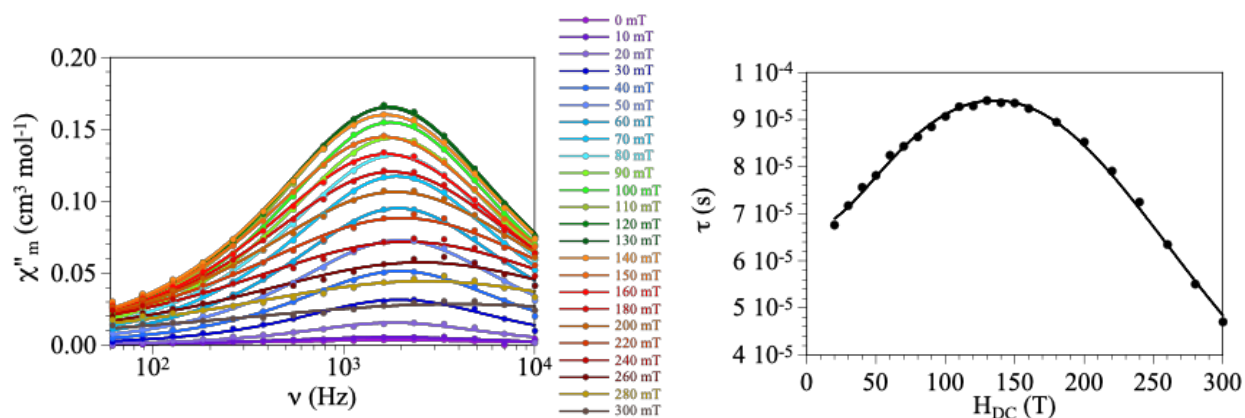
Figure IV.30 Frequency dependence of the out-of-phase AC susceptibility (χ'') under various applied DC fields at 1.9 K (left), and Field dependence of the relaxation time (τ) at 1.9 K showing optimization at 130 mT

While no AC signal is observed under zero DC field due to dominant QTM, the application of a DC field, optimally at 130 mT, effectively suppresses QTM, leading to the emergence of frequency-dependent AC susceptibility signals, a hallmark of field-induced SMMs. This behavior is consistent with the lifting of M_s degeneracy by the applied field, hindering ground-state QTM, as reported in related Co(II) and Fe(II) SMM studies [21-26].

The temperature dependence of the relaxation time at 130 mT, extracted from Debye fits, reveals a non-linear Arrhenius plot, suggesting a combination of Direct and Orbach relaxation processes, mirroring the behavior often observed in systems with multiple relaxation pathways [18-27]. The extracted effective energy barrier (Ueff = 28(2) K) and pre-exponential factor (τ_0 = $1.2(6) \times 10^{-7}$ s) align with values reported for field-induced mononuclear Co(II) SMMs.
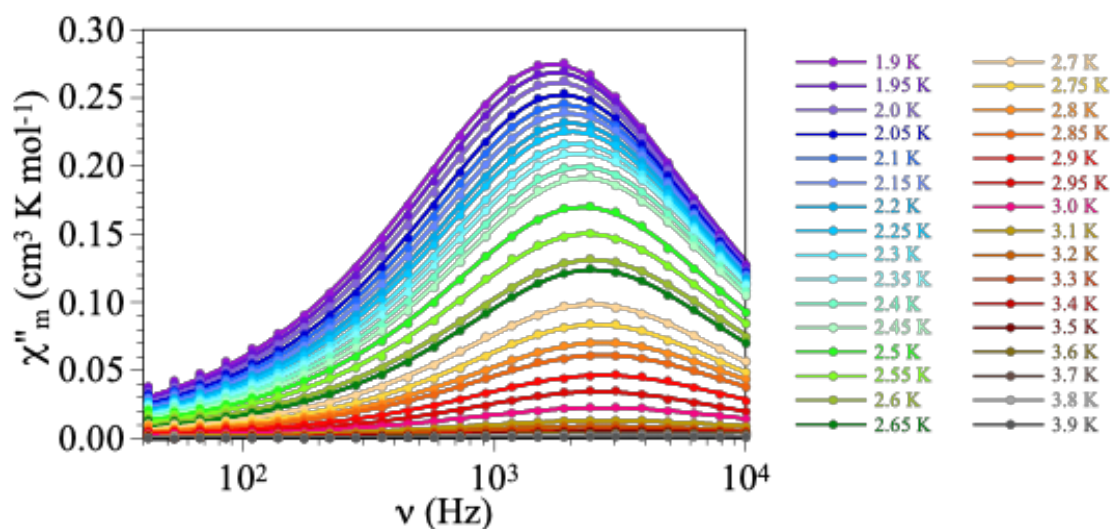
Figure IV.31 Frequency-Dependent Out-of-Phase AC Susceptibility (χ'') of C9 complex at Various Temperatures under H_{DC} = 130 mT

In summary, the magnetic behavior of C9 is characterized by field-dependent slow relaxation of magnetization, driven by the synergistic effects of significant magnetic anisotropy and the suppression of QTM by an applied DC field. This, coupled with the observed relaxation dynamics involving both Direct and Orbach processes, firmly establishes C9 as a compelling example of a field-induced mononuclear Co(II) SMM.
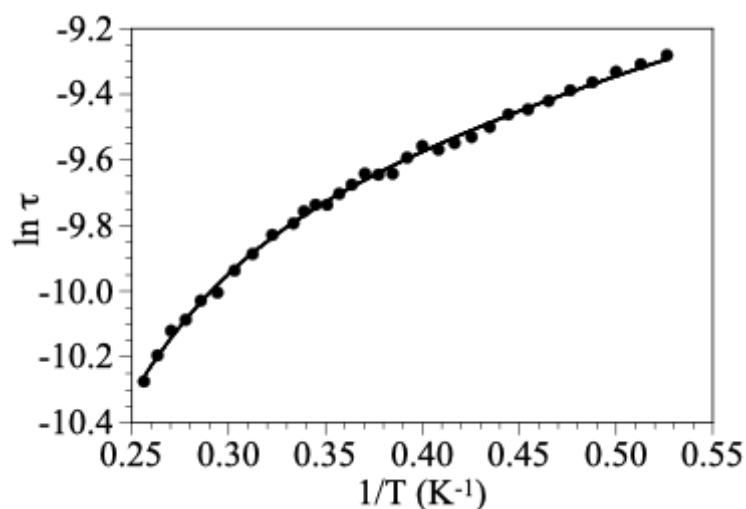
Figure IV.32 Arrhenius plot of the relaxation time (ln τ vs. 1/T) under 130 mT DC field showing Direct and Orbach contributions to the relaxation mechanism

This study contributes to the expanding field of Co(II)-based SMMs, highlighting the potential for designing and fine-tuning slow magnetic relaxation in molecular systems for applications in molecular magnetism and spintronics [28].

IV.4.2 iron (II)

The magnetic susceptibility measurements of C3 were measured using a SQUID magnetometer from 300 K to 10 K under an external magnetic field of 10 kOe, to study its SCO behavior.
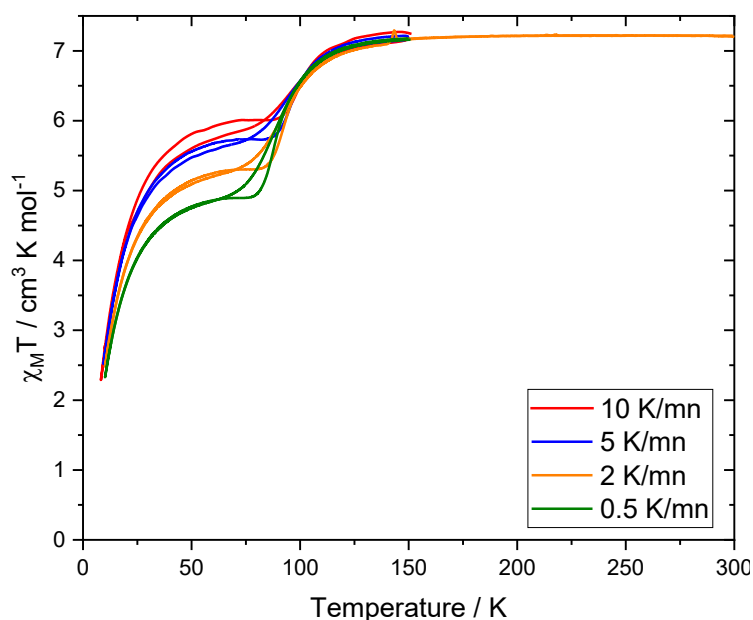
Figure IV.33 The χmT vs. temperature graph, plotted at various temperature scan rates under a 10 kOe external magnetic field for Compound C3

For the C3 compound, the χMT product of 5.24 cm³ K mol⁻¹ at 65 K does not correspond to a mixture of high-spin (HS) and low-spin (LS) states for the two Fe(II) sites, suggesting a potentially incomplete spin crossover. Furthermore, the hysteresis shape closely resembles the behavior observed when the metastable HS* state, present at low temperatures, overlaps with the stability region of the hysteresis loop [29–34]. To investigate the occurrence of kinetic trapping of the metastable HS state, two experiments were conducted. In the first experiment, the thermal spin crossover was recorded at varying temperature scan rates, ranging from 0.5 K/min to 10K/min (Figure 33).
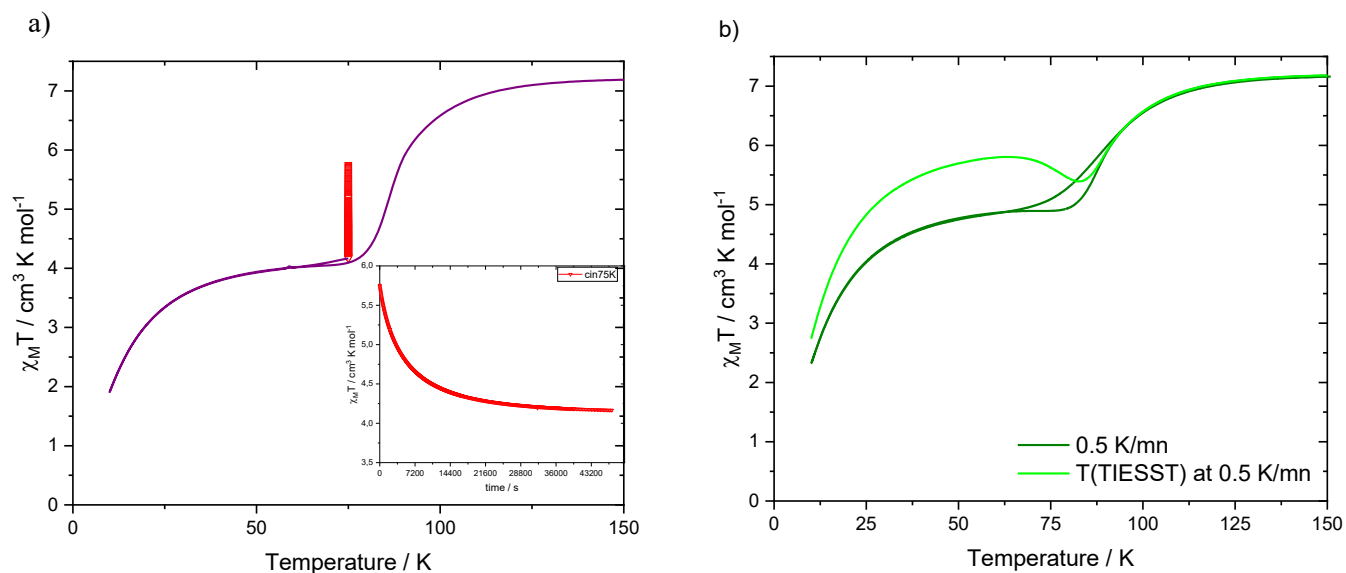
Figure IV.34 (a) Evolution of the χMT product of C3 at 75 K as function of time (∇, inset) and consecutive thermal cycle (-); (b) thermal dependence of the χMT product of C3 recorded at 0.5 K/mn under a 10 kOe external magnetic field before thermal quenching (-) and after thermal quenching (TIESST) (-).

It was observed that faster temperature scan rates resulted in a greater residual HS population at low temperatures, a clear indication of kinetic trapping of the HS metastable state [29–36]. This was further confirmed by monitoring isothermal relaxation kinetics at 75 K after rapidly cooling the sample at 10 K/min (Figure 34a). Initially, the χMT product decreased exponentially from 5.75 to 4.16 cm³ K mol⁻¹ over twelve hours. Beyond this point, the relaxation appeared to reach a plateau, indicating a long-lived state. Notably, the final χMT value of 4.16 cm³ K mol⁻¹ was lower than that observed during slow cooling at 0.5 K/min and closely matched the value expected for one Fe(II) site in the HS state. This finding confirms that only one Fe(II) site undergoes a spin crossover. Upon cooling and heating, a transition curve with a switching temperature of approximately 87 K was recorded for the active Fe(II) site, likely without any associated hysteresis.

The second experiment aimed to probe kinetic trapping by rapidly cooling the sample to 10 K to maximize the quenching of the HS* state (Figure 34b). This approach relates to Thermally

Induced Excited Spin-State Trapping (TIESST) [35]. At 10 K, TIESST did not appear to be effective. However, when warming the sample at 0.5 K/min to record the T(TIESST) curve, a distinct difference was observed compared to the thermal spin crossover curve recorded at the same scan rate. The T(TIESST) curve increased to 5.82 cm³ K mol⁻¹ at 65 K, exhibited a T(TIESST) temperature around 75 K, reached a minimum at 82 K, and then increased again, eventually overlapping with the thermal spin crossover curve. This behavior is characteristic of the overlap between the stable HS state above the spin crossover temperature and the metastable HS* state below it [29–32].

conclusion

The findings of this chapter underscore the versatility of 1,2,4-triazole-based Schiff base ligands in forming diverse coordination complexes with transition metals. These complexes exhibit a rich array of structural and magnetic properties, driven by the interplay of metal-ligand interactions and crystallographic arrangements. The study not only enhances the understanding of transition metal coordination chemistry but also highlights the potential of these materials for applications in molecular magnetism, catalysis, and materials science. Future work could explore the tuning of ligand frameworks to achieve targeted functionalities and expand the scope of their industrial and technological applications.

References

[1] Schiff, H. (1864). Mittheilungen aus dem Universitätslaboratorium in Pisa: eine neue Reihe organischer Basen. Justus Liebigs Annalen der Chemie, 131(1), 118-119.

[2] Sathyanarayana, R., & Poojary, B. (2020). Exploring recent developments on 1, 2, 4-triazole: Synthesis and biological applications. Journal of the Chinese Chemical Society, 67(4), 459-477.

[3] Cao, Y., & Lu, H. (2021). Advances in the application of 1, 2, 4-triazole-containing hybrids as anti-tuberculosis agents. Future Medicinal Chemistry, 13(23), 2107-2124.

[4] Bikas, R., Mirzakhani, P., Noshiranzadeh, N., Sanchiz, J., Krawczyk, M. S., Kalofolias, D. A., & Lis, T. (2020). Synthesis, crystal structure and magnetic properties of a pentanuclear Mn (III) cluster with 1, 2, 4-triazole based Schiff base ligand. Inorganica Chimica Acta, 505, 119461.

[5] Phadke Swathi, N., Alva, V. D., & Samshuddin, S. (2017). A review on 1, 2, 4-triazole derivatives as corrosion inhibitors. Journal of Bio-and Tribo-Corrosion, 3(4), 42.

[6] Specklin, D. (2014). Propriétés magnétiques et structurales de complexes moléculaires supportés par des ligands de type acyle-hydrazone (Doctoral dissertation, Université de Strasbourg).

[7] Bouslimani, N., Clément, N., Rogez, G., Turek, P., Bernard, M., Dagorne, S., ... & Welter, R. (2008). Synthesis and magnetic properties of new mono-and binuclear iron complexes with salicyloylhydrazono dithiolane ligand. Inorganic chemistry, 47(17), 7623-7630.

[8] Bouslimani, N., Clément, N., Rogez, G., Turek, P., Choua, S., Dagorne, S., & Welter, R. (2010). Stability, molecular structures and magnetic properties of dinuclear iron complexes supported by benzoic hydrazide derivative ligands. Inorganica Chimica Acta, 363(1), 213-220.

[9] Li, B., Sun, X., Cheng, G., & Ji, Z. (2009). Synthesis, Crystal Structure and Bioactivities of a Novel Propeller Shaped Manganese Complex with the Ligand N′-Benzylidenesalicylhydrazide. Chinese Journal of Chemistry, 27(7), 1312-1316.

[10] Larson, E. J., & Pecoraro, V. L. (1991). The peroxide-dependent. mu. 2-O bond formation of manganese complex [Mn (IV) SALPN (O)] 2. Journal of the American Chemical Society, 113(10), 3810-3818.

[11] Benamara, N. (2020). Conception de ligands fonctionnels pour l'élaboration de réseaux magnétiques à base d'ions du fer, du cobalt ou de terre rare (Doctoral dissertation, Université de Strasbourg; Université Ferhat Abbas (Sétif, Algérie)).

[12] Calancea, S. (2013). Synthèse et caractérisations de nouveaux complexes binucléaires à transfert d'électron de type {Fe (μ-CN) M}(M= Fe, Mn, Co) (Doctoral dissertation, Université Sciences et Technologies-Bordeaux I).

[13] Zein, S. (2005). Études théoriques des composés à transition de spin mono-et bi-nucléaires (Doctoral dissertation, Université Claude Bernard-Lyon I).

[14] Groom, C. R., Bruno, I. J., Lightfoot, M. P., & Ward, S. C. (2016). The Cambridge structural database. Structural Science, 72(2), 171-179.

[15] Wu, A. Q., Zheng, F. K., Cai, L. Z., Guo, G. C., Mao, J. G., & Huang, J. S. (2003). One-dimensional chain structure of catena-poly [[[(1, 10-phenanthroline) copper (II)]-μ-dicyanamido] perchlorate]. Acta Crystallographica Section E: Structure Reports Online, 59(5), m257-m259.

[16] Wood, P. A., Allen, F. H., & Pidcock, E. (2009). Hydrogen-bond directionality at the donor H atom—analysis of interaction energies and database statistics. CrystEngComm, 11(8), 1563-1571.

[17] Kahn, O. (1993). Molecular Magnetism, VCH Publ. Inc.: New York, NY, USA, 393.

[18] Gatteschi, D., Sessoli, R., & Villain, J. (2006). Molecular nanomagnets (Vol. 5). Oxford University Press, USA.

[19] Podgajny, R., Korzeniak, T., Przychodzeń, P., Gimenez-Saiz, C., Rams, M., Kwaśniak, M., & Sieklucka, B. (2010). Magneto–Structural Correlations in Discrete MnII-WV Cyano-Bridged Assemblies with Polyimine Ligands.

[20] Christou, G., Gatteschi, D., Hendrickson, D. N., & Sessoli, R. (2000). Single-molecule magnets. MRS bulletin, 25(11), 66-71.

[21] Guo, F. S., Day, B. M., Chen, Y. C., Tong, M. L., Mansikkamäki, A., & Layfield, R. A. (2017). A dysprosium metallocene single-molecule magnet functioning at the axial limit. Angewandte Chemie International Edition, 56(38), 11445-11449.

[22] Li, L. H., Peng, Y., Zhang, S., Xiao, T., Song, Y., Ye, H. Y., ... & Hu, Z. B. (2023). Effect of Subtle Changes on the Slow Relaxation Behavior of Co (II) Ions Based Metal-Organic Frameworks. Crystal Growth & Design, 23(4), 2099-2105.

[23] Nain, S., Kumar, M., & Ali, M. E. (2023). The impact of spin-vibrational coupling on magnetic relaxation of a Co (ii) single-molecule magnet. Physical Chemistry Chemical Physics, 25(21), 14848-14861.

[24] Malinová, N., Juráková, J., Brachňaková, B., Midlíková, J. D., Čižmár, E., Santana, V. T., ... & Šalitroš, I. (2023). Magnetization slow dynamics in mononuclear Co (II) field-induced single-molecule magnet. Crystal Growth & Design, 23(4), 2430-2441.

[25] Li, J. Y., Huang, Y. L., Li, T. C., Li, Y., Wang, L. X., Zhang, L., ... & Xiang, J. (2023). Slow Magnetic Relaxation in a Mononuclear 8-Coordinate Fe (II) Compound Bearing the Phenanthroline-Amide Ligand. Zeitschrift für anorganische und allgemeine Chemie, 649(20), e202300138.

[26] Li, G. L., Wu, S. Q., Zhang, L. F., Wang, Z., Ouyang, Z. W., Ni, Z. H., ... & Sato, O. (2017). Field-Induced Slow Magnetic Relaxation in an Octacoordinated Fe (II) Complex with Pseudo-D 2 d Symmetry: Magnetic, HF-EPR, and Theoretical Investigations. Inorganic chemistry, 56(14), 8018-8025.

[27] Guo, Y. N., Xu, G. F., Guo, Y., & Tang, J. (2011). Relaxation dynamics of dysprosium (III) single molecule magnets. Dalton Transactions, 40(39), 9953-9963.

[28] Woodruff, D. N., Winpenny, R. E., & Layfield, R. A. (2013). Lanthanide single-molecule magnets. Chemical reviews, 113(7), 5110-5148.

[29] Paradis, N., Chastanet, G., & Létard, J.-F. (2012). Spin crossover studies. European Journal of Inorganic Chemistry, 2012(23), 3618.

[30] Paradis, N., Chastanet, G., Varret, F., & Létard, J.-F. (2013). Investigations into thermal spin transitions. European Journal of Inorganic Chemistry, 2013(5), 698.

[31] Varret, F., Boukheddaden, K., Chastanet, G., Paradis, N., & Létard, J.-F. (2013). Mechanisms of kinetic trapping in Fe(II) compounds. European Journal of Inorganic Chemistry, 2013(7), 763.

[32] Paradis, N., Chastanet, G., Palamarciuc, T., Rosa, P., Varret, F., Boukheddaden, K., & Létard, J.-F. (2015). Thermal and structural insights into spin transitions. Journal of Physical Chemistry C, 119(36), 20039.

[33] Money, V. A., Carbonera, C., Halcrow, M. A., Howard, J. A. K., & Létard, J.-F. (2007). Thermal hysteresis in Fe(II) spin crossover complexes. Chemistry—A European Journal, 13(20), 5503.

[34] Chakraborty, P., Enachescu, C., Walder, C., Bronisz, R., & Hauser, A. (2012). Thermally induced excited spin-state trapping. Inorganic Chemistry, 51(19), 9714.

[35] Chastanet, G., Desplanches, C., Baldé, C., Rosa, P., Marchivie, M., & Guionneau, P. (2018). A critical review of the T (LIESST) temperature in spin crossover materials− What it is and what it is not. Chemistry Squared-Chem2, 2, 2.

[36] Yu, X., Chen, T. Y., Ye, Y. S., & Bao, X. (2020). Spin crossover in mononuclear Fe (II) complexes based on a tetradentate ligand. Journal of Physics: Condensed Matter, 32(17), 174001.

General Conclusion

This thesis embarked on a journey to explore the intricate world of multifunctional molecular materials, focusing on the design, synthesis, characterization, and theoretical understanding of novel 1,2,4-triazole-based Schiff base ligands and their transition metal complexes. By bridging the fields of corrosion inhibition and molecular magnetism, specifically SCO and slow magnetic relaxation, this research aimed to develop and investigate compounds possessing both switchable magnetic properties and the ability to protect metals from degradation.

The research presented in this thesis yielded several significant outcomes:

1. Successful Design, Synthesis, and Characterization of Novel Ligands and Metal Complexes: Employing meticulous synthetic procedures, a series of novel 1,2,4-triazole-based Schiff base ligands were successfully designed and synthesized. These ligands were subsequently used to prepare a diverse range of metal complexes, including one- and two-dimensional coordination complexes with Cu(II), Co(II), Fe(II), and Ni(II). Comprehensive characterization using techniques such as X-ray crystallography confirmed the successful formation of the synthesized compounds.

2. Comprehensive electrochemical studies demonstrated the exceptional corrosion inhibition capabilities of newly synthesized triazole-based Schiff base compounds (Trz-C, Trz-D, and Trz-E) for XC48 carbon steel in acidic media. Multiple analytical techniques, including gravimetric measurements, potentiodynamic polarization, and electrochemical impedance spectroscopy (EIS), revealed that the inhibition efficiency increases proportionally with inhibitor concentration, with Trz-C emerging as the most effective compound. Temperature-dependent analyses suggested that the primary protection mechanism involves physisorption of the inhibitor molecules onto the steel surface. Scanning electron microscopy (SEM) provided direct evidence for the formation of a protective molecular film, confirming the proposed inhibition mechanism.

3. Detailed quantum chemical calculations using density functional theory (DFT) revealed crucial insights into the electronic properties and molecular behavior of the synthesized ligands and their complexes. The analysis encompassed frontier molecular orbital energies (HOMO-LUMO), electronic energy gaps, and molecular electrostatic potential distributions, providing a theoretical framework to understand the observed corrosion

inhibition efficiencies. The computational results aligned closely with experimental observations, validating the integrated experimental-theoretical methodology and offering predictive capabilities for molecular design. This theoretical investigation established clear structure-property relationships, enabling rational design strategies for enhanced performance in future applications.

4. The synthesized metal complexes exhibited diverse magnetic behaviors correlated with their structural characteristics. Binuclear Co(II) complexes (C2, C5, C7) demonstrated antiferromagnetic coupling, while the one-dimensional coordination polymer (C9) showed field-induced slow magnetic relaxation typical of SMM. The binuclear Fe(II) complex (C3) displayed scan-rate dependent spin crossover behavior, indicating kinetic trapping of metastable high-spin states. Single-crystal X-ray diffraction analyses revealed crucial structural features, including coordination geometries and intermolecular interactions, that govern these magnetic properties. The detailed crystallographic characterization provided fundamental insights into magnetic exchange pathways, anisotropy, and relaxation mechanisms in these complexes.

In essence, this doctoral research has made significant strides in advancing our understanding of the design principles and structure-property relationships governing the behavior of multifunctional molecular materials. By seamlessly integrating cutting-edge experimental techniques with state-of-the-art theoretical methodologies, this work has paved the way for the development of next-generation materials with tailored properties, addressing critical challenges in diverse technological domains, ranging from corrosion mitigation to molecular electronics and data storage. The findings presented herein provide a solid foundation for future investigations into the fascinating interplay between molecular structure, electronic properties, and macroscopic behavior in advanced materials.

Appendix

Crystallographic Data

Trz-B

Table 1. Crystallographic data and refinement parameters for compound 1

Identification code	Compound(1)
Formula	$C_{18}H_{16}N_8O_2$
$D_{calc.}$/ g cm^{-3}	1.379
μ /mm^{-1}	0.097
Formula Weight	376.39
Size/mm^3	? ×? ×?
T/K	300(2)
Crystal System	monoclinic
Space Group	P2$_1$/n
a/Å	5.15070(10)
b/Å	28.8569(10)
c/Å	12.1988(4)
α /°	90
β /°	91.5650(10)
γ /°	90
V/Å^3	1812.47(9)
Z	4
Z'	1
Wavelength/Å	0.71073
Radiation type	MoK$_\alpha$
Θ_{min}/°	2.697
Θ_{max}/°	30.600
Measured Refl's.	61069
Indep't Refl's	5580
Refl's I≥2 σ(I)	3930
R$_{int}$	0.0679
Parameters	261
Restraints	0
Largest Peak	0.181
Deepest Hole	-0.237

Trz-C

Table 2. Crystallographic data and refinement parameters for compound 2

Identification code	Compound(2)
Formula	$C_9H_7BrN_4O$
$D_{calc.}$/ g cm^{-3}	1.701
μ /mm^{-1}	3.930
Formula Weight	266.10
Size/mm^3	? ×? ×?
T/K	298(2)
Crystal System	monoclinic
Space Group	P2$_1$/c
a/Å	13.609(8)
b/Å	10.428(6)
c/Å	7.348(5)
α /°	90
β /°	94.63(3)
γ /°	90
V/Å^3	1039.3(11)
Z	4
Z'	1
Wavelength/Å	0.71073
Radiation type	MoK$_\alpha$
Θ_{min}/°	2.464
Θ_{max}/°	30.499
Measured Refl's.	30256
Indep't Refl's	3149
Refl's I≥2 σ(I)	2005
R_{int}	0.0683
Parameters	137
Restraints	0
Largest Peak	1.586
Deepest Hole	-1.200

Trz-D
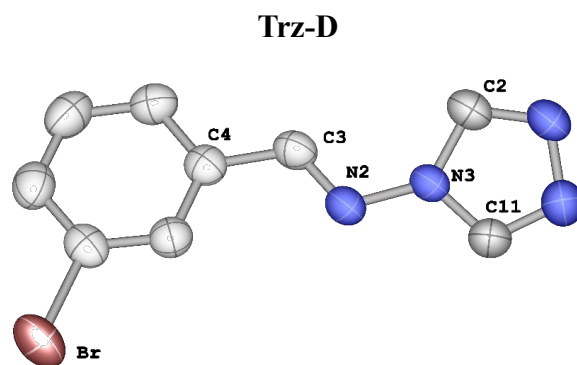
Table 3. Crystallographic data and refinement parameters for compound 3

Identification code	Compound(3)
Formula	$C_9H_7N_4Br_1$
$D_{calc.}$/ g cm^{-3}	1.761
μ /mm^{-1}	4.799
Formula Weight	251.08
Size/mm^3	? ×? ×?
T/K	300(2)
Crystal System	orthorhombic
Space Group	$P2_12_12_1$
a/Å	3.9578(3)
b/Å	11.2674(9)
c/Å	37.981(3)
α /°	90
β /°	90
γ /°	90
V/Å^3	1693.7(2)
Z	4
Z'	1
Wavelength/Å	0.71073
Radiation type	MoK$_\alpha$
Θ_{min}/°	2.102
Θ_{max}/°	30.588
Measured Refl's.	24269
Indep't Refl's	5200
Refl's I≥2 σ(I)	3814
R_{int}	0.0296
Parameters	217
Restraints	0
Largest Peak	0.509
Deepest Hole	-0.415

Trz-E
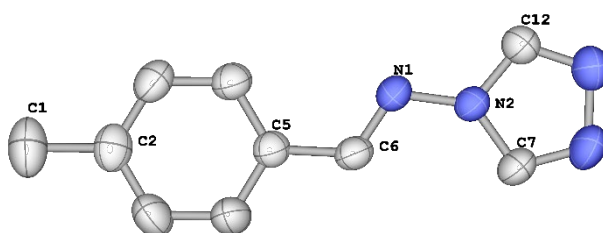
Table 4. Crystallographic data and refinement parameters for compound 4

Identification code	Compound(4)
Formula	$C_{10}H_{10}N_4$
$D_{calc.}$/ g cm^{-3}	1.210
μ /mm^{-1}	0.078
Formula Weight	186.21
Size/mm^3	? ×? ×?
T/K	298(2)
Crystal System	trigonal
Space Group	R-3
a/Å	34.198(10)
b/Å	34.198(10)
c/Å	4.5405(18)
α /°	90
β /°	90
γ /°	120
V/Å^3	4599(3)
Z	6
Z'	0.333333
Wavelength/Å	0.71073
Radiation type	MoK$_\alpha$
Θ_{min}/°	2.382
Θ_{max}/°	33.821
Measured Refl's.	31321
Indep't Refl's	4060
Refl's I≥2 σ(I)	2382
R_{int}	0.0781
Parameters	128
Restraints	0
Largest Peak	0.691
Deepest Hole	-0.310

[Cu(Trz-A)₂(NCS)₂]
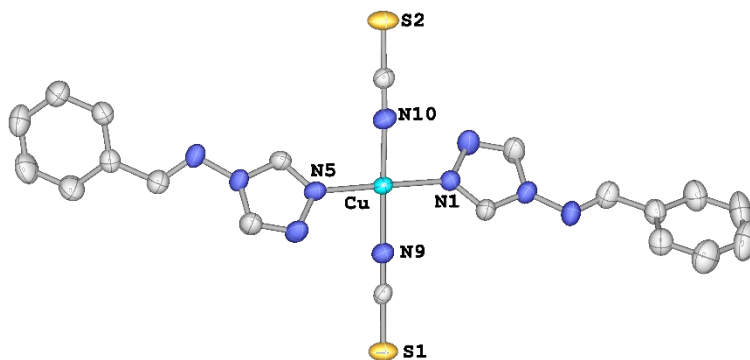
Table 5. Crystallographic data and refinement parameters for compound 5

Identification code	Compound(5)
Formula	$C_{20}H_{16}CuN_{10}S_2$
$D_{calc.}$/ g cm^{-3}	1.580
μ /mm^{-1}	1.213
Formula Weight	524.09
Size/mm^3	0.25×0.04×0.02
T/K	295.0(2)
Crystal System	monoclinic
Space Group	$P2_1$
a/Å	5.6095(11)
b/Å	14.205(3)
c/Å	13.952(3)
α /°	90
β /°	97.74(3)
γ /°	90
V/Å^3	1101.5(4)
Z	2
Z'	1
Wavelength/Å	0.71073
Radiation type	MoK$_a$
Θ_{min}/°	2.868
Θ_{max}/°	28.340
Measured Refl's.	24070
Indep't Refl's	5502
Refl's I≥2 σ(I)	4065
R$_{int}$	0.0703
Parameters	299
Restraints	1
Largest Peak	0.365
Deepest Hole	-0.469

[Co₂(Trz-D)₅(NCS)₄]·DMF

Table 6. Crystallographic data and refinement parameters for compound 6

Identification code	Compound(6)
Formula	$C_{52}H_{42}Br_5Co_2N_{25}S_4O$
$D_{calc.}$/ g cm^{-3}	1.504
μ /mm^{-1}	3.289
Formula Weight	1678.70
Size/mm^3	? ×? ×?
T/K	301(2)
Crystal System	monoclinic
Space Group	C2/c
a/Å	20.1648(7)
b/Å	18.7782(6)
c/Å	19.6113(7)
α /°	90
β /°	108.730(2)
γ /°	90
V/Å^3	7032.7(4)
Z	8
Z'	1
Wavelength/Å	0.71073
Radiation type	MoK$_a$
Θ_{min}/°	2.431
Θ_{max}/°	25.714
Measured Refl's.	101864
Indep't Refl's	6683
Refl's I≥2 σ(I)	4534
R_{int}	0.0753
Parameters	488
Restraints	706
Largest Peak	2.817
Deepest Hole	-0.715

[Fe₂(Trz-D)₅(NCS)₄]·DMF

Table 7. Crystallographic data and refinement parameters for compound 7

Identification code	Compound(7)
Formula	$C_{52}H_{42}Br_5Fe_2N_{25}S_4O$
$D_{calc.}$/ g cm^{-3}	1.470
μ /mm^{-1}	3.156
Formula Weight	1672.53
Size/mm^3	? ×? ×?
T/K	301(2)
Crystal System	monoclinic
Space Group	C2/c
a/Å	20.413(9)
b/Å	18.865(8)
c/Å	19.744(8)
α /°	90
β /°	108.766(12)
γ /°	90
V/Å^3	7199(5)
Z	8
Z'	1
Wavelength/Å	0.71073
Radiation type	MoK$_a$
Θ_{min}/°	2.419
Θ_{max}/°	26.359
Measured Refl's.	110573
Indep't Refl's	7330
Refl's I≥2 σ(I)	4522
R_{int}	0.0961
Parameters	488
Restraints	706
Largest Peak	3.452
Deepest Hole	-0.639

[Ni₂(Trz-D)₅(NCS)₄]·DMF

Table 8. Crystallographic data and refinement parameters for compound 8

Identification code	Compound(8)
Formula	$C_{52}H_{42}Br_5Ni_2N_{25}S_4O$
$D_{calc.}$/ g cm^{-3}	1.521
μ /mm^{-1}	3.392
Formula Weight	1678.22
Size/mm^3	? ×? ×?
T/K	301(2)
Crystal System	monoclinic
Space Group	C2/c
a/Å	19.9650(12)
b/Å	18.7714(11)
c/Å	19.6130(10)
α /°	90
β /°	108.9470(10)
γ /°	90
V/Å^3	6952.1(7)
Z	8
Z'	1
Wavelength/Å	0.71073
Radiation type	MoK$_a$
Θ_{min}/°	2.950
Θ_{max}/°	24.756
Measured Refl's.	67975
Indep't Refl's	5894
Refl's I≥2 σ(I)	3822
R_{int}	0.0953
Parameters	488
Restraints	712
Largest Peak	2.455
Deepest Hole	-0.891

[Co$_2$(Trz-E)$_5$(NCS)$_4$]
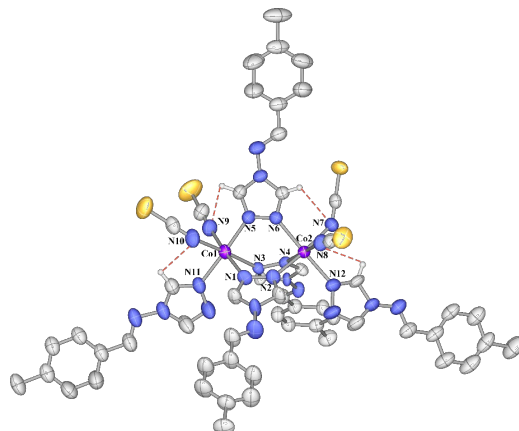
Table 9. Crystallographic data and refinement parameters for compound 9

Identification code	Compound(9)
Formula	C$_{54}$H$_{50}$Co$_2$N$_{24}$S$_4$
D$_{calc}$./ g cm^{-3}	1.277
μ /mm^{-1}	0.677
Formula Weight	1281.26
Size/mm^3	? ×? ×?
T/K	299(2)
Crystal System	triclinic
Space Group	P-1
a/Å	11.9476(6)
b/Å	14.1611(7)
c/Å	21.3278(9)
α /°	75.1160(10)
β /°	74.7880(10)
γ /°	78.4840(10)
V/Å^3	3331.2(3)
Z	31
Z'	15.5
Wavelength/Å	0.71073
Radiation type	MoK$_a$
Θ_{min}/°	2.421
Θ_{max}/°	24.796
Measured Refl's.	195001
Indep't Refl's	11432
Refl's I≥2 σ(I)	9635
R$_{int}$	0.0905
Parameters	1168
Restraints	1792
Largest Peak	0.566
Deepest Hole	-0.439

[Ni₂(Trz-E)₅(NCS)₄].H₂O

Table 10. Crystallographic data and refinement parameters for compound 10

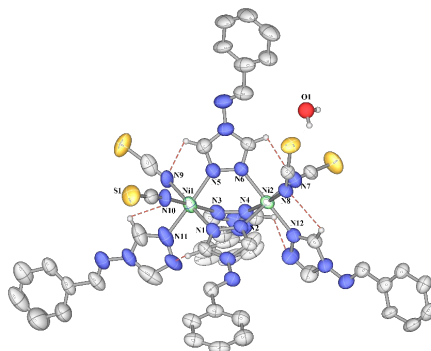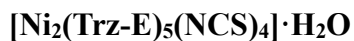| Identification code	Compound(10)
Formula	$C_{54}H_{52}Co_2N_{24}S_4O$
$D_{calc.}/\ g\ cm^{-3}$	1.302
$\mu\ /mm^{-1}$	0.754
Formula Weight	1298.80
Size/mm³	$? \times ? \times ?$
T/K	301.00
Crystal System	triclinic
Space Group	P-1
a/Å	11.9313(16)
b/Å	14.100(2)
c/Å	21.213(3)
$\alpha\ /°$	75.313(5)
$\beta\ /°$	74.908(4)
$\gamma\ /°$	77.890(5)
V/Å³	3293.3(8)
Z	2
Z'	1
Wavelength/Å	0.71073
Radiation type	MoK$_a$
$\Theta_{min}/°$	2.244
$\Theta_{max}/°$	24.799
Measured Refl's.	143403
Indep't Refl's	11297
Refl's I≥2 σ(I)	8860
R_{int}	0.0646
Parameters	1147
Restraints	2582
Largest Peak	0.790
Deepest Hole	-0.584

$[Co_2(Trz\text{-}E)_5(NCS)_4]\cdot H_2O\cdot EtOH$

Table 11. Crystallographic data and refinement parameters for compound 11

Identification code	Compound(11)
Formula	$C_{51}H_{46}Co_2N_{24}S_4O_2$
$D_{calc.}$/ g cm^{-3}	1.344
μ /mm^{-1}	0.739
Formula Weight	1273.19
Size/mm^3	? ×? ×?
T/K	301(2)
Crystal System	triclinic
Space Group	P-1
a/Å	11.6399(7)
b/Å	13.4074(7)
c/Å	21.3764(10)
α /°	93.570(2)
β /°	104.569(2)
γ /°	107.586(2)
V/Å^3	3043.1(3)
Z	2
Z'	1
Wavelength/Å	0.71073
Radiation type	MoK$_a$
Θ_{min}/°	2.337
Θ_{max}/°	26.493
Measured Refl's.	186517
Indep't Refl's	12536
Refl's I≥2 σ(I)	9741
R_{int}	0.0558
Parameters	729
Restraints	0
Largest Peak	0.887
Deepest Hole	-0.826

[Ni₂(Trz-E)₅(NCS)₄]·H₂O

Table 12. Crystallographic data and refinement parameters for compound 12

Identification code	Compound(12)
Formula	$C_{49}H_{42}Ni_2N_{24}S_4O$
D_{calc}./ g cm^{-3}	1.351
μ /mm^{-1}	0.819
Formula Weight	1253.17
Size/mm^3	? ×? ×?
T/K	299(2)
Crystal System	triclinic
Space Group	P-1
a/Å	11.6793(5)
b/Å	13.3193(6)
c/Å	21.3078(9)
α /°	92.343(2)
β /°	105.326(2)
γ /°	107.827(2)
V/Å^3	3016.4(2)
Z	2
Z'	1
Wavelength/Å	0.71073
Radiation type	MoK$_a$
Θ_{min}/°	2.332
Θ_{max}/°	28.332
Measured Refl's.	189338
Indep't Refl's	15018
Refl's I≥2 σ(I)	9186
R_{int}	0.0865
Parameters	719
Restraints	0
Largest Peak	1.118
Deepest Hole	-0.560

[Co(dca)₄(Trz-E)₂].MeOH
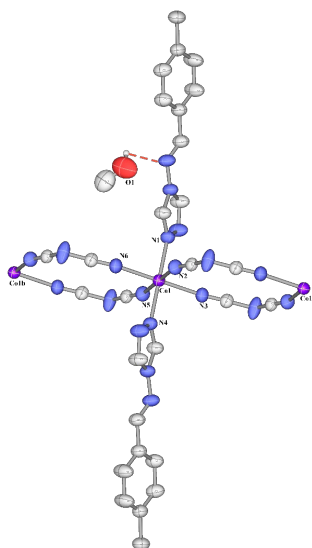
Table 13. Crystallographic data and refinement parameters for compound 13

Identification code	Compound(13)
Formula	$C_{29}H_{24}CoN_{20}O$
$D_{calc.}/\ g\ cm^{-3}$	1.402
$\mu\ /mm^{-1}$	0.665
Formula Weight	584.81
Size/mm³	? ×? ×?
T/K	300(2)
Crystal System	triclinic
Space Group	P-1
a/Å	7.3228(3)
b/Å	9.1267(5)
c/Å	10.8659(6)
$\alpha\ /°$	82.884(2)
$\beta\ /°$	84.182(2)
$\gamma\ /°$	74.435(2)
V/Å³	692.41(6)
Z	1
Z'	0.5
Wavelength/Å	0.71073
Radiation type	MoK$_a$
$\Theta_{min}/°$	2.328
$\Theta_{max}/°$	31.575
Measured Refl's.	52439
Indep't Refl's	4575
Refl's I≥2 σ(I)	3149
R_{int}	0.0882
Parameters	197
Restraints	0
Largest Peak	1.224
Deepest Hole	-0.641

[Cu(Trz-C)₂(NCS)₂]

C11a

C11b
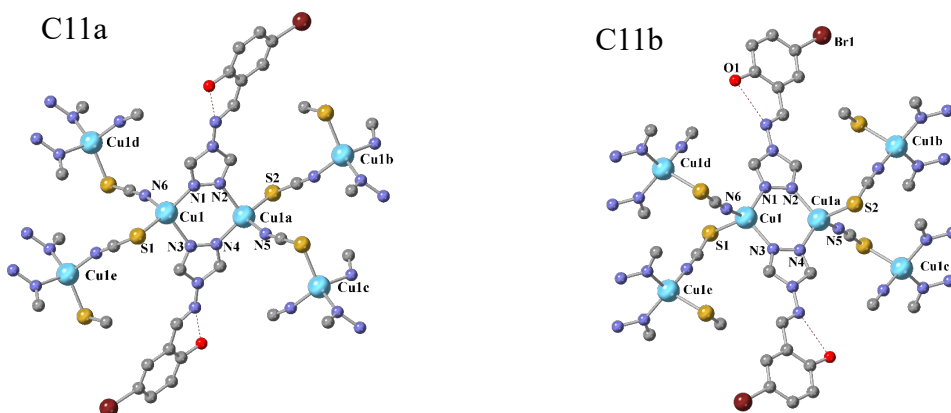
Table 14. Crystallographic data and refinement parameters for compounds 14a and 14b

Identification code	Compound(14a)	Compound(14b)
Formula	$C_{22}H_{14}Br_2Cu_2N_{12}O_2S_4$	$C_{22}H_{14}Br_2Cu_2N_{12}O_2S_4$
$D_{calc.}$/ g cm^{-3}	1.906	2.032
μ /mm^{-1}	4.713	5.025
Formula Weight	893.59	893.59
Size/mm^3	0.32×0.04×0.04	0.21×0.03×0.02
T/K	295.0(2)	295(2)
Crystal System	monoclinic	monoclinic
Space Group	P2$_1$/n	P2$_1$/n
a/Å	14.051(3)	13.6394(8)
b/Å	6.0591(12)	6.6669(4)
c/Å	24.293(5)	15.0103(9)
α /°	90	90
β /°	139.08(3)	111.414(3)
γ /°	90	90
V/Å^3	1354.6(7)	1270.70(13)
Z	4	4
Z'	1	1
Wavelength/Å	0.71073	0.71073
Radiation type	MoK$_a$	MoK$_a$
Θ_{min}/°	2.560	2.531
Θ_{max}/°	32.041	32.068
Measured Refl's.	44099	46913
Indep't Refl's	4681	4411
Refl's I≥2 σ(I)	2909	3292
R_{int}	0.0810	0.0699
Parameters	173	173
Restraints	0	0
Largest Peak	1.198	0.876
Deepest Hole	-0.815	-0.726

Abstract

This thesis explores multifunctional materials based on 1,2,4-triazole-derived Schiff base ligands and their transition metal complexes, with a particular focus on corrosion inhibition and magnetic properties. Notably, the synthesized ligands exhibited remarkable corrosion inhibition for XC48 CS in acidic media, achieving efficiencies up to 80.00%. To understand this behavior, structure-property relationships were elucidated, highlighting the importance of molecular design in achieving effective protection. Furthermore, a series of novel mono- and binuclear complexes, along with coordination polymers, were synthesized using Cu(II), Co(II), Ni(II), and Fe(II) ions. Detailed structural insights into these complexes were obtained through X-ray diffraction studies. Importantly, magnetic studies revealed a diverse range of behaviors, including antiferromagnetism, slow magnetic relaxation characteristic of SMM behavior, and SCO. Moreover, DFT calculations supported the experimental findings, providing further insight into the electronic structure and reactivity of these compounds.

Keywords : triazole, DFT, spin-crossover, SMM, corrosion inhibitor, X-ray diffraction

ملخص

تتناول هذه الأطروحة دراسة المواد متعددة الوظائف القائمة على ليجندات قاعدة شيف المشتقة من 1,2,4-تريازول ومركباتها مع معادن الانتقالية، مع التركيز بشكل خاص على تثبيط التآكل والخصائص المغناطيسية. أظهرت الليجندات المُحضرة فعالية عالية في تثبيط تآكل الفولاذ الكربوني في البيئات الحمضية، حيث وصلت الكفاءة إلى 80.00%. لفهم هذا السلوك، تم تحديد العلاقة بين البنية والخواص، مما يبرز أهمية التصميم الجزيئي لتحقيق حماية فعّالة. بالإضافة إلى ذلك، تم تحضير سلسلة من المركبات الأحادية والثنائية النواة، بالإضافة إلى بوليمرات التنسيق، باستخدام أيونات Cu(II)، Co(II)، Ni(II)، و Fe(II). وفرت دراسات حيود الأشعة السينية رؤى تفصيلية حول البنية التركيبية لهذه المركبات. كشفت الدراسات المغناطيسية عن مجموعة متنوعة من السلوكيات، بما في ذلك السلوك المضاد للمغناطيسية، والاسترخاء المغناطيسي البطيء المميز لسلوك المغناطيسات الجزيئية الأحادية (SMM)، وظاهرة الانتقال المغزلي (SCO). علاوة على ذلك، دعمت حسابات DFT النتائج التجريبية، مما وفّر فهماً أعمق للبنية الإلكترونية ونشاط هذه المركبات.

الكلمات المفتاحية : تريازول، نظرية الكثافة الوظيفية (DFT)، الانتقال المغزلي (SCO)، جزيء مغناطيسي أحادي (SMM)، مثبط التآكل، حيود الأشعة السينية.